Multi-photon Nonlinear Fluorescence Emission in Upconversion Nanoparticles for Super-Resolution Imaging

by Chaohao CHEN

Thesis submitted in fulfilment of the requirements for the degree of

Doctor of Philosophy

under the supervision of Dr. Fan Wang, Prof. Dayong Jin, Dr. Qian Peter Su, Dr. Peter Reece

University of Technology Sydney
Faculty of Science

04/09/2020

Certificate of Original Authorship

I, Chaohao CHEN declare that this thesis is submitted in fulfilment of the requirements for the award of Doctor of Philosophy, in the School of Mathematical and Physical Sciences, Faculty of Science, at the University of Technology Sydney.

This thesis is wholly my own work unless otherwise reference or acknowledged. In addition, I certify that all information sources and literature used are indicated in the thesis.

This document has not been submitted for qualifications at any other academic institution.

This research is supported by the Australian Government Research Training Program.

Production Note:
Signature: Signature removed prior to publication.

Date: 04/09/2020

For my lover

Rui Zhao

Acknowledgements

First and foremost, I would like to express my deep and sincere gratitude to my supervisors. I am particularly grateful to Prof. Jin for offering the opportunity to pursue a PhD in such a great research platform, to Dr Wang for the patient advises and guidances in the experiment designs and modelling simulations, to Dr Su for mentoring the knowledge in biological engineering and Dr Peter Reece in the optical engineering. I would like to thank each of them for their constructive criticisms and helpful discussions on my PhD thesis. Their research attitudes always inspire me to work happily and professionally.

I would like to address a special thanks to Mr Baolei Liu for help developing the image process algorithm, Mr Xuchen Shan for the Labview code and Mr Yongtao Liu for the help of energy level simulations. I would like to acknowledge to Mrs Xiangjun Di, Mr Dejiang Wang and Mr Baoming Wang for their help with cell culture that involved in this thesis. I would also like to thank Dr Jiayan Liao and Dr Shihui Wen for the high-quality upconversion nanoparticle synthesis.

I would like to mention all the member of the IBMD (past and present), who has provided technical supports or experiments suggestions and assistance. I enjoy working with these lovely people and appreciate their help whenever I get any experimental difficulties. I would like to thank all of the friends I have who exist outside the realm of research during the three years in Sydney. Thanks for being so understanding and always keeping my feet on the ground.

I would like to thank my supportive family for their continuous supports and love throughout my whole life. Specially thanks to my wife Rui Zhao, for her understanding and incalculable contribution to our little family.

Finally, I would like to acknowledge the Australian Government Research Training Program and the China Scholarship Council Scholarship for providing the scholarship and research opportunities.

Format of Thesis

This thesis consists of five chapters. Chapter 1 is the introduction and in Chapters 2-4 the research results are the focus on applying optical nonlinear response curves of upconversion nanoparticles. The objective is to implement new modalities of super-resolution microscopies. Chapter 5 concludes this thesis with a summation of the main themes covered in this investigation. This thesis flowchart is illustrated below.

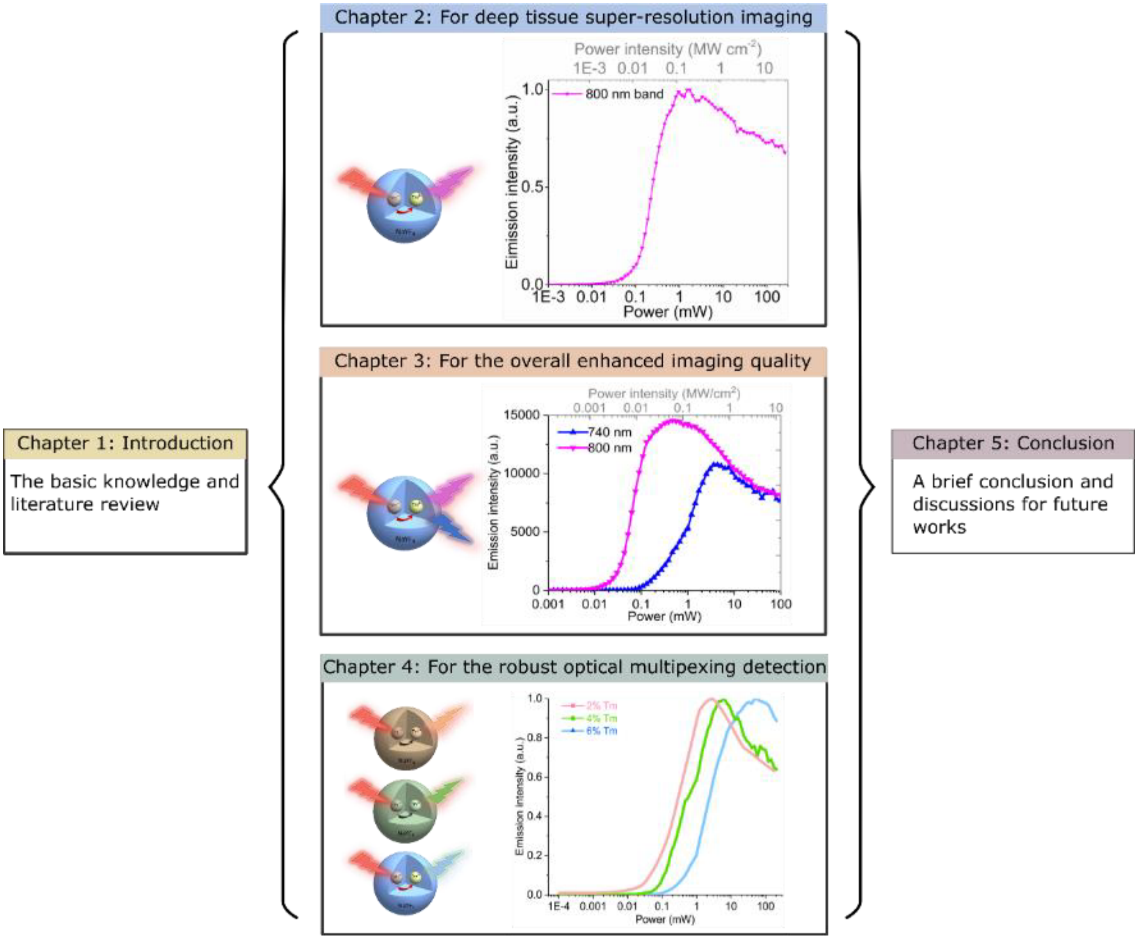

This thesis summarizes the key results from my PhD research program, in which the topic covered is super-resolution microscopy and nanoparticle-based super-resolution microscopy. My PhD sets out to develop new super-resolution microscopy methods using advanced nanomaterials. The main bulk of the framework developed for this thesis consists of three results chapters. The first chapter describes the use of a near-infrared nonlinear response curve from a single nanoparticle to develop a deep tissue super-resolution imaging method. The second results chapter takes advantages of the two response curves from two emission bands of a single nanoparticle, which yields two things: the overall improved image quality; and increased imaging speed. In the third chapter concerning the results, I explore the multiple emission curves derived from different nanoparticles for robust optical multiplexing detection. Lastly, the conclusion and discussions for future research are provided.

List of Publications

- Articles

1. **Chen, C.**, Liu, B., Liu, Y., Liao, J., Wang, F. & Jin, D. Fourier domain heterochromatic fusion for single beam scanning super-resolution microscopy. (Under revision)
2. **Chen, C.**†, Wang, F.†, … & Jin, D. Multi-photon near-infrared emission saturation nanoscopy using upconversion nanoparticles. *Nature Communications (2018),* 9:3290.
3. **Chen, C.**, Liu, Z. & Jin, D. Bypassing the limit in volumetric imaging of mesoscale specimens. *Advanced Photonics (2019)* 1.2 : 020502.
4. Liu, B., **Chen, C.**, Di, X., Wang, F. & Jin, D. Upconversion nonlinear structured illumination microscopy. *Nano Letter (2020)* 20, 7, 4775-4781.
5. Liao, J., Jin, D, **Chen, C.**, Li, Y. & Zhou, J. Helix shape power-dependent properties of single upconversion nanoparticles. *Journal of Physical Chemistry Letters (2020)* 11, 8, 2883-2890.
6. Liu, Y., Wang, F., Liu, H., Fang, G., Wen., **Chen, C.** … & Jin, D. Super-Resolution Mapping of Single Nanoparticles inside Tumor Spheroids. *Small (2020)* 10.1002. 201905572.
7. Clarke, C., Liu, D., Wang, F., Liu, Y., **Chen, C.**, ... & Jin, D. Large-scale dewetting assembly of gold nanoparticles for plasmonic enhanced upconversion nanoparticles. *Nanoscale (2018)* 10 (14), 6270-6276.

- Publication in the conference proceeding

8. **Chen, C.,** Wang, F…. & Jin, D. Upconversion nanoparticles assisted multi-photon fluorescence saturation microscopy. In Nanoscale Imaging, Sensing, and Actuation for Biomedical Applications XVI (Vol. 10891, p. 108910S). International Society for Optics and Photonics. SPIE 2019

- Patents

9. Wang, F., Jin, D. & **Chen, C.** A super-resolution imaging method, a plurality of upconversion nanoparticle fluorophores, and a super-resolution scanning microscope. WO2020028942A1, 2020-02-13. WIPO (PCT)
10. **Chen, C.,** Jin, D. & Wang, F. A super-resolution imaging method, a plurality of upconversion nanoparticle fluorophores, and a super-resolution scanning microscope. AU2018902855A0, 2018-08-16, (Australian Patent)

([1,2,8,9,10] are closely related to my PhD program)

Table of Symbols

λ	Acoustic radiation force	α	Objective aperture angle
n	Refractive index	I_{max}	Maximum STED beam power
I_{sat}	Saturation intensity	$h\nu$	Photon energy
σ	Cross-section of excitation	τ_{fl}	Fluorescence lifetime
T_1	The metastable dark triplet state	N	Total captured number of photons
s	The standard deviation of Gaussian function	b	The standard deviation of the background noise
I_{FED}	Image of FED	I_{Gau}	Image of a Gaussian beam
I_{Dou}	Image of a doughnut beam	r	A normalising coefficient
R_{tr}	The transmission ratio	P	The beam power
r_o	The loss rate of the objective lens	t_τ	The exposure time
A	The area of the focused laser spot	f	The pulse frequency
t_p	The pulse duration	α_λ	The attenuation coefficient
l	The path length	h_o	The FWHM of confocal PSF
ς	The saturation factor	k_{BA}	The carrier transition rate
σ_{TPA}	The molecular cross-section	$h_{em}(x)$	PSF of emission
$h_{exc}(x)$	PSF of the excitation beam	η	Emission response curve
$h_c(x)$	PSF of the confocal system	PSF_{Gau}	Gaussian PSF
PSF_{Dou}	Doughnut PSF	OTF_{eff}	Processed effective OTF
I_{eff}	Processed effective image	OTF_{Gau}	Gaussian OTF
OTF_{Dou}	Doughnut OTF		

Abbreviations

UCNPs	upconversion nanoparticles
NIRES	near-infrared emission saturation
PSFs	point speared functions
FWHM	full width at half maximum
SEM	scanning electron microscopy
TEM	transmission electron microscopy
TIRF	total internal reflection fluorescence
SNOM	scanning near-field optical microscopy
RESOLFT	reversible saturable or switchable optical fluorescence transitions
STED	stimulated emission depletion
GSD	ground-state depletion
SIM	structured illumination microscopy
PALM	photoactivated localisation microscopy
STORM	stochastic optical reconstruction microscopy
OTF	optical transfer functions
SPEM	saturated pattern excitation microscopy
SMLM	single-molecule localisation microscopy
FRC	Fourier ring correlation
SOFI	super-resolution optical fluctuation imaging
PAINT	point accumulation for imaging in nanoscale topography
QDots	quantum dots
CDots	carbon dots
PDots	polymer dots
AIE	aggregation-induced emission

UV	ultraviolet
ACQ	aggregation caused quenching
FED	fluorescence emission difference
MPLSM	multi-photon laser scanning microscopy
NIR	near-infrared
CW	continuous-wave
SW	single wavelength
VPP	vortex phase plate
HWP	half-wave plate
PBS	polarised beam splitter
DM	dichroic mirror
QWP	quarter-wave plate
BPF	bandpass filters
MMF	multimode fibre
SPAD	single-photon counting avalanche photodiode
OA	oleic acid
PFA	Paraformaldehyde
DFT	discrete Fourier transform
FFT	fast Fourier transform
THF	tetrahydrofuran
BSA	bovine serum albumin
BSA	bovine serum albumin
ISM	imaging scanning microscopy
LLS	lattice light sheet

Table of Contents

List of Figures

List of Tables

Abstract

Due to the unique optical properties gained by converting near-infrared light to shorter wavelength emissions, upconversion nanoparticles (UCNPs) have attracted considerable interest. Their superior features, including their multi-wavelength emissions, optical uniformity, background suppression, photostability and deep penetration depth through the tissue, make them extremely suitable for biological and biomedical applications. By taking advantage of their multi-photon nonlinear emissions in UNCPs, the goal of this thesis is to develop UCNPs-based super-resolution microscopy methods to address the challenges currently facing nanoscopy, for instance complexity, stability, limited penetration through the tissue and low throughput. The methods being investigated in this thesis make concrete the specific advantages in terms of image depth, speed, overall quality, and multiplexing potentials. To unlock a new mode of deep tissue super-resolution imaging, I first developed the near-infrared emission saturation (NIRES) nanoscopy by taking advantage of near-infrared-in and near-infrared-out optical nonlinear response curve from a single upconversion nanoparticle. This approach only requires two orders of magnitude that are lower than the excitation intensity, which is generally required for conventional multi-photon dyes. This work achieves a super-resolution of sub 50 nm, less than 1/20th of the excitation wavelength, and can image single UCNP through a 93 µm thick liver tissue.

To improve the overall imaging quality and simplify the system setups, I further exploited the distinct nonlinear photon response curves from the two emission bands in UCNP, and explored an opportunity for a tightly focused doughnut excitation to generate distinct spectral dependent point speared functions (PSFs). With controllable PSFs from multi-channel emissions by the excitation power density, this work presents the possibility of achieving super-resolution imaging under saturated fluorescence excitation via PSF engineering. Moreover, I developed a multicolour Fourier fusion algorithm to enlarge the optical system's frequency shifting ability, and yield an enhanced imaging quality at a higher imaging speed. By realising the uniform and distinct nonlinear emission curves from different nanoparticles, this work posits a new optical encoding dimension for multiplexing imaging. Proposed here is a robust PSF engineering strategy to extract emitter properties. This work extends the multiplexing capacity of UCNPs and offers new

opportunities for their applications. These methods are my contributions to the search for a stable, viable, and multifunctional optical imaging modality for the nanoscale context.

Chapter 1 Introduction

Optical microscopy has played a critical role in biological and medical fields since it allows us to investigate and discover the fine structures which are invisible to the naked eye. With the first microscope [1], British physicist Robert Hook discovered the plant cell wall structure in 1665. A contemporary Dutch scientist, A. Leeuwenhoek utilized a homemade microscope to observe the body’s inner workings on a microscopic level, seeing bacteria, sperm and even blood cells flowing through capillaries [2]. With further developments in optical microscope technology in the next few centuries, imaging of cells and their biological structures has enabled us to understand the functioning of cells. During the last three decades, continuous advances in technology and modern research methods have promoted the imaging field via a broad, interdisciplinary effort, leading to crucial improvements like better labelling, more in-depth observation, and increased spatial and temporal resolution. The significance of imaging modalities was recognized as the essential breakthrough invention when in 2014 the Nobel Prize in Chemistry was awarded 'for the development of super-resolved fluorescence microscopy'. The full potential capabilities of different super-resolution microscopy methods have yet to be explored, so the best approach to the advanced applications remains uncertain. For this reason, super-resolution imaging is an active field because nanometre resolution imaging is providing valuable insights into various biological systems, which important implications for future research [3].

Given the excellent luminescence characteristics of rare earth elements, this thesis applies upconversion nanomaterials on rare earth elements to optical super-resolution technologies, which lays the foundation for solving the challenges of super-resolution technology and single nanoparticle identification. The thesis covers fundamental physics and several main experiments that support them, including photoluminescence, optical nonlinear response, and imaging processing. These topics help to develop the field of upconversion nanoparticles (UCNPs) and super-resolution imaging. The thesis focuses on understanding the process of multi-photon nonlinear fluorescent emission in UCNPs. By combining the advanced imaging processing algorithm, this thesis develops multiple optical microscopy systems for biological imaging at the nanoscale.

Since this thesis falls under the domain of super-resolution microscopy, Chapter 1 firstly provides a general introduction of sub-diffraction imaging techniques. Moreover, this chapter discusses the development of fluorescent nanoparticle assisted super-resolution microscopes in biological and chemical analysis. This thesis aims to develop a stable and straightforward super-resolution approach by using nonlinear optical response in UCNPs.

1.1 Diffraction limit in microscopy

Based on experimental evidence and basic principles of physics, Abbe proposed a famous and vital conclusion which is that the resolution of the microsystem could not be reached by diffraction limit [4]. Specifically, the structures with the size under micrometre are not resolvable using a conventional light microscope due to diffraction. Abbe described the transverse dimension of the far-field microsystem focal spot as follows with this equation:

$$\Delta r \approx \frac{\lambda}{2n\sin\alpha} = \frac{0.61\lambda}{NA} \tag{1-1}$$

Where λ represents the wavelength, n is the refractive index of the medium between the sample and the objective, α is the semi-objective aperture angle, and NA represents the numerical aperture. The size of the refractive index n and the aperture half-angle α are constrained by objective technical conditions. Equation (1-1) represents the full width at half maximum (FWHM) of the point spread function (PSF) and is commonly used as a quantitative definition of resolution in far-field light microscopy.

Confronted with the resolution limit imposed by diffraction described in Equation (1-1) , scientists first opted for the obvious solution by increasing the numerical aperture or reducing the wavelength of the excitation laser. Nevertheless, the resolution of the optical microscopy was limited to approximately half wavelength of the light, even with perfect lenses and optimal alignment. Instead of visible light, the researcher ultimately employed an electron beam as a powerful approach to probe the sample to obtain more detailed information after realising the wave nature of electrons. Following the same physical principle but with a smaller wavelength down to one nanometre, electron microscopes such as the scanning electron microscopy (SEM) and transmission electron microscopy (TEM) [5], reveal the subcellular structure and atomic organization of the materials with accuracy approaching the angstrom range. However, the utility of those electron imaging approaches come with significant restrictions in a life science research due to the vacuum operation requirement precluding the observation of living imaging. Moreover, according to principles of signal detection, electron microscopes imposed a limitation on the specific label and visualized multiple cellular structures in one organic sample. Furthermore, transmission and scanning electron microscopes were relatively costly and time-consuming.

Compared to electron microscopy, fluorescent microscope still had a unique place in the life sciences since fluorescence imaging was compatible with cells, which enabled minimally invasive optical-based observation of events occurring through long periods of time. By taking advantage of the properties of evanescent waves, total internal reflection fluorescence (TIRF) microscopy [6] achieved high axial resolution but was still around the diffraction limit. Another near-field technique, scanning near-field optical microscopy (SNOM) [7] employed the evanescent light wave at the end of a fibre tip. The fluorescent signal from the sample surface could be collected to form an optical image, whose resolution depended on the aperture size instead of the wavelength. However, the interior of the cell was not visible with the SNOM technique, because the intensity of the evanescent wave exhibited exponential decay as a function of the distance from the boundary. Thus, SNOM could only collect high-resolution information near the surface of the sample, providing accurate information while remaining limited to the throughput in the case of slice techniques, as well as the volumetric images.

For studying sub-cellular structures and proteins within living cells, it would be advantageous to devise optical far-field methods that can image at this length scale [8]. Over the past several decades, far-field fluorescence microscopy using focused light has become an essential tool in several scientific disciplines including physical, chemical, and biomedical research, especially in living cells and organisms. However, the diffraction of light-imposed limitations on the spatial resolution, restricting the optical microscope's applicability. Therefore, it remains a pivotal challenge to improve the resolution of far-field fluorescence light microscopy while retaining significant advantages.

1.2 Super-resolution technology

Recent years have witnessed the development of super-resolution far-field optical microscopy techniques. To describe breaking the diffraction barrier in far-field microscopy, Stefan Hell introduced the concept of reversible saturable or switchable optical fluorescence transitions (RESOLFT). This involved switchable or reversibly saturable fluorophore transitions, where the diffraction barrier was overcome by a saturated optical transition (depletion) between two optically distinguishable states (on/off) in fluorescent molecules. To distinguish the fluorescent molecule from the adjacent ones, it technically lied on how to "switch" the fluorescent of each emitter, or how to control the fluorescence molecules switching between bright and dark states. For this consideration, optical super-resolution technologies introduced new factors from the photophysical and photochemical processes of fluorescent emitting, enabling the optical switching of fluorescent molecules.

According to the fundamental principles, super-resolution technology could be divided into two categories to deliver the resolution at nano-level. The first type of super-resolution technology mainly utilizes sub-diffraction-limit pattern excitation methods. Among the methods that improve resolution by pattern excitation modification, the most important techniques are referred to as stimulated emission depletion (STED) microscopy [9][10], ground-state depletion (GSD) microscopy [11] and structured illumination microscopy (SIM) [12]. The second technique relies on stochastically detecting the precise localization of single molecules, including photoactivated localization microscopy (PALM) [13] and stochastic optical reconstruction microscopy (STORM) [14]. There are many variations based on these schemes, as well as advanced imaging process methods which could be combined to improve the performance of those existing imaging modalities.

1.2.1 **Patterned excitation approach**

1.2.1.1 **Stimulated emission depletion (STED) microscopy**

In 1990, Stephen Hell proposed the concept of STED microscopy. Then he developed the first experiment of STED microscopy with his colleagues four years later [9]. STED also was the first technique successfully applied to super-resolution biological imaging of fixed cells [10]. As stated above, STED employed spatially modulated and saturable transitions between two fluorescent molecular states to engineer the PSF (**Figure 1-1**). The principle of this technique relied on a time-sequential readout of fluorescent probe photoswitching.

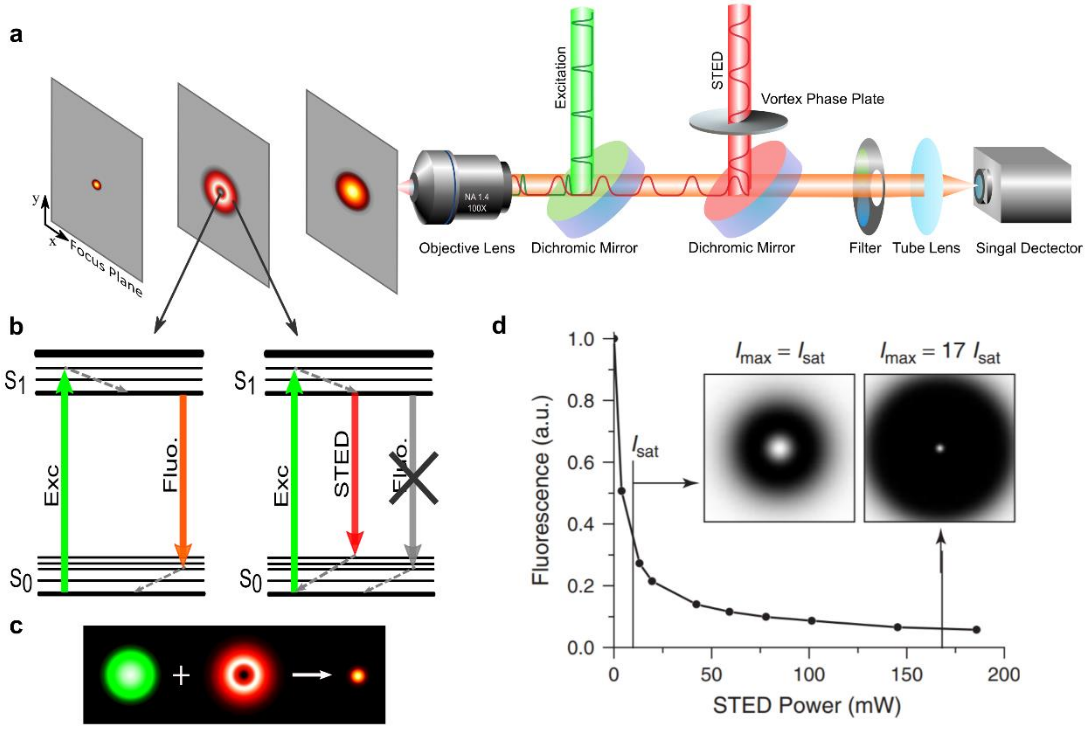

Figure 1-1 | The principle of a STED microscope. (**a**) Experimental setup for STED microscopy. (**b**) The simplified energy levels of the fluorescent switching in STED. (**c**) A schematic illustration of a STED microscopy. (**d**) The nonlinear depletion curve is shown as the normalized fluorescent signal curve is plotted as a function of the STED laser power. The insets show simulated depletion efficiency profiles for different values of maximum STED intensity [15].

A conventional STED optical setup configuration is presented in **Figure 1-1a** showing the phase plate, excitation and depletion lasers (green and red beams, respectively), dichromatic mirrors, objective, and tube lens. The probe is illuminated under two synchronized ultrafast tiny aligned sources consisting of an excitation pulse laser followed by a doughnut-shaped depletion pulse laser which is also named the STED beam. Generally, the pulse width of the excitation laser is shorter than that of the counterpart. By taking advantage of the time scales for molecular relaxation, pulsed lasers create radially symmetric depletion regions. **Figure 1-1b** demonstrates that fluorophores occur when a molecule encounters a photon that matches the energy gap between the ground (S_0) and excited (S_1) states. Upon interaction between the photon and excited fluorophore, the excited fluorophores instantaneously return to the ground state through stimulated emission before fluorescence emission can occur. Consequently, the STED beam can effectively deplete the fluorescence in the selected zones near the focal spot of the excited fluorophores (**Figure 1-1c**). The deactivation of the fluorophores occurs in the whole focus volume, excluding the centre of focus.

STED microscopy is one type of PSF engineering technique that sharpens the size of the focal spot, equivalent to expanding the microscope spatial frequency passband. Although both laser beams remain diffraction-limited, the final achievable resolution can easily bypass the diffraction limit since the STED beam is shaped to feature a near zero-intensity point at the centre of focus with the exponentially growing intensity toward the periphery. The nonlinear depletion of the excited fluorescent state by the STED beam constitutes the basis for achieving images with resolution under the diffraction limit (**Figure 1-1d**) [15]. Most spontaneous fluorescence can be depleted once the power of the STED beam is above the statured threshold. With the increased STED beam power, the 'nonfluorescent area' is expanding, but with little impact on the fluorescence in the central area. When two laser pulses are superimposed, only probes that sit in the centre of the STED beam can have the fluorescence emission, significantly restricting the emission and narrowing the size of the effective PSF. The FWHM of the remaining effective PSF is well approximated by an expanded form of Equation (1-2):

$$\Delta r_{STED} \approx \frac{\lambda}{2n \sin \alpha \sqrt{1+\left(\frac{I_{max}}{I_{sat}}\right)}} \tag{1-2}$$

where $I_{sat} = \frac{hv}{\tau_{fl}\sigma}$ is defined as the characteristic threshold intensity at which half of the maximal fluorescent signal is elicited, I_{max} is the maximum STED beam power, hv is the photon energy, σ is the cross-section of excitation, and τ_{fl} is the fluorescence lifetime of the excited state.

By increasing the power of the depletion laser, we can obtain an arbitrarily small Δr_{STED} to overcome the diffraction limit. Underlying Equation (1-2), the effective resolution increase with STED is proportional to the power of the depletion laser. The resolution is theoretically not fundamentally limited by diffraction anymore, but rather by the residual intensity in the doughnut minimum in practice and the material properties, like the largest I_{max} that may be tolerated by the specimen. It becomes problematic at extremely intense laser powers that are likely to cause destruction and rapid photobleaching of the fluorescent probe. By taking the nonbleaching feature of the nitrogen-vacancy (NV) centre in diamond [16], the highest resolution of 5.8 nm has been reported under the laser intensity of 3.7 GW/cm^2. For the biological structure imaging, the STED system can achieve a resolution of 20 nm with organic dyes [17], and a resolution of 50 nm with fluorescent proteins [18].

For recording a complete image, both lasers are raster scanned across the samples, similar to the conventional confocal microscope. One of the advantages of STED microscopy is that effective resolution increase is entirely dictated by the experimental configuration and the laser beam powers applied to the sample. Moreover, the image is acquired as the beam scans along with the sample without additional image processing for the first generation of STED microscopy. Meanwhile, the imaging speed of STED has reached up to 200 fps [10] and up to 28 fps for the biological samples [17].

It has been three decades since the first concept of STED was proposed, and much work has documented the enhanced performance of this imaging system, especially for those advanced versions to address the improvements in axial resolution for three-dimensional (3D) imaging. By coupling two STED depletion beams with two opposing objective lenses as a 4Pi-style configuration, researchers have developed iso-STED [19] to improve resolution in both the lateral and axial directions significantly. This technique yields an isotropic PSF with a resolution reaching 40 nm along the axes. Such an asymmetrical focal spot has benefits in recording high-resolution images from deep within biological cells and tissues, such as visualizing the essential structures in the mitochondria of intact cells [20]. Moreover, digital image processing can be employed to reduce the effect of side-lobes and other artefacts that compromise the PSF. By exploiting the saturated fluorescence excitation, a compressed sensing approach [21] has been recently reported to demonstrate the potential to obtain 3D super-resolved imaging, principally through a single 2D raster scan with tightly focused PSF.

1.2.1.2 **Ground state depletion (GSD) microscopy**

Apart from STED microscopy, GSD microscopy [11] employs the similar RESOLFT principle described above by using laser featured with a central zero node to optical switch-off the fluorescent probe. As illustrated in **Figure 1-2b**, the photoswitching mechanism in the GSD system involves transiently shelving the fluorescent molecule in a metastable dark triplet state (T_1), which is done by applying an additional laser with an appropriate wavelength. The fluorophore can be excited to a higher energy level and fall back to a long-lived dark triplet state. In other words, electrons remain in the metastable

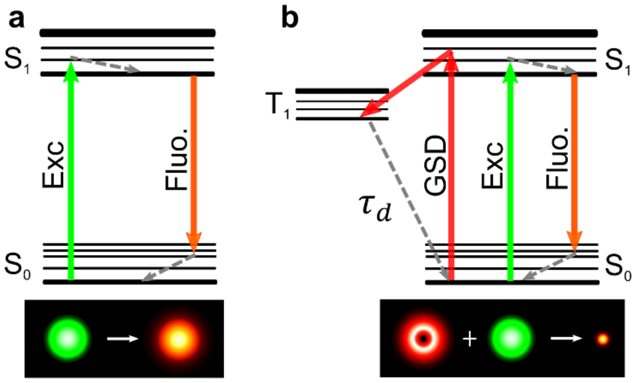

Figure 1-2 | The principle of a GSD microscope. (**a**) A simplified energy level of stimulated emission. (**b**) An energy level illustration of a GSD. S_0 is the ground state, S_1 is the excited state, T_1 is a metastable triplet state.

state for relatively long durations, which means fluorescent emission occurs only with very low probability. Regardless of this, the metastable state can be populated by repetitively exciting the fluorophore to increase the probability of a non-radiative intersystem crossing transition to T_1 from S_1.

GSD enables over-resolution by switching fluorescent molecules between bright and dark states using different wavelengths lasers according to the basic concepts of RESOLFT. Fluorescence imaging recovery is mission-critical since GSD relies on scanning the sample like STED microscopy. Slightly different from STED, GSD forbids the electron transitions on the periphery by using a doughnut-shaped beam to deplete the fluorescent molecules from ground state to triplet state. Thus, only the fluorescent molecules in the centre zoom can have fluorescence emission, sharpening the effective PSF of the system. Compared to STED, GSD exploits the ability of electron transitions in the long-lived dark triplet state, which requires much less depletion laser power.

Optical transitions in the triplet state have been reported in conventional synthetic probes, such as ATTO dyes, rhodamine, carbocyanine, Alexa Fluors, BODIPYs, and fluorescein. One of the most significant challenges for GSD microscopy is to select suitable fluorescent materials because of the potential photobleaching issue in driving fluorophores to dark triplet states. Moreover, the excited fluorophores to the triplet state must eventually be able to relax to the ground state after removing the depletion beam. As a result, there must be a trade-off between the intersystem crossing rate, the optical shelving time, and photobleaching activity. Unfortunately, there are a few fluorescent proteins or fluorescent molecules matching these specific requirements, subsequently restricting the widespread use of GSD.

1.2.1.3 **Structured illumination microscopy (SIM)**

Unlike the above point scanning super-resolution modalities, SIM bypasses the diffraction barrier without the requirement of photon switching fluorophores [12]. It is a widefield technique that extracts the higher resolution by exploiting the interference

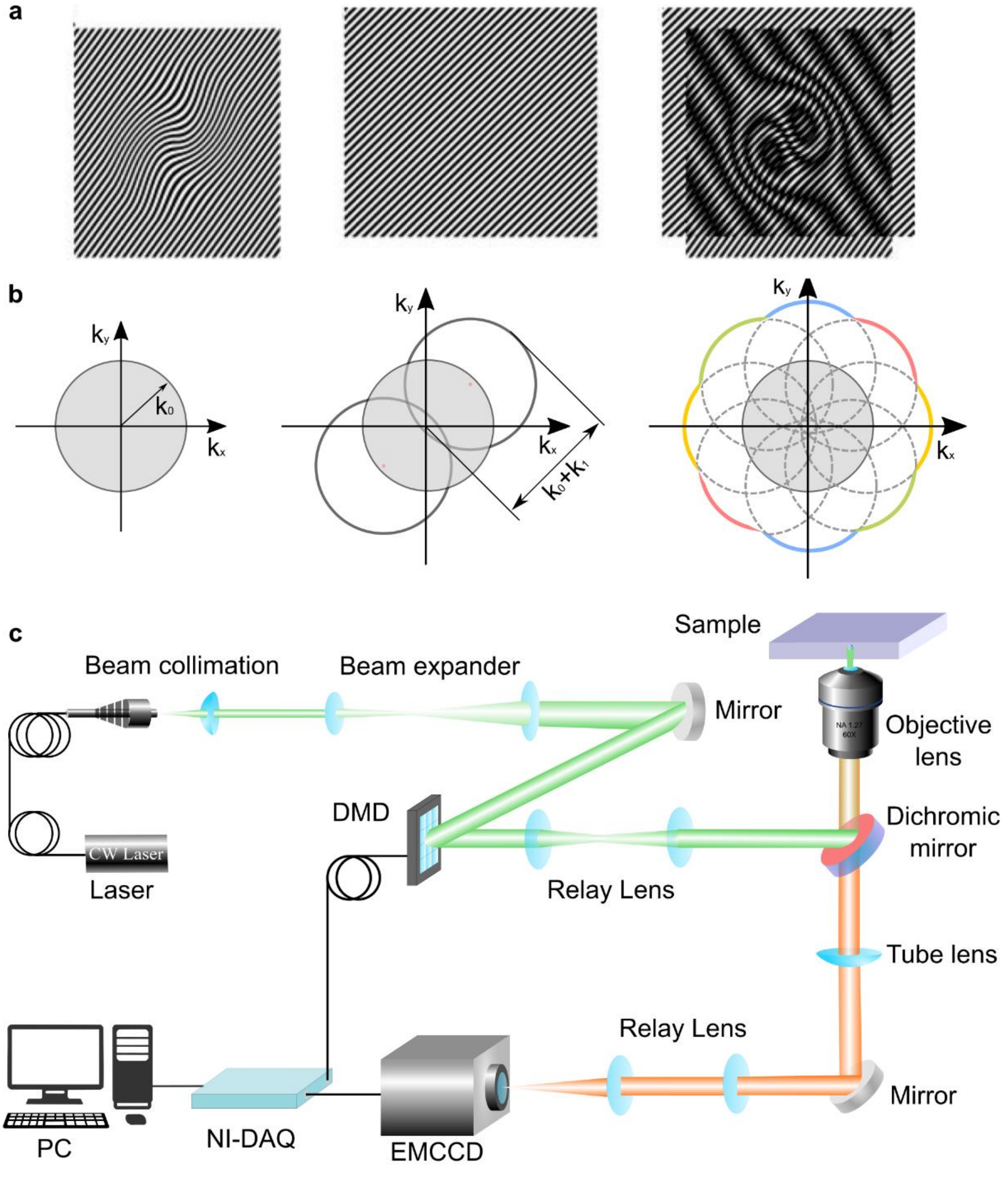

Figure 1-3 | The principle of a SIM microscope. (**a**) An unknown sample structure is multiplied by a known regular illumination pattern to generate a beat moiré fringes pattern. [12] (**b**) The corresponding Fourier components. The moiré fringes occur at the spatial difference frequencies between the pattern frequency and each spatial frequency component of the sample structure. They can be coarse enough to observe through the microscope (**c**) Experimental setup for SIM microscopy [90].

(moiré patterns) of diffraction orders when two grid patterns are overlaid at an angle (**Figure 1-3a**). As shown in **Figure 1-3b**, SIM typically requires closely spaced periodic patterns to down-modulate the high spatial frequency information in the sample so that with the support of optical transfer functions (OTF) the high-frequency information can be reconstructed. Since the resolution is only enhanced in the direction perpendicular to the line-shaped zero nodes, the pattern must be rotated in several directions to cover many angles in the focal plane. With a specialized image processing algorithm, high-frequency information can be extracted from the raw data to produce a reconstructed image, doubling the resolution of traditional diffraction-limited light microscopy. This method uses a grid array of line-shaped intensity maxima and minima instead of the conventional doughnut-shaped excitation beam that is employed by other PSF engineering techniques of STED and GSD described above. The mechanism of the enhanced resolution can be described in terms of spatial frequencies and Fourier components.

The nonlinear structured illumination schemes, such as saturated pattern excitation microscopy (SPEM) [22] and saturated structured illumination microscopy (SSIM) [12], have demonstrated to take advantage of emission saturation where high-resolution information is acquired in the system. In SPEM and SSIM, two powerful interfering beams from the same light source generate a standing wave grid pattern to form the structured illumination. Due to exposure to the intense illumination, most of the exposed fluorescent probes within the specimen saturate, leaving only narrow dark line-shaped volumes having a period of approximately 200 nm at the edges of the interference pattern. By increasing the excitation power, the nonlinear saturated photo-response can help to further improve the resolution of SIM in the regime of 50 nm and resolve sub-cellular structures. New advances made in de-noising process and modified excitation conditions have been applied to SIM, so that Hessian-SIM and grazing incidence SIM, have been recently developed with high imaging speed. They are applied to observations of ultrastructures of cellular organelles and their structural dynamics, such as mitochondrial cristae.

The next challenge is to explore the possibilities of using these techniques for thick tissue neuroscience imaging and nanomedicine tracking, as the strong scattering and absorption aberrate the structured illumination patterns and introduce unwanted out-of-focus light, both deteriorating the imaging resolution. For addressing this challenge, near-infrared excitation has been implemented to mitigate the absorption. Two-photon or multi-photon excitation in conjugation to spot scanning SIM have been reported to improve the imaging depth through tissue but at the price of low speed caused by the spot scanning scheme. Organic fluorescent dyes and proteins are the most common imaging probes for SIM, because of their outstanding staining and specific ability to target organelles. Nevertheless, these probes require a tightly focused and high-power pulsed laser to activate the multi-photon absorption process, due to their small multi-photon absorption cross-section. The required high excitation power, especially by nonlinear SIM, limits long-duration visualization of sub-cellular structure in living cells.

1.2.2 **Single-molecule localization**

1.2.2.1 **Stochastic optical reconstruction microscopy (STORM)**

Single-molecule localization microscopy (SMLM) is another class of super-resolution microscopy technique used to achieve images at high spatial resolutions under 20 nm, such as photoactivation localization microscopy (PALM)[13], stochastic optical reconstruction microscopy (STORM) [14]. Differing from the fluorophore chemistry "on-off" switching exploited in STED, the STORM techniques rely on the methodology of temporally optical modulating the fluorescent of the emitters (**Figure 1-4**).

Since the basic working principles of STORM and PALM work are similar, this section focuses on introducing STORM to explain the repeated rounds of imaging via photo-activation stochastic on-off switching mechanisms [23]. STORM technology explores the "blinking" property of many conventional fluorescent dyes to induce the temporal photoswitching concept between bright and dark states (**Figure 1-4b**). As demonstrated in **Figure 1-4a**, by applying a high-intensity laser light, the majority of fluorophores in a diffraction-limited region can be excited to a stable and reversible dark state which has a varied lifetime range [24]. Followed with another back-pumping laser, single molecules can switch to the bright state at any given point of time, stochastically emitting fluorescence for a short time before return to the dark state. The fluorescence signals produced by those molecules cycling between bright and dark states are recorded over time [25]. Finally, a super-resolution image is reconstructed from a set of frames with an algorithm that extracts all identified emitters’ localization information from the recorded data (**Figure 1-4d**).

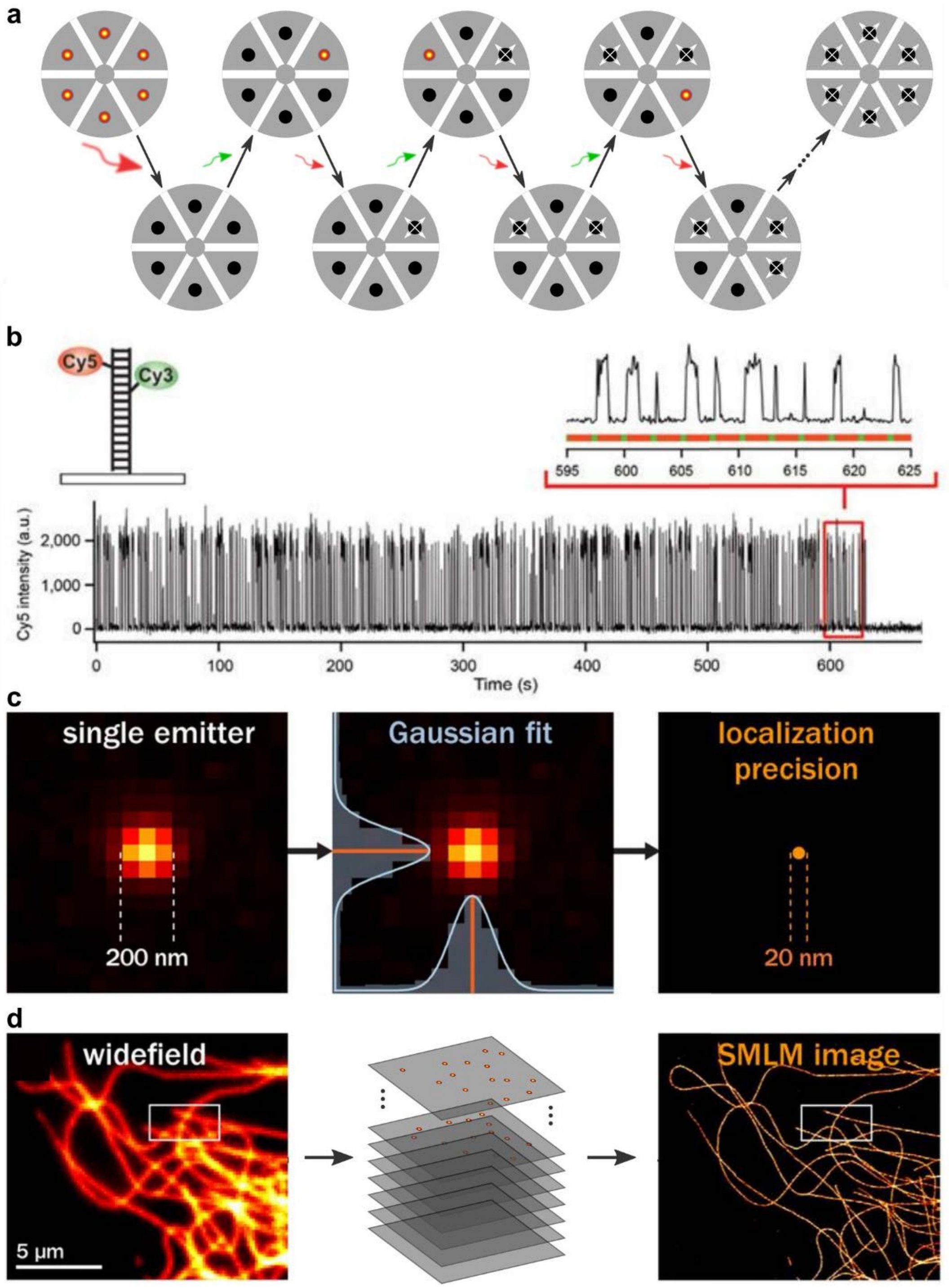

Figure 1-4 | The principle of an SMLM microscope. (**a**) Fluorophores-switching in a diffraction limit region. (**b**) The photoswitching characteristics of the Cy5 and Cy3 applied in SMLM. (**c**) Gaussian fitting for single emitter localization. (**d**) The SMLM image processing for a single composite super-resolution reconstruction. [23]

The detection precision of the single-molecule position depends on the signal intensity (**Figure 1-4c**). The precision centroid position of every single emitter is based on statistical curve-fitting algorithms, most often to a Gaussian function fitting, which is equivalent to a level of precision scaling with the square root of the total number of collected photons. The purpose of this method is to determine both the mean value of the standard error in the fitted position (σ) and the photon distribution (μ), according to Equation (1-3):

$$\sigma = \sqrt{\frac{s^2}{N} + \frac{\left(\frac{a^2}{12}\right)}{N} + \frac{4\sqrt{\pi}s^3b^2}{aN^2}} \tag{1-3}$$

Where s is the standard deviation of Gaussian function approximating the PSF of the emitter, N is the total captured number of photons, b is the standard deviation of the background noise, and a is the pixel size of the detector.

This equation takes the effect of photon shot noise, finite pixel size of the detector, background noise into consideration. STORM is based on the knowledge that the localization accuracy of a single fluorescent molecule can be achieved as low as 10 nm when the measured photon distribution of the emitter is approximately 1,000 photons. In the case of negligible background, Equation (1-3) is written as follows:

$$\sigma = \frac{s}{\sqrt{N}} \tag{1-4}$$

As described by Equation (1-3) and (1-4), the most critical elements in achieving the precise localization in STORM imaging are to maximize the detected photon from the emitter, which simultaneously minimizes the background fluorescence emission and detector noise.

It is worth noting that localization precision of a single emitter is not equivalent to the optical resolution of the reconstructed STORM image, which means the classic sampling FWHM standard techniques do not apply to STORM data. Furthermore, Nyquist-Shannon sampling theory which is also referred to as the Nyquist criterion, has defined the theoretical smallest sampling frequency. At the very least it needs to be doubled the size of the highest spatial frequency of an optical microscope. In other words, the labelling density of the imaged specimen should be two-fold smaller than the thinnest structural feature in the discerned image. The image performance of STORM is highly dependent on several parameters, including localization uncertainty, the density of the rendered molecule, sample drift, and photoswitching kinetics. Recently, the Fourier ring correlation (FRC) [26] has become a widespread integral and practical measurement to determine image resolution in optical super-resolution microscopy. It accounts for all the above factors directly from experimental data alone. By analyzing the trade-off between labelling density and localization uncertainty in FRC measurement, quantification of the spatial correlations also presents a way to estimate the average number of localizations per emitter, contributing to the image. Moreover, the decorrelation analysis [27] is another compelling method to analyse the image quality.

By taking advantage of the blinking mechanism, there is another technique called super-resolution optical fluctuation imaging (SOFI) [28] to achieve fast sub-diffraction imaging, which allows much higher labelling density comparing with STORM. Since the instrumentation is typically more straightforward for localization-based as compared with pattern illumination-based modalities, the STORM-type super-resolution techniques have been much promoted for biomedical research applications. However, single-molecule approaches typically require thousands of individual frames of image data for single reconstructions, limiting these techniques to live-cell imaging. Several developments have successfully presented that time-resolved imaging of multiple targets can be promising tools. Techniques have been investigated to track the movement of up to thousands of protein molecules in the same live-cell simultaneously, yielding sub-diffraction information on the underlying cellular dynamics from particle tracks in multicolour experiments.

1.2.2.2 **Point accumulation for imaging in nanoscale topography (PAINT)**

It should be noted that rapid advances are being made in the field of SMLM, so researchers are interested in advanced techniques with emerging solutions. Although STORM has successfully addressed many biological questions in imaging, it limits the times of observations for the labelled molecule due to fluorophore bleaching, leading to under-sampling of the actual underlying biology. Thus, the requirement of multiple repeated observations of molecules has pushed the field to explore techniques that allow a fluorophore to bind with a specific target. This binding method is then employed to reconstruct of interest via PAINT [29].

PAINT microscopy uses a similar concept in STORM that localizes enough single molecules by isolating the fluorescent events in time and space in a sub-diffraction limited region, reconstructing a high-resolution composite image (**Figure 1-5**). However, instead

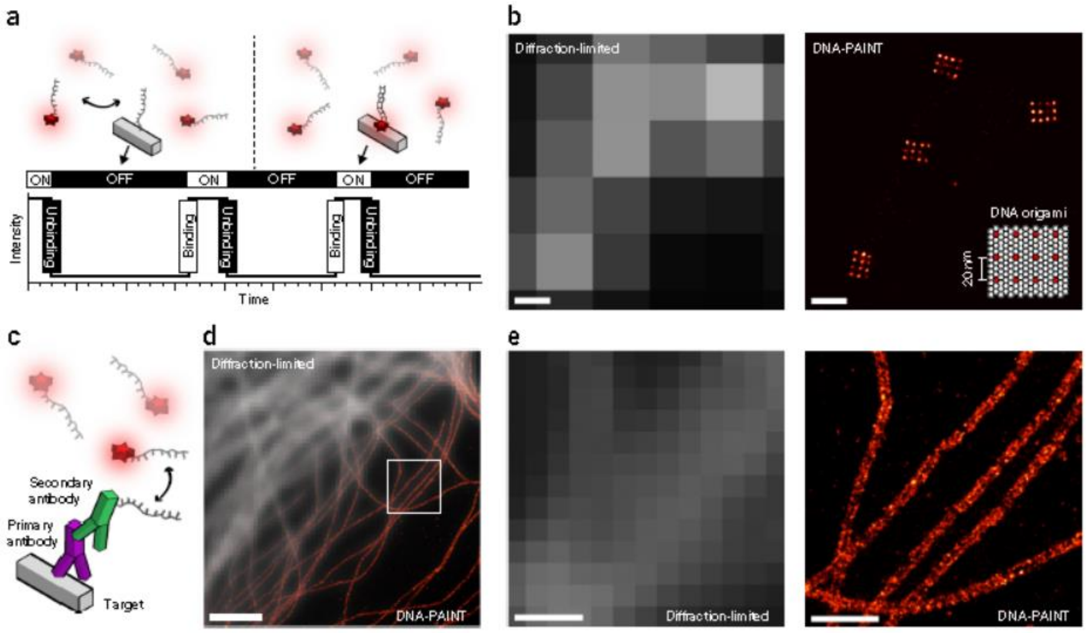

Figure 1-5 | The principle of a PAINT microscope. (**a**) DNA-PAINT concept. (**b**) Diffraction-limited (left) and super-resolved DNA-PAINT images (right) of DNA origami nanostructures. (**c**) In situ protein-labelling strategy for DNA-PAINT using primary and DNA-conjugated secondary antibodies. (**d**) Overlay of a diffraction-limited α-tubulin image (top left) with a super-resolved DNA-PAINT image (bottom right). (**e**) Close-ups of the highlighted area in **d**, comparing diffraction-limited image (left) with DNA-PAINT super-resolved image (right). [29]

of labelling the target stochastic photo-activation molecules with a permanently fixing the fluorophore, PAINT relies on the transient binding of probes to the structure of interest. Transient binding occurs on a time scale short enough to isolate a single emission rather than observe a fluorescence 'spike' due to immobilization of the fixed probe. The probe is rapidly dissociated and photobleached so that a new probe can serve as the replacement

PAINT is straightforward to implement without particular experimental conditions to achieve the required photoswitching. The first iteration of PAINT was initially demonstrated in 2006 [30], using intermittent collisions between a small environment-sensitive dye Nile Red and giant unilamellar vesicles. It is worth noting that PAINT builds a super-resolution reconstruction with the theoretically infinite number of emission events which only are limited by the time and reagents available in practical experiments. To achieve the appropriate super-resolved image, SMLM collects the data in as large a set as possible. This is a highly significant advance in PAINT, as it is intrinsically optimized to maximize the molecular sampling rate.

However, further technical development will be required to alleviate the challenges when employing this approach. Firstly, it is difficult for the original PAINT approach to specifically label a variety of biomolecules, because interactions are mainly restricted to electrostatic coupling or hydrophobic interactions. As a result, PAINT faces the challenge to find available compatible probes. For high-quality single-molecule localization, there is a critical requirement to control the binding events in a suitable time range. It will not have enough signal to estimate the precise localization if the binding lasts too short, while the spatiotemporal separation of each emitter will be another problem with a long binding time. Moreover, PAINT has another challenge caused by the high background fluorescence, which limits the technique to being conducted in conjunction with a robust optical sectioning modality.

Deoxyribonucleic Acid (DNA) represents a promising candidate for developing an imaging method of the PAINT concept by establishing a precisely programmable interaction system. By labelling the probe to short DNA oligos with the specific antibody, DNA-based PAINT (DNA-PAINT) [31] has demonstrated itself to be a powerful tool for super-resolution microscopy. Specifically, the engineered oligos with a relatively low affinity are introduced into the system and bind transiently, allowing a theoretically unlimited time of localization and detection (**Figure 1-5a**). Relying on different antibodies conjugated to oligos with a high number of orthogonal docking strands to carry out the spectrally distinct dyes, Exchange PAINT [32] makes it possible for multiplexing imaging at a high resolution. Similarly, the quantitative method of PAINT (qPAINT) [33] provides an orthogonal way to extract and compare quantitative information. With new advances being made in the development of Förster Resonance Energy Transfer (FRET)-PAINT [34], background-free imaging has been achieved with non-specific binding. Combined with fluorescence lifetimes [35], this technique has been developed to classify different docking species on origami with the cost of executing quantitative measurements. Therefore, new modalities are desired to combine the advantages of these labelling methods, allowing more challenging experiments to observe and quantify proteins in their native environment.

All in all, the DNA-PAINT imaging framework offers several advantages over STED, SIM, or STORM, resulting in possibilities for new technological developments and biological applications. However, we do note there are limits to the achievable image acquisition speed when compared with those traditional super-resolution techniques.

1.3 Nanoparticles in super-resolution techniques

With the advantages of the small size and biocompatibility, organic dyes and fluorescent proteins are now widespread imaging probes in the above far-field super-resolution microscopies. However, the disadvantages of current fluorescent proteins and molecular dyes are also apparent in the super-resolution applications, particularly for the long-term tracking of single molecular and real-time imaging of subcellular structures. Typically, they are too dim to offer enough signal in fast imaging and can be rapidly photobleached under the excitation light. Therefore, the super-resolution community seeks alternative probes with intense brightness and resistance to photobleaching, in order to revolutionize microscopy by revealing the events inside the cells.

Although nanoparticles have larger sizes compared with dye molecules and proteins, several groups have successfully induced fluorescent nanoparticles into the imaging communities to explore capability in functional subcellular imaging [36]. Nanoparticles have attracted a great of attention as the excellent candidates for bio-labelling and biosensing [37], drug delivery [38], cancer therapy [39], long-term molecular tracking [40], solar cell application [41] and triggering chemical reaction [42] due to their remarkable photophysical properties. For the potential applications of nanoparticles, mapping of the centres within individual nanoparticles has become significantly important. Recently, a variety of super-resolution modalities have utilized nanoparticles as fluorescent nanoprobes, including quantum dots (QDots), carbon dots (CDots), polymer dots (PDots), aggregation-induced emission (AIE) dots and UCNPs. This section reviews the recent progress made in these fluorescent nanoparticles in super-resolution imaging.

1.3.1 Quantum dots (QDots)

As the first generation of inorganic nanoparticles used as biomedical imaging probes (**Figure 1-6a**), QDots are the artificial semiconductor nanocrystals with diameters ranging from 2-10 nm with remarkable electronic and fluorescent properties [43][44]. By controlling their sizes, QDots can emit distinctive colours of light [45]. Also, they are resistant to photobleaching with intense brightness compared with conventional dyes. QDots have other exceptional photophysical properties, such as broad excitation spectra, significant absorption coefficient and narrow-band symmetric emission spectra.

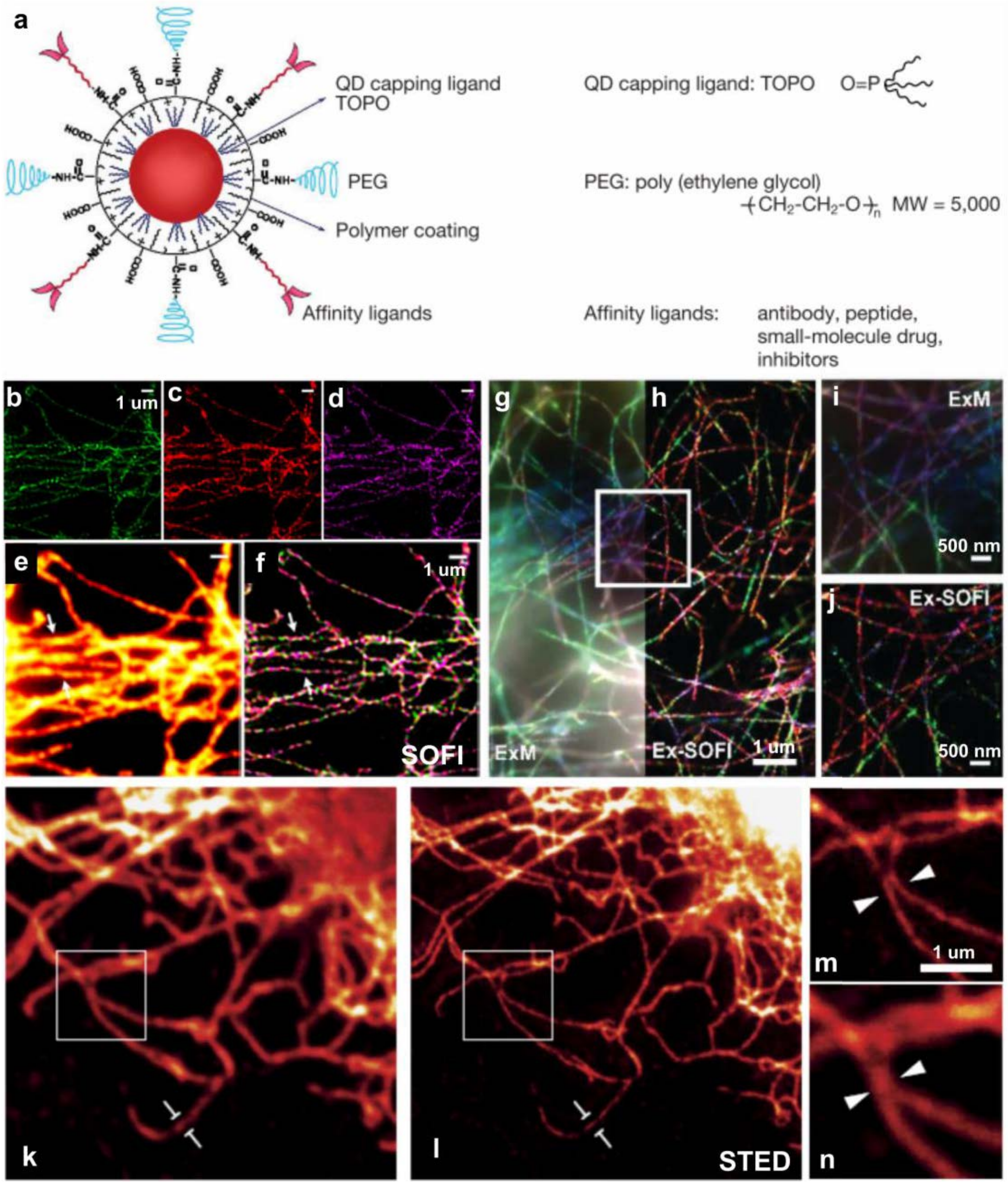

Figure 1-6 | Immunofluorescence imaging results of with QDots. (**a**) Structure of a multifunctional QDots, showing the capping ligand TOPO, an encapsulating copolymer layer, tumour-targeting ligands (such as peptides, antibodies or small-molecule inhibitors) and polyethylene glycol (PEG).[43] (**b**–**d**) SOFI images of microtubule labelled with QDots525, QDots625 and QDots705, respectively. [47] (**e**) The confocal image. (**f**) Multicolour merged image of (**b**)-(**d**). (**g** & **h**) ExM imaging of Qdot605 labelled acetylated microtubule, Qdot655 labelled tyrosinated microtubule and Qdot705 labelled detyrosinated microtubule, respectively. [48] (**i** & **j**) ExM and ExSOFI images of boxed regions in (**g** & **h**), respectively. (**k**) Image of confocal with QDots. [51] (**l**) Image in STED in the same region. (**n**) Inset from (**l**), white square, with distinct QDots that could not be separated by confocal (**m**).

Due to their blinking property [28][46], QDots have functioned well as a promising probe in real-time optical microscopy with SOFI, improving both spatial and temporal resolution. Multicolour QDots (**Figure 1-6b-j**) have recently been used to achieve higher labelling densities in the biological applications [47][48]. As based by calculating the statistical moments of each pixel, SOFI provides single-molecule localization information for quantifying target molecules. On the other hand, several kinds of available commercial QDots have successfully expanded the application scope in STED microscopy [49][50]. Stephan Hell utilizes CdSe@ZnS QDots (QDots 705) to demonstrate STED microscopy [51] with lateral resolutions down to 50 nm for single QDots and 85 nm for microtubule in HeLa cells (**Figure 1-6k-n**).

Although QDots are promising probes to facilitate nanoscopy resolution in standard super-resolution modalities, they still require relatively intense laser (over 340 mW) and exhibit issues concerning phototoxicity [51]. In addition to the general concerns of photobleaching, the high power depletion laser may also cause thermal instability, leading to artifacts in images. Besides, QDots blinking and broad absorption spectrum represented the significant limitations in the context of particle tracking and long-term image acquisition [49]. Due to the poor penetrating ability, no work has yet investigated QDots’ ability to label tissue structures. Further work should focus on increasing the labelling efficiency of QDots in a thick specimen by using small size or optimizing the immunostaining method.

1.3.2 **Carbon dots (CDots)**

Compared to semiconductor QDots, which typically contain heavy metals constituents which are highly toxic to the biological sample [43], CDots have emerged as a hugely attractive option as subcellular targeting probes [52]. CDots are fluorescent carbon materials consist of sp2 or sp3 carbon and oxygen-based or nitrogen-based groups, with a tiny size smaller than 5 nm [53]. Furthermore, CDots can be produced inexpensively through a single-step procedure on a large scale (**Figure 1-7a**). Following these promising conclusions, the process in super-resolution microscopy has demonstrated that CDots are promising labelling agents [54][55].

CDots' photoblinking properties make them an excellent candidate for SOFI [52][54]. A type of 4.5-nm CDots has been developed with a burst-like blinking behavior and has been demonstrated for imaging microtubules (**Figure 1-7b-k**). With the development of near-infrared emissive in CDots, STED microscopy has improved spatial resolution down to 30 nm for imaging in both fixed and living cells, demonstrating the potential of CDots

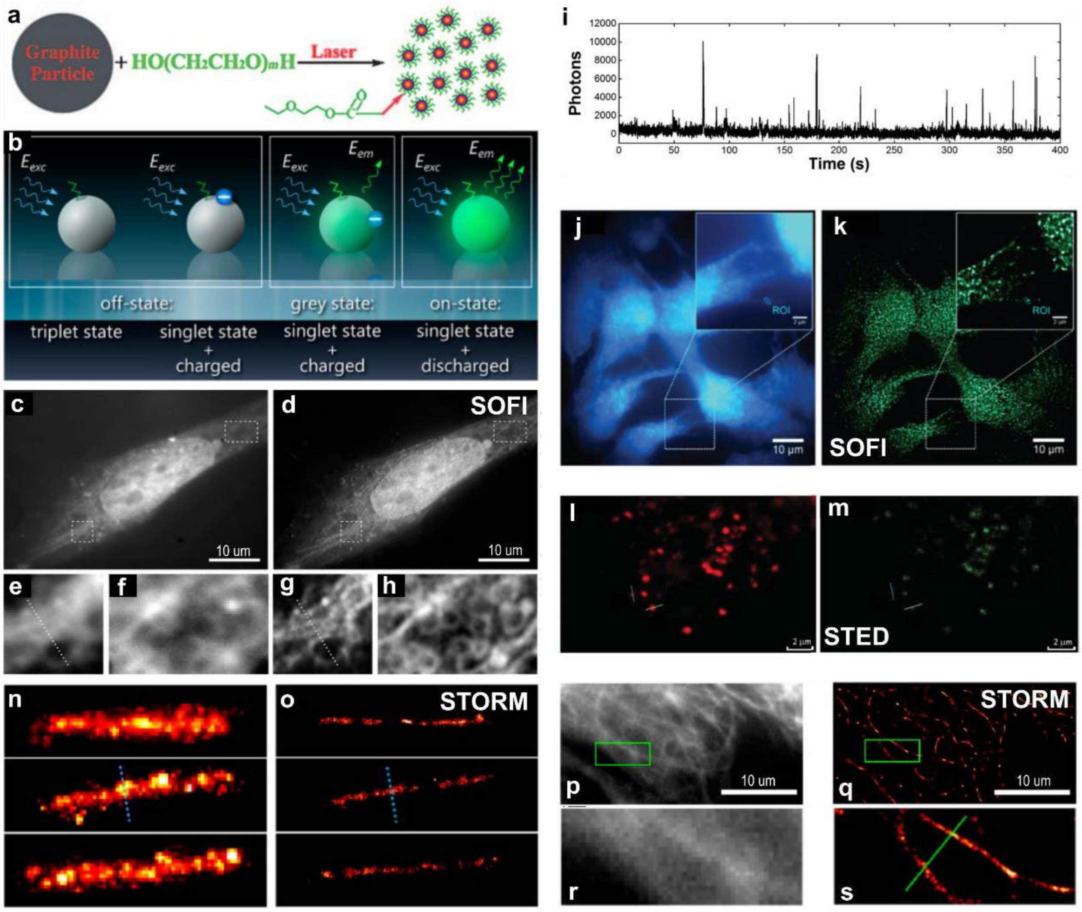

Figure 1-7 | Super-resolution imaging of CDots-labelled structures inside a cell. (**a**) One-step synthesis of CDots in PEG200N solvent [53] (**b**) Scheme presenting the possible mechanism of on-, off-, and grey states of CDots. [54] (**c**) Fluorescence wide-field image of a Saos-2 cell. (**d**) Second-order SOFI image of (**c**). (**e** & **g**) and (**f** & **h**) Two subareas of the cell wide-field and SOFI images, respectively. (**i**) A representative fluorescence trace of an individual CDots. [52] (**j**) Fluorescence wide-field image of CDots in fixed trout epithelial gill cells. (**k**) SMLM image of (**j**). (**i**) Confocal imaging of CDots in fixed MCF7 cells. [56] (**m**) STED image of the same region in (**c**). (**n**) High-density super-resolution imaging of CDots-stained samples. [57] (**o**) Super-resolution reconstructed image of (**n**). (**p**) Confocal imaging of CDots-labelled structures inside a cell and on the plasma membrane. (**q**) STORM image of the same region in (**p**). (**s**) Inset from (**q**), green square, with distinct CDots that could not be separated by confocal (**r**).

for super-resolution visualization of cellular dynamics (**Figure 1-7i-m**) [56]. Apart from this, CDots present reversibly photoswitchable feature when combined with an electron acceptor molecule [57][58]. With CDots-stained microtubules in fixed and live trout gill epithelial cells, STORM has achieved a resolution of 25 nm (**Figure 1-7n-s**), making possible super-resolution imaging of the clustering and distribution of membrane protein receptors [36].

The main drawback of CDots is that the wavelengths of excitation beams are confined in the ultraviolet (UV) range, causing cell death and also having the problem of tissue penetration for bio-imaging. As the promising fluorescent nanoprobe for super-resolution microscopy, we need more investigations to improve the quality of CDots further [59], particularly in mass production. Another significant challenge is the uncertain nature of the chemical groups on the surface of CDots, which originates from a lack of control during the synthetic process. Furthermore, it requires more characterization techniques to understand the fluorescent mechanism operating in CDots.

1.3.3 Polymer dots (PDots)

Semiconducting PDots have demonstrated their capacity as a convincing alternative in fluorescent labelling owing to their prominent optical performance, and they have displayed broad applications in bioimaging. Recently, the process has demonstrated the advantage of PDots for SOFI imaging by regulating their outstanding optical properties

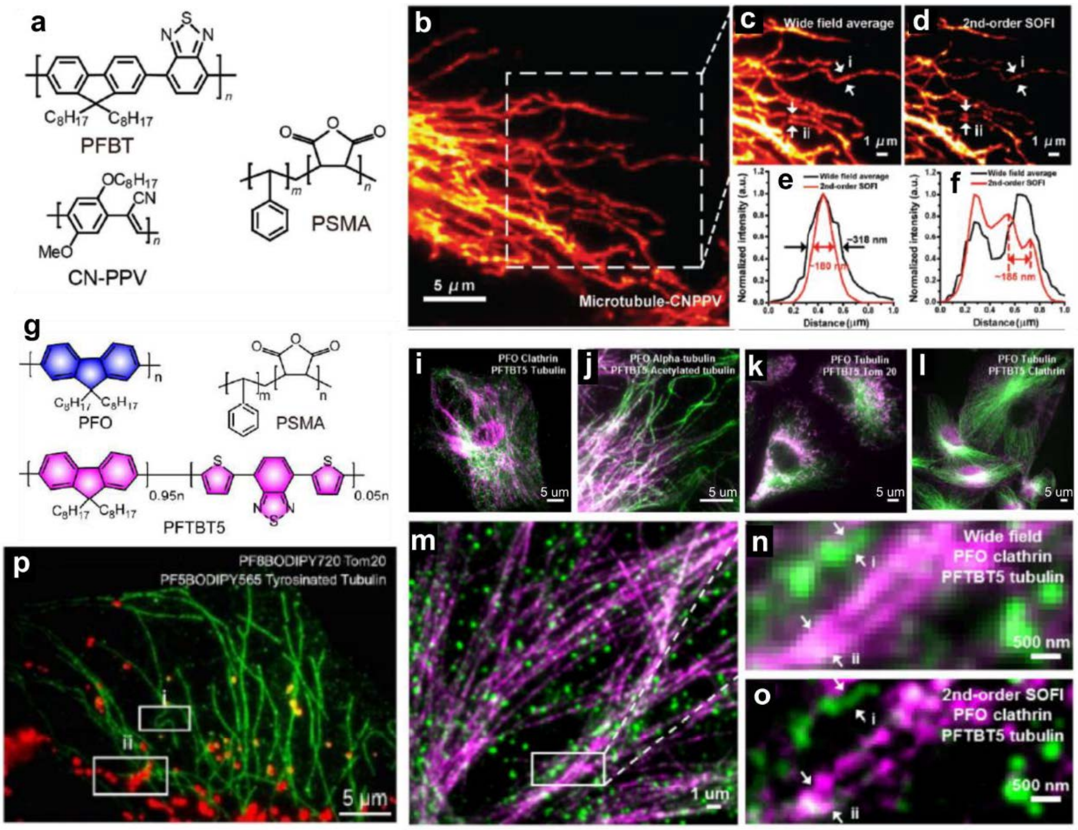

Figure 1-8 | Super-resolution nanoscopy of subcellular structures labelled with small photoblinking PDots. (**a**) Chemical structures of small PFBT and CN-PPV PDots. [60] (**b**) Conventional wide-field imaging of tubulin labelled with small CN-PPV PDots. (**c**) The magnified area in the square in panel (**b**). (**d**) 2nd-order SOFI image generated from panel (**c**). (**e**) & (**f**) The intensity profiles of the white arrows shown in panels (**c**) & (**d**). (**g**) Chemical structures of small PFO and PFTBT5 PDots. [61] (**i**) Dual-colour imaging of microtubule filaments and clathrin-coated vesicles. (**j**) alpha and acetylated microtubule. (**k**) Microtubule and mitochondria. (**l**) Microtubule filaments and clathrin-coated vesicles. (**m**) Wide-field imaging of CCPs labelled with PFO PDots and microtubules labelled with PFTBT5 PDots. (**n**) The magnified region in the white box in (**m**). (**o**) Second-order SOFI image from panel (**n**). (**p**) A wide-field image of PF5BODIPY565 labelled tyrosinated-α-tubulins and PF8BODIPY720 labelled mitochondria membranes. [62]

such as high brightness, resistance to bleaching, and tunable properties for *in vitro* and *in vivo* imaging [60][61][62][63].

PDots are particles that consist predominantly of π-conjugated polymers [60] with an extra small (10 nm or less), which are suitable for fluctuation-based super-resolution imaging of subcellular structures (**Figure 1-8**). By coating an inert polymer (styrene-co-maleic anhydride) (PSMA) (**Figure 1-8a**), the researchers design the small blinking PDots with surface carboxyl groups for biomolecular conjugation. Since the small size confers improved biocompatibility, PDots have demonstrated their ability to label a variety of subcellular organelles such as microtubules (**Figure 1-8b-f**), the nuclear, mitochondria and envelope [61]. For investigating protein-protein interactions and multiplexed subcellular structures imaging, a further process has developed the other two types of PDots (**Figure 1-8g**), namely PFO and PFTBT5 PDots [61], with different spectral and relatively fluorescent emission bands, respectively. With these small PDots, indirect immunofluorescence imaging of the microtubule network in BS-C-1 cells is performed via dual-colour labelling (**Figure 1-8i-o**). Furthermore, streptavidin-conjugated PDots present prominent dual-colour subcellular labelling with a high signal-to-noise ratio, enhancing the resolution of single microtubules to ~60 nm in the 8th-order SOFI (**Figure 1-8p**) [62].

The small photoblinking PDots are not only promising probes for SOFI imaging but they are also suitable for other emission blinking-based sub-diffraction methods, including Bayesian analysis of blinking and bleaching microscopy [64] and bleaching/blinking assisted localization microscopy [65]. However, the challenge is retaining the extraordinary photophysical properties while decreasing the size of PDots. Typically, the brightness of PDots drops proportionally to the number of emitters in a particular volume. Moreover, a smaller size causes the more substantial surface quenching of the PDots due to the increased ratio of surface area to volume. With the optimal design of new semiconducting polymers, for example crystal host and dopant concentrations, synthesis of much smaller size, PDots will significantly improve our ability to identify different subcellular structures with super-resolution techniques.

1.3.4 Aggregation-induced emission (AIE) dots

Although the QDots, CDots and PDots have shown their advantages in fluorescent imaging with their photoblinking properties over a time sequence, organic dyes are still the common choices for biological applications because they are easily modified and have high biocompatibility. However, traditional organic fluorophores suffer from aggregation caused quenching (ACQ) [66] due to the intense intermolecular π-π stacking interactions. Specifically, the ACQ effect induces bright emission in dilute solution but weakened or quenched emission in the aggregated labelling on targeted tissues or organs, limiting the cope of fluorophores for practical applications. Fortunately, AIE dots [67][68] contain a large number of molecules within small particles (14-nm) that have a unique photophysical phenomenon very different to the ACQ effect, enabling bright emission in highly aggregated states. The primary mechanism of AIE effect is that the physical constraint in the aggregated states restricts free intramolecular motions, diminishing the

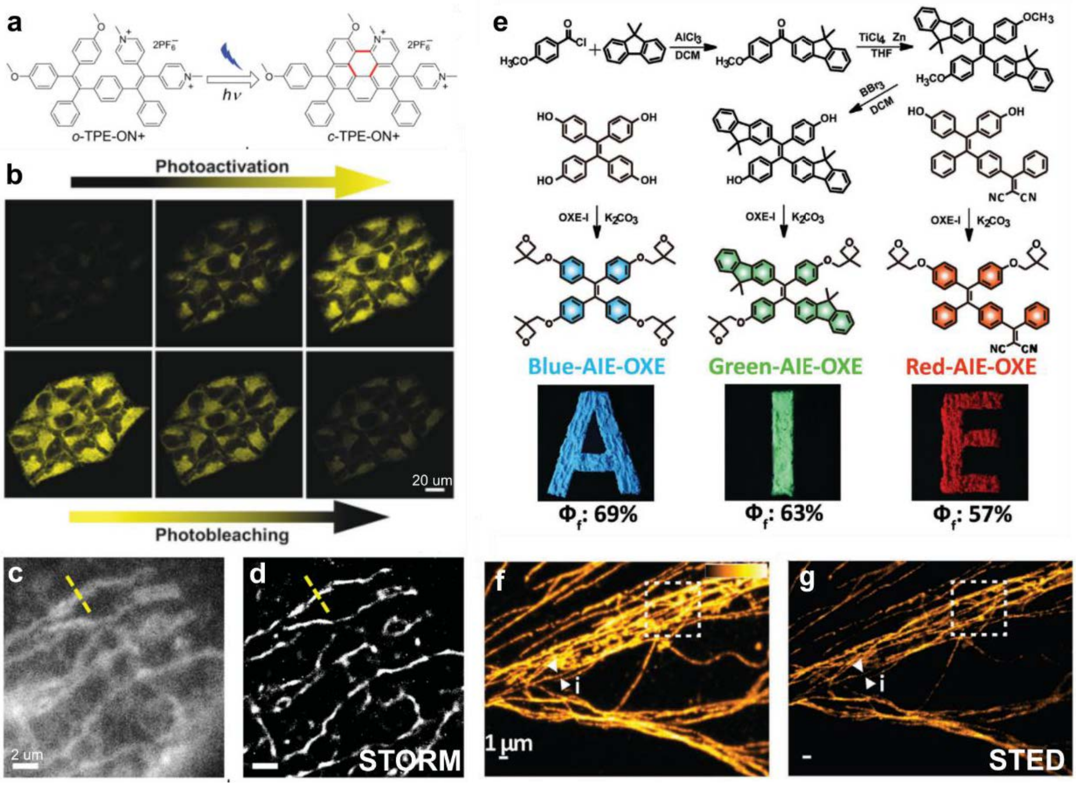

Figure 1-9 | Super-resolution imaging of the subcellular structures labelled using AIE dots. (**a**) Photocyclodehydrogenation process of o-TPE-ON+. [73] (**b**) Photoactivation and photobleaching behaviors in fixed HeLa cells recorded by confocal microscopy. (**c**) Diffraction-limited image with totally blurred structure. (**d**) STORM super-resolution image of (**c**). (**e**) Synthetic routes and structures of the Blue-AIE dots, Green-AIE dots, and Red-AIE dots; fluorescence images of the solid powders of the three molecules under 365 nm UV light and their quantum yields. [75] (**f**) Confocal imaging of the microtubule structures labelled using the Red-AIE dots. (**g**) STED images of (**f**).

nonradiative decay of the excited state energy. Moreover, most AIE dots present low toxicity and high biocompatibility with high resistance to photobleaching even under intense laser irradiation [69].

AIE dots have served as viable fluorescent probes for specific subcellular labelling in super-resolution visualization methods [70][71][72]. By tracking the intensity trace of fluorescence turn-on photoactivatable probe named o-TPE-ON+ (**Figure 1-9a**), Tang et al. have demonstrated a novel photoswitching AIE dots for STORM imaging to monitor the dynamic of mitochondria in nanoscale level (**Figure 1-9b-d**) [73]. Furthermore, a series of AIE-active fluorescent probes are synthesized for detection and super-resolution imaging of β-amyloid fibrillation deposits in mouse brain slices [74]. Recent studies demonstrate the application of AIE dots in STED imaging of microtubule structures at a 95-nm resolution of fixed cells (**Figure 1-9e-g**) [69][75]. With advanced processes established in the synthetic probes, STED microscopy extends the application to image AIE-stained mitochondria in living cells with a resolution of 74 nm [66].

Meanwhile, it seems more significant to develop new AIE dots with different emission colour via diverse structures, covering the entire visible spectrum for super-resolution microscopes. In particular, the AIE dots have near-infrared, or far-red emission will be ideal because they do only minor photo-damage to biological samples, high sensitivity in living systems, and there is minimal interference from the background autofluorescence.

1.3.5 **Lanthanide-doped upconversion nanoparticles (UCNPs)**

Although the nanoparticles mentioned above have demonstrated considerable advantages in super-resolution imaging for biological research, only a few analyses have conducted long term tracking and super-resolution imaging in deep biological tissues. The main reason is that the excitation and emission of these nanoparticles are located at the range of visible and ultraviolet wavelength with a low penetration ability in the deep tissue [76]. Moreover, these fluorescent nanoparticles are relatively photostable compared with the dyes and proteins, but is still a major challenge for these nanoparticles in resisting the photobleaching under excitation over several hours for long-term observation [77].

Addressing the issues mentioned above, UCNPs serve as a new type of multi-photon probes with high density emitters in small volumes. Each UCNP contains thousands of co-doped lanthanide ions that form a network of photon sensitizers and activators, which

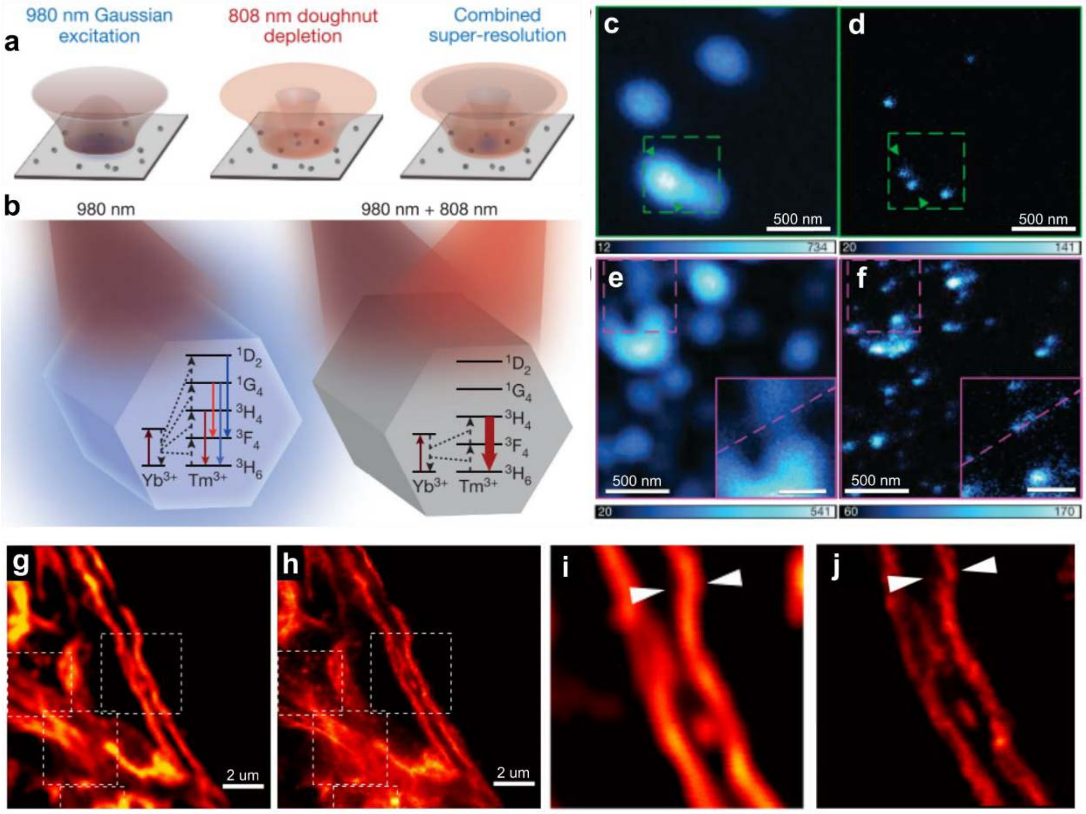

Figure 1-10 | Subdiffraction imaging with UCNPs. (**a**) Diagrams of the UCNP-assisted STED super-resolution imaging. [79] (**b**) Energy level diagrams of Yb/Tm co-doped UCNPs under 980 nm illumination (left), and under both 980 nm and 808 nm illumination (right). (**c&d**) Confocal (left) and super-resolution (right) images of the 40-nm 8% Tm-doped UCNPs. (**e&f**) Confocal (left) and super-resolution (right) images of the 13-nm 8% Tm-doped UCNPs.(**g**) Diffraction-limited image of UCNP stained cytoskeleton structures. [80] (**h**) STED super-resolution image of (**g**). (**e**) The confocal image from panel in (**g**). (**j**) STED image of (**i**).

have the unique optical property of converting near-infrared (NIR) to shorter wavelength NIR, visible and ultraviolet emission [78]. UCNPs have attracted considerable attention due to their superior physicochemical features, such as significant anti-Stokes spectral shifts, background-free, photostable, low toxicity and high imaging penetration ability.

1.3.5.1 **UCNPs in STED microscopy**

Recent studies have indicated that UCNPs with thousands of emitters per nanoparticle can serve as suitable single-molecule probes, enabling bright emission in super-resolution imaging. A UCNP-assisted STED nanoscopy with low saturation intensity has achieved sub-30 nm optical resolution in resolving the cluster of single 13 nm UCNPs (**Figure 1-10c-f**) [79]. Specifically, the 808 nm STED beam with the similar the energy band ($^3H_4 \rightarrow {}^3H_6$) can trigger stimulated emission to depopulate metastable $^3H_4$ level, consequently inhibiting upconverted emission from higher excited levels (blue emission from $^1G_4$ and

$^1D_2$, **Figure 1-10b**). Moreover, the continued work further presents a resolution of 80 nm in resolving cellular cytoskeleton protein structures (**Figure 1-10g-j**) [80].

Although UCNP-assisted STED reduces two orders of magnitude power than conventional dye-based STED, several restrictions still exist. Firstly, like the other STED-like modalities, the depletion beam requires much higher power than that of the excitation laser. Secondly, this STED scheme calls for a proficient skill in aligning dual laser beams, which confines the technique to specialized laboratories and applications. Thirdly, the low-efficiency four-photon emission in these UCNP-assisted STED methods is not suitable for the high sensitivity super-resolution imaging. Furthermore, the specific requirement of the depletion beam to match the targeted bandgap of the energy levels in UCNPs, limiting the preponderance in varies of emission wavelengths. In this regard, a more convenient and efficient approach will be imperative to utilize UCNPs in super-resolution microscope instead of a stimulated emission procedure.

1.3.5.2 **UCNPs in FED microscopy**

As a derivative scheme of STED, fluorescence emission difference (FED) microscopy [81] is a promising approach that addresses the above challenges in the commercialized laser scanning microscopy system without the requirement of specific dyes and emission spectrum. FED achieves super-resolution imaging by subtracting the image of focused doughnut lasers beam (I_{Dou}) from the one of Gaussian beam (I_{Gau}) with an appropriate normalizing coefficient (r), according to Equation (1-5):

$$I_{FED} = I_{Gau} - r * I_{Dou} \tag{1-5}$$

However, the probes applied in FED microscopy regularly suffer from the photobleaching problem. By introducing Er^{3+} activated UCNPs with red emission (660 nm), the nonbleaching FED microscopy achieves 172 nm resolution by using 800 nm 10 $MWcm^{-2}$ excitations [82]. Parallel to this work, we use UCNPs to unlock a novel mode of near-infrared emission saturation (NIRES) microscopy for super-resolution imaging inside the deep tissue, with much lower excitation intensity than that required in conventional dyes [83]. By exciting with a 980 nm doughnut-shaped beam and detecting at 800 nm, NIRES resolves the single UCNP with a resolution of sub 50 nm through 93 μm thick liver tissue. Further research suggests a new research direction that improves the resolution of near-infrared nanoscopy by optimizing the material properties of UCNPs [84]. Combined with the self-healing Bessel beam, we explore this sub-diffraction imaging modality to map single nanoparticles inside a strong scattering tumour cells spheroid [85][86].

1.3.5.3 **UCNPs in super-linear microscopy**

As FED microscopy requires two different modulated images for subtraction process, additional data acquisition may compromise the performance of FED due to the sample drifting issue. With the excitation orthogonalized UCNPs, one-scan FED microscopy eliminates the issues as mentioned above by using two synchronized Gaussian and doughnut beams [87]. On the other hand, photon avalanche in UCNPs is employed to bypass the diffraction limit by using a single Gaussian beam [88]. This simple modality relies on the highly nonlinear dependence of the emission intensity on the excitation power. According to Equation (1-6), the resolution is inversely proportional to the number of photons involved in the emission process:

$$\Delta r = \frac{\Delta r_0}{\sqrt{N}} = \frac{\lambda}{2NA\sqrt{N}} \tag{1-6}$$

Where Δr is the resolution, Δr_0 is the single-photon diffraction-limited resolution, *N* is the number of photons involved in the emission process or the order of nonlinearity, λ is the excitation wavelength, and *NA* is the numerical aperture of the objective lens.

Thus, it is possible to realize sub-diffraction imaging is possible when $N > 1$ since the intensity of multi-photon luminescence near the centre of the excitation beam spot will be enhanced relative to the intensity near its edges. This is due to the multi-photon luminescence intensity scaling as $I_{lum} = P_{in}^N$, where P_{in} is the incident power density. According to the theoretical simulation modelling, it evaluates the feasibility of resolving 20-nm features when the nonlinearity exceeds 80 [88]. Furthermore, a similar approach provides experimental evidence by realizing 3D sub-diffraction imaging in a biological sample on a conventional confocal setup [89].

1.3.5.4 **UCNPs in nonlinear SIM**

Compared with the wide-field structured microscopy, these point-by-point laser scanning modalities suffer from the low frame rate. Most recently, our group reported a strategy of upconversion nonlinear SIM to create video-rate super-resolution imaging through thick biological tissues [90]. The unique nonlinear photoresponse of UCNPs enables the onset of an efficient nonlinear mode on SIM for obtaining high-frequency harmonics in the

Fourier domain of the imaging plane, making nonlinear SIM possible with gentle excitation power. We further demonstrate that fine-tuning of the doping concentrations in UCNPs can modify the nonlinearity of the photon response to further enhance the resolution to 1/7th of the excitation wavelength. Based on time-wavelength-space conversion, the multi-photon upconversion time-encoded SIM surpasses the speed limitation on image acquisition with modulation and scanning rate of 50 MHz while maintaining low excitation power [91]. The progress made in nonlinear SIM using UCNPs lies in the improved resolution under a low excitation power, particularly for single nanoparticles dynamic tracking through deep tissues. The structure illumination also can extend to self-evolving ghost imaging [92] to increase the imaging speed in deep tissue by using a feedback-based approach.

To achieve a low phototoxicity sub-diffraction imaging with lower excitation power, controllable synthesis procedure of UCNPs will further benefit the energy transfer process and resultant saturation intensity properties. Although there remain several challenges to specific labelling UCNPs to the subcellular structures in live cells, recent progress made in the functionalization of UCNPs, enabling bio-conjugation [93][94][95][96], cell optogenetics [97][98] and long-term tracking in cells [99][100], will empower UCNPs to track more biological events. The tuning of multiple emission colours [101][102] and lifetimes [103] of UCNPs will permit multiplexed subcellular structures imaging and long-term single molecules tracking in deep tissues [36].

1.4 Aim and outline

This thesis investigates the multi-photon nonlinear emission of UCNPs to implement three innovative super-resolution microscopies, delivering several specific advantages compared to existing modalities. Specifically, this thesis develops imaging approaches by employing different emission intensity response curves on the excitation power: (1) single nonlinear near-infrared emission response curve in a single UCNP; (2) multiple diverse photoresponse curves in a single UCNP; and (3) uniform and distinct nonlinear emission curves from different ions-doped UCNPs.

Chapter 2 develops and validates a new mode of near-infrared emission saturation nanoscopy that has both excitation and emission in the near-infrared wavelength range by employing UCNPs. This chapter conducts powerful deep tissue super-resolution microscopy through a doughnut-shaped laser beam, which requires several orders of magnitude lower excitation intensity than that required for conventional multi-photon dyes. The work opens the door for low power robust super-resolution imaging through deep tissue. This chapter further suggests a new research direction that is improving the resolution of near-infrared nanoscopy by optimizing the material properties of UCNPs.

Chapter 3 proposes and characterizes a novel concept by using the diverse heterochromatic nonlinear photoresponses in UCNP, this will improve image resolution and acquisition speed for super-resolution microscopy with PSF engineering. This work suggests that a single doughnut-shaped beam can simultaneously generate both Gaussian and doughnut PSFs in different emission colours. By investigating the PSFs in the Fourier domain, this work indicates that doughnut PSF contains more information at a high spatial frequency than Gaussian PSF while loses the contents in the medium frequency range. Furthermore, this work develops a multicolour Fourier spectral fusion algorithm to enlarge the frequency shifting coverage of the optical system. It thereby achieves the effective super-resolution PSF by fusing Fourier components from each emission band and processing OTF that contains the maximum spatial information. This approach opens a new perspective to perform super-resolution with minimum distortion and information loss.

Chapter 4 demonstrates an innovative method for single nanoparticle identification by realizing the uniform and distinct nonlinear emission curves from different ions doped UCNPs. This work points out a new optical encoding dimension by exploring the nonlinear photo-response properties. Moreover, the chapter presents a robust strategy to carry out the photo-response curves by applying PSF engineering to code the emitter emission properties. Combined with pattern recognition technology, this approach can easily classify single biomarkers by realizing noticeable features of their emission patterns.

Chapter 5 summarizes this thesis and provides conclusions for this research. The methods investigated in this thesis make concrete the specific advantages in terms of image depth, speed, overall quality and precision. These methods represent our contribution to the topic, by seeking a stable, viable, and multifunctional optical imaging modality at the nanoscale. Moreover, the last chapter provides several potential research directions for future analyses.

Chapter 2 Multi-photon near-infrared emission saturation nanoscopy for deep tissue imaging by using UCNPs

Multi-photon fluorescence microscopy (MPM), using near-infrared excitation light, provides increased penetration depth, decreased detection background, and reduced phototoxicity. Using the STED approach, MPM can bypass the diffraction limitation, but it requires both spatial alignment and temporal synchronization of high power (femtosecond) lasers, which is limited due to the probes' inefficiency. Here, we report that UCNPs can unlock a new mode of NIRES nanoscopy for deep tissue super-resolution imaging with excitation intensity several orders of magnitude lower than that required by conventional MPM dyes. Using a doughnut beam excitation from a 980 nm diode laser and detecting at 800 nm, we achieve a resolution of sub 50 nm, 1/20th of the excitation wavelength, in imaging of single UCNP through 93 μm thick liver tissue. This method offers a simple solution for deep tissue super-resolution imaging and single-molecule tracking.

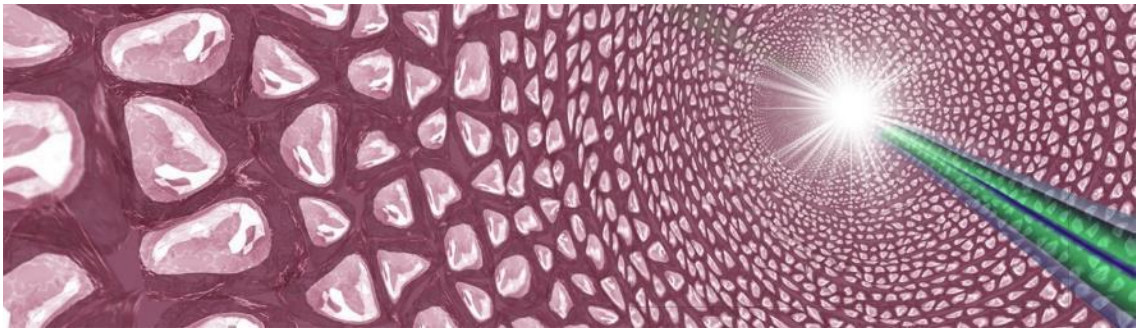

The contents of this chapter have been published in:

C. Chen *et al.*, "Multi-photon near-infrared emission saturation nanoscopy using upconversion nanoparticles," *Nat. Commun.*, no. 9, p. 3290, 2018.

C. Chen, F. Wang, S. Wen, Y. Liu, X. Shan, and D. Jin, "Upconversion nanoparticles assisted multi-photon fluorescence saturation microscopy," *Proc. SPIE 10891, Nanoscale Imaging, Sensing, Actuation Biomed. Appl. XVI, 108910S*, p. 25, 2019.

Wang, F., Jin, D. & **Chen, C.** "A super-resolution imaging method, a plurality of upconversion nanoparticle fluorophores, and a super-resolution scanning microscope." *WO2020028942A1*, 2020-02-13. *WIPO (PCT)*

2.1 Background

Brighter, more biocompatible nanoparticles have been utilized as the fluorescent nanoprobes, allowing more clearly long-term biological observations. Typically, the fluorescent signal is proportional to illumination dose due to their linear fluorescence response to excitation. The fluorescence of several unusual probes can respond in a nonlinear way under certain conditions, including stimulated emission [104], fluorescence saturation [105], saturated photoswitching [106] or stochastic photoswitching [14]. An extensive variety of techniques is exploited by employing these probes with nonlinear photophysical behaviour to achieve sub-diffraction imaging [107].

However, single-molecule localization across thick scattering specimens still presents challenges [108], which requires a technique with a high penetration depth of illumination through the refractive index mismatching thick tissue while still maintaining sub-diffraction ability [107]. Moreover, densely-labelled biological specimens are hindered by tissue scattering of both emission and excitation light, which increases background and degrades both contrast and optical sectioning [109]. Multi-photon laser scanning microscopy (MPLSM, also known as nonlinear, two-photon or three-photon scanning microscopy) is an alternative method for imaging the biological samples with tens to hundreds of microns thickness [110]. The principle of multi-photon excitation is to employ two or more lower-energy photons, instead of the conventional excitation process with only one excited photon, to stimulate the fluorescent group (**Figure 2-1**). Compared with single-photon excited microscopy, multi-photon microscopy with the increased

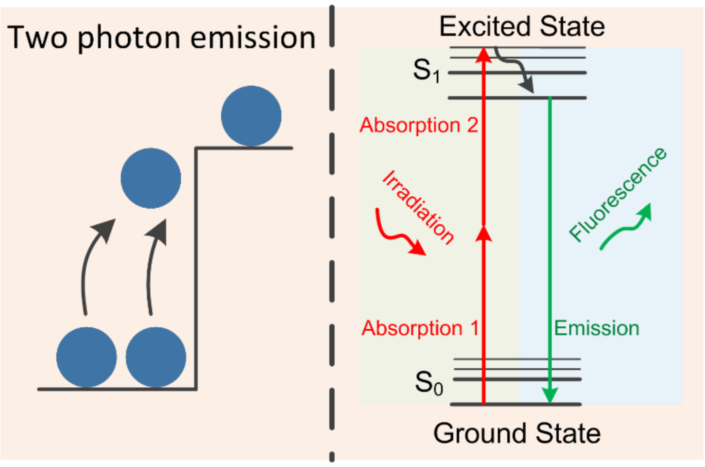

Figure 2-1 | Diagram of the conventional two-photon emission. A molecule absorbs two photons at the same time. The transition energy for this process is equal to the sum of the energies of the two photons absorbed. S_0 is the ground state, S_1 is the excited state.

wavelength of the excitation light enables the visible or the NIR excitation to replace the UV light, which results in in-depth penetration, less light scattering in the tissues and is more biologically friendly to the living sample. When the focused excitation beam passes through the thick sample, an effective excitation process occurs only in the region with a high photon flux near the focal spot. This limits the amount of sufficient excitation volume required to enhance the signal-to-background ratio and reduce out-of-plane photobleaching.

Nevertheless, the spatial resolution of traditional MPLSM is physically limited by diffraction to hundreds of nanometers, and the NIR wavelengths employed for excitation in MPLSM prevent the accurate imaging of the subcellular features at the nanoscale [111][112]. Advances in super-resolution fluorescence techniques allow high-resolution fluorescence imaging of biological samples at resolutions beyond the diffraction limit. STED microscopy has been successfully applied in conjunction with 2PLSM (STED2P) to achieve super-resolution imaging of 2P-excited (2PE) fluorescence [113]. STED2P has been demonstrated to produce five-fold improvement in 2P imaging resolution in fixed cultured cells. Contemporary implementations in tissue have used a continuous-wave (CW) STED laser, which reduces the efficiency of the depletion process. STED has been proposed coupled with 2PE microscopy combining the advantages of 2PE with its super-resolution ability. A method is proposed to perform 2PE-STED imaging using a single wavelength (SW) and, consequently, the very same laser source for 2PE and depletion to achieve 80 nm at 168 mW [114].

Two-photon light-sheet microscopy [115] can extend the penetration of illumination by using a longer wavelength of light, but is still limited by the depth-of-focus and requires two-side illumination to reach a 250-μm-wide field-of-view. Furthermore, images from light-sheet microscopy are affected by tissue scattering of emitted fluorescence photons, which degrades the lateral image resolution in deep layers. In a 1P imaging system, scattering due to the collagen matrix inhibits high-resolution imaging deep into this sample, but 2P ISIM permits observation of fine details at depths of ~100 μm [109]. Live imaging of dendritic spines with the 60-nm resolution was achieved and demonstrated that the technique allows accurate quantification of neuronal morphology up to 30-mm deep in living brain tissue by Pulsed STED Two-Photon Excitation Microscopy [112].

The nonlinear MPM [116], also known as two-photon or three-photon scanning microscopy, uses near-infrared excitation that penetrates as deep as hundreds of microns [110] through the so-called transparent biological window [76]. Near-infrared light does not excite autofluorescence background and has minimal phototoxicity, ideal for live-cell imaging. However, the longer wavelength used in MPM leads to a lower resolution, hindered by the diffraction limit (λ/2NA) [116] [117]. STED approach can minimize the area of illumination at the focal point to achieve super-resolution imaging [11][118][119]. This approach has enabled MPM [113][114] to deliver five folds of improvement in resolution in imaging fixed cells. Employing two spatially aligned and temporally synchronized femtosecond lasers in a sophisticated pulsed STED [120][121], a super-resolution of 60 nm at a depth of 50 μm has been achieved for imaging dendritic spines in living brain tissue [112][122]. Nevertheless, it requires high-power and expensive femtosecond lasers for MPM to achieve super resolution. This is due to the poor efficiency of the nonlinear multi-photon process, for instance small multi-photon absorption cross-sections of the probes [114].

UCNPs are typically doped with ytterbium sensitizer ions (Yb^{3+}), which absorb the photons located in the near-infrared region and transfer their excitation to activator ions (**Figure 2-2**) [77][123]. Thulium (Tm^{3+}) co-doped UCNPs, able to convert 980 nm NIR photons into strong 800 nm near-infrared emissions, are promising for background-free deep tissue imaging. The sensitizer Yb^{3+} ions have much larger absorption cross-section in near-infrared compared to dye molecules used in MPM [42][124], benefiting from its

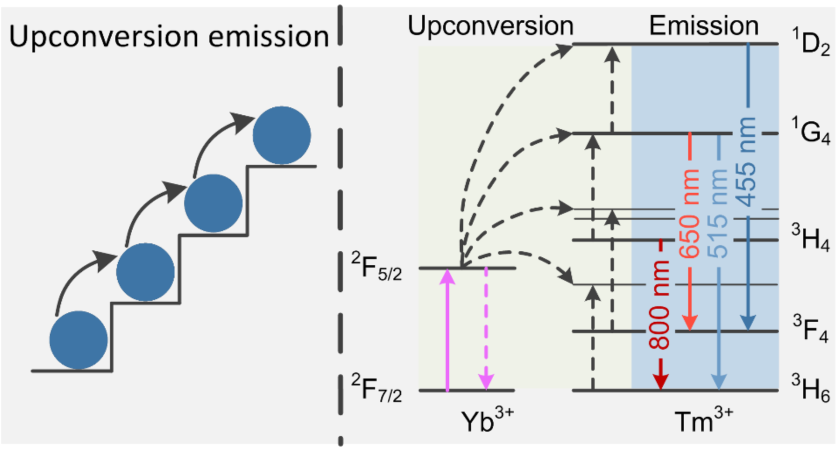

Figure 2-2 | Diagram of upconversion emission in UCNPs. The sensitizer ions sequence absorbs photons and pass to the activator ions which have multiple long-lived intermediate states to facilitate the multiphoton upconversion process.

linear absorption. Moreover, the photon upconversion process is a sequential absorption process where the activator ions, such as Tm^{3+}, have multiple long-lived intermediate states to facilitate the multiphoton upconversion process [78]. Therefore, UCNPs bypass the crucial requirement of simultaneous absorption of more than two photons from the femtosecond lasers, providing several orders of magnitude lower excitation threshold than what most efficient multi-photon dyes normally have [42].

UCNPs have been recently discovered as being suitable for STED-like super-resolution nanoscopy with sub-30 nm optical resolution in resolving the cluster of single UCNPs [79]. A resolution of 80 nm has been further demonstrated in resolving subcellular protein structures [80]. However, this scheme is not suitable for deep tissue super-resolution imaging, because the 4-photon upconversion emissions, at a wavelength around 455 nm, will attenuate rapidly through deep tissue. Ideally a near-infrared-in and near-infrared-out configuration, by detecting emissions above 700 nm from UCNPs, would enable upconversion nanoscopy imaging in deep tissue.

Here we report that setting the 980 nm excitation laser will create a doughnut beam enabled super-resolution imaging of single UCNPs through deep tissue. Low power coherent excitation at 980 nm can quickly saturate the metastable level that emits bright near-infrared emission (800 nm), and the nonlinear power-dependent emission curve (saturation curve) is sharp. Both play an essential role in enabling a new mode of NIRES nanoscopy, ideal for deep tissue super-resolution imaging, with remarkable light penetration depth, ultra-low auto-fluorescence background and minimum photo-toxicity. We further demonstrate that fine-tuning of the doping concentration and material design of UCNPs can further improve their optical properties to enhance resolution, suggesting a new topic for the material sciences community to investigate, specifically more efficient super-resolution probes through deep tissue.

2.2 Advantage of UCNPs in deep tissue imaging

To meet the requirements of super-resolution imaging through deep tissue, we first calculate and examine the minimum excitation/depletion energy density (J cm^{-2}) for fluorescent proteins [121], quantum dots [51], semiconductor nanowires segments [125] and UCNPs [79] used in the STED and GSD approaches. **Table 2-1** summarizes the critical parameters for these probes to calculate the normalized energy densities for deep

Table 2-1 | Key parameters of various imaging modalities for deep tissue using nanoparticles.

Nanoscope	Probe	λ_{ex} (nm)	λ_{dep} (nm)	f (MHz)	Pulse duration t_p (ps)	Power intensity I (mW)	Energy intensity I_Q (J cm^{-2})
STED [51]	1PE-QD	628	-	38	1.2	0.05	7.9×10^{-5}
		-	775	38	1200	150	
STED [121]	2PE-FP	850	-	76	0.13	2.7	9.4×10^{-3}
		-	580	76	200	4.4	
STED [79]	MP-UCNP	980	-	CW	-	1	7.6×10^{-7}
		-	808	CW	-	40	
GSD [125]	1PE-SEMI	700	Non	80	5	5	2.5×10^{-4}
NIRES [83]	MP-UCNP	980	Non	CW	-	75	1.2×10^{-6}

tissue imaging. To compare the maximum laser-induced energy dosage, required by different probes to achieve nanoscopy through deep tissue, we calculate the energy density (I_Q) of both excitation and depletion laser during excitation time of 200 fs through 100 μm skin tissue.

We can calculate the required I_Q according to:

$$R_{tr} = e^{-\alpha_\lambda l} \tag{2-1}$$

$$I_Q = \frac{P r_o t_\tau}{A f t_p R_{tr}} \tag{2-2}$$

Where R_{tr} is the transmission ratio of an electromagnetic wave penetrating a material (Beer's law); P is the beam power; r_o is the loss rate of the objective lens; t_τ is the exposure time; A is the area of the focused laser spot; f is the pulse frequency; t_p is the pulse duration; α_λ is the attenuation coefficient; λ is the wavelength; and l is the path length. Note that the value of f and t_p is 1 for CW laser. The loss rate of the laser through the objective lens is based on our current system ($r_o = 0.43$), and the areas of the focused laser spots are $A_{\text{gau}} = 3.76 \times 10^{-9}\ \text{cm}^2$ for Gaussian beam and $A_{\text{dou}} = 7.81 \times 10^{-9}\ \text{cm}^2$ for doughnut beam.

From **Figure 2-3**, it is evident that the tissue attenuates more power for shorter wavelength [126], which requires considerable power in the visible range to achieve a high resolution if using the one-photon excitation (1PE) scheme. It explains why two-photon excitation (2PE) in the near-infrared range is the commonly used method. Nevertheless, multi-photon probes have microscopic absorption cross-sections, thereby

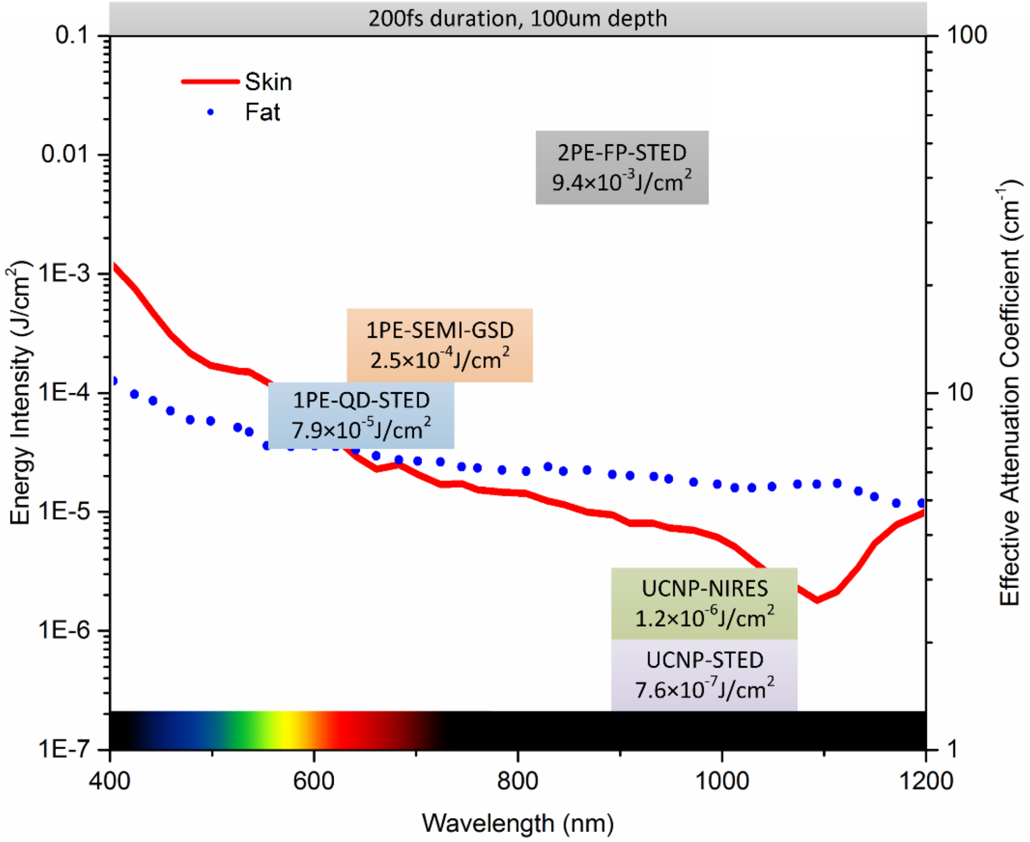

Figure 2-3 | Summary of the minimum energy densities required by a range of optical probes for deep tissue super-resolution imaging. In order to facilitate the comparison, we normalize the excitation/depletion power to certain pulse period (200 fs) through 100 μm tissue. The red and blue curves indicate the light effective attenuation coefficient in the tissue. [126] 1PE, one-photon excitation; 2PE, two-photon excitation; QD, quantum dots; FP, fluorescent protein; SEMI, semiconductor nanowires segments.

requiring even more excitation power. In contrast, taking both advantages of the near-infrared excitation wavelength and broad absorption cross-section, UCNPs provide a potential solution by only requiring minimal laser power through the deep tissue.

2.3 Principle of NIRES nanoscopy

2.3.1 **Photon transition system in UCNPs**

The approximate function of optical resolution in a STED or GSD microscope has been derived, releasing the famous square root law as described in Equation (1-2). The FWHM of STED PSF with a fluorophore that contains two energy levels (**Figure 2-4a**) can be represented as:

$$\Delta x = \frac{h_0}{\sqrt{\varsigma}} \tag{2-3}$$

Here h_0 denotes the FWHM of confocal PSF. $\varsigma = \frac{I_{STED}^{Max}}{I_S}$ denotes the saturation factor. I_S is referred to as the saturation intensity where the emission intensity decreases to half of the maximum. I_{STED}^{Max} represents the maximum amplitude of the STED beam profile.

The validity of this function of FWHM in STED can actually be extended for two-photon STED and two-photon negative GSD where the fluorophore is excited by absorbing two photons with energy below its bandgap. This can be done by modifying the function of saturation intensity as Equation (2-4):

$$I_S = \sqrt{\frac{k_{BA}}{\sigma_{TPA}}} \tag{2-4}$$

Here k_{BA} is the carrier transition rate from excited state B to ground state A, σ_{TPA} denotes the molecular cross-section with two-photon absorption.

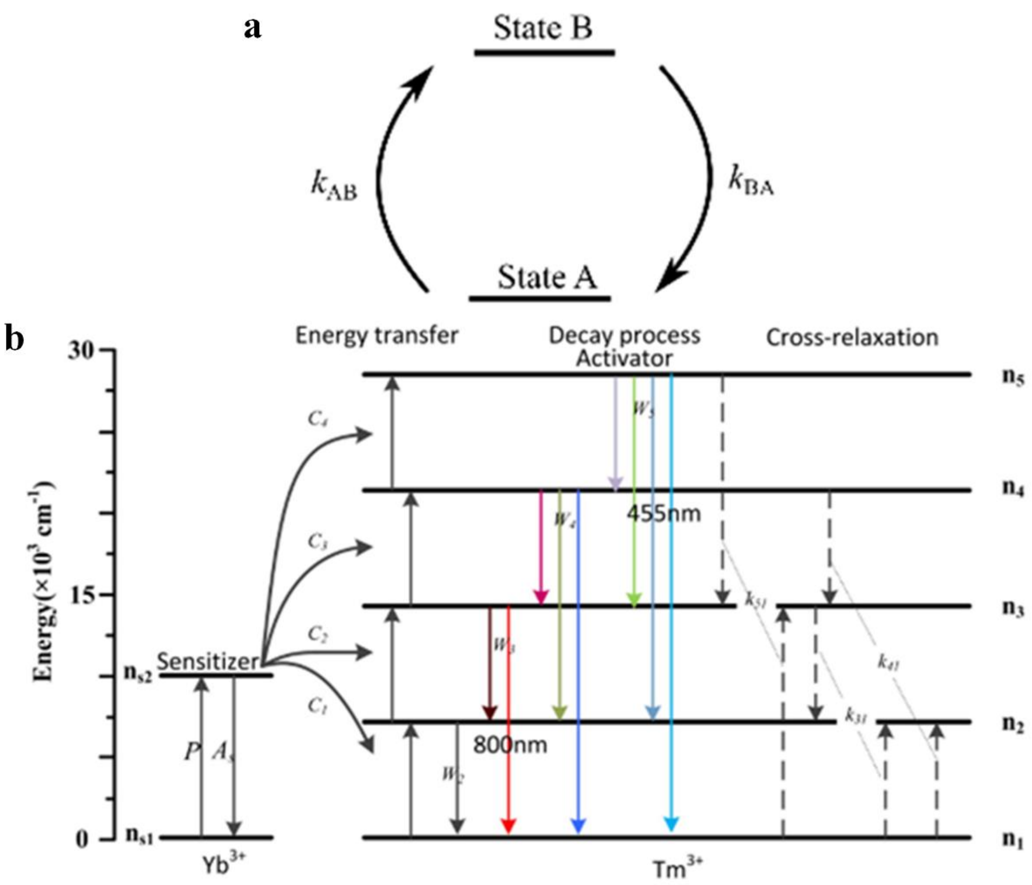

Figure 2-4 | Rate transition system of UNCPs. (**a**) The energy level diagram of the two-level system, with excited state B and ground state A. (**b**) The energy level diagram of Tm^{3+} and Yb^{3+} doped UCNP.

In this chapter, the NIRES nanoscopy has a similar physical process with two-photon negative GSD but may not be able to use the existing function of resolution as Equation (2-3). UCNP has a much more complex rate transition system (**Figure 2-4b**) than the aforementioned two-level system, with rate Equations (2-5) to (2-10). **Table 2-2** displays the values of critical constants and rate parameters used in the simulations:

$$\frac{dn_1}{dt} = -c_1 n_1 n_{S2} + a_{21} w_2 n_2 + a_{31} w_3 n_3 + a_{41} w_4 n_4 + a_{51} w_5 n_5 - k_{41} n_1 n_4 - k_{31} n_3 n_1 - k_{51} n_5 n_1 \tag{2-5}$$

$$\frac{dn_2}{dt} = c_1 n_1 n_{S2} - c_2 n_2 n_{S2} - a_{21} w_2 n_2 + a_{32} w_3 n_3 + a_{42} w_4 n_4 + a_{52} w_5 n_5 + k_{41} n_1 n_4 + 2k_{31} n_1 n_3 \tag{2-6}$$

$$\frac{dn_3}{dt} = c_2 n_2 n_{S2} - c_3 n_3 n_{S2} - (a_{31} + a_{32}) w_3 n_3 + a_{43} w_4 n_4 + a_{53} w_5 n_5 + 2k_{51} n_5 n_1 + k_{41} n_4 n_1 - k_{31} n_3 n_1 \tag{2-7}$$

$$\frac{dn_4}{dt} = c_3 n_3 n_{S2} - c_4 n_4 n_{S2} - (a_{43} + a_{42} + a_{41}) w_4 n_4 + a_{54} w_5 n_5 - k_{41} n_1 n_4 \tag{2-8}$$

$$\frac{dn_5}{dt} = c_4 n_4 n_{S2} - (a_{54} + a_{53} + a_{52} + a_{51}) w_5 n_5 - k_{51} n_1 n_5 \tag{2-9}$$

$$\frac{dn_{S2}}{dt} = P_{980} n_{S1} - w_{S2} n_{S2} - (c_1 n_1 + c_2 n_2 + c_3 n_3 + c_4 n_4) n_{S2} \tag{2-10}$$

Here we simplify the energy level which involves two energy levels associated with the sensitizer Yb^{3+} ions and five associated levels with the activator Tm^{3+} ions; n_{S1}, n_{S2}, n_1, n_2, n_3, n_4 and n_5 are the populations of ions on energy levels of $^2F_{7/2}$, $^2F_{5/2}$, $^3H_6$, $^3H_5/^3F_4$, $^3F_{2,3}/^3H_4$, $^1G_4$ and $^1D_2$ respectively; c_i is the energy transfer ratio between Yb^{3+} on the

Table 2-2 | The values of key constants and rate parameters used in the simulations [79].

w_2 (s^{-1})	w_3 (s^{-1})	w_4 (s^{-1})	w_5 (s^{-1})	w_{s2} (s^{-1})
63000	20000	15000	33000	8000
a_{51}	a_{52}	a_{53}	a_{54}	
0.24	0.23	0.2	0.33	
a_{41}	a_{42}	a_{43}	a_{31}	a_{32}
0.18	0.24	0.58	0.27	0.73
c_1 (s^{-1})	c_2 (s^{-1})	c_3 (s^{-1})	c_4 (s^{-1})	
62000	50000	70000	5000	
k_{31} (s^{-1})	k_{41} (s^{-1})	k_{51} (s^{-1})	P_{980} (s^{-1})	
140000	185000	500000	280000	

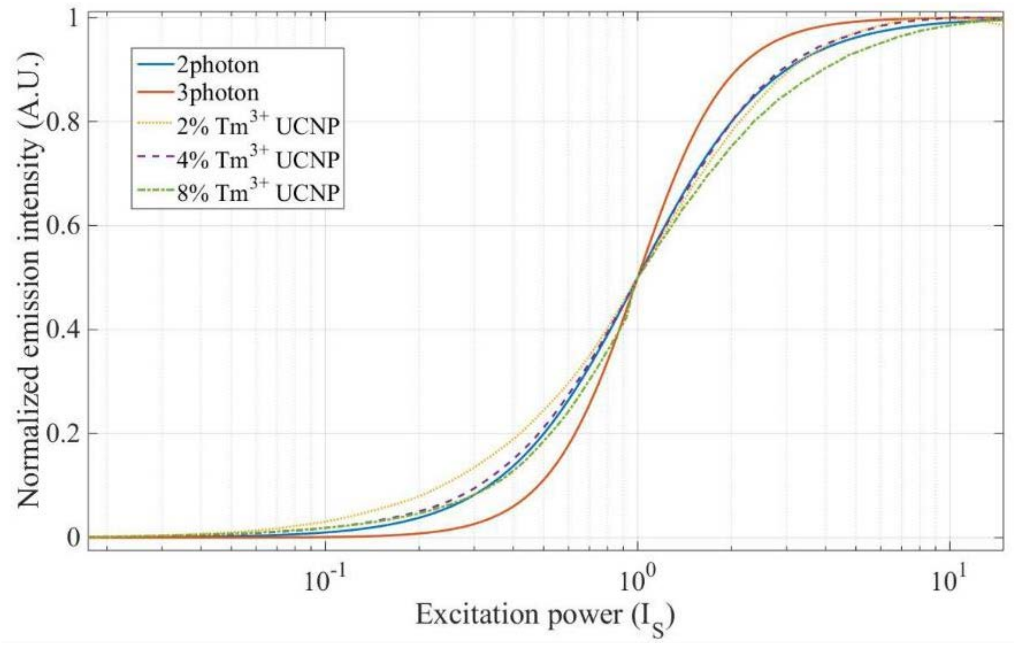

Figure 2-5 | Simulated excitation power-dependent emission intensity. Two-photon excited two energy level system (labelled as 2 photons), three-photon excited two energy level system (labelled as 3 photons) and UCNPs with 2%, 4% and 8% Tm^{3+} doping. It is noted that the excitation power is normalized to saturation intensity (I$_S$) where the emission intensity drops by half.

excited level and Tm^{3+} both on the ground and the intermediate levels; K_{ij} is the cross-relaxation coefficients between the state i and j; a_{ij} is the branching ratio from energy level i to j; W_i is the intrinsic decay rate of Tm^{3+} on level i; P is the absorption rate of Yb^{3+}; n_3 ($^3H_4$) is the excited state used in this work. Therefore, the resultant carrier number (emission intensity) function of excitation power differs significantly from that for the two-photon excited two-level system as shown in **Figure 2-5**. The result is a further difference in the function of the resolution NIRES nanoscopy.

2.3.2 Saturation effect with the doughnut-shaped beam

Following a similar study done on confocal microscopy with saturated excitation [127], we define the effective PSF of the NIRES as:

$$\begin{cases} h_{eff}(x) = h_{em}(x) \times h_c(x) \\ h_{em}(x) = \eta(i) \times h_{exc}(x) \end{cases} \tag{2-11}$$

Here $h_{em}(x)$ is the PSF of emission; $h_{exc}(x)$ is the PSF of the excitation beam (doughnut beam for NIRES); η is excitation power-dependent emission intensity curve; and $h_c(x)$ is the PSF of the confocal collection system. The FWHM of the intensity dip in h_{eff} represents the resolution for NIRES nanoscopy. The experimentally measured PSF (h_{exp})

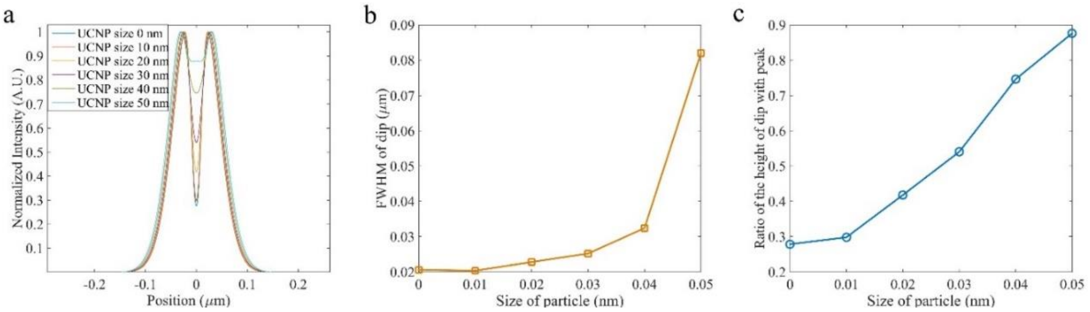

Figure 2-6 | Theoretical simulation of the image of single UCNP by NIRES. (**a**) The PSF of UCNP with size ranging from 0 nm to 50 nm. (**b**) The FWHM of the dip in h_{exp} for UCNPs with different size. (**c**) The ratio of the height value of the dip with the peak value in h_{exp} for UCNPs with different size. The UCNPs with 4% Tm^{3+}, 20% Yb^{3+} are used in this simulation. The excitation peak intensity is 100 times larger than the saturation intensity of UCNP.

of NIRES is the convolution between the h_{eff} and the spatial profile (h_{UCNP}) of nanoparticle as below:

$$h_{exp} = h_{eff} * h_{UCNP} \tag{2-12}$$

The deconvolution process on h_{exp} results in a measured h_{eff}, in which the FWHM of the dip represents the resolution of NIRES. In this paper, the resolution is calculated through deconvolution of experimental measured PSF.

The theoretical simulation of h_{exp} for different particle size is shown in **Figure 2-6a**, where the PSF of UCNP with size 0 nm indicates the h_{eff}. This outcome indicates that a larger particle size leads to a larger value of the FWHM of h_{exp} (**Figure 2-6b**) and the dip height of h_{exp} (**Figure 2-6c**), which in turn reduces resolution. It is notable that, the FWHM of the dip of h_{exp} can be smaller than the size of particle (**Figure 2-6b**) when the FWHM of h_{eff} is smaller than the particle's size. This stems from the doughnut-shaped PSF of h_{eff}. If the shape of h_{eff} is a Gaussian function, the FWHM of the PSF after convolution is always larger than the size of the particle.

2.3.3 Emission saturation enabled sub-diffraction resolution

NIRES nanoscopy takes advantage of multi intermediate ladder-like energy levels of UCNPs (**Figure 2-7a**), easily converting 980 nm photons into 800 nm photons. The emission saturation curve of the two-photon state $^3H_4$ (800 nm) (**Figure 2-7b**) shows an early onset of upconversion emissions at low excitation power density and sharp rising-up slope, reflecting its nonlinear energy transfer assisted photon upconversion process.

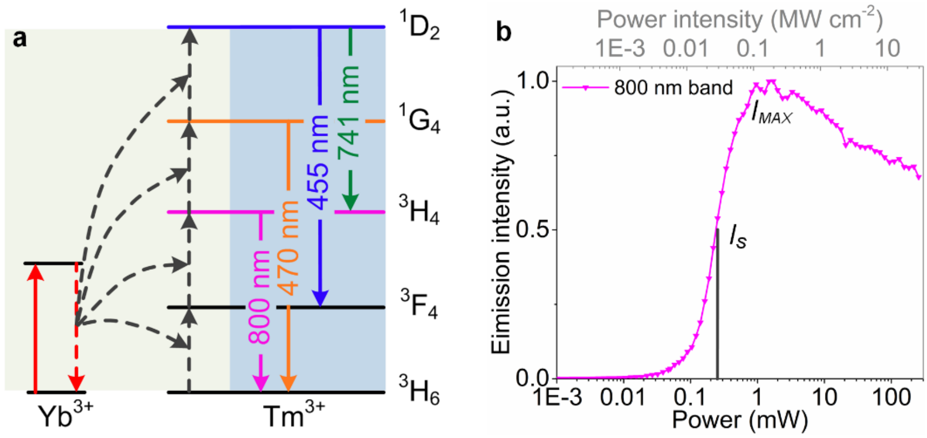

Figure 2-7 | The simplified energy levels and 800 nm emission power dependence of Yb^{3+} and Tm^{3+} co-doped UCNPs. (**a**) The sensitizer Yb^{3+} ions initiate the photon upconversion process by a linear and sequential absorption of 980 nm excitation. Due to the multiple long-lived intermediate states, the energy is stepwise transferred onto the scaffold energy levels of emitters Tm^{3+}. This eventually facilitates multiphoton upconversion emissions, including those from the four-photon upconversion excited state $^1D_2$ (455 nm & 741 nm), three-photon state $^1G_4$ (470 nm), and two-photon excited state $^3H_4$ (800 nm). (**b**) The saturation intensity curve of the 800 nm emissions derives from UCNPs (40 nm $NaYF_4$: 20% Yb^{3+}, 4% Tm^{3+}) under 980 nm excitation.

The decrease in the saturation curve under high excitation power (larger than 2 mW) is due to the energy being further upconverted from $^3H_4$ to the higher energy states.

For generating a super-resolution image of the single nanoparticle by NIRES, we employ a tightly-focused doughnut-shaped excitation beam to scan across a sample containing UCNPs. Only when a single UCNP sits in the middle of the doughnut beam, NIRES generates a negative contrast. By using the definition of resolution in GSD microscopy [128], the FWHM of the dip at the measured PSF of a single UCNP defines the

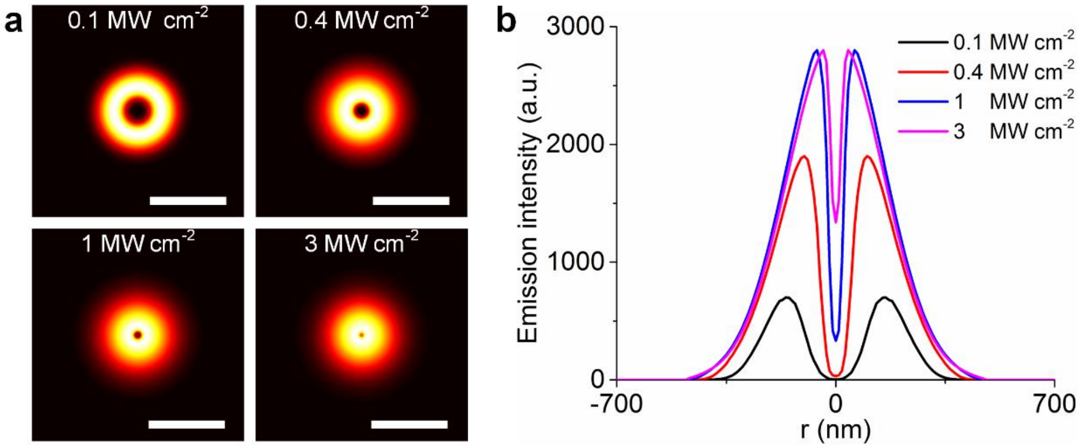

Figure 2-8 | The principle of NIRES nanoscopy using UCNP as a multi-photon probe for deep tissue imaging. (**a**) The simulated 'negative' contrast images of the saturated upconversion emission of a single UCNP at four different excitation powers of 0.1 MW cm^{-2}, 0.4 MW cm^{-2}, 1 MW cm^{-2} and 3 MW cm^{-2}. (**b**) Cross-section profiles in (**a**). Pixel size, 10 nm. Scale bar is 500 nm.

experimental resolution achieved by NIRES (**Figure 2-8b**). By taking advantage of the uniform size of monodisperse UCNPs, we can calculate the actual resolution of NIRES through deconvolution with the size of a single nanoparticle. With the nonlinear excitation process, the optical resolution of NIRES is limited by diffraction limitation under low excitation power (**Figure 2-8a**, 0.1 MW cm^{-2}, 0.4 MW cm^{-2}). However, this limitation can be easily broken with high power (1 MW cm^{-2}, 3 MW cm^{-2}) using a purpose-built NIRES setup, shown in Section 2.4.1.

The resolution of NIRES at a specific excitation power density is primarily determined by the emission saturation curve of UCNPs (**Figure 2-7b**). In our case, there are three features from the curve affecting the resolution. The first feature is the saturation intensity point (I_S) to achieve the half value of the maximum emission intensity [129]. The second feature is the power point (I_{MAX}) which sets out to achieve the maximum emission intensity with fixed I_S. In other words, smaller I_{MAX} indicates the more superlinear shape of the curvature between I_S and I_{MAX}. The third feature is the onset value of the curve, which is defined as the power point (in the unit of I_S) to achieve e^{-2} of the maximum emission intensity. Tremendous onset indicates a more underlinear shape of the curvature between 0 and I_S.

When excitation power is smaller than I_S, the nanoparticle has not reached the non-saturation condition. The acquired image of the UCNPs reflects the PSF of the doughnut beam because the emission signal is proportional to the excitation intensities. When the applied laser intensity is over I_S, the acquired pattern will be affected due to the optical nonlinear response of the emitter. The emission saturation should result in the expansion of the obtained image and sharpened the dip at the centre of the doughnut pattern, as shown in **Figure 2-8a**. To be specific, the increased excitation power elevates the fluorescence at the centre region, while the fluorescence signals away from the centre retain the same values since they have already reached the maximum. Typically, it is easy to overcome the diffraction limitation by employing relative high laser much over I_S. Lower values of I_S and/or I_{MAX} shrink the size of a dark spot in the doughnut emission PSF, thereby enhancing the resolution. The more significant onset of the curve offers a lower depth of the PSF to yield a better resolution.

2.4 Methods

2.4.1 Experimental setup

All the measurements were performed on a home-built microscopy system equipped with a 3-axis closed-loop piezo stage (stage body MAX311D/M, piezo controller BPC303; Thorlabs) and a vortex phase plate (VPP, VPP-1a, RPC Photonics). **Figure 2-9** shows the schematic drawing of the experimental setup, where UCNPs were excited by a polarization-maintaining single-mode fibre-coupled 980 nm diode laser (BL976-PAG900, controller CLD1015, Thorlabs). The first half-wave plate (HWP, WPH05M-980, Thorlabs) and a polarized beam splitter (PBS, CCM1-PBS252/M, Thorlabs) were employed to precisely adjust the excitation power by rotating HWP electronically. The purpose of the second HWP was to turn the polarization from horizontal (P polarized) to vertical (S polarized). Confocal scanning was acquired without the VPP via the auxiliary two flexible mirrors, as shown in the dotted portion of **Figure 2-9**. After collimation, the excitation beam was reflected by the short-pass dichroic mirror (DM, T875spxrxt-UF1,

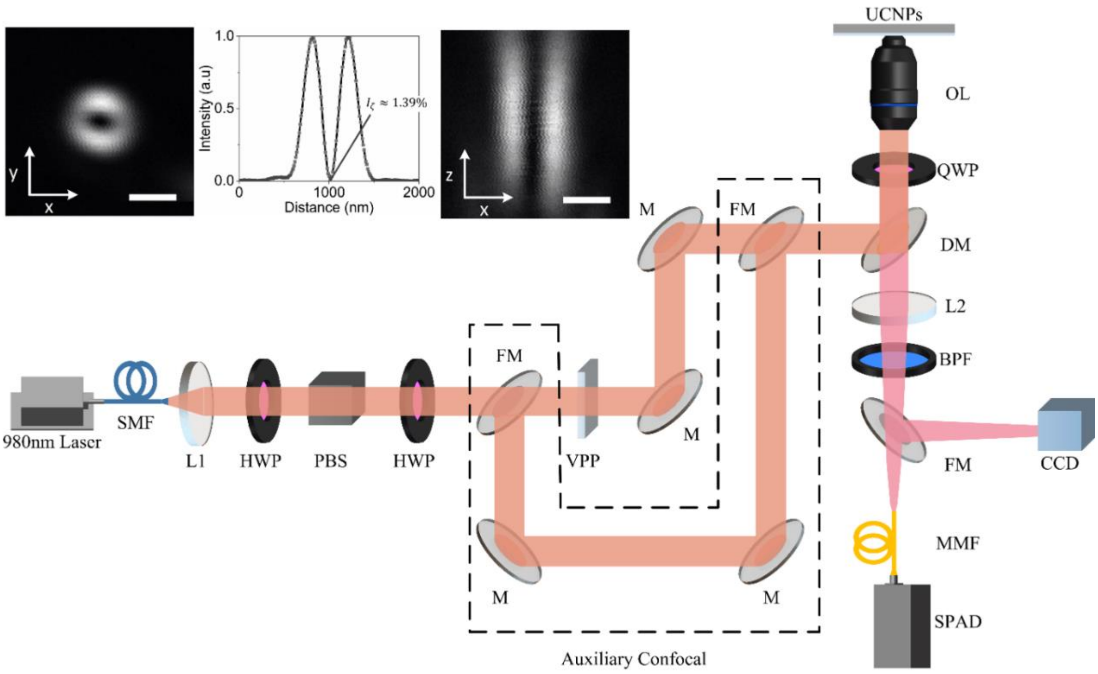

Figure 2-9 | Experimental setup for NIRES nanoscopy (SMF, single-mode fibre; MMF, multi-mode fibre; L1, collimation lens; L2, collection lens; HWP, half-wave plate; QWP, quarter-wave plate; PBS, polarized beam splitter; VPP, vortex phase plate; M, mirror; FM, flexible mirror; DM, dichroic mirror; OL, objective lens; BPF, band-pass filter; SPAD, single-photon avalanche diode; CCD, charge-coupled device). The dotted portion is designed for auxiliary confocal with two flexible mirrors to bypass the VPP in the main optical path. Inset shows PSF of the NIRES is measured by scattering of a 100 nm gold bead in reflection (path not shown). The I_ξ (ratio value of the intensity at the doughnut centre to the max intensity of the beam) is measured as 1.39%. Scale bars: 500 nm.

Chroma), and focused through a high numerical aperture objective (UPlanSApo, 100×/1.40 oil, Olympus) to the sample slide. A quarter-wave plate (QWP, WPQ05M-980, Thorlabs) was adopted to transform the excitation beam from linear polarization to circular polarization, in order to obtain optical super-resolution images. Photoluminescence was collected in the same way and split from the excitation beams by DM. The emission signals were filtered by bandpass filter (BPF, ET805/20M, Chroma) or short pass filter (SPF, FF01-842/SP-25, Semrock), coupled into multimode fiber (MMF, M42L02, Thorlabs), and then detected by a single-photon counting avalanche photodiode (SPAD, SPCM-AQRH-14-FC, Excelitas). The MMF could also be switched to a miniature monochromator (iHR550, Horiba) for measuring upconversion emission spectra. Typical excitation powers for the recording of super-resolution NIRES images varied from 5 mW to 100 mW. All powers were measured at the back aperture of the objective lens. Pixel dwell times were adjusted to ~3 ms.

2.4.2 **Materials**

$YCl_3\cdot 6H_2O$ (99.99%), $YbCl_3\cdot 6H_2O$ (99.99%), $TmCl_3\cdot 6H_2O$ (99.99%), NH_4F (99.99%), NaOH (99.9%), oleic acid (OA, 90%), and 1-octadecene (ODE, 90%) were purchased from Sigma-Aldrich.

2.4.2.1 **Synthesis of UCNPs**

$NaYF_4$: Yb, Tm nanocrystals with different Tm doping (from 2% to 8%) were synthesized according to our previously reported method [79][130]. Taken $NaYF_4$: 20% Yb, 2% Tm as an example, one mmol $RECl_3$ (RE = Y, Yb, Tm) with the molar ratio of 78:20:2 were added to a flask containing 6 ml OA and 15 ml ODE. The mixture was heated to 170 °C under argon for 30 min to obtain a clear solution and then cooled down to about 50 °C, followed by adding 5 mL methanol solution of NH_4F (4 mmol) and NaOH (2.5 mmol). After stirring for 30 min, the solution was heated to 80 °C under argon for 20 min to remove methanol, and then the solution was further heated to 310 °C for another 90 min. Finally, the reaction solution was cooled down to room temperature, and nanoparticles were precipitated by ethanol and washed with cyclohexane, ethanol and methanol three times to get the $NaYF_4$: 20% Yb, 2% Tm nanoparticles.

For the nanoparticles with the desired size or core-shell structure, layer-by-layer epitaxial growth had been employed. The shell precursors preparation was similar to that for the core nanoparticles synthesis, until the step where the reaction solution was slowly heated to 150 °C and kept for 20 min. Instead of further heating to 300 °C to trigger nanocrystal growth, the solution was cooled down to room temperature to yield the shell precursors. For epitaxial growth, 0.15 mmol as-prepared core nanocrystals were added to a containing 6 ml OA and 6 ml ODE. The mixture was heated to 170 °C under argon for 30 min, and then further heated to 300 °C. Next, 0.25 ml as prepared shell precursors were injected into the reaction mixture and ripened at 300 °C for 4 min, followed by the same injection and ripening cycles for several times to get the nanocrystals with the desired size. Finally, the slurry was cooled down to room temperature, and the formed nanocrystals were purified according to the above procedure.

We synthesized other several kinds of core nanoparticles for similar size with different doping Tm doping concentrations (from 1% to 8%), $NaYF_4$: 20%Yb^{3+}, 2%Er^{3+} and $NaYF_4$: 40%Yb^{3+}, 4%Tm^{3+} using the same method.

2.4.2.2 **Hydrophilic UCNPs**

In order to obtain hydrophilic UCNPs, we washed the OA from the UCNP surface. We first added 500 μL 97% Ethyl Alcohol to 500 μLUCNPs in cyclohexane, followed with centrifuged at 9000 round per minute (rpm) for 10 min. Removing the supernatant and adding 500 μL 97% Ethyl Alcohol and 500 μL 0.2 M HCl to precipitant, followed with a vortex to dissolved. Then the solution was centrifuged at 9000 rpm for 10 min to remove the oleic acid. The supernatant was removed and 500 μL water and 200 μL 97% Ethyl Alcohol were added to the precipitant, followed by a vortex for dissolving. Next, the UCNPs without OA were washed with Milli-Q water twice to get the final hydrophilic UCNPs.

2.4.2.3 **Preparation of slides for single nanoparticle measurement**

A coverslip was washed with ethanol through ultrasonication and dried. 10 μl of the nanoparticles (diluted to 0.01 mg/ml in cyclohexane) was dropped onto the surface of the coverslip and left to dry naturally. The coverslip was put onto a glass slide and air bubbles were squeezed out.

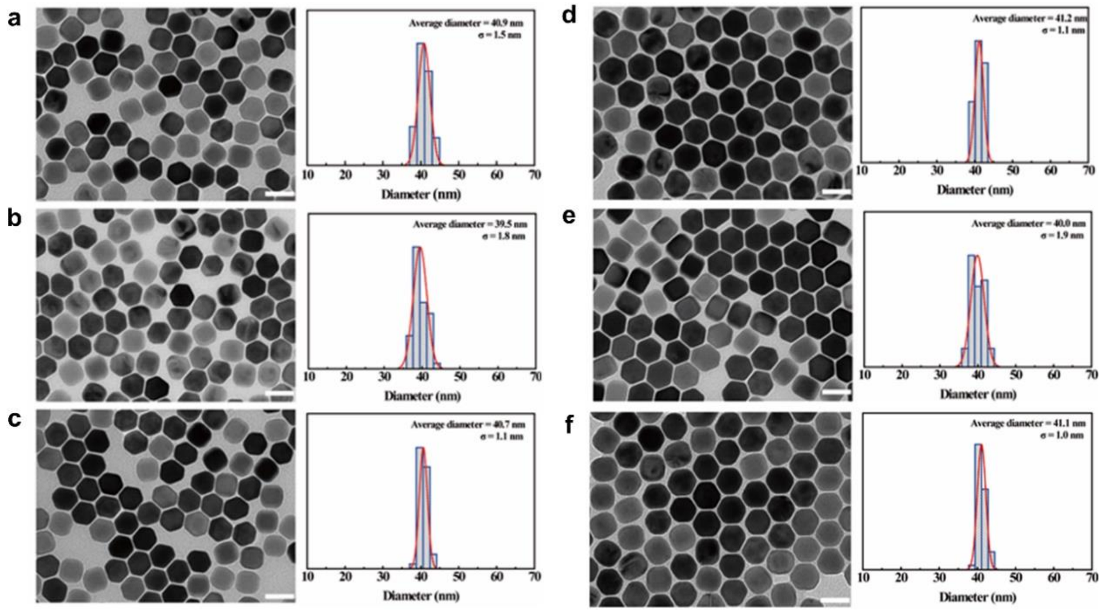

Figure 2-10 | TEM images (left) and size distribution histograms (right) of the nanoparticles. (**a**) $NaYF_4$: 20% Yb, 2% Tm. (**b**) $NaYF_4$: 20% Yb, 3% Tm. (**c**) $NaYF_4$: 20% Yb, 4% Tm. (**d**) $NaYF_4$: 20% Yb, 6% Tm. (**e**) $NaYF_4$: 20% Yb, 8% Tm. (**f**) $NaYF_4$: 40% Yb, 4% Tm. Scale bar is 50 nm.

2.4.2.4 **Characterization techniques**

2.4.2.4.1 **Transmission electron microscopy (TEM) imaging**

The morphology of the formed materials was characterized *via* TEM imaging (Philips CM10 TEM with Olympus Sis Megaview G2 Digital Camera) with an operating voltage of 100 kV. The samples were prepared by placing a drop of a dilute suspension of nanocrystals onto copper grids. **Figure 2-10** shows the TEM images of the synthesized UCNPs.

2.4.2.4.2 **The measurements of upconversion emission spectra**

The emission spectra of the UCNPs were measured on a home-built confocal microscope. The experimental setup was depicted in **Figure 2-9**. The light source was a polarization-maintaining single-mode fibre-coupled 980 nm diode laser (BL976-PAG900, controller CLD1015, Thorlabs). After collimation, the excitation beam was reflected by the short-pass dichroic mirror (DM, T875spxrxt-UF1, Chroma), then focused through a high numerical aperture objective (UPlanSApo, 100x/1.40 oil, Olympus) to the sample slide. The emission signals were collected through the same objective lens and filtered by a short-pass filter (SPF, FF01-842/SP-25, Semrock). Finally, the singles were coupled into multimode fibre (MMF, M42L02, Thorlabs) which were connected with the spectrometer

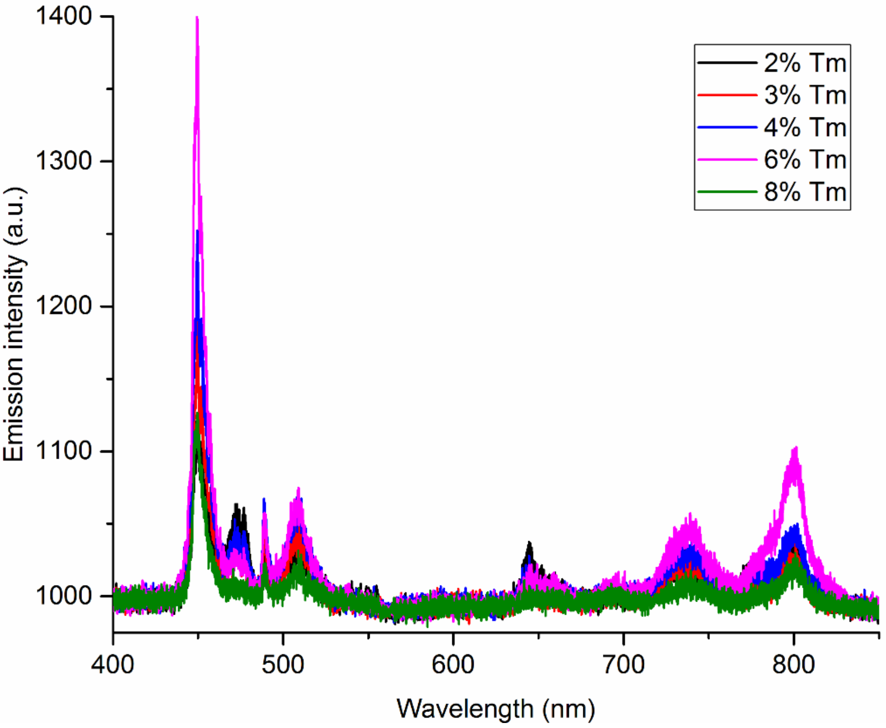

Figure 2-11 | The upconversion emission spectra from UCNPs. The emissions were obtained for UCNPs solution ($NaYF_4$: 20% Yb^{3+}, x% Tm^{3+} nanoparticles, x=2, 3, 4, 6 and 8) under 980 nm excitation laser.

(QEpro, Ocean Optics). The exposure time of the experiment was set to 100 ms. The upconversion emission spectra of these series UCNPs solutions are shown in **Figure 2-11**.

2.4.2.4.3 **The measurements of saturation intensity curves**

The measurements were done on the home-built confocal microscope. A half-wave plate (HWP, WPH05M-980, Thorlabs) and a polarized beam splitter (PBS, CCM1-PBS252/M, Thorlabs) were employed to precisely adjust the excitation power by rotating HWP electronically. The purpose of the second HWP was to turn the polarization from horizontal (P polarized) to vertical (S polarized). A quarter-wave plate (QWP, WPQ05M-980, Thorlabs) was adopted to transform the excitation beam from linear polarization to circular polarization to obtain optical confocal images. Photoluminescence was collected using the same method and split from the excitation beams by the short-pass dichroic mirror (DM, T875spxrxt-UF1, Chroma). The emission signals were filtered by bandpass filters (BPF, ET808/20M, Chroma) and a short-pass filter (SPF, FF01-842/SP-25, Semrock), coupled into multimode fibre (MMF, M42L02, Thorlabs), and then detected by a single-photon counting avalanche photodiode (SPAD, SPCM-AQRH-14-FC,

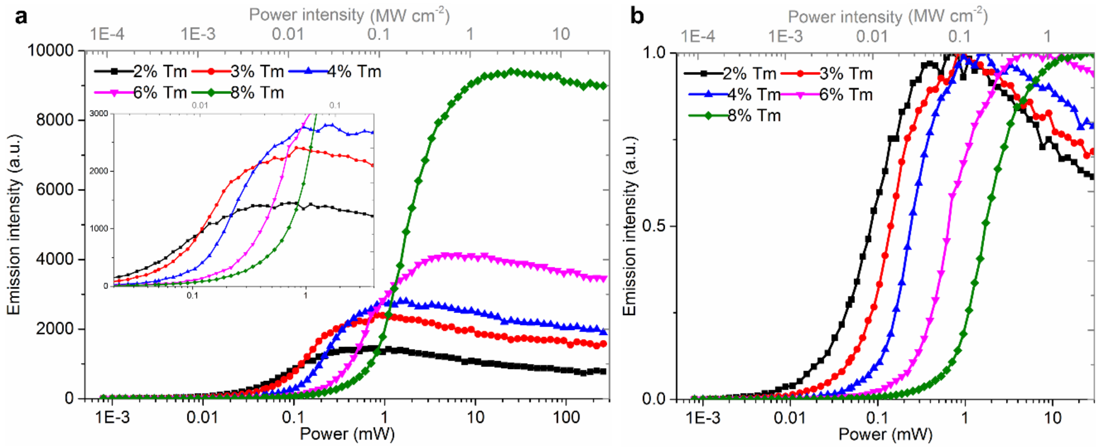

Figure 2-12 | The saturation intensity curve of the 800 nm emissions from UCNPs. (**a**) 800 nm emission saturation curves obtained for a single UCNP ($NaYF_4$: 20% Yb^{3+}, x% Tm^{3+} nanoparticles, x = 2, 3, 4, 6 and 8) under 980 nm excitation. (**b**) Normalized emission saturation curve to the maximum intensity.

Excelitas). Pixel dwell times were adjusted to ~50 ms. Thus, the 800 nm emission saturation intensity curves of these UCNPs can be acquired by electronically rotating HWP to control the excitation power (**Figure 2-12**).

2.4.3 Biological samples

2.4.3.1 Preparation of HeLa cell samples

The human cervical cancer (HeLa) cells were obtained from the American Type Culture Collection (ATCC®CCL-2™). The cells were incubated in Dulbecco's High Glucose Modified Eagle's Medium (DMEM) which contained 10% fetal bovine serum (FBS) and was incubated at 37 °C and 5% CO_2.

For the internalization of UCNPs, 5*10^5 HeLa cells were seeded on a glass coverslip in a six-well plate with 2% FBS for 24 hours. Then, 30 µg/ml hydrophilic UCNPs were put into each well to for two hours internalization, followed by washing with phosphate buffer saline (PBS) three times, five minutes per time, to make sure removal of all UCNPs that were not internalized. Then, the cover slide was mounted on a glass slide. In order to avoid the moving of nanoparticles in the cell, the sample was kept at 4 °C for 10 minutes before the microscopy measurement.

2.4.3.2 Preparation of tissue sample preparation

Mice post-euthanasia were injected with a lethal dose of Xylazine and Ketamine mixture, and the mice were transcardially perfused with saline to remove blood content. Brain,

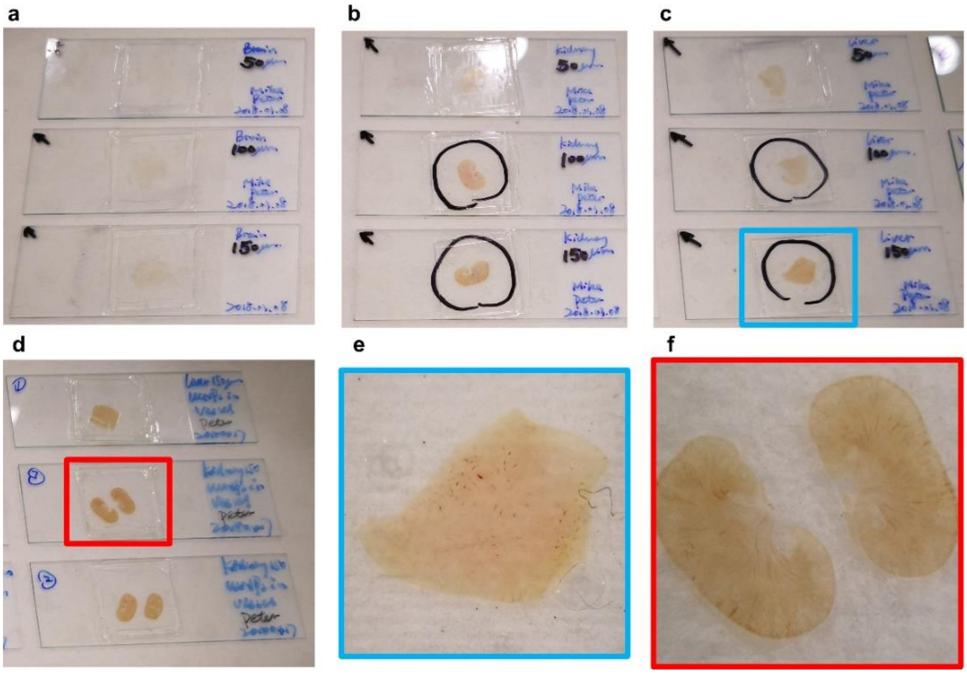

Figure 2-13 | Photographs of different mouse tissue slices on glass slides. (**a**) Brain tissue slices. (**b**) Kidney tissue slices. (**c**) Liver tissue slices. (**d**) Kidney and liver tissue with blood slices. (**e**) The magnified tissue slice of the blue square in (**c**). (**f**) Zoom-in of the tissue slice of red square in (**d**).

kidney and liver tissue samples were collected and fixed in 4% Paraformaldehyde (PFA) overnight at 4 °C and sectioned into 100 μm, 150 μm, 200 μm in thickness, using an automated vibratome (Leica VT1200 S). The brain, kidney and liver sections were then mounted in glycerol containing 0.05 mg/ml UCNPs for NIRES imaging. All procedures performed on mice were approved by the Animal Care and Use Committee, the University of Sydney Animal Ethics Committee (2017/1197).

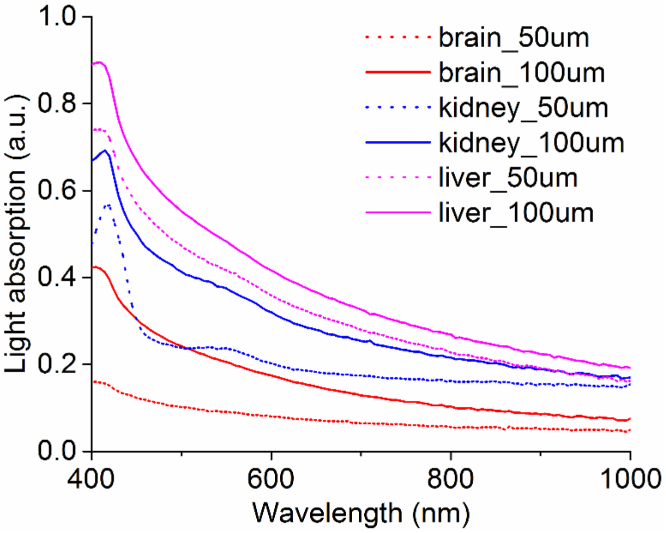

Figure 2-14 | UV–vis absorption spectra of the 50 μm and 100 μm live, brain, and kidney tissue slice samples, respectively.

To demonstrate the advance of the longer wavelength for deep tissue penetration (**Figure 2-13**), we use the UV-Vis spectrophotometer (Cary 60 UV-Vis, Agilent Technologies) to measure the light absorption through 50 µm and 100 µm liver, brain, and kidney tissue slice samples, respectively (**Figure 2-14**). As can be seen, the extinction rates of these tissues decrease in general when increasing the light wavelength in the visible and near-IR region.

2.5 Results and discussion

2.5.1 **Optimal emission band**

From the fluorescence spectrum profiles of UCNPs under continuous-wave 980 nm excitation laser in **Figure 2-11**, we select four main emission peaks at 455 nm, 470 nm, 741 nm and 800 nm to investigate the effect of emission band on the resolution of NIRES. **Figure 2-15a** shows the images of single UCNPs ($NaYF_4$: 20% Yb^{3+}, 4% Tm^{3+}) with different bandpass filters under a doughnut beam. The corresponding cross-section

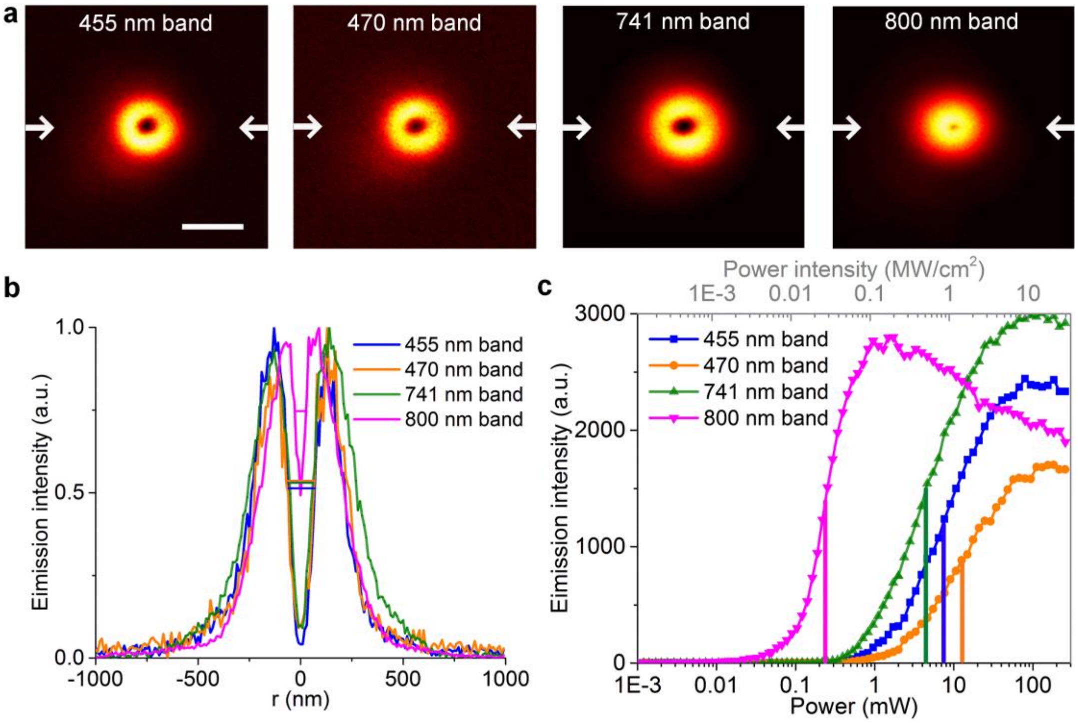

Figure 2-15 | Optimal emission band to achieve high resolution under the same excitation power. (**a**) Experimental images of a single UCNP ($NaYF_4$: 20%Yb, 4%Tm) obtained with the doughnut beam at 455 nm, 470 nm, 741 nm and 800 nm emission bands and full emission, respectively. The laser power was fixed at 30 mW which was measured at the objective back aperture. Scale bar, 500 nm; Pixel dwell time, 3 ms; pixel size, 10 nm. (**b**) Emission intensity profiles along with the arrows in (**a**) to indicate the resolution change at different emission peaks. (**c**) Emission saturation curves obtained for a single UCNP in a different colour.

profiles are presented in **Figure 2-15b**. According to the emission saturation curves in **Figure 2-15c**, I_S of 800 nm peak is 0.088 MW/cm^2, which is much smaller than the rest of the emission bands. Compared with 455 nm emission peak under the fixed excitation power, 800 nm emission band improves the resolution from 147.7 nm to 50.3 nm. Depending on the excitation power, the fluorescence is stimulated sequentially according to the energy levels (**Figure 2-7a**). It is easier to generate the 800 nm upconversion emission from the lower $^3H_4$ intermediate level than the four-photon 455 nm fluorescence from $^1D_2$ to $^3H_6$. Interestingly, although I_S of the full emission is nearly equal to 455 nm peak, the FWHM of full emission is twice larger than that of blue emission (**Figure 2-15b**). Thus, detecting the signal at 800 nm as the optimal emission band not only offers a deep penetration but also helps achieve high resolution with low excitation power.

2.5.2 Resolution dependent on Tm-doped and excitation power

The saturation curve of UCNP can be optimized by tuning the doping concentration of emitters (**Figure 2-12**). UCNPs with lower Tm^{3+} doping concentration can quickly reach the saturated point with lower values of I_S and I_{MAX} due to their smaller energy transfer ratio [80] and resultant lower saturated carrier flow rate. This is proportional to the laser-induced carrier generation rate. The lower values of I_S and I_{MAX} favour achieving higher resolution. However, lower Tm^{3+} doped UCNPs have a smaller onset of their saturation

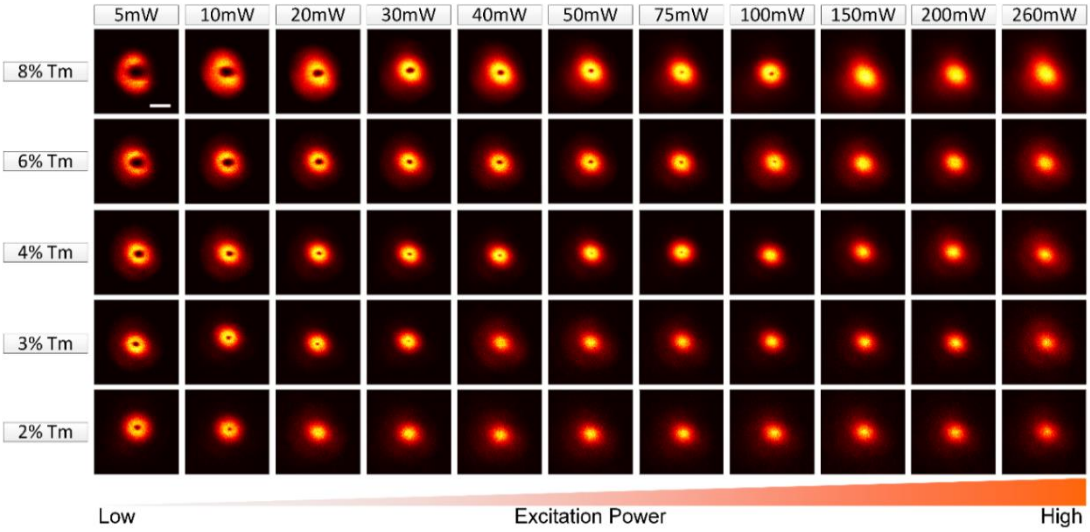

Figure 2-16 | The acquired images of different Tm^{3+} doping concentration of UCNP (NaYF$_4$: 20% Yb^{3+}, x% Tm^{3+}, ~40 nm in diameter) under different excitation power. Pixel dwell time, 3 ms; pixel size, 10 nm. Scale bar is 500 nm.

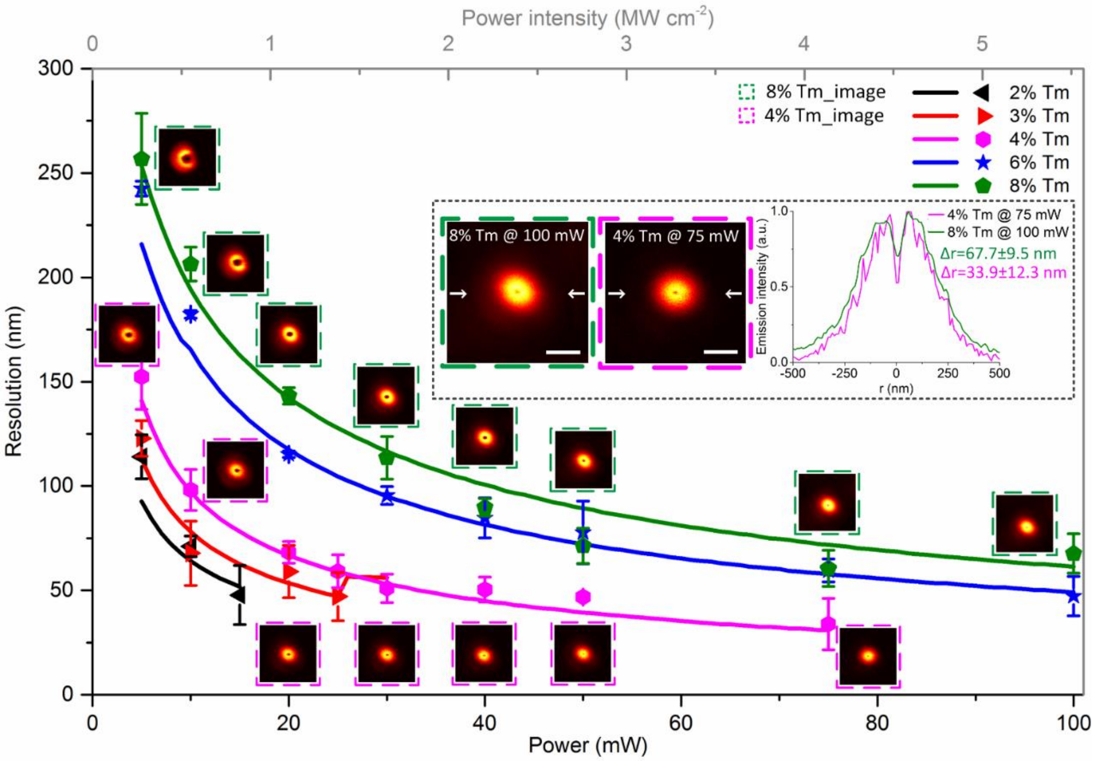

Figure 2-17 | Super-resolution scaling Δ*r* of UCNPs (NaYF$_4$: 20% Yb^{3+}, *x*% Tm^{3+}, ~40 nm in diameter; *x* = 2, 3, 4, 6 and 8) as a function of the excitation power (intensity). The dots of experimental data fit well to the simulation results (solid lines). Error bars indicate standard deviations from line profiles of several measurements. Insets, NIRES images of 8% Tm^{3+} doped UCNPs at 5.5 MW cm^{-2} (left), 4% Tm^{3+} one at 4 MW cm^{-2} (middle), and the corresponding cross-section profile lines (right). Pixel dwell time, 3 ms; pixel size, 10 nm. Scale bar is 500 nm.

curve (2% Tm^{3+} in **Figure 2-12b**), which substantially affects the resolution. Consequently, it is hard for UCNPs with 2% and 3% Tm^{3+} to achieve higher resolution even by increasing the excitation power (**Figure 2-16** & **Figure 2-17**). UCNPs with high Tm^{3+} doping concentration have sharper curvature in the onset of the saturation curves. However, the values of I_S and I_{MAX} (**Figure 2-12b**) are too high due to more massive energy transfer ratio [80] and higher cross-relaxation rate [79] for high Tm^{3+} doped UCNP. Therefore no higher resolution benefit is evident.

According to **Figure 2-12b**, 4% Tm^{3+} doped UCNPs have larger onset value than 2% and 3% Tm^{3+} doped UCNPs, and smaller I_{MAX} value than 6% and 8% Tm^{3+} doped UCNPs. Therefore 4% is the best doping concentration for NIRES. It is notable that even though the best resolution for 4% Tm^{3+} will be similar to that for the two-photon excited system, 4% Tm^{3+} still can produce a much better resolution with limited excitation power because it has much smaller I_S. As shown in **Figure 2-17**, UCNPs with 6% and 8% Tm^{3+} require higher power to achieve the same resolution as that for 4% Tm^{3+} UCNPs, optimized for

NIRES. With that, the highest resolution for singe nanoparticle imaging is 33.9 ± 12.3 nm (**Figure 2-17** inset) at an excitation power density of 4 MW cm^{-2}.

As explained in Section 2.3, the conventional method of square root law is not suitable to fit the resolution of NIRES due to the unique saturation curve of UCNPs. However, **Figure 2-16** still demonstrates a similar trend in that the resolution was enhanced with an increase of excitation intensity over a suitable range. The resolution starts to worsen when increasing the excitation power beyond the range, especially for the low doped concentrations. Referring to negative modality, the location of the single UCNPs in the scanned image is in the sense of local minima or zero in the focal spot (**Figure 2-9**). In the actual beam modulation, the centre dip of the doughnut intensity distribution is not precisely zero at the focal plane, which causes the fluorescence to elevate at the centre, especially under conditions of intense power (**Figure 2-16**). When two or more UCNPs with relatively small distance are excited at the focal plane, the minimum fluorescence values increase due to the emissions having overlapped, reducing the image contrast and creating difficulties in extracting the target signals from the image. Recognizing this effect when two or more nanoparticles overlapped, we simulate the merged two negative-shaped profiles with a certain central point shift simulation in **Figure 2-18**. By using the profile with FWHM at 50 nm, two dips are apparent with a distance larger than 40 nm,

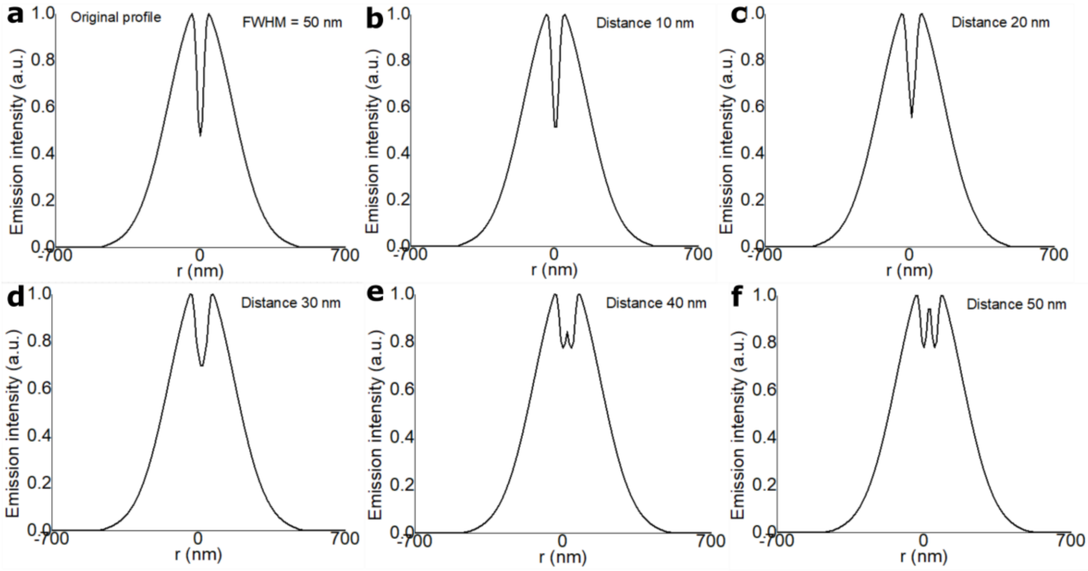

Figure 2-18 | Two cross-section line profiles with negative-shaped PSF overlapping with different centre distance from 10 nm to 50 nm. (**a**) The original negative-shaped profile. (**b-f**) The merged profiles of the two same profiles with different central distances, 10 nm (**b**), 20 nm (**c**), 30 nm (**d**), 40 nm (**e**), 50 nm (**f**), respectively.

while it is impossible to resolve the two points with a smaller distance. To eliminate the effect of this interference to obtain a high practical resolution, we assert that the value of the minima fluorescence at the centre should be less than half of the maximum.

2.5.3 Resolution improved by Yb-doped and core-shell structure

Figure 2-19 further explores the resolution enhancement by changing the sensitizer concentration Yb-doped (20% and 40%). **Figure 2-19a** shows 800 nm emission saturation curves of different Yb-doping UCNPs. The emission peak is selected at 800 nm, and the laser power is fixed at 10 mW. The scanned fluorescence images are

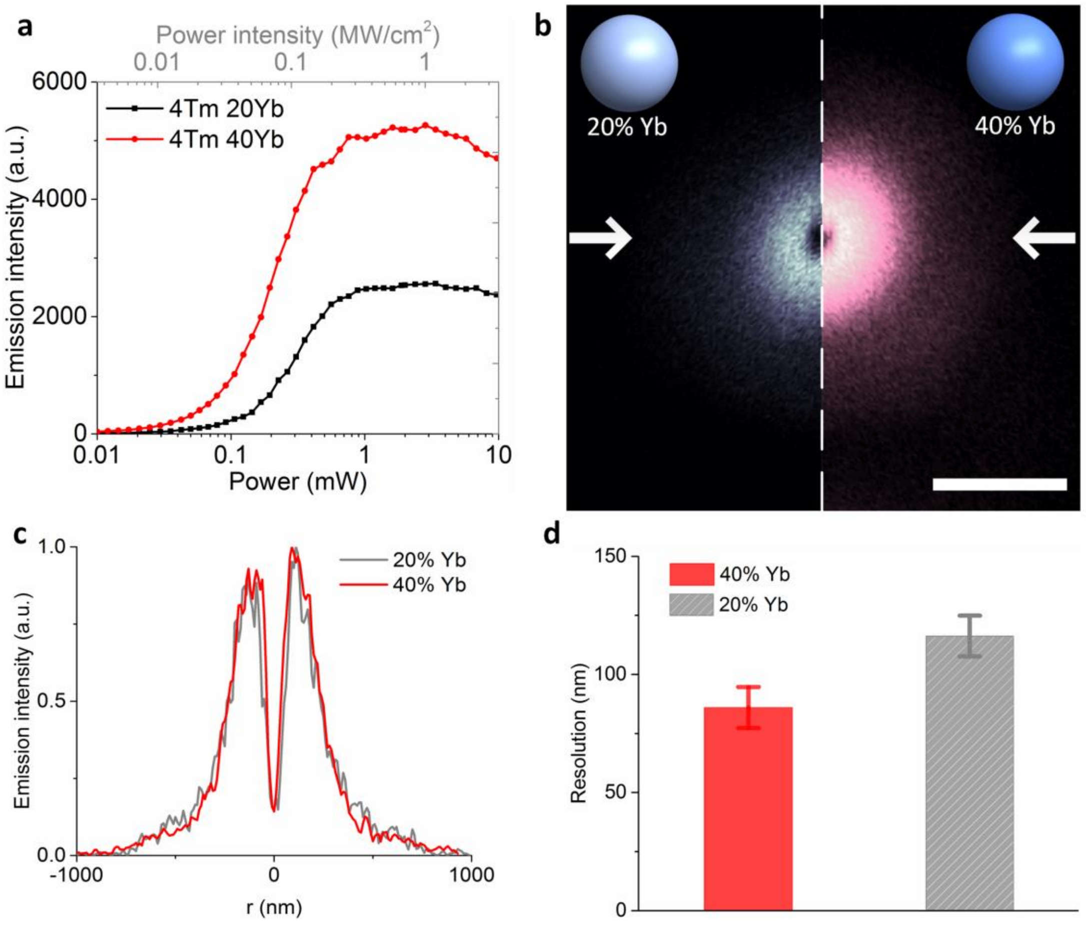

Figure 2-19 | The resolution can be improved by increasing sensitizer concentration. (**a**) 800 nm emission saturation curves of different Yb-doped UCNPs. (**b**) Images of a single 40 nm 20%Yb, 4%Tm-doped UCNP (left) and 40 nm 40%Yb, 4%Tm-doped UCNP (right) obtained with the doughnut beam. (**c**) Emission intensity profiles across the two UCNPs in (**b**). (**d**) statistical resolution in (**c**). The emission peak was selected at 800 nm and the laser power is fixed at 10 mW which is measured at the objective back aperture. Error bars indicated standard deviations from line profiles of five measurements. Scale bar is 500 nm; Pixel dwells time, 3 ms; pixel size, 10 nm.

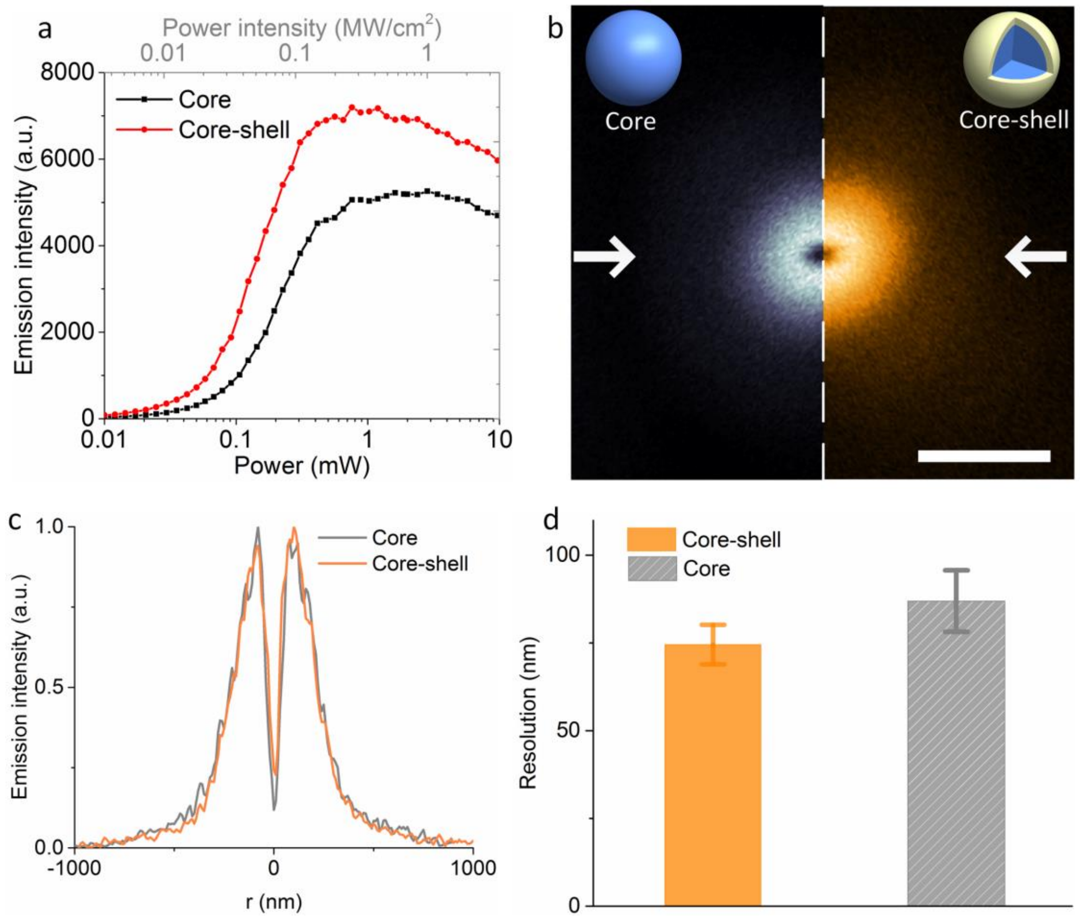

Figure 2-20 | The resolution can be improved by adding an inert shell. (**a**) 800 nm emission saturation curves of UCNPs with or without an inert shell. (**b**) Images of a single 40 nm 40%Yb, 4%Tm-doped UCNP (left) and 5 nm inert shell UCNP (right) obtained with the doughnut beam. (**c**) Emission intensity profiles across the two UCNPs in (**b**). (**d**) statistical resolution in (**c**). The emission peak was selected at 800 nm and the laser power is fixed at 10 mW which is measured at the objective back aperture. Error bars indicated standard deviations from line profiles of five measurements. Scale bar is 500 nm; Pixel dwells time, 3 ms; pixel size, 10 nm.

illustrated in **Figure 2-19b** with their corresponding cross-section profiles presented in **Figure 2-19c**. As shown in **Figure 2-19d,** these comparisons indicate that the resolution is changed from 117.3 ± 8.7 nm to 86 ± 8.7 nm after increasing Yb-doping concentration from 20% to 40%. From these curves in **Figure 2-19a**, we find that the *Is* is left moving and results in improving the resolution. High sensitizer concentration has a lower threshold and saturation point, enabling high resolution under a fixed excitation power compared to its low doped counterpart.

A further investigation of the inert effect on the resolution of NIRES is shown in **Figure 2-20**. Protected by a 5 nm thickness core-shell structure, **Figure 2-20a** presents that nanoparticles can be brighter and sensitive. As a result, the dip size in the core-shell

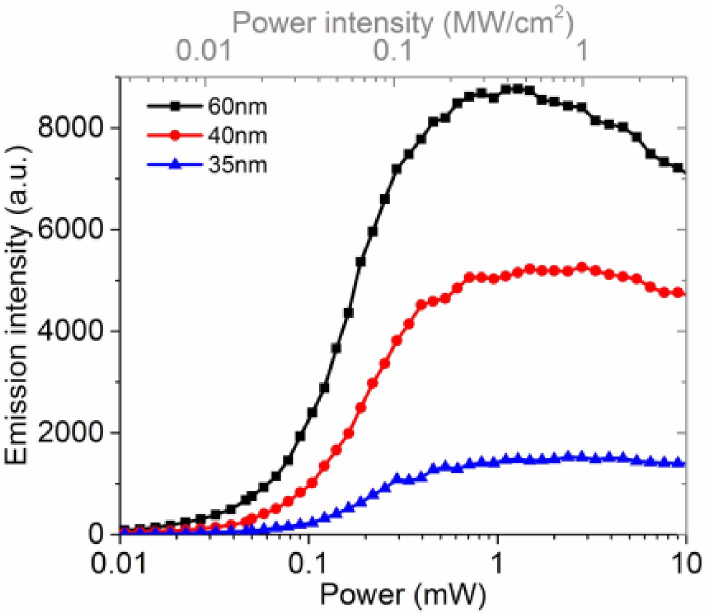

Figure 2-21 | 800 nm emission saturation curves of UCNPs with different size. UCNPs is NaYF4: 40%Yb^{3+}, 4%Tm^{3+}. The investigated sizes of UCNPs are 35 nm, 40 nm and 60 nm.

UCNPs is smaller than the one without a core-shell (**Figure 2-20). Figure 2-20c** depicts the corresponding cross-section profiles. The emission peak and laser power are set in the same way as the sensitizer concentration comparison. As shown in **Figure 2-20d**, these comparisons indicate that the dip size in the centre can be reduced to 74.57 ± 5.62 nm after coating a 5 nm $NaYF_4$ shell.

From these curves in **Figure 2-19a** and **Figure 2-20a**, we find that the left moving I_s results in the improvement of the resolution. In **Figure 2-21**, the emission response curves have a left moving tendency when increasing the nanoparticle size. However, for the size parameter, the I_s of smaller size UCNP presents as a 'fake right moving' due to the low emission signal down to the noise level. As a result, this phenomenon leading the smaller UCNPs requires a higher excitation power to obtain the same resolution compared with larger UCNPs, which does not match our simulation result in **Figure 2-6a**. For this reason, we conclude that the resolution of NIRES microscopy can be further improved by optimizing the activator concentration, excitation power intensity, sensitizer concentration and designing a core-shell structure. It suggests a topic with huge potential for the material sciences community to investigate and improve the resolution of NIRES nanoscopy.

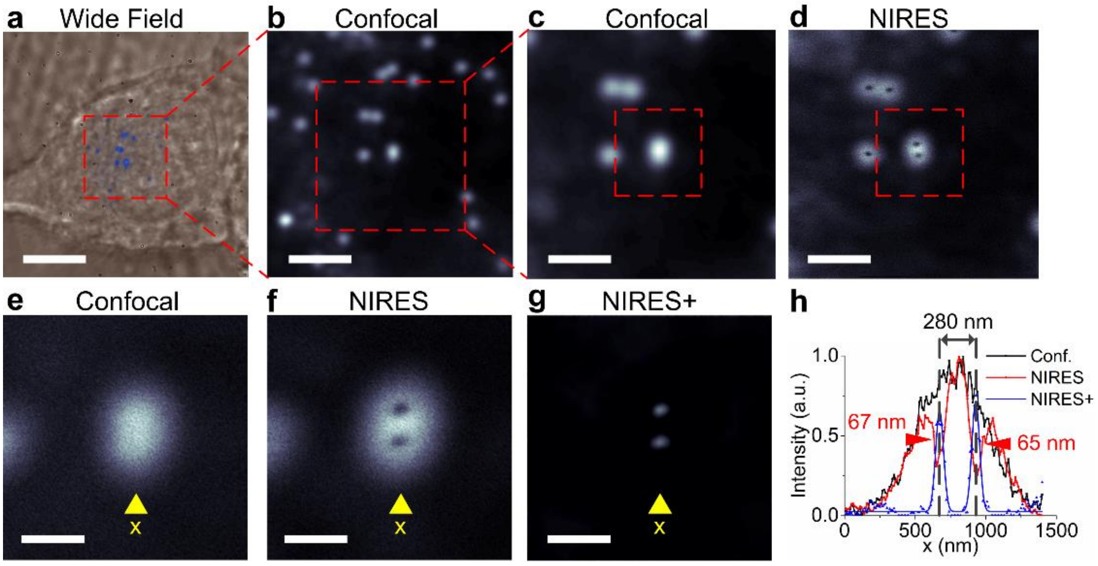

Figure 2-22 | NIRES super-resolution imaging of single UCNPs inside the HeLa cell. (**a**) Bright-field and fluorescence wide-field image of UCNPs taken up by a HeLa cell. (**b**) and (**c**) Confocal images of areas of (10 µm × 10 µm) and (6 µm × 6 µm), respectively. (**d**) NIRES image showing two UCNPs in a diffraction limit area. Zoom-in of the confocal image (**e**) and NIRES image (**f**). (**g**) The positive NIRES image by subtracting (**f**) from (**e**). (**h**) Cross-section line profiles of UCNPs in the confocal image (**e**), raw NIRES image (**f**), and positive NIRES image (**g**). The pixel dwells time for confocal and NIRES is 3 ms. The pixel size for confocal and NIRES is 10 nm. The scale bar is 7.5 µm in (**a**), 2.5 µm in (**b**), 1.5 µm in (**c**) and 500 nm in (**d**) – (**g**).

2.5.4 **Resolving single UCNPs inside HeLa cell**

We verify the power of NIRES modality by resolving the single 40-nm UCNPs inside HeLa cells. **Figure 2-22a** shows the wide-field imaging of multiple UCNPs inside the HeLa cell. **Figure 2-22b** & **c** display the large confocal scanning at the centre region with size (10 µm×10 µm) and (6 µm×6 µm), respectively. **Figure 2-22d** shows that NIRES can clearly distinguish UCNPs within a diffraction limit area, which cannot be resolved by the conventional confocal microscope (**Figure 2-22c**). Like the saturated absorption competition microscopy [131], higher excitation power will elevate the dip in the PSF of emission for NIRES to the maximum point of PSF. This is according to the saturation curve (**Figure 2-15c**) and thereby switches the NIRES into confocal microscopy, subsequently obtaining a “Gaussian image”. The subtraction of the “Gaussian image” with respect to negative NIRES image will further provide a positive NIRES image [51], resulting in a positive NIRES image (**Figure 2-22g**). The intensity line profiles (**Figure 2-22h**) show that the distance between the two UCNPs is 280 nm. Moreover, **Figure 2-23** provides more data using NIRES to resolve single UCNPs with a resolution of 72.1 nm in a biological environment.

Table 2-3 | FWHM of 455 nm, 800 nm confocal and NIRES at different depth of a tissue slice.

	0 μm	15 μm	55 μm	75 μm	93 μm
455 nm	321.2 ± 15.7 nm	329.8 ± 24.3 nm	341.5 ± 18.9 nm	359.4 ± 14.5 nm	400.7 ± 16.4 nm
800 nm	445.0 ± 10.5 nm	423.3 ± 27.5 nm	481.7 ± 34.3 nm	475.0 ± 33.5 nm	488.3 ± 17.6 nm
NIRES	49.6 ± 11.1 nm	42.4 ± 6.2 nm	42.4 ± 7.2 nm	48.0 ± 7.3 nm	38.2 ± 14.3 nm

2.5.5 Deep tissue imaging by NIRES

We further examine the penetration depth and resolution of NIRES imaging through deep tissue (**Figure 2-24**). In this experiment, 4% Tm^{3+} 40% Yb^{3+} co-doped UCNPs are attached behind a 93 μm thick slice of mouse liver tissue (**Figure 2-13**), which allows UCNPs diffuse into the tissue slice for super-resolution imaging of single UCNPs from different depths (**Figure 2-24**). Due to the aforementioned strong attenuation for visible emissions (shown in **Figure 2-24b** and **Figure 2-14**), through a 93 μm liver tissue slice, there is only 11.3% of 455 nm emission left in confocal imaging (**Figure 2-24c**). In contrast, 38.7% of a strong signal at 800 nm is detectable in both confocal imaging (in red) and NIRES (in magenta) super-resolution imaging. More encouragingly, by increasing excitation power to compensate for the aberration induced distortion on excitation PSF[132], a relatively consistent resolution of sub-50 nm has been maintained without any aberration correction through tissue as deep as 93 μm (**Figure 2-24d** with the corresponding data in **Table 2-3**). **Figure 2-25** presents super-resolution scaling Δr of UCNPs as a function of the excitation power at 93 μm depth inside liver tissue. The lower refractive index[133][134] of tissue for NIR light results in less aberration than that for

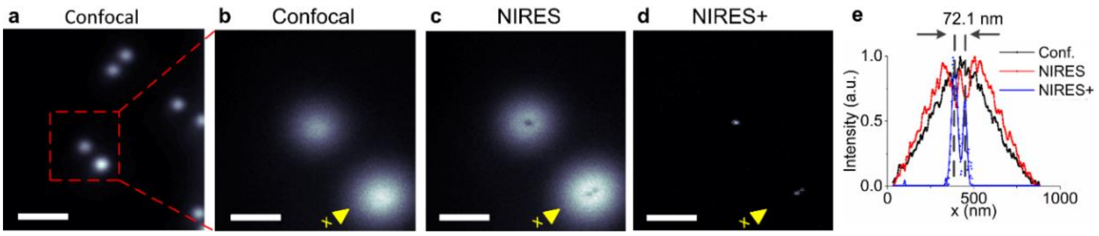

Figure 2-23 | Resolved two particles with distance below the diffraction limit. (**a**) Confocal scanned image (6 μm × 6 μm) of the UCNPs sample. (**b**) Magnified the red dotted square in (**a**). (**c**) The same position obtained by NIRES, with distinct UCNPs that could not be separated by confocal. (**d**) The positive NIRES sub-diffraction image by (**c**) subtracted from (**b**). (**e**) Cross-section line profile of UCNPs in raw NIRES image (**c**), subtracted image (**d**) and confocal image (**b**). Pixel dwell time, 3 ms; pixel size, 10 nm. Scale bar, 1.5 μm in (**a**); 500 nm in (**b**) – (**d**).

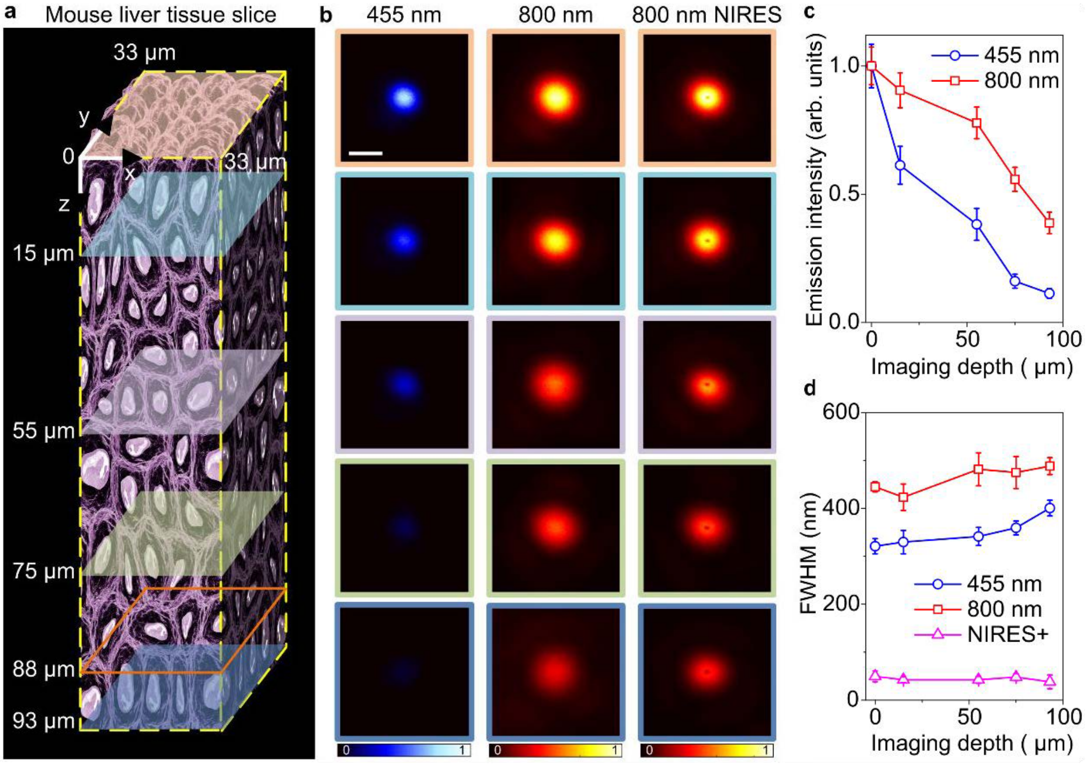

Figure 2-24 | The penetration depth of different emission bands and optical resolution of different imaging modalities at different depth of a liver tissue slice. (**a**) An illustration of a mouse liver tissue slice with 93 μm thickness. (**b**) Single-particle imaging at different depth in liver tissue. Left, confocal images from 455 nm emission; middle, confocal images from 800 nm emission; right, the corresponding NIRES images. (**c**) The normalized emission attenuation at different depths through the liver tissue. (**d**) The corresponding FWHM in (**b**); The resolutions of NIRES in (**d**) are 49.6 ± 11.1 nm (0 μm), 42.4 ± 6.2 nm (15 μm), 42.4 ± 7.2 nm (55 μm), 48.0 ± 7.3 nm (75 μm), 38.2 ± 14.3 nm (93 μm). Benefiting from the controlled synthesis of intensity monodispersed UCNPs, every single nanoparticle can be distinguished from each cluster by comparing their emission intensity to statistical averaged value. The pixel dwell time for confocal and NIRES is 3 ms. The pixel size for confocal and NIRES is 10 nm. The scale bar is 500 nm.

visible beam, which also contributes to the high resolution achieved by NIRES for single nanoparticle imaging.

Figure 2-25 further examines the resolution power of NIRES in resolving single UCNPs from nanoparticle clusters in deep tissue. **Figure 2-25a** shows a bright field image of an 88 μm liver tissue slice, merged with the fluorescence image of four clusters of UCNPs (in magenta). At this depth, 800 nm confocal microscopy (**Figure 2-25b**) does not provide sufficient resolution to image single UCNPs within a diffraction limit area (**Figure 2-25c** & **d**). In contrast, NIRES nanoscopy can resolve single UCNPs by either negative (**Figure 2-25e** & **f**) or positive images (**Figure 2-25g** & **h**). The two typical areas of confocal and NIRES/NIRES+ images, marked by the orange square (**Figure 2-25c**, **e** & **g**) and green square (**Figure 2-25d**, **f** & **h**), respectively, clearly illustrate the sub-50 nm resolution

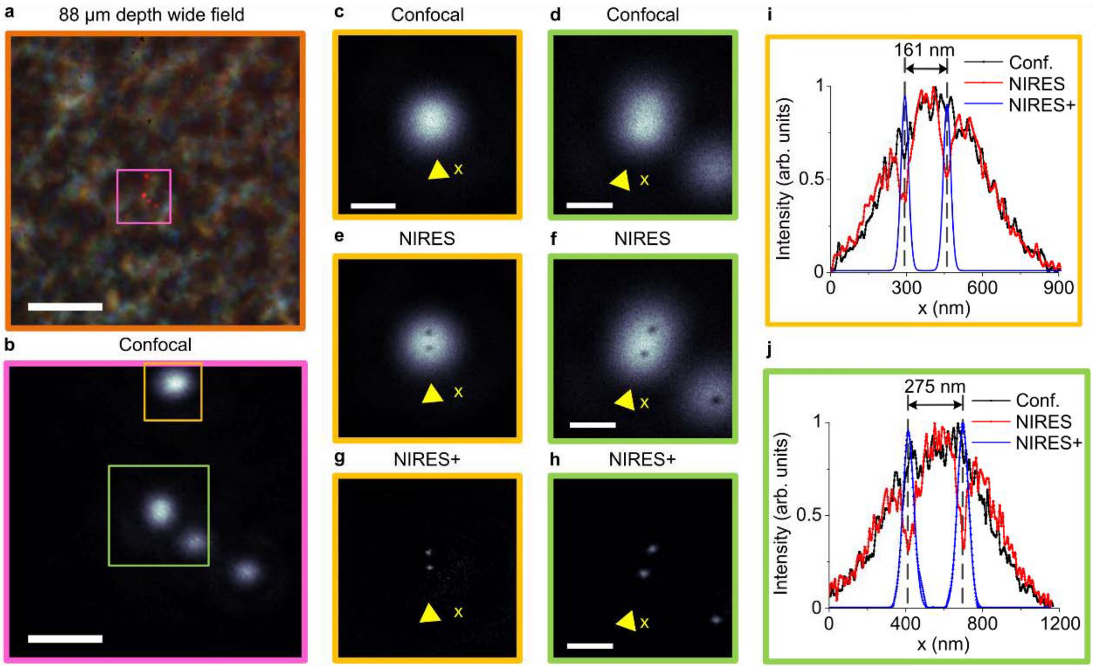

Figure 2-25 | NIRES nanoscopy for super-resolution imaging of single UCNPs through deep mouse liver tissue. (**a**) Bright-field and fluorescence wide-field image of UCNPs at 88 µm depth inside a mouse liver tissue slice. (**b**) Confocal images of a 6 µm×6 µm area containing clusters of UCNPs. (**c**) and (**d**) are the zoom-in confocal images of two areas of interest from (**b**). (**e**) and (**f**) are the raw data of NIRES images of (**c**) and (**d**). (**g**) and (**h**) are the processed data of NIRES+ images of (**e**) and (**f**). (**i**) Line profiles of UCNPs from the confocal image (**c**), raw NIRES image (**e**), and positive NIRES image (**g**). (**j**) Line profiles of UCNPs from confocal image (**d**), raw NIRES image (**f**), and positive NIRES image (**h**). The pixel dwells time for confocal and NIRES is 3 ms. The Pixel size for confocal and NIRES is 10 nm. The scale bar is 8 µm in (**a**) and 1.5 µm in (**b**) and 500 nm in (**c**) – (**h**).

achieved by NIRES nanoscopy, in resolving single UCNPs separated with 161 nm and 275 nm (**Figure 2-25i** and **j**). To compensate the scattered excitation power through the thick tissue, the excitation power density to achieve the best resolution in the depth of 88 µm is 5.5 MW cm^{-2}.

Notably, the resolvable distance of 161 nm is not the limit of NIRES. For instance, UCNPs with a distance 72 nm can be resolved as shown in **Figure 2-23**. **Figure 2-26** provides additional data showing that the best resolutions of 54 nm and 62 nm have been achieved through an 85 µm mouse kidney tissue slice and a 92 µm brain tissue slice, respectively. From the high brightness (20000 photon counts per second, in contrast to the low detection background of 1000 photon counts per second) of a single UCNP emitting at 800 nm through a 93 µm tissue, we estimate the limit in imaging depth to detect a single nanoparticle by NIRES should be around 175 µm. An objective lens with longer working distance (around 100 µm used in our current setup) should be used to confirm this limit in future research.

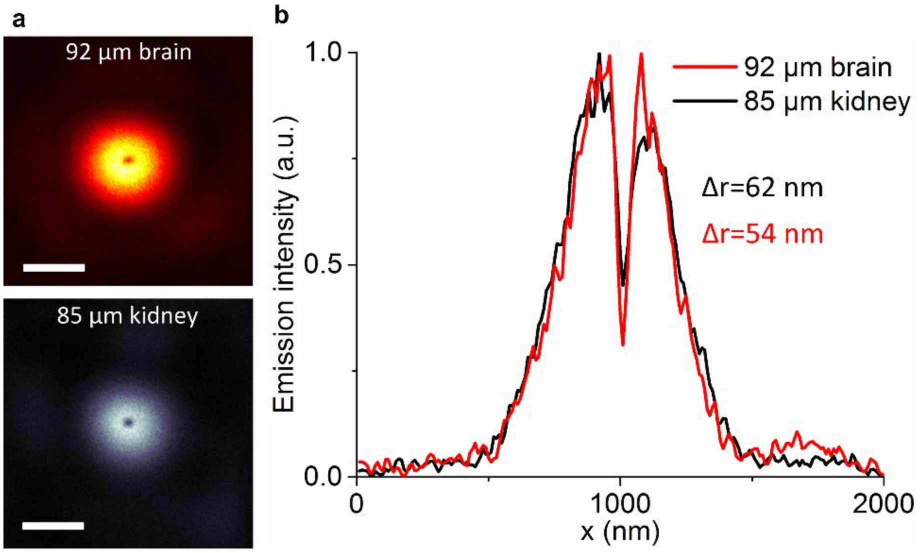

Figure 2-26 | NIRES images in the deep mouse brain and kidney tissue. (**a**) NIRES image at 92 µm depth inside brain tissue (upper) and 85 µm depth inside kidney tissue (bottom), respectively. (**b**) The corresponding cross-section profile lines. The pixel dwells time, 3 ms; pixel size, 10 nm. Scale bar, 500 nm.

2.5.6 Discussion

980-nm light has a significant absorption in bio-samples, which may heat the surrounding media by causing sample damage issues. To bypass this challenge, Wu et al. demonstrate a similar FED microscopy using UCNPs [82], with 172 nm resolution achieved using 800 nm 10 MW cm^{-2} excitation and 660 nm emission detection. Combined with the self-healing Bessel beam, our group further explore this sub-diffraction imaging modality to map single nanoparticles inside a strong scattering tumour cells spheroid [85]. On the other hand, we report a strategy of the nonlinear SIM towards video-rate super-resolution imaging through thick biological tissues [90]. The unique nonlinear photoresponse of UCNPs makes possible the onset of an efficient nonlinear mode on SIM for obtaining high-frequency harmonics in the Fourier domain of the imaging plane. It enables nonlinear SIM to achieve the resolution to 1/7th of the excitation wavelength with a gentle excitation power.

The engineered nanocrystals offer a new strategy to surpass the diffraction limit for current techniques, providing alternatives to conventional modalities typically using organic dyes and other nanoparticles. With the field enhancement by the localized surface plasmon resonance of the metal materials [135][136][137], it can get a reduced excitation power required to obtain resolution improvement. The new developed large scale assembles [138] of plasmonic metal nanoparticles onto single UCNPs gives a possible way for further investigation. Besides, while rare-earth nanocrystals-based down–conversion [139] for sub-diffraction imaging in the NIR-IIb window is promising, one photon down-conversion is easier to generate under the low excitation power. Due to the bright emission, the particles can be synthesized so that they are smaller, which makes it possible to explore the potential of biological probes.

2.6 Conclusion

In conclusion, this work demonstrates a multi-photon fluorescence saturation microscopy for super-resolution imaging to circumvent the specific requirement of probes in STED-like modalities. Compared with our recent work reporting low excitation power STED[79], the NIRES approach presented here achieves the same level of imaging resolution (< 50 nm) using a simple setup. NIRES offers a great deal of simplicity and stability, as an advanced tool to achieve super-resolution in deep tissue, and is superior to the conventional MPM approaches [140][141]. In contrast to the conventional methods by increasing the excitation power to achieve super-resolution, this emphasizes the fluorescent rising slope and threshold enable us to improve the resolution through the synthesis of probes. The key feature of this approach is that it can be applied to any nonlinear optical probes with fluorescence saturation for the sub-diffraction imaging. To achieve super-resolution imaging using low laser power and a longer wavelength, i.e. to reduce phototoxicity applied to live cells, controlled synthesis of UCNPs will further optimize the energy transfer process and resultant saturation intensity properties. In this way the bio-photonics can surpass the diffraction limit. The recent progress made on the functionalization of UCNPs, enabling bio-conjugation, cell optogenetics [142] and long-term tracking in the cell [143], will empower NIRES to track more biological events. The tuning of multiple emission colours and lifetimes [103] of UCNPs will allow NIRES to undertake multiplexed super-resolution imaging of subcellular structures and long-term tracking of single molecules in deep tissue [36].

Chapter 3 Fourier domain heterochromatic fusion for super-resolution microscopy by point-spread-function engineering

With the advantages of nonlinear photon response, the optical resolution of fluorescence microscopy has overcome the diffraction limit. PSF engineering is a super-resolution imaging approach that encodes emitter properties in the shape of the PSF. However, complexed excitation setups or repetitive scans are needed, which explains the issues of low speed, poor stability and operational complexity associated with the current laser scanning approaches. These techniques mostly focus on single colour emission, restricting the available and flexible benefits from multicolour implementation. Herein, we propose a strategy by extending the capabilities of PSF engineering to the spectral regime. Exploiting the distinct nonlinear photon response of each emission band in the single upconversion nanoparticle, we explore an opportunity for a tightly focused doughnut excitation to generate distinct spectral dependent PSFs. By heterochromatic Fourier spectral fusion, we show the fused OTF can cover both low and high frequency information to yield the overall enhanced image quality. We show single upconversion nanoparticles can be super-resolved with a spatial resolution of 50 nm, 1/20th of the excitation wavelength. This work further suggests a new scope for developing nonlinear multi-colour emitting probes to improve the image quality and noise control in super-resolution nanoscopy.

3.1 Background

To overcome the optical diffraction limit, several techniques have been developed in the past two decades [3]. On the one hand, linear modalities such as SIM [108] introduce a particular geometry of the illumination, such as fringes [22] and speckles [144][145] to enhance resolution. However, the maximal resolution improvement is restricted by a factor of 2 over conventional wide-field microscopy. On the other hand, several methods have pushed more modest resolution enhancement by exciting the fluorescent probes in a nonlinear regime, either inducing binary stochastic methods [146][147] or under saturated conditions [148][83]. The saturated optical transition can be stimulated emission [118][119], ground-state depletion [125][128][148], absorption [12][83][149] or fluorescence photo-switching [150]. As a consequence, the designing of illumination with patterned light excitation [21] then becomes an essential scheme for the super-resolution imaging modalities.

SIM-based processing algorithms for point-scanning patterned illumination approaches [151] have been developed to obtain extraordinary efficacy of resolution enhancement, as a focused spot is a special type of structured illumination [152][153]. When considering the resolution limit of an imaging system, it is easier to consider the associated frequency space. The higher spatial frequencies correspond to a better-resolved image. The OTF is the direct Fourier transform of the PSF, contains all the spatial frequencies permitted by the objective. The origin of the spatial resolution limit is the finite support of the OTF of a microscope's optics in the frequency domain, limiting maximum Fourier mode that is still transmitted in the optics. Compared to the wide-field sinusoidal pattern that contains only one direction frequency, a tiny focused spot is a pattern that contains all the frequencies possibly supported by the objective [152]. Since the resolution increase is achieved by the frequency components of the focal spot, introducing higher-than-classically-allowed spatial frequencies into the excitation spot would allow for a better than 2-fold gain in resolution. As nonlinearity in the fluorescence results in an equivalent excitation PSF with extended frequency content [153], computational nonlinear scanning microscopy further enhances the spatial resolution [21]. However, the lack of high-frequency components in OTF with Gaussian PSF, prohibiting substantial improvement of resolution under fluorescence saturation.

One promising direction is through PSF engineering [154][155], involves altering an optical system in such a way as to generate a non-classical excitation or detection PSF. It has already encoded the emitter properties in the shape of the emission PSF to improve the resolution in confocal microscopy [81], extend the microscope's depth of field [156][157], and enhance the localization precision in all three dimensions [158][159][23]. The most prominent example of PSF engineering is generating a doughnut-shaped beam in STED microscopy [119]. Since the width of the central dark spot is sub-diffraction [131], it contains higher spatial frequencies in the doughnut PSF than a diffraction-limited Gaussian spot [160]. By using a structure-shaped excitation spots exclusively with the advantage of fluorescence saturation, the doughnut pattern-based modalities [105][128][161] have been demonstrated their ability to extract the extraordinary information at the higher spatial frequency for resolution enhancement.

Nevertheless, these techniques mostly focus on single colour emission, restricting the benefits from multicolour implementation. As a prerequisite in order to extract the more extensive coverage of spatial information to enhance the quality of super-resolution images, these advances still require specialized optics to meet the particular excitation conditions or multiple scans in detection to produce images with multiplexed PSF. As a consequence, the complex optics elements and efforts in maintaining the proper alignments and system stabilities are the critical limiting factors for point-scanning super-resolution microscopes. It is hoped to widely use these in material sciences and biology laboratories.

Here, we propose a strategy by extending the capabilities of PSF engineering from the spatial domain to the colour region. Using a single doughnut-shaped beam point-scanning illumination, we investigate the heterochromatic nonlinear responses and saturated fluorescence emissions of UCNPs. Exploiting the distinct nonlinear photon response of each emission band in UCNPs, we explore an opportunity for a tightly focused doughnut excitation to generate distinct spectral dependent PSFs. With the controllable PSFs from multi-channel emissions, we demonstrate the possibility to achieve super-resolution imaging by a single scan under saturated fluorescence excitation via PSF engineering either in the spatial domain or Fourier domain. We further develop a multicolour Fourier spectral fusion algorithm to enlarge the frequency shifting coverage of the optical system. What is subsequently achieved is the effective super-resolution PSF by fusing Fourier components from each emission bands and processing OTF that contains the maximum spatial information.

3.2 Spatial frequency domain

For a better understanding of this Fourier domain fusion method, we briefly go through the necessary theoretical knowledge about the spatial frequency domain [162][163], including the spatial frequency, spectrum, 1D and 2D Fourier transform, fast Fourier transform, image convolution and deconvolution and image filtering.

3.2.1 Image spatial frequency and spectrum

For a two-dimensional (2D) plane, an image can be defined as a 2D functions $f(x, y)$ to describe the intensity or brightness values distribution at the real spatial coordinates (x, y) in an image plane. By considering a row of pixels in the image, we can also define it as

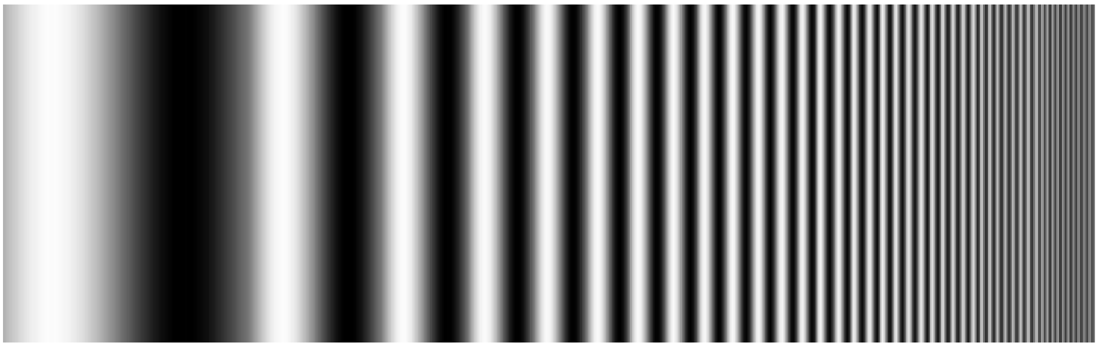

Figure 3-1 | The line pairs in an image plane. The wider space between the bars on the left-hand side means the low spatial frequency, indicating low image resolution. The narrower space on the right-hand side represents the high spatial frequency, which means the high image resolution.

the one-dimensional signal. The form of this signal is similar to the traditional signal in the temporal domain. Nevertheless, here the image signal is defined in the spatial domain. As a consequence, the frequency of the image is also known as the spatial frequency, which reflects the change of the pixel grayscale of the image in the space. For the image signal, the spatial frequency refers to the number of periodic changes of the brightness within unit length (**Figure 3-1**). For example, concerning the image of a wall, due to the flat distribution of grey value, the low-frequency component is strong, while the high-frequency component is weak. For images with rapid spatial variations, such as chessboard, the high frequencies are relatively intense and the low frequencies relatively faint.

The concept of spatial frequency is fundamental to all aspects of imaging. Typically, we describe the image resolution by using spatial frequency, which in terms of "line pairs per mm" (**Figure 3-1**). The highest resolution indicates the ability to resolve the closest spacing of white and black bars. Since a pair of lines are like peaks and crests of adjacent waves, line pairs per mm is a measure of spatial frequency.

An alternative spatial frequency-based representation is to use a spectrum of different frequency components over the image. With the direct 2D Fourier transform of a spatial function $f(x, y)$, we can obtain the 2D spectrum $F(u, v)$ of spatial frequencies with no information loss. The Fourier transform of the image obtains the spectrum diagram, which is actually the distribution diagram of the image gradient. Note that there is no point-to-point correspondence between the spectrum diagram and the original spatial representation, even in the case of no frequency shift. In fact, the point on the spectrum presents the gradient, which is the intensity difference between two adjacent points on the image. Besides, the value of the point on the spectrum depends on the component of this gradient (frequency) of the corresponding plane wave on the overall image. Moreover, the spatial representation $f(x, y)$ can be recovered from the corresponding spectrum through reverse conversion.

In image processing, both spatial and spectrum representations are equivalent to each other. Such spatial to spectral transformation simplifies image processing to some extent. Through the transformation of image information, it is conducive to the processing, processing or filtering of unnecessary information, and the enhancement or extraction of interesting parts or features.

3.2.2 **Fourier transform**

Due to the computational mechanism of the computer, it is not able to process the continuous and infinite single. In the image process, the Fourier transform is an operation that transforms data from the spatial domain into the frequency domain, converting the signal into a sinusoidal signal with many different frequencies and different amplitudes. As most of the targeted images are complex and lack any strong periodicity, the Fourier transform is a mathematical tool that provides a unique and powerful way to obtain and analyse the image spatial frequencies. It can analyse the components of the signal and deconstruct the waveform as a weighted sum of sinusoidal functions with no information loss. The sine and cosine components for the decomposition are called the basic functions of the decomposition. The weighted sum of these basis functions is called a Fourier series in Equation (3-1):

$$f(x) = \frac{1}{2}a_0 + \sum_{n=1}^{\infty} \left(a_n \cos\frac{n\pi x}{L} + b_n \sin\frac{n\pi x}{L}\right) \tag{3-1}$$

$$a_0 = \frac{1}{L}\int_0^{2L} f(x)dx \tag{3-2}$$

$$a_n = \frac{1}{L}\int_0^{2L} f(x)\cos\left(\frac{n\pi x}{L}\right)dx \tag{3-3}$$

$$b_n = \frac{1}{L}\int_0^{2L} f(x)\sin\left(\frac{n\pi x}{L}\right)dx \tag{3-4}$$

where the weighting factors for each cosine (a_n) and sine (b_n) function are the Fourier coefficients, and the index n specifying the number of cycles of the sinusoid that fit within one period $2L$ of the function $f(x)$ is a dimensionless frequency of a basis function. A

1D function with period 2L is uniquely represented by two infinite sequences of coefficients. The notion of a Fourier series can also be extended to complex coefficients. Consider a real-valued function $f(x)$:

$$f(x) = \sum_{n=-\infty}^{\infty} A_n e^{inx} \tag{3-5}$$

Then substitute the Euler's formula to (3-5):

$$\int_{-\pi}^{\pi} f(x)\, e^{-inx} dx = \int_{-\pi}^{\pi} \left(\sum_{n=-\infty}^{\infty} A_n e^{inx} \right) e^{-imx} dx = 2\pi A_n \tag{3-6}$$

so

$$A_n = \frac{1}{2\pi} \int_{-\pi}^{\pi} f(x)\, e^{-inx} dx \tag{3-7}$$

For a function periodic in $\left[-\frac{L}{2}, \frac{L}{2}\right]$, it becomes:

$$f(x) = \sum_{n=-\infty}^{\infty} A_n e^{i\left(\frac{2\pi nx}{L}\right)} \tag{3-8}$$

$$A_n = \frac{1}{L} \int_{-\frac{L}{2}}^{\frac{L}{2}} f(x)\, e^{-i\left(\frac{2\pi nx}{L}\right)} dx \tag{3-9}$$

3.2.2.1 **1D continuous Fourier transform and inverse transform**

The Fourier transform generalizes the limiting case of the complex Fourier series $L \to \infty$. By using continuous $F(u)du$ to replace the discrete An and setting $\frac{n}{L} \to u$, then change the sum to an integral, and Equation (3-9) finally becomes the 1D continuous Fourier transform:

$$F(u) = \int_{-\infty}^{\infty} f(x) e^{-i2\pi ux} dx \tag{3-10}$$

1D continuous Fourier inverse transform:

$$f(x) = \int_{-\infty}^{\infty} F(u) e^{i2\pi ux} du \tag{3-11}$$

3.2.2.2 **2D continuous Fourier transform and inverse transform**

The Fourier series decomposition equally holds for 2D images. Based on Equation (3-12), the 2D continuous Fourier transform $F(u,v)$ of the function $f(x,y)$ is defined as:

$$F(u,v) = \int_{-\infty}^{\infty} \int_{-\infty}^{\infty} f(x,y) e^{-i2\pi(ux+vy)} dx\, dy \tag{3-12}$$

Where u and v are the numbers of cycles fitting into one horizontal and vertical period, respectively. With the given $F(u, v)$, the inverse 2D Fourier transform $f(x, y)$:

$$f(x,y) = \int_{-\infty}^{\infty}\int_{-\infty}^{\infty} F(u,v)e^{i2\pi(ux+vy)}du\,dv \tag{3-13}$$

3.2.2.3 **1D discrete Fourier transform and inverse transform**

In the digital image process, each image function $f(x, y)$ is defined over discrete instead of the continuous domain. Consequently, we employ a discrete Fourier transform (DFT) for image processing. For the single variable discrete function $f(x)$ (x = 0, 1, 2, ... M-1), the 1D discrete Fourier transform $F(u)$ is defined as:

$$F(u) = \frac{1}{M}\sum_{x=0}^{M-1} f(x)e^{-\frac{i2\pi ux}{M}} \tag{3-14}$$

Where u = 0, 1, 2, …, M-1.

1D inverse DFT:

$$f(x) = \sum_{u=0}^{M-1} F(u)e^{\frac{i2\pi ux}{M}} \tag{3-15}$$

Where x = 0, 1, 2, …, M-1.

3.2.2.4 **2D discrete Fourier transform and inverse transform**

The use of sampled 2D images of finite extent leads to the following 2D DFT of an $M\times N$ image as follows:

$$F(u,v) = \frac{1}{MN}\sum_{x=0}^{M-1}\sum_{y=0}^{N-1} f(x,y)e^{-i2\pi\left(\frac{ux}{M}+\frac{vy}{N}\right)} \tag{3-16}$$

Where u = 0, 1, 2, …, M-1; v= 0, 1, 2, …, N-1.

With the given $F(u, v)$, the inverse 2D Fourier transform $f(x, y)$:

$$f(x,y) = \sum_{u=0}^{M-1}\sum_{v=0}^{N-1} F(u,v)e^{i2\pi\left(\frac{ux}{M}+\frac{vy}{N}\right)} \tag{3-17}$$

Where x = 0, 1, 2, …, M-1; y= 0, 1, 2, …, N-1.

3.2.3 **Fast Fourier transform**

As introduced in section 3.2.2, the Fourier transform makes it possible for the computer to calculate and analyse the signals. However, the transformation requires a lot of calculation, including convolution, which has challenged the performance of the computer, especially for hardware implementation. For example, we calculate the $F(u,v)$ involves a summation over all image pixels from the image $f(x,y)$ with dimensions $N \times N$. The overall operations of a DFT calculating the spectrum with N^2 values are $O(N^4)$. However, such an algorithm is impractical.

Fortunately, the fast Fourier transform (FFT) is a more efficient algorithm that can significantly reduce the computational complexity to calculate DFT. The 1D FFT speeds up calculations due to a possibility to represent a Fourier transform of length N being a power of two in a recursive form, as the sum of two Fourier transforms of length N/2. The recursion ends at the point of computing simple transforms of length 2. Thus, the FFT algorithm computes a 1D Fourier transform for N points in only $O(N\log N)$ multiplies and adds, becoming a practical and essential way on computers. Therefore the complexity of the 2D FFT becomes $O(N^2\log N)$ from $O(N^4)$. In particular, the more sample points involved, the more efficient of FFT algorithm. A function or signal can be converted between the time domain and the frequency domain by a pair of mathematical operators, which is similar to the Fourier transform. Based on the successive doubling method, the original Fourier transform can be divided into two recursive formulas:

$$F(u) = \frac{1}{2}[F_{even}(u) + F_{odd}(u)W_{2K}^{u}] \tag{3-18}$$

$$F(u+K) = \frac{1}{2}[F_{even}(u) - F_{odd}(u)W_{2K}^{u}] \tag{3-19}$$

Where u = 0, 1, 2, …, M-1; M = 2K, $F_{even}(u)$ and $F_{odd}(u)$ are the Fourier values of K points.

3.2.4 **Convolution and deconvolution**

Image convolution is a typical method for image processing. The purpose of image convolution is to make use of the spatial relationship between pixels and their adjacent pixels and realize blurring, sharpening, edge detection and other functions through the operation of weighted sum. The calculation process of image convolution is the process of the weighted sum of image $f(x,y)$ local pixel blocks by a convolution kernel $w(a,b)$, as Equation (3-20). **Figure 3-2** presents the process of image convolution. The convolution kernel is essentially a fixed-size array of weights with the points in the centre.

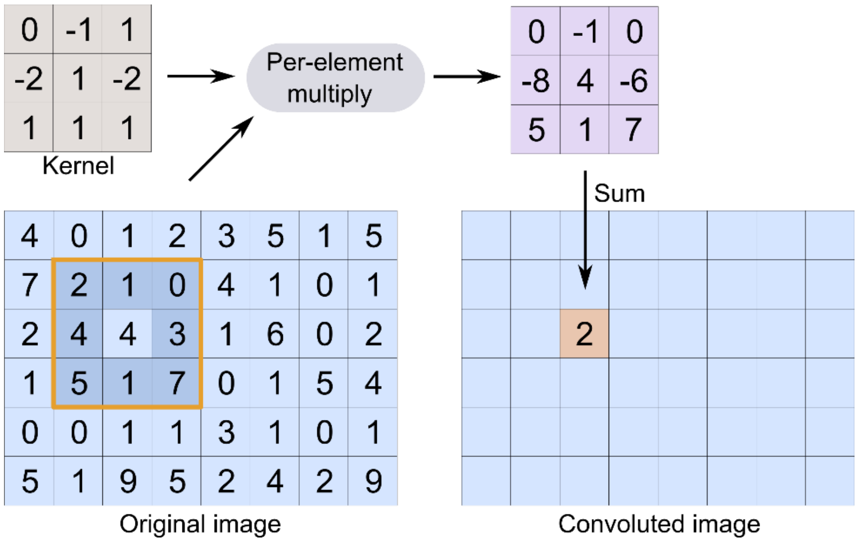

Figure 3-2 | The process of image convolution. For each pixel of the image, the product of its neighborhood pixels and the corresponding elements of the filter matrix is calculated and then added as the value of the pixel position.

$$f(x,y) * w(a,b) = \sum_{\substack{(a,b)\in w \\ (x-a,y-b)\in f}} f(x-a,y-b)w(a,b) \tag{3-20}$$

For the 2D discrete convolution:

$$f(x,y) * h(x,y) = \frac{1}{MN}\sum_{m=0}^{M-1}\sum_{n=0}^{N-1}\int f(m,n)h(x-m,y-n) \tag{3-21}$$

The Fourier transform of the convolution of two signals is equal to the product of their Fourier transforms. Moreover, the Fourier transform of the convolution of two spatial functions is the product of the Fourier transforms of the two functions.

$$f(x,y) * h(x,y) \Leftrightarrow F(u,v)H(u,v) \tag{3-22}$$

$$f(x,y)h(x,y) \Leftrightarrow F(u,v) * H(u,v) \tag{3-23}$$

Deconvolution is an algorithm-based method to reverse the effects of convolution on recorded data, which is widely applied in image processing. The convolution kernel $w(a,b)$ is also known as the PSF, specifying how the imaging process impacts a point source. The perfect process forms for a point source an image with a single bright point and other zero-valued pixels, while the real process produces an area of non-zero pixels such that a grey level profile across this area follows the PSF. For deconvolving an image, the PSF has to be known or estimated from measurements of the image.

By image deconvolution, one attempts to revert the blurring effect of the microscope, and thus increase image contrast and sufficient resolution, by using the PSF as prior information. Deconvolution can be performed in a single step, e.g., by Wiener or then iteratively, e.g., by Richardson-Lucy. In this chapter, we use the Richardson-Lucy algorithms. Since deconvolution is an iterative process, the deconvoluted results depend on the number of iterations. Typically, we need to try a few more times to get the best results.

The iterative Richardson-Lucy algorithm can be described with the following:

$$o_{k+1} = \left\{ \frac{i}{h \otimes o_k + b} \otimes h^* \right\} O_k \tag{3-24}$$

where O_k and o_{k+1} are the current and next object estimates, i is the original image, h is the PSF, h^* its mirrored version and b a background term.

3.2.5 Image filtering

Image filtering in the spatial domain is performed by convolution with an appropriate kernel. This operation selects the information in the frequency domain, but it is difficult to quantify this impact in the spatial domain. The frequency domain is more natural to specify these effects. As described in Equation (3-22) and (3-23), the Fourier transform converts the image from the spatial domain to the frequency domain, while the inverse Fourier transforms recovers the spectrum domain to the spatial domain (**Figure 3-3a** & **d**). Using the corresponding relationship between spatial domain and frequency domain, we try to transform the spatial convolution filter into the frequency domain filter. Then

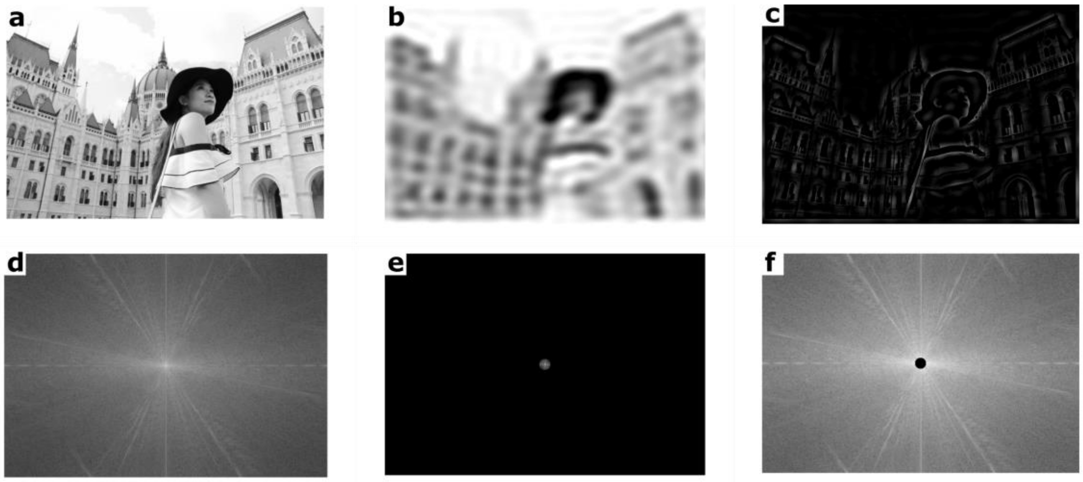

Figure 3-3 | Image filtering in the spatial domain. (**a**) The original image. (**b**) The low-pass filter image. (**c**) The high-pass filter image. (**d**) The Fourier frequency domain of the original image. (**e**) The corresponding low-pass frequency domain of (**b**). (**f**) The corresponding high-pass frequency domain of (**c**).

we transform the processed image back to the spatial domain, achieving the purpose of image filtering.

3.2.5.1 **Ideal filter**

The low-pass filter can filter out the high-frequency component through the low-frequency component. In the image process, the low-frequency component refers to the part of the image that does not change much. The low-pass filtered image has fewer sharp details than the original image while highlighting the smooth transition part (**Figure 3-3b**). An ideal sharp cut-off filter (**Figure 3-3e**) simply blocks all frequencies at distances larger than a fixed filter radius D_0 (cut-off frequency) from the centre (zero frequency) of the spectrum:

$$H(u,v) = \begin{cases} 1, & D(u,v) < D_0 \\ 0, & D(u,v) \geq D_0 \end{cases} \tag{3-25}$$

On the contrast, the high-pass filter can filter out the low-frequency component through the high-frequency component. In the image process, the high-frequency component refers to the part of the image with extensive changes, which corresponds to the edge, detail and texture information of the image. The high-pass filtered image has a smooth transition with less grayscale than the original image while highlighting the edge and other details (**Figure 3-3c**). An ideal high pass filter (**Figure 3-3f**) suppresses all frequencies up to the cut-off one and does not change frequencies beyond this border:

$$H(u,v) = \begin{cases} 0, & D(u,v) < D_0 \\ 1, & D(u,v) \geq D_0 \end{cases} \tag{3-26}$$

The ideal bandpass filtering preserves a specific range of frequencies and suppresses all others. Conversely, band-stop filtering suppresses a range of frequencies and preserves all other frequencies:

$$H(u,v) = \begin{cases} 0, & D(u,v) < D_0 - \frac{W}{2} \\ 1, & D_0 - \frac{W}{2} \leq D(u,v) \leq D_0 + \frac{W}{2} \\ 0, & D(u,v) > D_0 + \frac{W}{2} \end{cases} \tag{3-27}$$

Where W is the bandwidth; on the other hand, the ideal band-stop filter is just using one minus the bandpass.

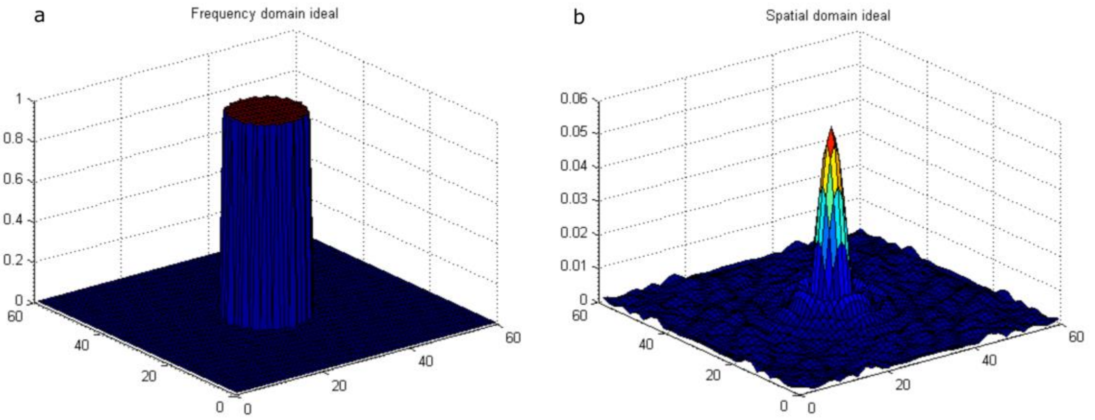

Figure 3-4 | The ideal image filter. (**a**) Ideal filtering in the frequency domain. (**b**) Ideal filtering in the spatial domain. The ideal filter has ring artifacts. The spatial image has a violent vibration.

From **Figure 3-3b**, we find the low pass filtered image produces some "ring artifacts", which refers to the shock at the sharp change in the grey level of the output image. The main reason is that the selected ideal filter has an abrupt change in the frequency domain (**Figure 3-4a**). The shape of the ideal low-pass filter in the frequency domain is a rectangle, so its inverse Fourier transform in the spatial domain is a *sinc* function (**Figure 3-4b**). Therefore, the spatial function of a filter with a window function is somewhat similar to the *sinc* function after inverse Fourier transform. To prevent the artifacts and receiving smooth data, we usually employ the other two kinds of filters, i.e. Butterworth filter and Gaussian filter, in the imaging process instead of the ideal filter.

3.2.5.2 **Butterworth filter**

The Butterworth low pass filter function is written as:

$$H(u,v) = \frac{1}{1+\left[\frac{D(u,v)}{D_0}\right]^{2n}} \tag{3-28}$$

where n denotes the degree of the filter, which controls how sharply the transition from pass-band to stop-band. The larger n is, the closer the filter is to the ideal filter. Compared to the ideal filter, Butterworth filter has a nearly equally flat response in the passband, but transitions to stop-band more smoothly, thus avoiding a sharp discontinuity at the cut-off (**Figure 3-6**). In contrast to Equation (3-28), we can get the high-pass Butterworth filter.

3.2.5.3 **Gaussian filter**

The Gaussian low pass filter is defined as:

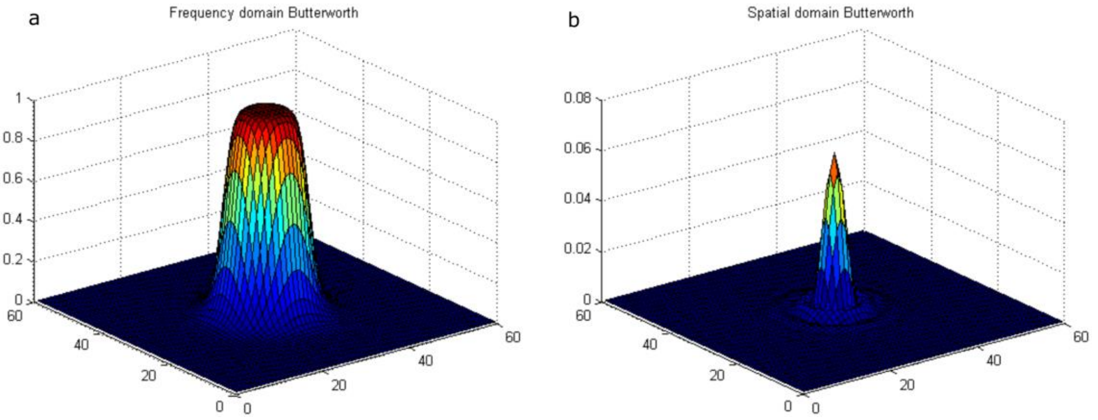

Figure 3-6 | The Butterworth image filter. (**a**) Butterworth filtering in the frequency domain. (**b**) Butterworth filtering in the spatial domain. The Butterworth filter has a flat response in the passband, but transitions to stop-band more smoothly when compared to the ideal filter.

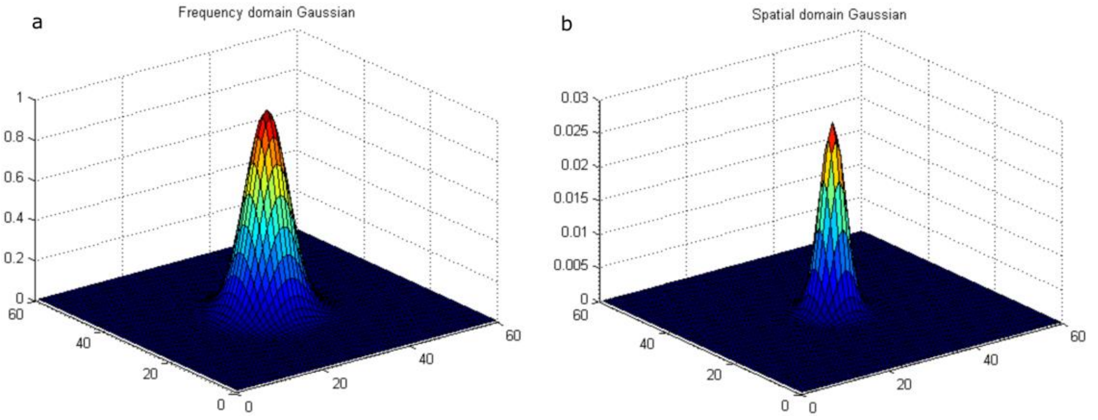

Figure 3-5 | The Gaussian image filter. (**a**) Gaussian filtering in the frequency domain. (**b**) Gaussian filtering in the spatial domain. The Gaussian filter has a smooth transition from pass-band to stopband when compared to the ideal filter.

$$H(u,v) = e^{\frac{-D^2(u,v)}{2{D_0}^2}} \tag{3-29}$$

Similarly to the Butterworth filter, the Gaussian filter has a smooth transition from pass-band to stopband (**Figure 3-5**). In contrast to Equation (3-29), we can obtain the high-pass Gaussian filter. In this chapter, we use the Gaussian filter for the simulation and experimental data process.

3.3 The multicolour PSF engineering super-resolution microscopy

By exploiting the fluorescence spectral dependence of the emitters in the focus plane, **Figure 3-7** presents the general concept of the multicolour PSF engineering super-resolution microscopy. It shows the PSFs versus emission wavelengths, synchronously generating different multicolour PSFs, red Gaussian PSF (PSF_{Gau}) and green doughnut

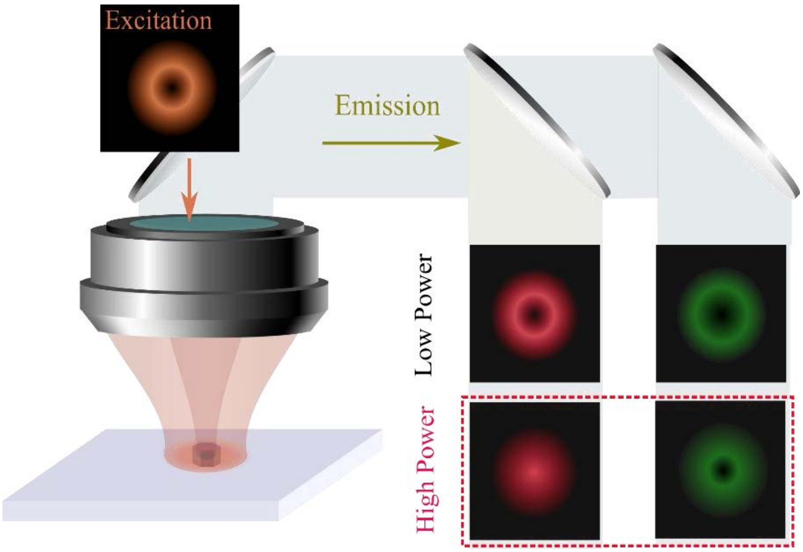

Figure 3-7 | The concept of multicolour PSF engineering super-resolution microscopy. One doughnut illumination beam can generate two different PSF in different colour channels. The two emissions are doughnut under low power, but the PSF in red colour turns to Gaussian under relatively high power.

PSF (PSF_{Dou}), under single doughnut excitation with relative intense power. The concept of this work is based on extracting the distinct features in nonlinear photon responses of multi-colour emission probes and engineering the PSF of the single probe in both the spatial and Fourier domains. In this section, we describe the image process algorithms underpinning the methods of FED image subtraction and heterochromatic Fourier spectrum fusion, respectively. Moreover, we evaluate their performance in nanoscopy through theoretical simulations.

3.3.1 **Image subtraction**

3.3.1.1 **Principle**

FED microscopy is an effective method that can improve the resolution of laser scanning microscopy based on the two sequential scans to obtain two images with a PSF_{Gau} and a PSF_{Dou}, respectively (**Figure 3-7**). As this approach is based on laser scanning microscopy, it can be added to a commercial system with only minor modifications by adding a vortex phase plate to generate a doughnut excitation beam. We achieve the super-resolution image (**Figure 3-8c**) by subtracting the image obtained by the doughnut (**Figure 3-8b**) beam scan from the image obtained from the Gaussian beam scan (**Figure 3-8a**). An appropriate normalizing coefficient (r), typically between 0.7 and 1, is used to

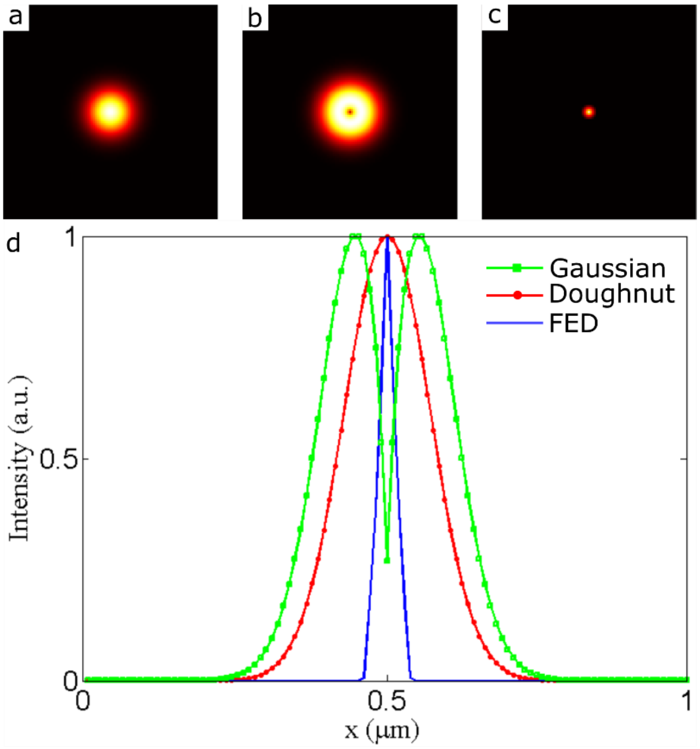

Figure 3-8 | The principle of the FED image subtraction. (**a**) The Gaussian PSF. (**b**) The Doughnut PSF. (**c**) The processed FED PSF by subtracting (**b**) from (**a**). (**d**) The corresponding cross-section profiles in (**a**) to (**c**).

adjust the imaging quality. To get a better visual image, we usually set the negative value as zero during the image process. The subtraction process follows Equation (3-30) and (3-31):

$$PSF_{FED} = PSF_{Gau} - r * PSF_{Dou} \tag{3-30}$$

$$I_{FED} = I_{Gau} - r * I_{Dou} \tag{3-31}$$

where PSF_{FED} is the processed effective PSF; PSF_{Gau} is Gaussian PSF; PSF_{Dou} is doughnut PSF; r is normalizing coefficient; I_{FED} is the processed image; I_{Gau} is the image taken with PSF_{Gau}; I_{Dou} is the image taken with PSF_{Dou}.

3.3.1.2 **Simulation**

To demonstrate the effect of the PSF on the FED image subtraction, we consider a numerical experiment in a series of patterns consisted of emitters with varying distances in **Figure 3-9**. In the centre region, the distance between these points is closer to each other. The points move further away as they spread out. This design allows us to get a distribution of points with different spatial frequencies in a plane. Rather than obtaining

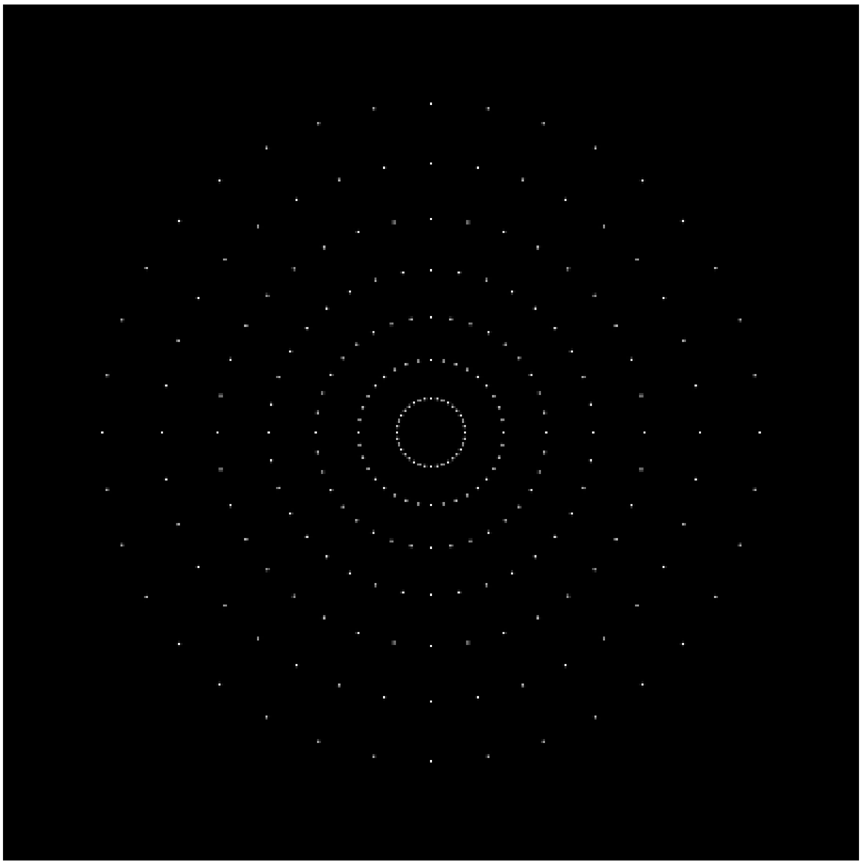

Figure 3-9 | A series of patterns consisted of emitters with varying distances for simulation.

the two images from two scans, we develop a super-resolution approach based on the two emission PSFs (Gaussian and doughnut) by exciting the nonlinear multi-colour probe. **Figure 3-10** demonstrates the simulation results of the FED image subtraction (simulation code in Appendix I). Compared with the image obtained from PSF_{Gau} (**Figure 3-10 a** & **d**), the resolution of the processed image by subtracting the emission PSF_{Dou} from the PSF_{Gau} has been significantly enhanced (**Figure 3-10 c** & **e**).

Although our new method has simplified two scans based modality of FED, the main shortcomings of both subtraction-based modalities suffer from the image distortion of artefacts and critical information loss. The subtraction balances the initial image's intensities, and the direct subtraction of normalized data sets often generates areas with negative intensity values, which is a potential source of data loss. To eliminate this effect, we introduce an appropriate normalizing coefficient r to adjust the strength of the subtraction. However, the r as a constant for the entire imaging area will cause over-subtracting and the resultant data loss. Most recently, researchers further employ a pixel

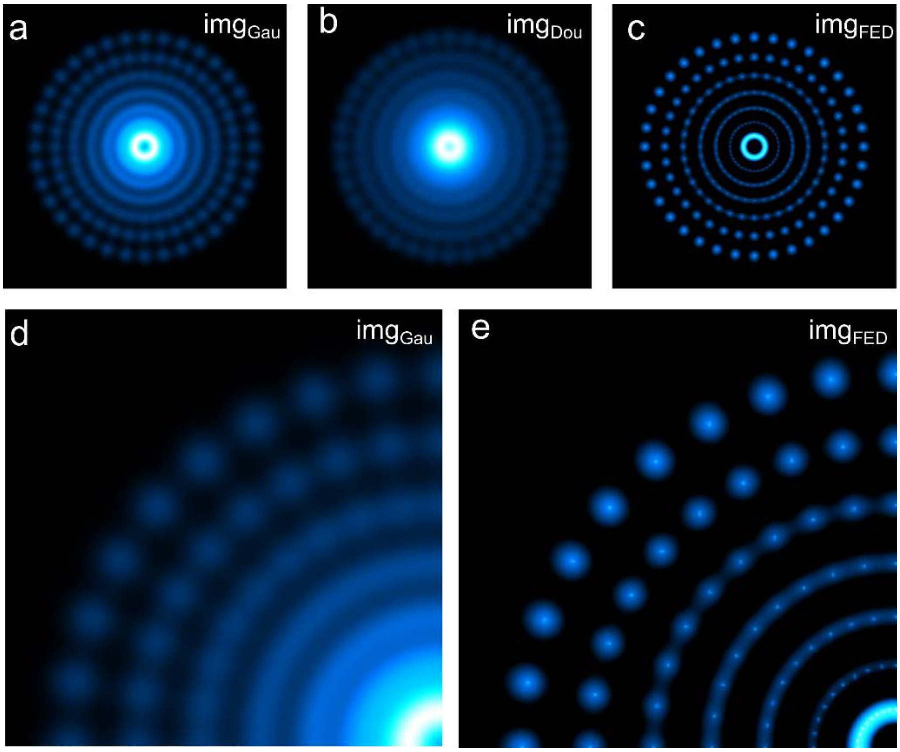

Figure 3-10 | Simulation result by FED image subtraction. (**a**) The scanning image by Gaussian PSF and (**b**) Doughnut PSF. (**c**) The processed result by subtracting the image in (**b**) from that in (**a**). (**d**) The magnified quarter image in (**a**). (**e**) The magnified quarter image in (**c**). In this simulation, the appropriate normalizing coefficient *r* is 0.9.

assignment [164] approach to adjust the contrast factor in each pixel, but at the expense of the overall resolution.

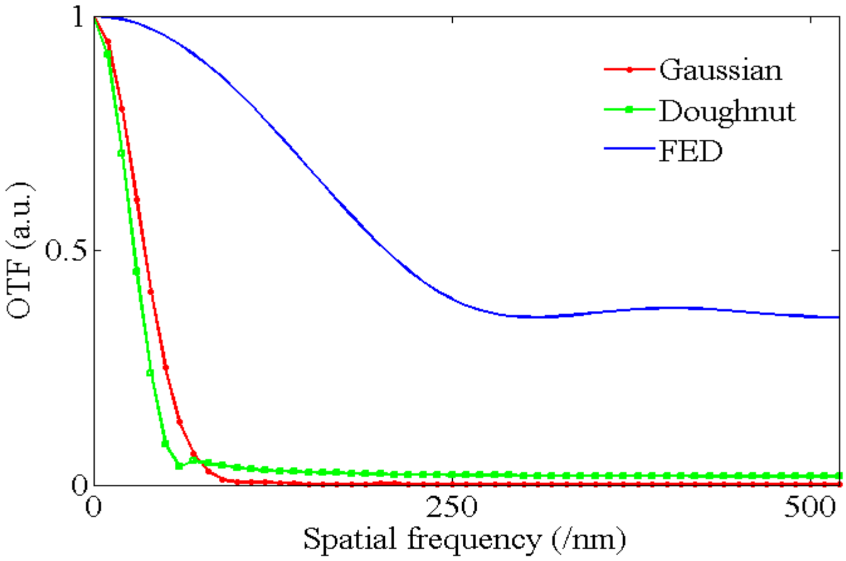

Figure 3-11 | The OTF profiled of the FED image subtraction.

As the processed image in **Figure 3-10 c & e**, the subtraction method creates an absence in critical spatial frequencies. Moreover, the processed image shows the dots with different sizes, apparently as the artefacts. We can explain this artifact by analyzing their OTF. From **Figure 3-11**, the OTF of the processed FED PSF has much larger frequency information compared to either ion PSF_{Dou} or PSF_{Gau}. However, we know the system cannot carry out such information in the original PSFs. As a sequence, the enhanced spatial frequency is often accompanied by the artificial error in this method.

3.3.2 Fourier fusion

3.3.2.1 Principle

Alternatively, we can transfer the heterochromatic saturated emission PSFs into Fourier domain and achieve the super-resolution imaging with frequency shifting mechanism conceptualization (simulation code in Appendix II). This strategy can effectively overcome any issues of information loss and image distortion associated with the spatial domain subtraction approach since Fourier domain OTF fusion can maximize the overall coverage of emission PSF patterns. By using a doughnut beam illumination, the spatial frequency components are encoded into both the doughnut excitation patterns, and the doughnut saturated emission patterns (Gaussian), including the high spatial frequency components being captured in the broader range of the detection OTF. **Figure 3-12** compares the difference in frequency components between OTFs obtained by two

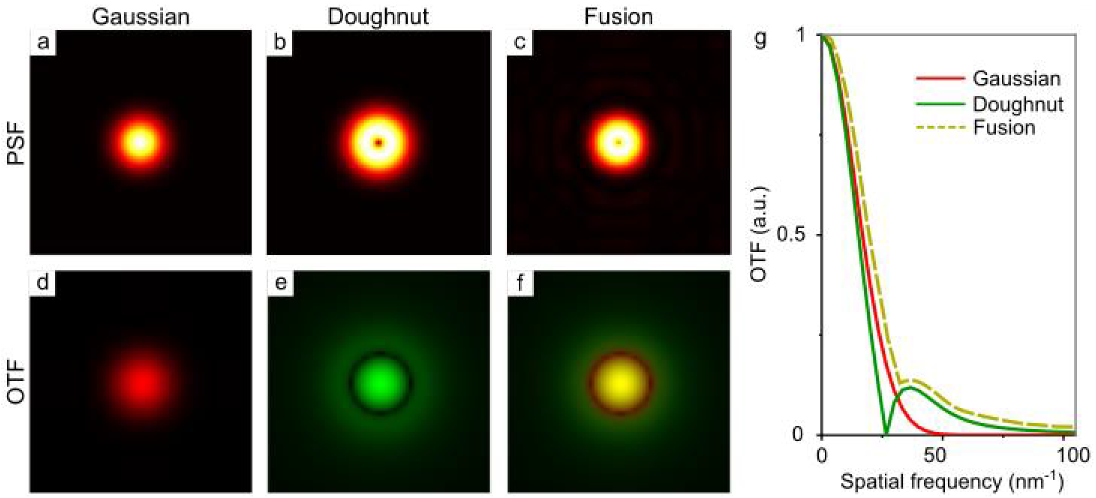

Figure 3-12 | Schematics of Fourier fusion for super-resolution microscopy. (**a**) Gaussian PSF. (**b**) Doughnut PSF. (**c**) Fourier fusion PSF. (**d**) OTF of Gaussian. (**e**) OTF of Doughnut. (**f**) OTF of Fourier fusion. (**g**) The corresponding cross-section profiles of OTF in (**d**) to (**f**).

emissions' PSFs. Obviously, PSF_{Dou} generates more content at a high spatial frequency than that generated by PSF_{Gau}. More significant content of high frequencies in OTF helps to recover high spatial frequency components in the image through the deconvolution algorithm.

However, the emission PSF_{Dou} has a gap in the intermediate frequency range, resulting in a deficiency at the mediate to low spatial frequencies (**Figure 3-12e**). Meanwhile this loss can be compensated by the OTF components generated from PSF_{Gau} (**Figure 3-12d**). Therefore, heterochromatic OTF fusion of saturated emission PSFs in Fourier domain takes advantage of both the PSF_{Dou} resolving power in providing high frequency content and the compensation effect from PSF_{Gau} in covering the medium frequency range (**Figure 3-12f**).

Following a similar study [165], we develop a heterochromatic Fourier spectrum fusion method to alleviate the frequency deficiency at specific frequency points as well as the partial deficiency induced by the saturation effect. The procedure is given by:

$$OTF_{eff} = OTF_{Gau} \times mask_{Gau} + OTF_{Dou} \times mask_{Dou} \times r_1 \tag{3-32}$$

$$I_{eff} = I_{Gau} \times mask_{Gau} + I_{Dou} \times mask_{Dou} \times r_1 \tag{3-33}$$

where OTF_{eff} and I_{eff} are the final processed effective OTF and image, respectively. OTF_{Gau} and OTF_{Dou} are the Fourier transform of the corresponding PSF_{Gau} and PSF_{Dou}, respectively. The $mask_{Gau}$ (Gaussian low pass, **Figure 3-13a**) and $mask_{Dou}$ (Gaussian high pass, **Figure 3-13b**) are the cut-off Fourier frequency filters, respectively. r_1 is a

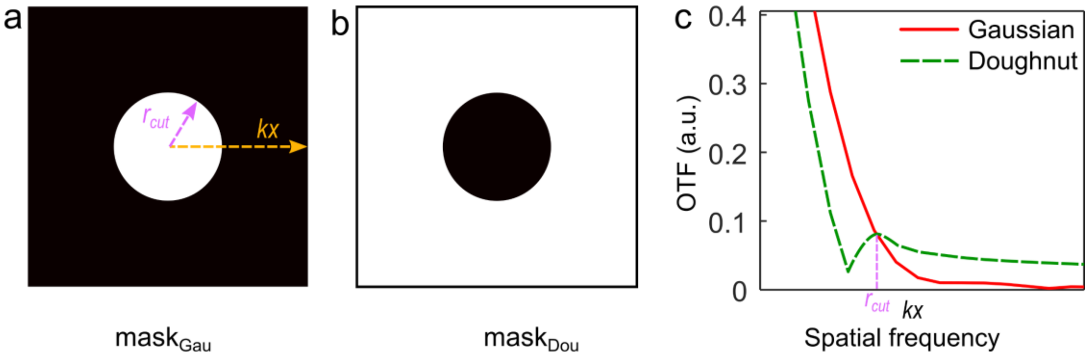

Figure 3-13 | Schematics of binary masks for Fourier fusion. (**a**) Mask$_{Gau}$ corresponds to a Gaussian low-pass filter used to block the high-frequency component above r_{cut}. The orange arrow of k_x denotes the direction of the spatial-frequency increase. **(b)** Mask$_{Dou}$ is a high-pass filter that permits the high-frequency component above $r_{cut.}$. **(c)** OTF profiles of Gaussian (red solid) and Doughnut (green dash), respectively. r_{cut} is a point selected at the intersection of Gaussian and Doughnut profiles.

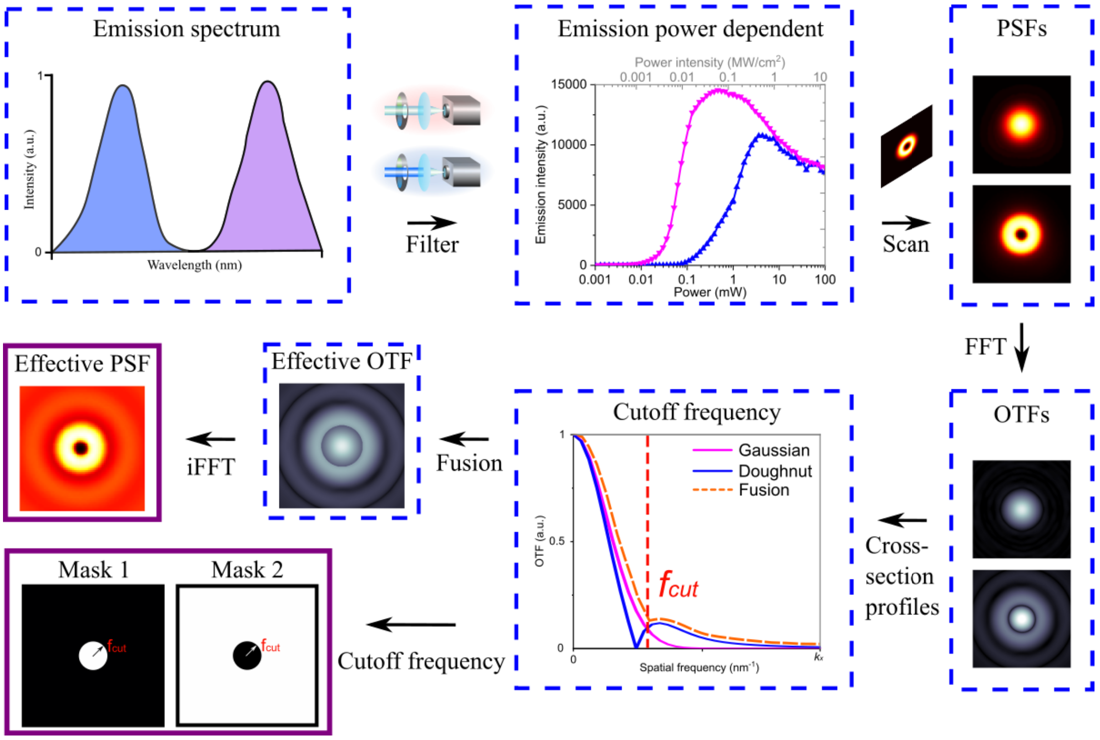

Figure 3-14 | Effective PSF for the fusion process by using the Gaussian and doughnut PSF. By selecting the cut-off frequency, we can obtain the PSF_{eff} and the low/high-frequency pass masks for imaging processing.

variable that modifies the ratio of these fused components for achieving the optimal synthetic system OTF_{eff}. I_{Gau} and I_{Dou} are the acquired images with the corresponding PSF_{Gau} and PSF_{Dou}, respectively.

The details in the image process are shown in **Figure 3-14** & **Figure 3-15**. Firstly, we obtain the effective PSF for the fusion process by using the Gaussian-like and doughnut PSF (**Figure 3-14**). In the beginning, the emission spectrum is collected to determinate the multiple emission bands (emission wavelength) of the fluorescent probes. As each emission band has different emission colour, the two power dependent curves are obtained by using wavelength band-pass filters or a dichroic mirror. The two different emission PSFs (Gaussian-like and doughnut) were measured by employing an intense doughnut-shaped beam to scan a single fluorescent probe. Both of the raw images may contain complementary information, which can be analysed by the OTF spectrum from each emission band through the fast Fourier transformation (FFT). By setting the cut-off frequency, the two different spectrums are fused into a single compound spectrum to yield an OTF_{eff}, referred to as the "segmented Fourier spectrum". For the PSF reconstruction, the inverse fast Fourier transformation (iFFT) is applied to yield the images with the

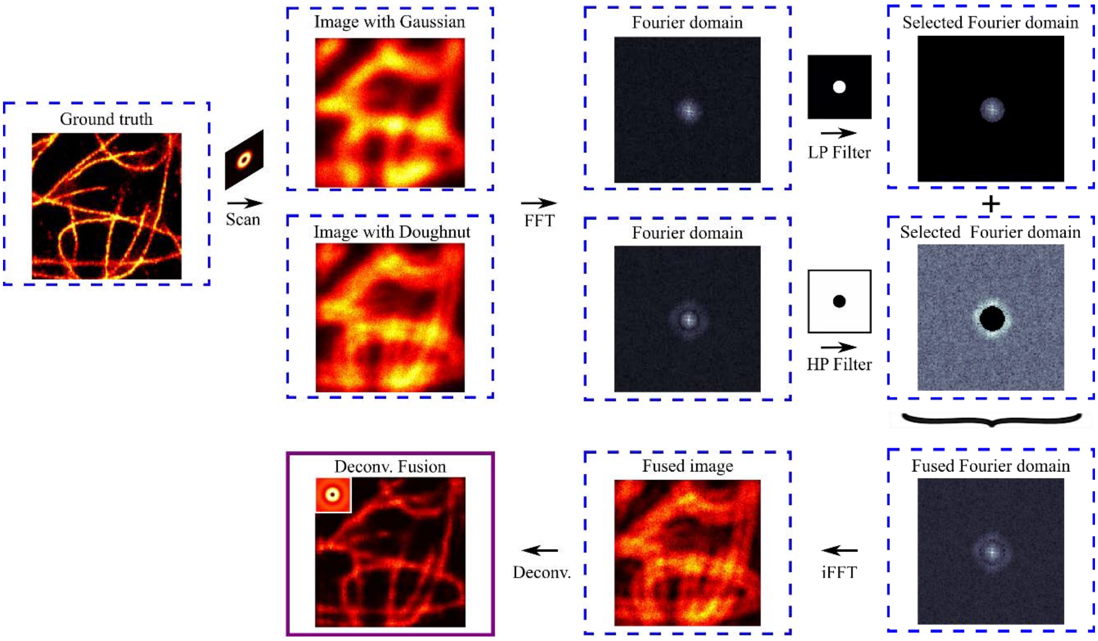

Figure 3-15 | The flow chart of the Fourier domain heterochromatic fusion method. The high-quality image is achievable for the fused image by Richardson-Lucy deconvolution with the PSF_{eff}.

emission PSF_{eff}. Meanwhile, the low/high-frequency pass masks are obtained for the next imaging processing step.

With the effective PSF and frequency masks, we can process the images by the Fourier domain heterochromatic fusion method (**Figure 3-15**). Firstly, the two images of different colour emission are obtained by using a focused doughnut-shaped beam to scan the specimen. Then the two images were converted to the Fourier domain through FFT. With the frequency filter masks (masks are from **Figure 3-15**), the information in the Fourier domain is selected by applying the low-pass (LP) mask for the image of Gaussian-like and high-pass (HP) mask for the counterpart. Subsequently, a new optimal Fourier domain is achieved by fusing these two selected Fourier domains. The fused image can be obtained by using iFFT. Finally, the high-quality image is achievable for the fused image by Richardson-Lucy deconvolution with the PSF_{eff} (PSF_{eff} is from **Figure 3-15**).

3.3.2.2 **Simulation**

To evaluate the imaging performance using the Fourier fusion PSF engineering, we perform a numerical simulation to scan different types of beams over a series of patterns, consisting of diffraction limit dots of single emitters (same as the pattern in **Figure 3-9**).

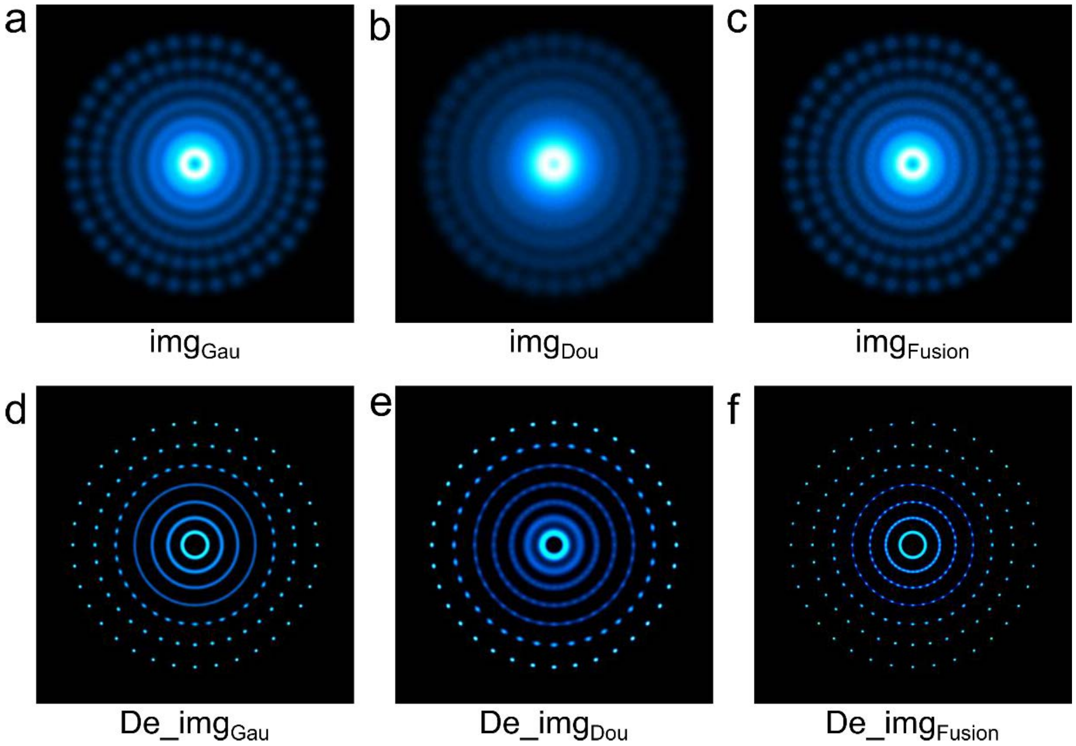

Figure 3-16 | A numerical study using the heterochromatic Fourier spectrum fusion algorithm to overcome the issues associated with frequency deficiency and imaging distortion. (**a**) The image obtained by using Gaussian PSF. (**b**) The image obtained using Doughnut PSF. (**c**) The image obtained using the fusion algorithm. (**d**) Richardson-Lucy deconvolution result of the image in (**a**). (**e**) Richardson-Lucy deconvolution result of the image in (**b**). (**f**) Richardson-Lucy deconvolution result of the image in (**f**). The iterations of the simulation are 180.

Figure 3-16 presents the image-resolving powers of the PSF_{Dou}, the saturated doughnut PSF_{Gau} , and the fused heterochromatic PSF_{eff} , as well as their corresponding deconvoluted images with iterations of 180.

For a clear comparison, we magnify the deconvoluted images in **Figure 3-17**. For the dots on the fourth ring (in green), the distance is too close for the Gaussian PSF to resolve them (**Figure 3-17a**), while the doughnut PSF provides a higher resolution that clearly resolves each dot (**Figure 3-17b**). For the dots with more sparse points on the third ring (in red), the doughnut PSF fails in providing some intermediate frequency information (see **Figure 3-17b**), which resulted in poorly resolved dots on the third circle.

To maximize the coverage of spatial information from the different emission PSFs and their corresponding Fourier domain components, we use the design Fourier binary masks (**Figure 3-13**) to fuse different PSFs in the deconvolution process and achieve the improved image quality with sufficient amount of details without distortion, as shown in

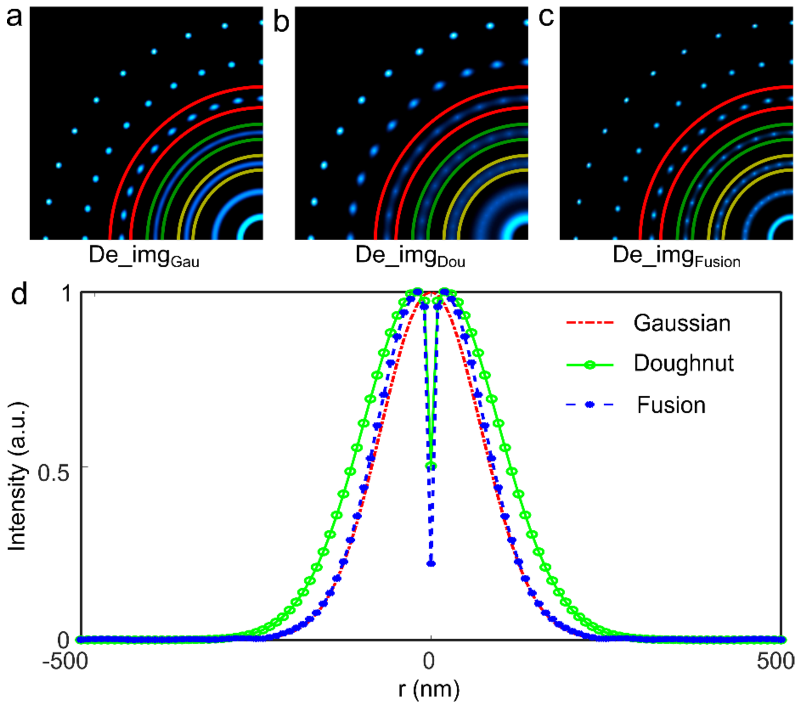

Figure 3-17 | The magnified images for the Gaussian, doughnut and Fourier fusion comparison. (**a**) The deconvoluted image obtained using Gaussian PSF. (**b**) The deconvoluted image obtained using Doughnut PSF. (**c**) The deconvoluted image obtained using the fusion algorithm. **(d)** The corresponding PSF profiles of Gaussian (red), Doughnut (green) and Fusion (blue), respectively.

Figure 3-17c. **Figure 3-18** demonstrates the corresponding OTF of the Gaussian,

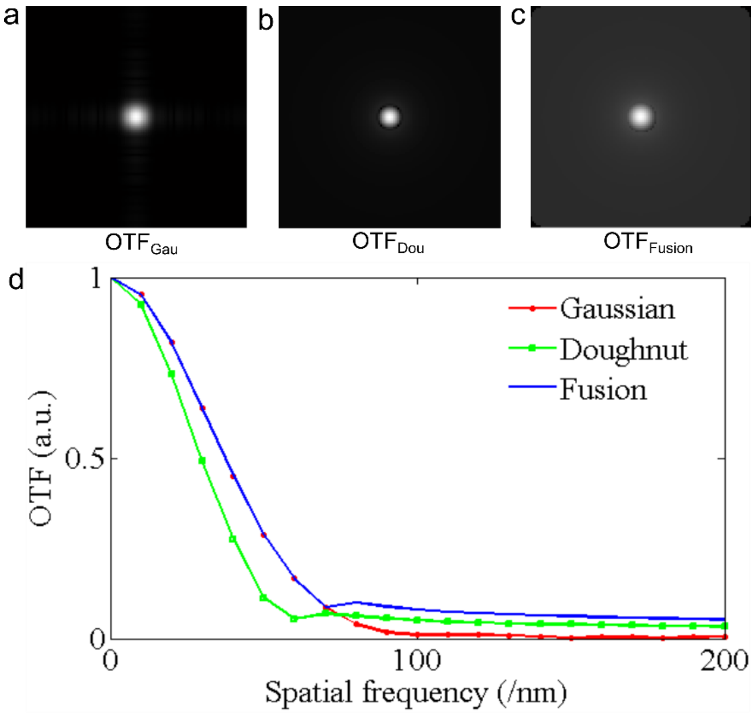

Figure 3-18 | The OTF for the Gaussian, doughnut and Fourier fusion comparison. (**a**) The OTF of Gaussian PSF. (**b**) The OTF of Doughnut PSF. (**c**) The OTF of the fusion. **(d)** The corresponding OTF profiles of Gaussian (red), Doughnut (green) and Fusion (blue), respectively.

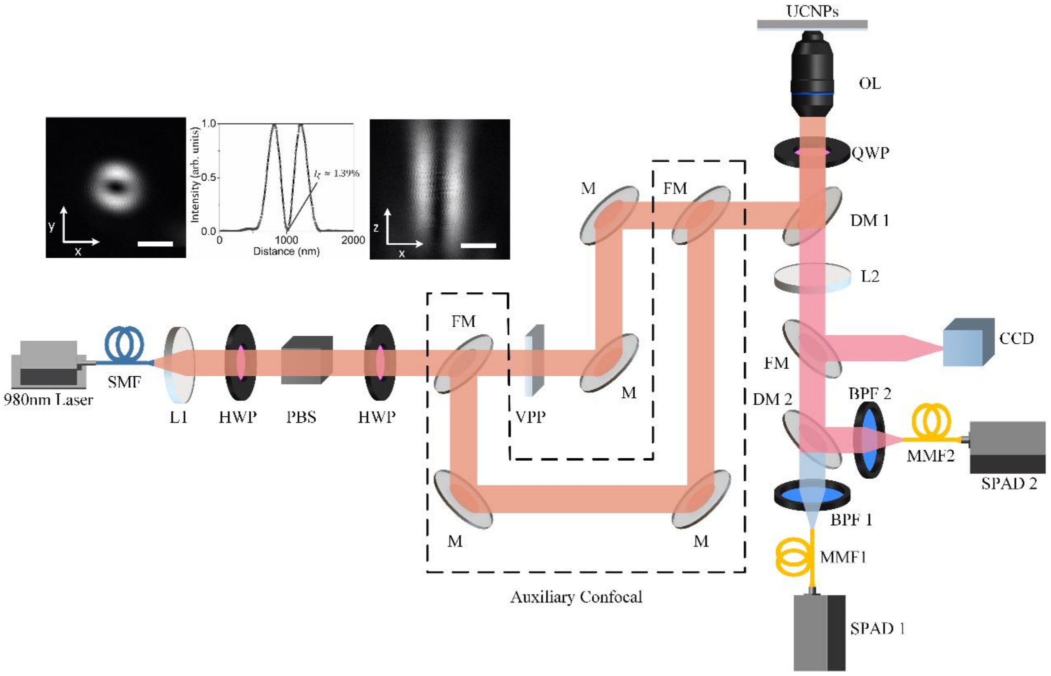

Figure 3-19 | Schematic of the single beam Fourier fusion super-resolution nanoscopy.

doughnut and Fusion PSF. This Fourier domain fusion approach utilizes all the complementary frequency contents (**Figure 3-18d**), simultaneously acquired from the single doughnut beam scanning, and maximize the image deconvolution process in super-resolution imaging. Given that the final detected signal is the saturated emission with enhanced contrast to the background noise, it successfully resolves the higher frequencies information that is otherwise covered by the noise in confocal scanning mode (see **Figure 3-17c** in the inner ring in yellow).

3.4 Methods

3.4.1 Experimental setup

All the measurements have been performed on the same home-built microscopy system setup in **Figure 2-9**. The only difference is the signal collection part (**Figure 3-19**). The emission signals are separated by the short-pass dichroic mirror (DM2, T785sp, Chroma), and purified by the bandpass filter (BPF1, ET740/60M, Chroma) and bandpass filter (BPF2, ET805/20M, Chroma), respectively.

3.4.2 **Materials**

3.4.2.1 **Synthesis of UCNPs**

We use the same method for the UCNPs synthesis and characterization (section 2.4.2).

3.4.2.2 **Surface modification of UCNPs**

Post-synthesis surface modification was implemented to transfer the UCNPs into hydrophilic and biocompatible before bioconjugation with Streptavidin. Surface modification was performed via ligand exchange with block copolymer composed of hydrophilic block poly(ethylene glycol) methyl ether acrylate phosphate methacrylate (POEGMA-b-PMAEP) [93]. In a typical procedure, 500 ul of OA-coated UCNPs (10 mg/mL) were dispersed in tetrahydrofuran (THF). Then the OA-capped UCNPs in THF were mixed with 5 mg copolymer ending in the carboxyl group in 2 mL THF. The above mixture was sonicated for 1 min, followed by incubation in a shaker overnight at room temperature. The polymer-coated UCNPs were purified four times by washing/centrifugation at 14860 rpm for 30 min with water to obtain the carboxyl group modified UCNPs. Subsequently, the supernatant was removed and the nanoparticles were dispersed in water for further conjugation with Streptavidin.

3.4.2.3 **Streptavidin-UCNPs**

The protocol of carbodiimide chemistry was adopted to conjugate the carboxyl group on the polymer with the amine groups of Streptavidin molecules. The UCNPs were re-activated by the EDC (100-folder molar ratio to UCNPs) in HEPES buffer (0.2 mM, pH 7.2) with slightly shaking at room temperature for 30 mins. The Streptavidin molecules (100 µM) were added to the above solution with 600 rpm shaking for 3 h reaction. The activated carboxyl-UCNPs were washed/centrifuged at 14680 rpm cycle twice to remove EDC and resuspended in HEPES buffer to obtain probe Streptavidin-UCNPs.

3.4.2.4 **Biotin-UCNPs**

Alternatively, we used the ligand exchange to get Biotin-UCNPs. Following the protocol in section 2.4.2.2, we obtained the ligand-free UCNPs removing the OA. The 50 mg Biotin was dissolved in 0.1M NaOH in 9 ml water under vigorous stirring for 30 mins at room temperature, adjusting the pH of the final solution to 8. 0.5 mL ligand-free UCNPs was added to the above solution drop by drop under 2 h stirring. After that, we added 10 ml DEG and kept stirring the solution stirring at 105°C for 1 h to remove water. The solution was transferred to 20 ml Teflon-line autoclave and incubated at 160°C 2 h. The final solution was washed/centrifuged at 14680 rpm cycle three times with ethanol and deionized water to obtain probe Biotin-UCNPs.

3.4.3 **Cellular immunofluorescence**

3.4.3.1 **Preparation of COS-7 cell samples**

3.4.3.1.1 **Cell resuscitation**

COS-7 Cell Line (African green monkey kidney epithelial cells) were brought from the International Trade in Endangered Species of Wild Fauna and Flora (CITES). The cells from the liquid nitrogen were thawed in a 37 ℃ water bath. This was followed by adding 5 ml of culture medium Dulbecco's High Glucose Modified Eagle Medium (DMEM) with 10% FBS to a T25 bottle, then frozen cell fluid was added to T25 bottle overnight for passaging.

3.4.3.1.2 **Cell passaging**

The cell culture medium was removed, washed twice with PBS. Then 1 ml of Pancreatic enzyme was added to T25 bottle, 37 degrees for 5 minutes, followed adding 3 ml of neutralizing trypsin, and 4 ml of culture medium were added to a T25 bottle. 1 ml of cells in culture medium was incubated in a glass-bottomed 35 mm dish at 37 °C and 5% CO_2 for 24 h. COS-7 cells were harvested when the confluency reached about 80−90%.

3.4.3.1.3 **Cell membrane extraction**

Before the immunostaining labelling, cells were washed with PBS twice and extracted with 0.2% Triton X-100 dissolved in prewarmed extracting buffer containing 0.1 M piperazine-N, N'-bis (2-ethanesul-fonic acid) (PIPES), 1 mM ethylene glycol-bis (β-aminoethyl ether)- N, N, N', N'-tetraacetic acid (EGTA), and 1 mM $MgCl_2$ at room temperature for about 40 s. Removing the extracting buffer and washed with Tris twice was the next step.

3.4.3.2 Microtubule imaging

For the immunostaining labelling, COS-7 cells were fixed with the 4% PFA for 10 min and then washed with PBS twice. COS-7 cells were permeabilized with 0.5% Triton-X100 for 5 min and blocked with blocking buffer containing 1% bovine serum albumin (BSA) and 0.5% Triton-X100 for 30 min. After that, the cells were kept in 1% BSA for an additional 30 min. COS-7 cells were stained with 1:50 primary antibody (rat anti-mouse anti-tubulin antibody, ab6160) dissolved in a blocking buffer for 1 h. Cells were washed with PBS containing 1% BSA and stained with 1:200 secondary antibody (donkey anti-mouse, Alex647) dissolved in blocking buffer for 1 h. Then, cells were washed with PBS containing 1% BSA twice and washed with Tris containing 1% BSA. COS-7 cells were stained with 0.065 mg/ml streptavidin-UCNPs in Tris containing 0.5% BSA, 0.5% Triton and 5 mM NaF for 1 h at room temperature. After that, the labelled cells were washed with 5 mM NaF and stored at 4 °C before imaging.

3.5 Results and discussion

3.5.1 Multicolour emission in UCNPs

We choose to use UCNPs and experimentally verify our approach. UCNPs represent an entirely new class of multi-colour emitting probes that rely on high densities of multi-photon emitters [166][167][168][169], which upconverts near-infrared photons into visible ones. Their exceptional brightness under microscopy and nonlinear optical

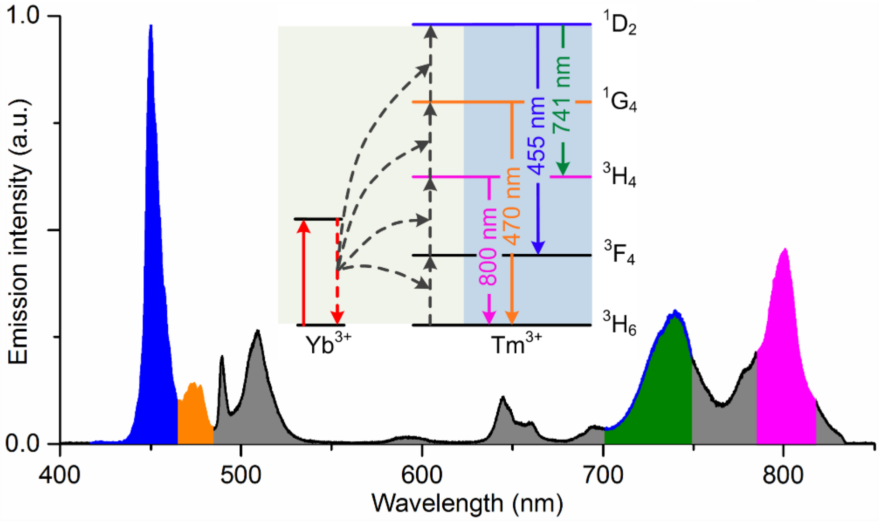

Figure 3-20 | The upconversion emission spectra from UCNPs. The emissions were obtained for UCNPs solution ($NaYF_4$: 40% Yb^{3+}, 4% Tm^{3+}) under 980 nm excitation laser.

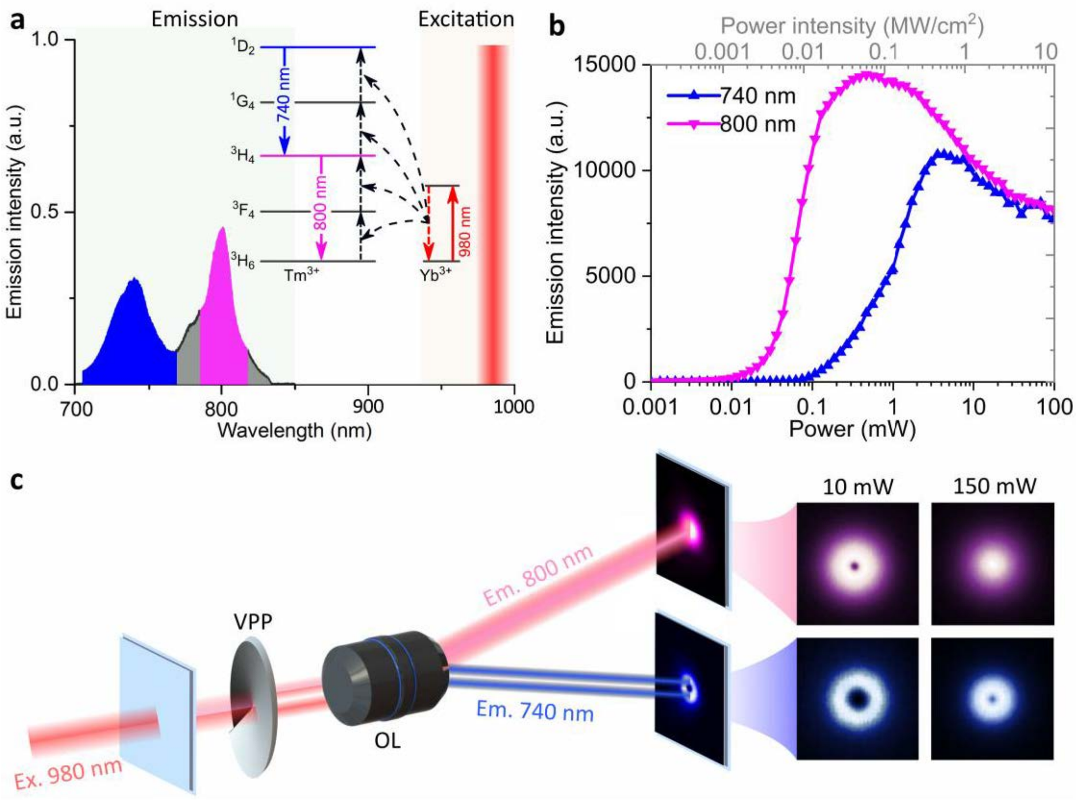

Figure 3-21 | Heterochromatic emission saturation contrast produced by UCNPs and power-dependent emission PSF patterns under a tightly focused doughnut beam illumination. (**a**) The upconversion emission spectrum of a typical 40 nm single nanoparticle ($NaYF_4$: 40% Yb^{3+}, 4% Tm^{3+}) upon 980 nm excitation laser at a power density of 10 MW/cm^2. Insert is a simplified energy level and upconversion process of Yb^{3+} and Tm^{3+} co-doped UCNPs. The multiphoton NIR upconversion emissions mainly from two-photon excited state (800 nm, $^3H_4 \rightarrow {}^3H_6$) and four-photon excited state (740 nm, $^1D_2 \rightarrow {}^3H_4$). (**b**) The two distinct power-dependent saturation intensity curves of the 800 nm and 740 nm emissions. (**c**) The power-dependent PSF patterns of two emission bands from a single UCNP under a doughnut-shaped excitation beam. Under the low excitation power (10 mW), both channels display the doughnut-shaped PSFs. The 800 nm emission converts to Gaussian PSF when increasing the laser power to 150 mW.

properties make UCNPs suitable as single-molecule probes [40][99][170][171][172] and super-resolution imaging [85]. **Figure 3-20** display the typical emission spectra of a 40-nm UCNP based on a $NaYF_4$ host co-doped with high-concentrations of 40% Yb^{3+} sensitizer ions and 4% Tm^{3+} activators ions under 980 nm excitation laser (power density of 10 MW/cm^2).

By taking the benefit from the multiple long-lived intermediate states (**Figure 3-21a**), the sensitized photon energy can be stepwise transferred onto the scaffold energy levels of Tm^{3+} emitters, which eventually facilitates the multiphoton upconversion emissions from the two-photon excited state (800 nm, $^3H_4 \rightarrow {}^3H_6$) and four-photon excited state (740 nm, $^1D_2 \rightarrow {}^3H_4$). The upconversion emission at 800 nm from the lower intermediate excited

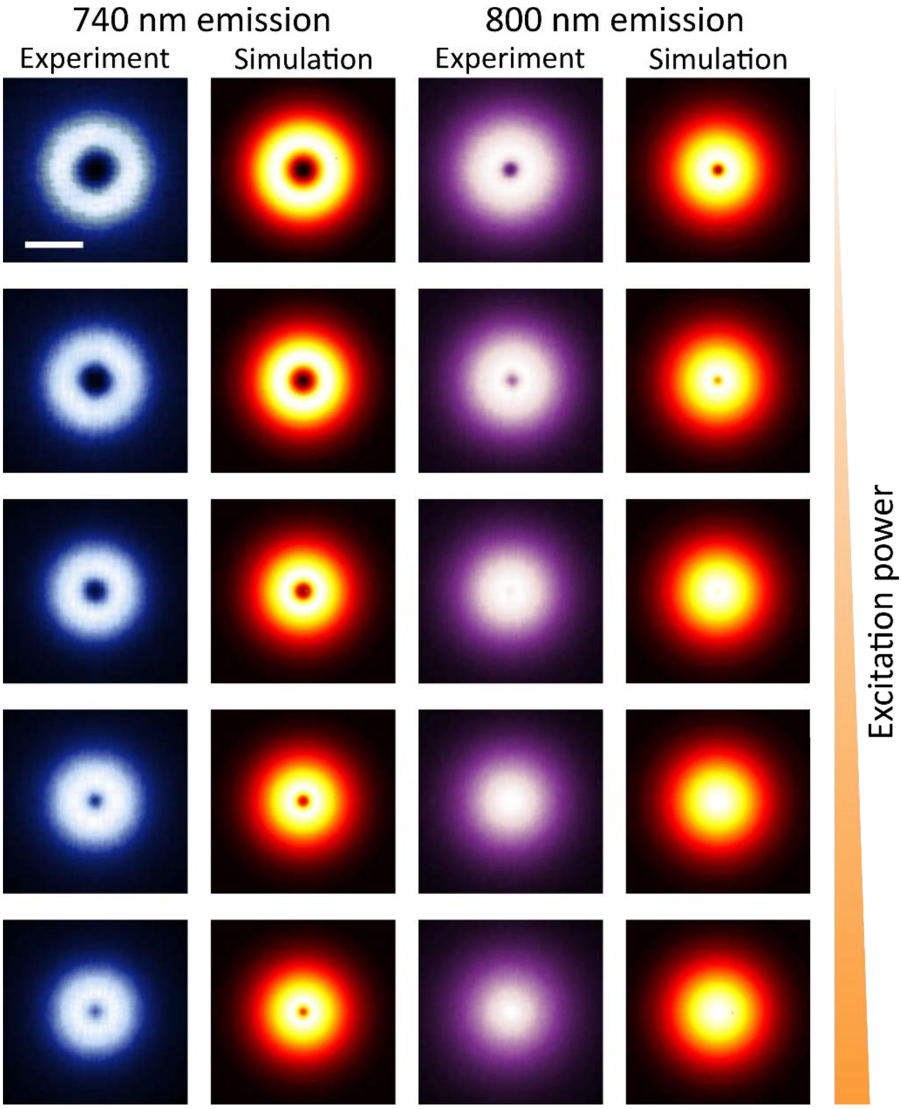

Figure 3-22 | The experimental and theoretical simulation of the process for generating Gaussian PSF under a doughnut beam. The power-dependent PSF patterns of two emission bands (740 nm and 800 nm) from a single UCNP when increasing the laser power from 10 mW to 150 mW. Pixel size, 10 nm. Scale bar is 500 nm.

level has a lower saturation threshold compared with emissions from the higher levels, as confirmed by the nonlinear fluorescence saturation curves shown in **Figure 3-21b**.

By taking advantage of the apparent contrast in saturation intensity curves of upconversion emissions from the multi-intermediate states [173], we scan the sample of single UCNPs using a tiny focused doughnut illumination beam and detect from multiple emission channels, including 800 nm and 740 nm (shown in **Figure 3-21c**). We find that under the low excitation power, both channels display the doughnut-pattern PSFs. The difference in heterochromatic saturated emission PSFs becomes significant with an

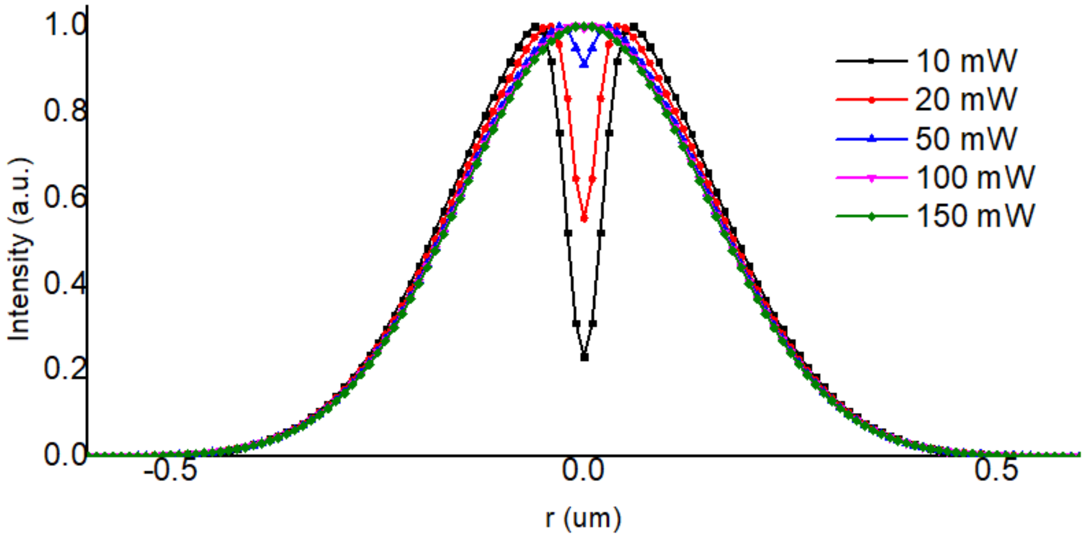

Figure 3-23 | The cross-section profiles of the simulated PSF at 800 nm emission band under different excitation power.

increased excitation power. Because of the non-zero feature at the centre dip of doughnut beam (around 1.4%, see **Figure 3-19**), at an intense power density, the 800 nm saturated emission PSF eventually becomes a "Gaussian PSF" with two-photon upconversion emission at centre reaching the maxima (**Figure 3-21c**). In contrast, the 740 nm saturated emission PSF remains a doughnut shape. The reason behind this is because the increased excitation power elevates the two-photon fluorescence at the centre to reach the maxima, while the fluorescence signals away from the centre keep at the same values since they have reached saturation.

For a better understanding of the process of generating a Gaussian emission PSF under a doughnut excitation, **Figure 3-22** demonstrates and compares the experimental and theoretical simulation. Moreover, **Figure 3-23** shows the cross-section profiles of the simulated PSF at 800 nm emission band for the comparison of how the excitation power affects the final emission PSF. We can find the centre dip rises sharply with the increased excitation power. Eventually, the doughnut-shaped profile turns to the Gaussian under a fully saturated power. It worth noting that as fully explained in section 2.5, we can reduce the excitation power by designing the optimal synthesis of UCNPs, including the activator and sensitizer doping concentration, core-shell structures, as well as choose the optimal emission bands.

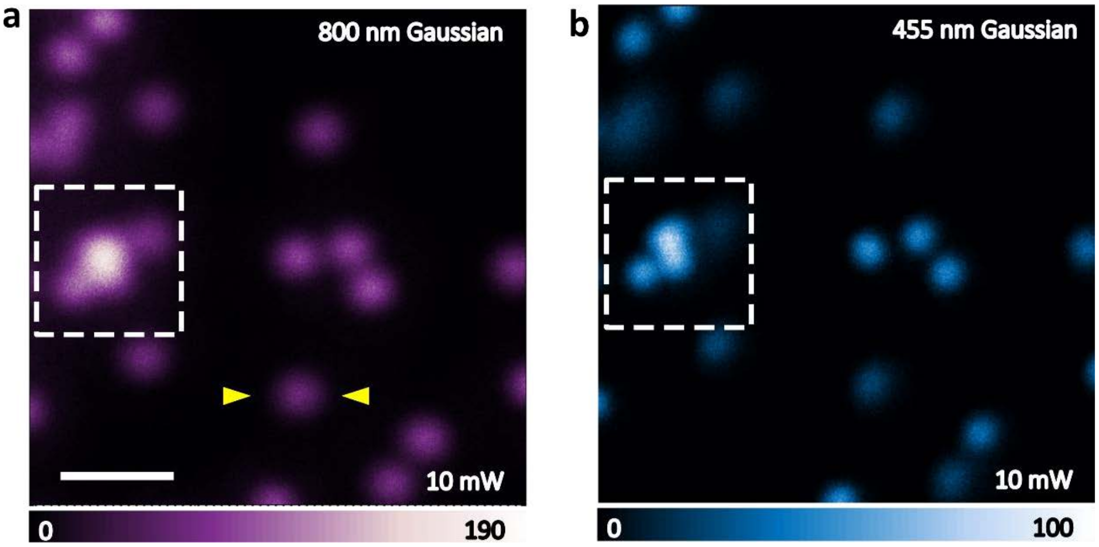

Figure 3-24 | The standard confocal images of UCNPs by scanning a standard Gaussian beam. (**a**) Emission band at 800 nm. (**b**) Emission band at 455 nm. The excitation power is 10 mW. The scale bars are 1.5 µm.

3.5.2 **Fourier fusion on single nanoparticles**

Using the heterochromatic PSF, we apply the Fourier spectrum fusion approach for imaging the UCNPs cluster. We first acquire the standard confocal images of 800 nm and 455 nm emission bands by scanning a standard Gaussian beam (**Figure 3-24**). Since the wavelength of 455 nm is almost half of 800 nm emission, the image of 455 nm emission has a resolution according to the diffraction limit Equation (1-1) We then obtain the pair

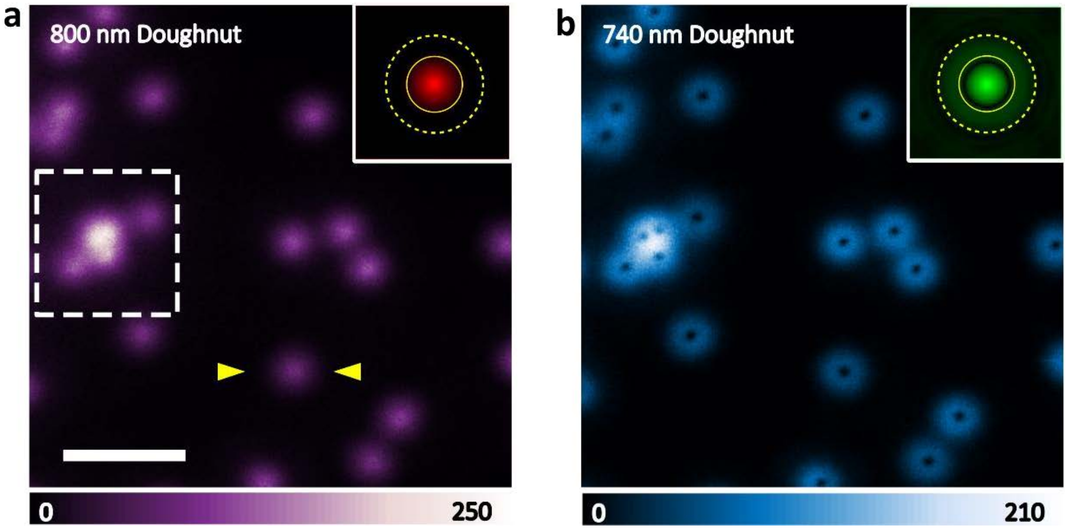

Figure 3-25 | The multicolour images of UCNPs by scanning a doughnut-shaped beam. (**a**) Emission band at 800 nm. Inset, the corresponding Fourier transform. (**b**) Emission band at 740 nm. Inset, the corresponding Fourier transform. The excitation power is 150 mW. The scale bars are 1.5 µm.

of contrast images at 800 nm and 740 nm by scanning a doughnut-beam (**Figure 3-25**). Neither confocal results (**Figure 3-24**) nor the over-saturated image (**Figure 3-25a**) provide sufficient resolution to distinguish single UCNPs within the diffraction limit area (the square with the dashed line in the images). The reason is that the Gaussian PSF cannot produce high spatial information.

In contrast, the 740 nm saturated emission doughnut PSF carries the high-frequency information from the clusters of single nanoparticles (**Figure 3-25b**), making it possible to differentiate the single nanoparticles from the clusters. By analyzing the Fourier transform of the "Gaussian" and doughnut PSF (inset images in **Figure 3-25**), the doughnut contains the information at a higher frequency in the Fourier domain (the outer circle with the dashed line). We can also find there is a gap in the medium frequency region (inner circle with the solid line). However, the Fourier transform of the "Gaussian" PSF can cover this gap.

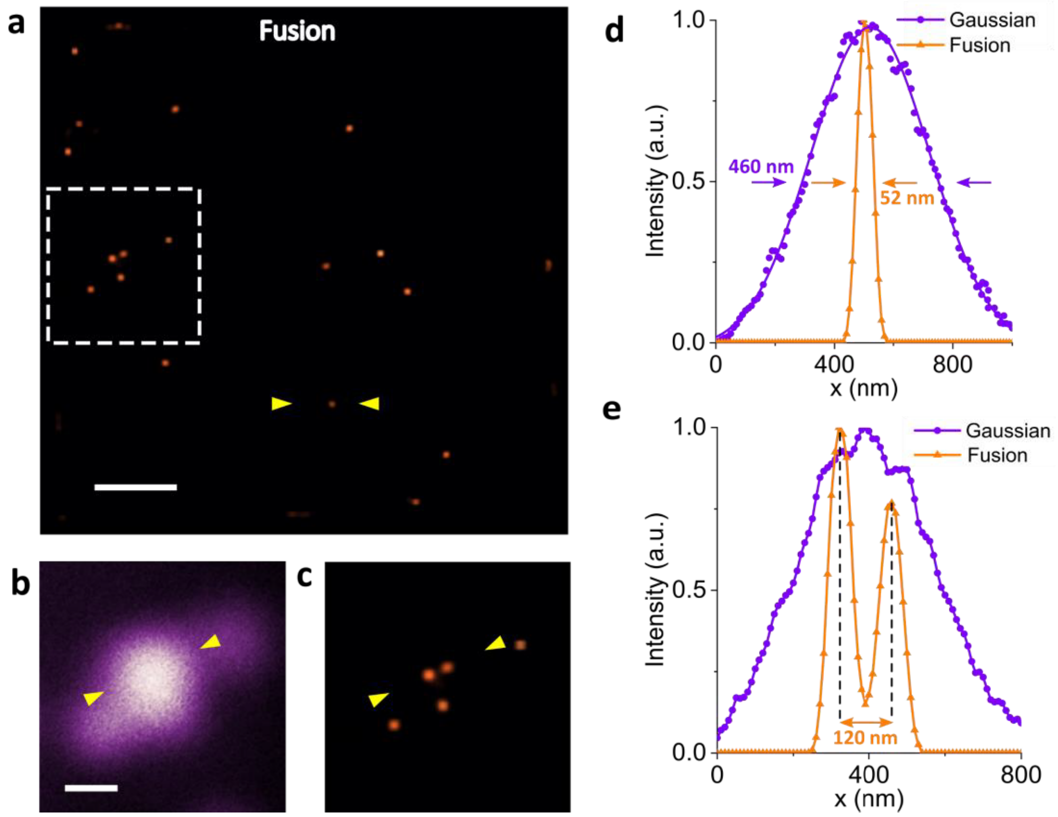

Figure 3-26 | Super-resolution imaging of single UCNPs using Fourier fusion. (**a**) Super-resolution imaging by Fourier-domain fusing 800 nm "Gaussian" emission and 740 nm doughnut emission in Figure 3-22. (**b**) and (**c**) are the magnified area of interest from Gaussian and fusion, respectively. (**d**) Line profiles of single UCNPs. (**e**) Line profiles of two nearby UCNPs from (**b**) and (**c**). Pixel dwell time, 1 ms. Pixel size, 10 nm. The scale bars are 1 μm in (**a**) and 500 nm in (**b** & **c**).

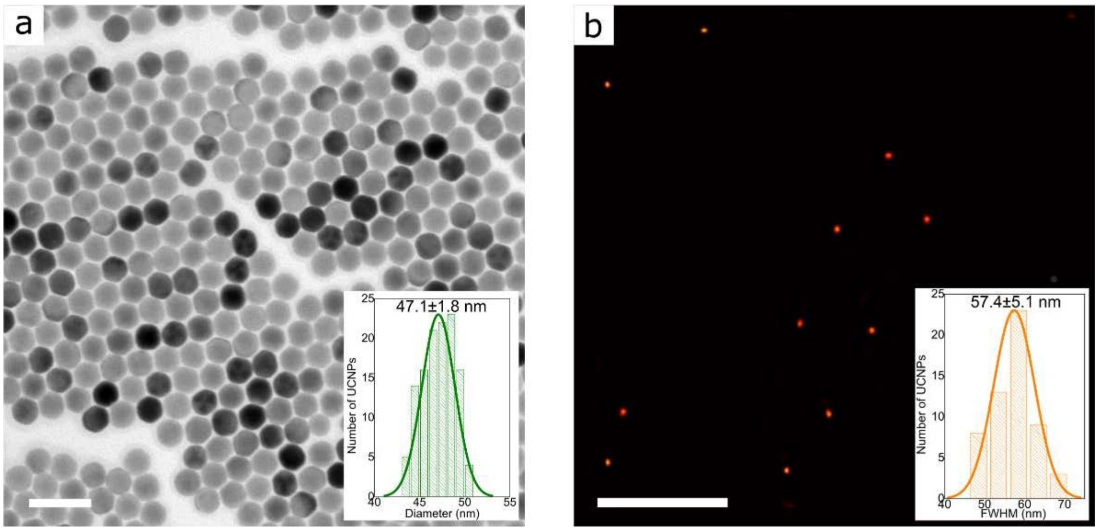

Figure 3-27 | The statistic size distribution of the nanoparticles NaYF$_4$: 40% Yb^{3+}, 4% Tm^{3+} in TEM and Fourier domain fusion super-resolution imaging. (**a**) TEM image of the nanoparticles. Inset is the statistic histogram of the size distribution, indicating the average size is 47.1 ±1.8 nm of over 100 samples. (**a**) Fourier domain fusion image of the nanoparticles. Inset is the statistic histogram of the size distribution, indicating the average full width at half maximum (FWHM) is 57.4 ±5.1 nm of over 50 samples. Scale bar is 100 nm in (**a**), 1500 nm in (**b**).

Using the Fourier domain heterochromatic fusion approach to saturated emission PSFs (Equation (3-32) & (3-33)), we achieve a high-quality image by fusing the "Gaussian"

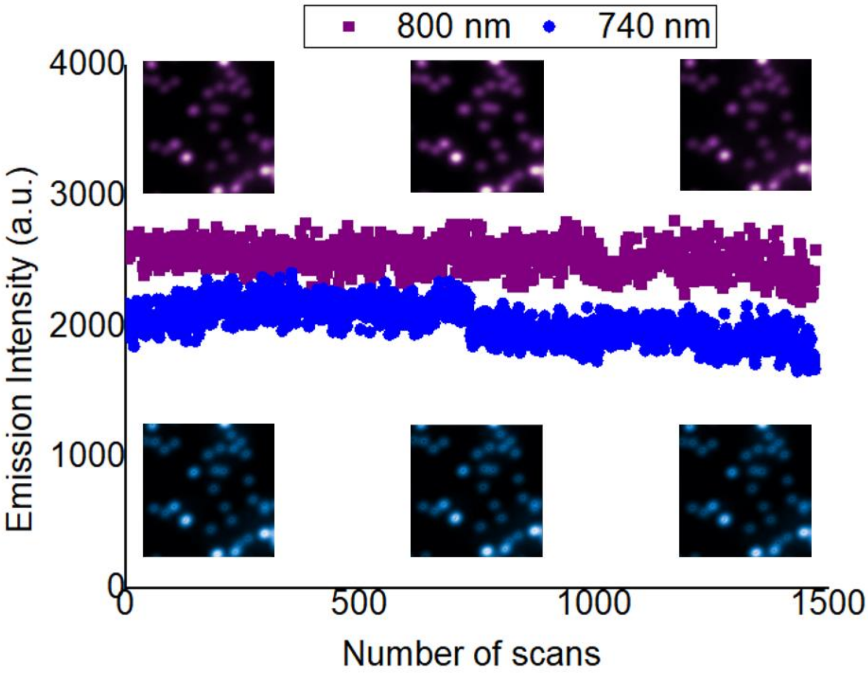

Figure 3-28 | Photo-stability tests of UCNPs used in super-resolution microscopy. Emission intensity against the number of scan repetitions for repeated scanning of UCNP images by the doughnut excitation beam. Excitation laser power is fixed at 150 mW and the signal is collected from the centre nanoparticle with exposure times 50 ms. Inset, the two-colour images are obtained at the beginning, middle and end of the scanning period. Dwell time is 1 ms.

and doughnut emissions (**Figure 3-26**). We demonstrate the ability in resolving the discrete nanoparticles with a discernible distance of 120 nm (**Figure 3-26c**). **Figure 3-26e** shows the corresponding line profile analysis. The spectrum-domain contrast, as a result of their nonlinear emission responses at multiple intermediate upconversion states, is the key in providing different degrees of saturated emission PSFs for heterochromatic OTF fusion. The magnified comparison images of **Figure 3-26b** & **c** demonstrate a significantly improved FWHM resolution of 52 nm (~λ/20) from 460 nm, compared with the results shown in **Figure 3-26d**. The average statistical FWHM of UCNPs in the processed Fourier fusion super-resolution images is 57.4 ± 5.1 nm (**Figure 3-27**).

For the long-term image acquisition and particle tracking, UCNP represents a significant advantage in photostability, compared with traditional organic fluorophores and fluorescent proteins. **Figure 3-28** further presents there is no bleaching issue in emission intensity even after 1,500 repetitive scans.

As the low excitation density is important for super-resolution nanoscopy to be used for biological applications, we further demonstrate the use of 2% Tm^{3+} and 40% Yb^{3+} UCNPs (**Figure 3-29**) to reduce the excitation power requirement. According to our previous works[83][84], the relatively low doping concentration of activators will facilitate UCNPs to achieve the emission saturation at low excitation power. As shown in **Figure**

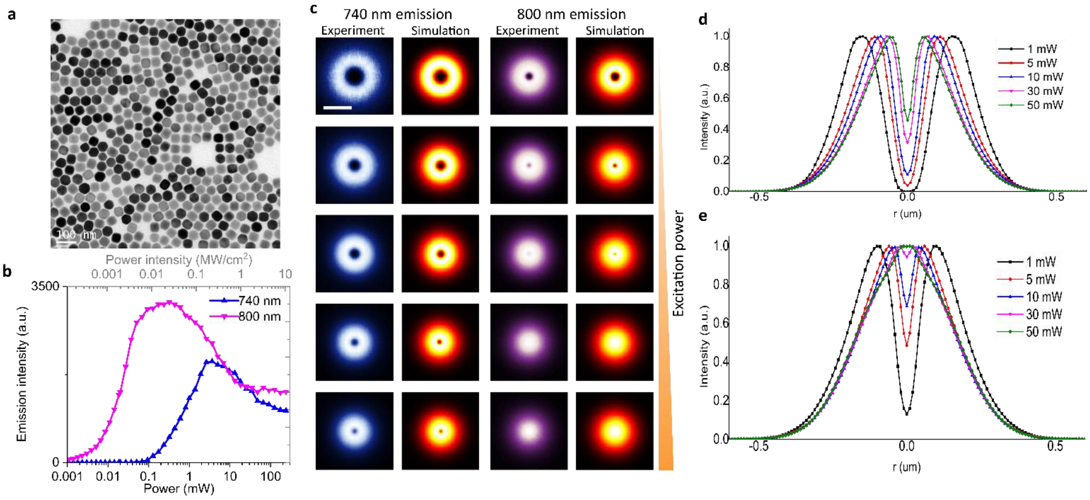

Figure 3-29 | Heterochromatic emission saturation contrast for the low lanthanide-doped UCNPs. (**a**) TEM images of the nanoparticles $NaYF_4$: 40% Yb^{3+}, 2% Tm^{3+}. The average size is around 50 nm. (**c**) The experimental and simulation results of the power dependent PSF patterns of two emission bands from a single UCNP when increasing the laser power from 1 mW to 50 mW. (**d** & **e**) The corresponding cross-section profiles of simulated 740 nm emission PSFs and 800 nm emission PSFs in (**c**), respectively. Scale bar is 100 nm in (**a**), and 500 nm in (**c**).

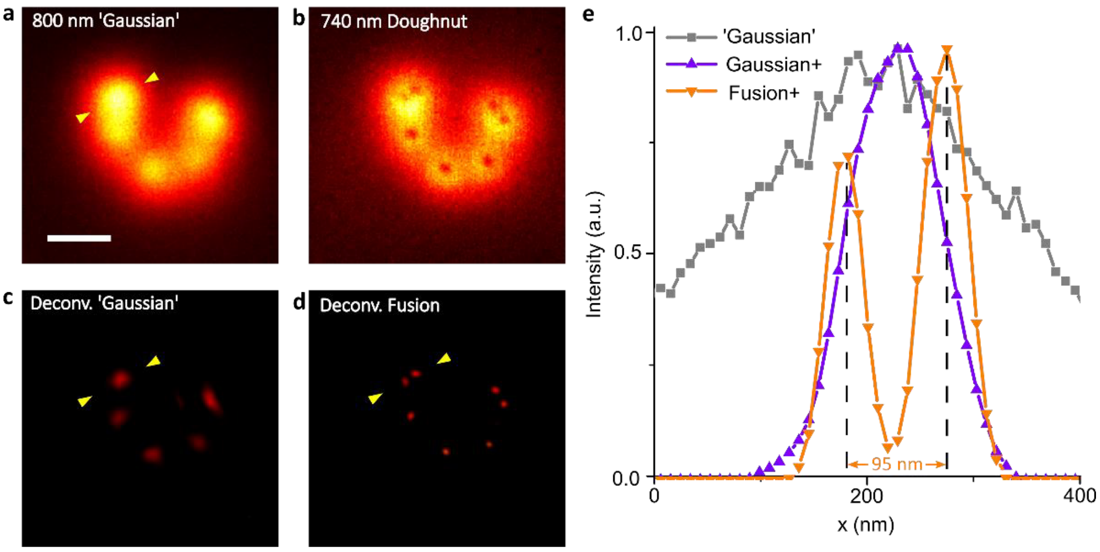

Figure 3-30 | The sub-diffraction imaging of the lower activator doped UCNPs (2% Tm^{3+} and 40% Yb^{3+}). (**a**) The 800 nm emission band image of UCNPs under a 980 nm doughnut beam excitation, which creates Gaussian-like (over-saturated doughnut) PSF. (**b**) The 740 nm emission band image of UCNPs under a 980 nm doughnut beam excitation, which provides doughnut PSF. (**c**) The deconvoluted results in (**a**). (**d**) The super-resolution imaging by Fourier domain fusing the 800 nm Gaussian-like emission in (**a**) and the 740 nm saturating doughnut emission in (**b**). (**e**) Line profiles of the two nearby UCNPs from (**a**), (**c**) and (**d**). The 980 nm laser power is 50 mW, which is measured at the back aperture of the objective lens. Pixel dwell time, 1 ms. Pixel size, 10 nm. The scale bar is 500 nm.

3-29, under 50 mW excitation, the 800 nm emission PSF turns to a Gaussian-liked profile, while the 740 nm emission PSF remains as a doughnut shape. Using the Fourier domain heterochromatic fusion method, as shown in **Figure 3-30**, we can resolve the two UCNPs with a distance of 95 nm. The corresponding excitation power density of 2.75 MW/cm^2 is well below the photo-toxic damage threshold for the living cells [85][99].

3.5.3 Comparison of different algorithms

As introduced in section 3.3, we can obtain the super-resolution image with the multicolour PSF engineering methods, including the FED subtraction and Fourier fusion algorithms. Based on the simulation, we have concluded that Fourier fusion offers a better quality image since the subtraction induces some artifacts and loses critical information. Moreover, deconvolution is a typical method to recover the original high-quality data in the image process. As introduced in section 3.2.4, we use the iterative Richardson-Lucy algorithm in this chapter. For demonstrating the advantage of the Fourier fusion approach, **Figure 3-31** compares the processed experimental image with those different algorithms.

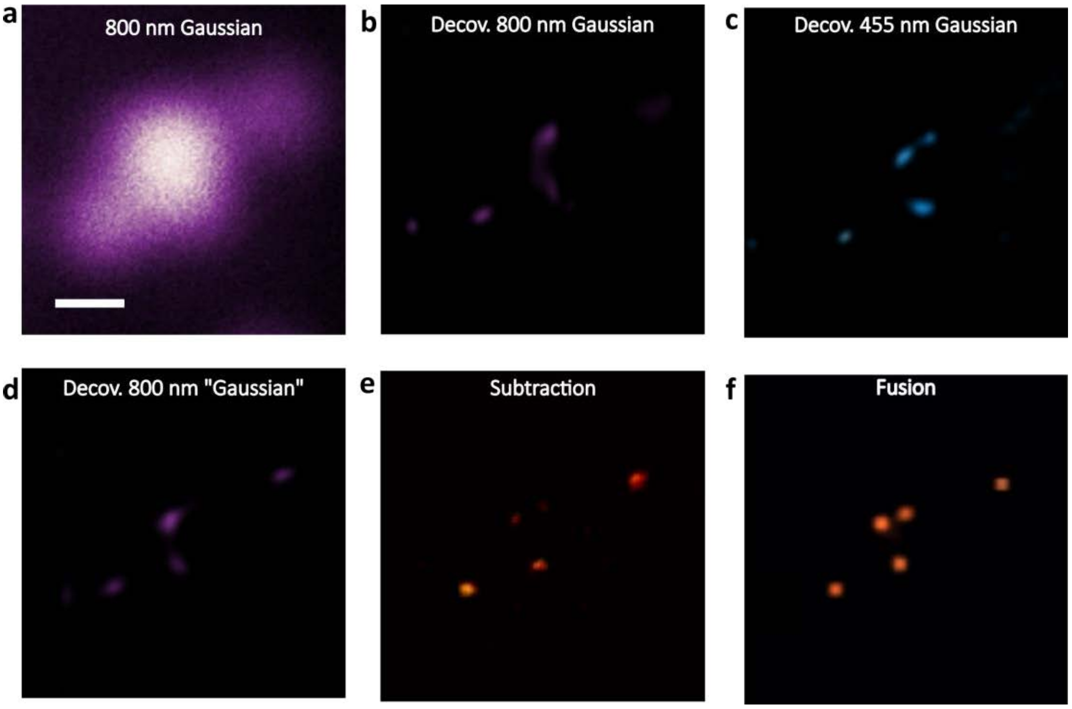

Figure 3-31 | Comparison of different algorithms. (**a**) Confocal image with Gaussian beam 800 nm. (**b**) The deconvolution of the Gaussian beam at 800 nm emission. (**c**) The deconvolution of the Gaussian beam at 455 nm emission. **(d)** The deconvolution of the "Gaussian" beam (super-saturated doughnut) at 800 nm emission. **(e)** The image of the FED subtraction algorithm. (**f**) The image of the Fourier fusion algorithm. The scale bar is 500 nm.

We select the UCNPs cluster in the diffraction limit volume that is highlighted by the dashed line in **Figure 3-25a**. **Figure 3-31a** presents the conventional confocal imaging by using a Gaussian beam at 800 nm emission. It is hard to distinguish the distribution of the UCNPs in this diffraction-limited region. By using the corresponding Gaussian PSF, **Figure 3-31b** shows that Richardson-Lucy deconvolution cannot resolve the single nanoparticles compared with the Fourier fusion method (**Figure 3-31f**). Although it seems the blue emission has doubled the resolution (**Figure 3-24b**), we still cannot get comparable information as the Fourier fusion (**Figure 3-31c**). Similar to the "Gaussian" generated from the doughnut saturation, the Richardson-Lucy deconvolution fails to get the super-resolution image. The Gaussian PSF cannot extract the information at the high spatial frequency.

With the two images in Gaussian and doughnut PSF (**Figure 3-25**), we obtain the resolved nanoparticles in **Figure 3-31e**. However, we can find that the brightness of the particles is significantly different, especially for the two closest particles. Moreover, the size of the processed UCNPs is not uniform, which is not consistent with our TEM images (**Figure 3-27a**). The experimental results of the processed FED subtraction match well with our simulation (**Figure 3-10d**), the enhanced spatial frequency of the FED subtraction method is often accompanied by artificial error. As a consequence, we know that the Fourier fusion is the best algorithm among these image process modalities.

3.5.4 Fourier fusion on continuous specimens

We know that the super-resolution imaging modality needs to achieve high-quality data with continuous biological specimens. We further demonstrate that the multicolour Fourier fusion approach can facilitate a simple method for simultaneous super-resolution imaging of microtubule network in cells [174]. **Figure 3-32a** shows the original image of the targeted microtubule network. Also, **Figure 3-32b** & **c** present the corresponding simulated images with Gaussian and doughnut PSF, respectively. We can see that the microtubule filaments in **Figure 3-32c** are hollow due to the effect of the doughnut-shaped beam.

With the iterative Richardson-Lucy deconvolution algorithm, **Figure 3-33** and **Figure 3-34** highlight the importance of compensating for the missing spatial frequency regions for bio-imaging applications. The high image resolutions in both transverse directions are achievable for the complexed samples, as the fine structures of microtubules can be resolved using Fourier domain fusion method. Imaging results show that sub-diffraction resolution in both transverse directions is achievable in biological samples, as evidenced by the observed fine structures of microtubules in the PSF Fourier fusion image shown in **Figure 3-33c**. We also find the Richardson-Lucy deconvolution can help us enhance the image resolution, even with the Gaussian PSF. From the cross-section profiles in **Figure 3-33d**, the doughnut PSF can resolve the information in the sub-diffraction region

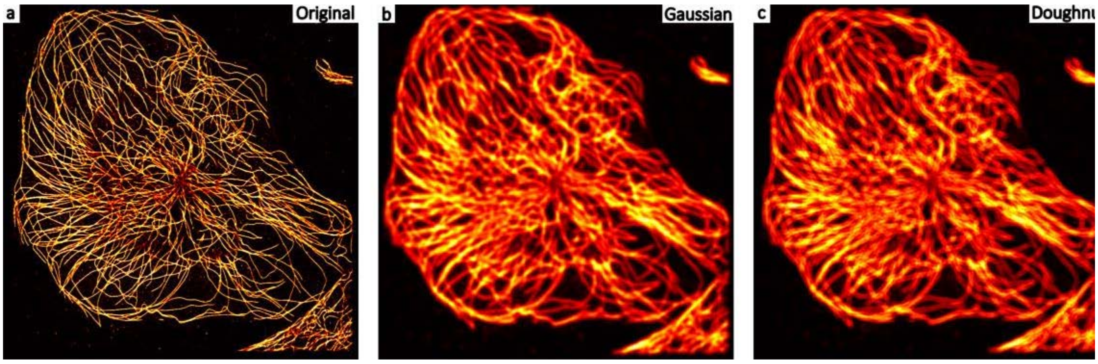

Figure 3-32 | Simulated images of the microtubule network. (**a**) The original image of the microtubule network.[174] (**b**) The convoluted image with the Gaussian PSF. (**c**) The convoluted image with the doughnut PSF.

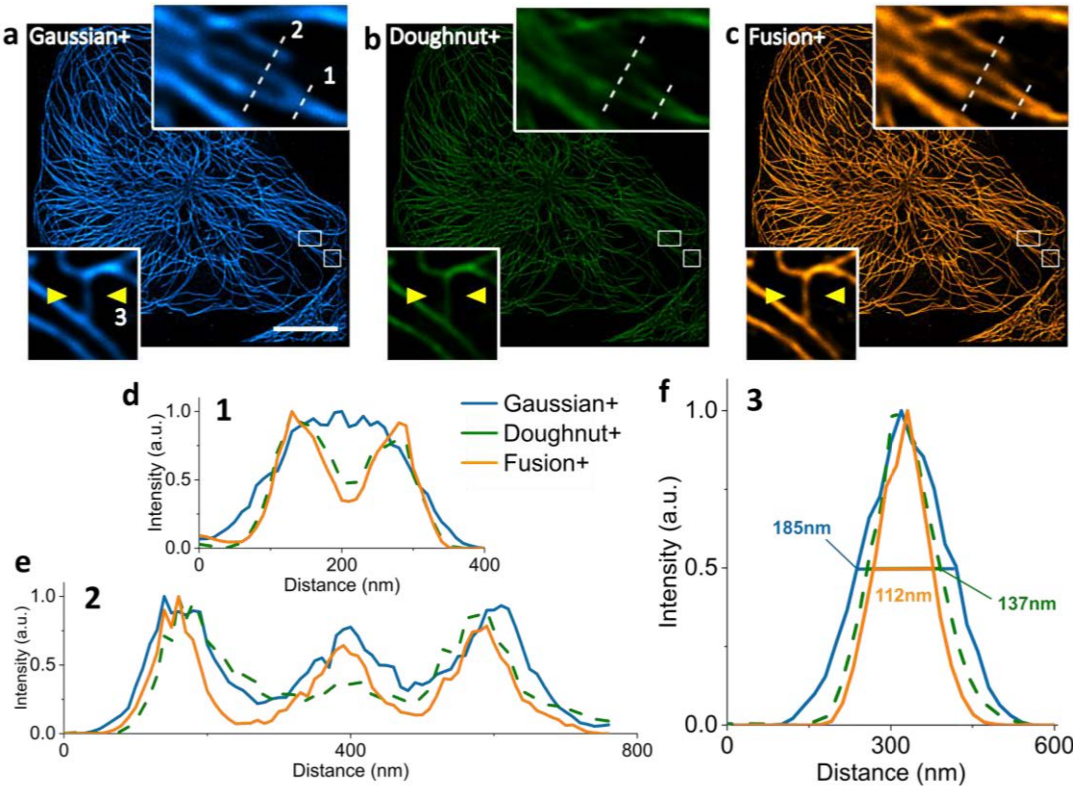

Figure 3-33 | Simulation of Fourier domain heterochromatic fusion imaging of cell microtubules. The deconvoluted results by **(a)** Gaussian, **(b)** Doughnut and **(c)** Fourier domain heterochromatic fusion. Inset of (**a**–**c**) are the magnified region of the microtubule. (**d-f**) Line profiles along the lines marked as 1-3 in (**a-c**). The scale bar is 10 µm.

compared to the Gaussian PSF. For the larger space sample, the Gaussian PSF can distinguish it while doughnut PSF fails (**Figure 3-33e**). Among the three PSF, our fusion method offers the best ability to resolve the samples. With the Fourier fusion algorithm, we are able to enhance the high-frequency information to increase the resolution further (**Figure 3-33f**). These results confirm the super-resolving capacity of multicolour PSF fusion engineering in the Fourier domain.

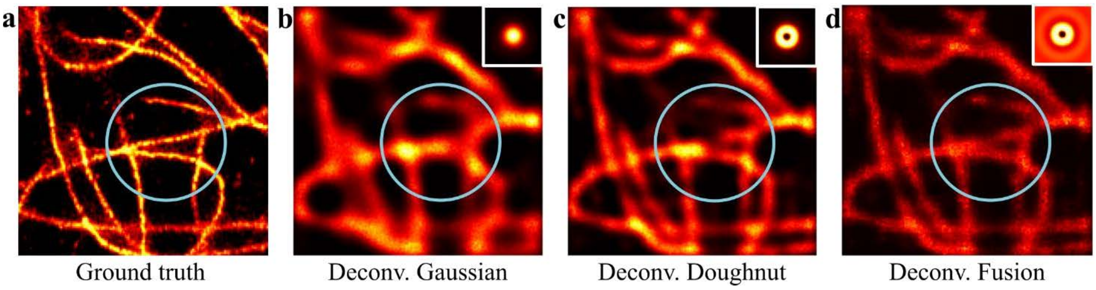

Figure 3-34 | Numerical study from Fourier domain heterochromatic fusion imaging of cell microtubules. (**a**) The ground truth of the simulated microtubules. (**b**) Gaussian-like PSF deconvolution imaging result. (**c**) Doughnut PSF deconvolution imaging result. (**d**) Fourier domain fusion PSF deconvolution imaging result based on (**a**) and (**b**).

3.5.5 Evaluating image resolution

Although several super-resolution microscopies claim they theoretically provide resolution at the nanoscale, the very different factors limit their resolution. From the basic knowledge of the spatial frequency in section 3.2, the image can be converted to the frequency domain by the Fourier transformation, consists of high frequency and low-frequency information. In other words, the quality of the image is not only dependent on the high-frequency information (high resolution in the spatial) but also the low frequency.

The conventional method for evaluating image resolution is measuring the FWHM. However, the FWHM criterion is laborious and often overestimates the effective resolution by selecting line cuts narrowed by background noise. Moreover, this method ignores the importance of information located at the medium and low frequency, which may affect the final quality of the image. Therefore, there is an urgent requirement for a robust and reliable method for measuring the effective resolution directly from the image.

Recently, the FRC analysis has been successfully applied to the super-resolution imaging field, since it is a straightforward, calibration-free, and user-friendly method to estimate the image resolution for the microscopy [26][175][176]. The FRC-based resolution metric shows terrific sensitivity to the image signal-to-noise ratio, as well as to all sample and system dependent factors. The fundamental idea behind FRC is to evaluate the effective cut-off frequency. The estimated effective resolution can be defined as the inverse of the effective cut-off frequency.

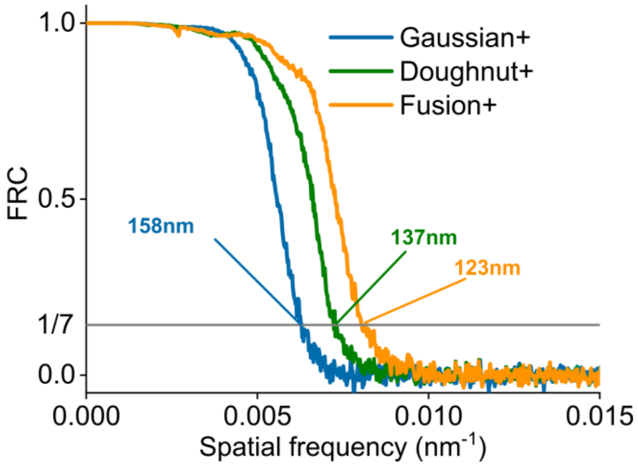

Figure 3-35 | FRC analysis on the imaging quality of Gaussian, doughnut and Fourier fusion PSFs.in Figure 3-33a-c.

To validate the performance of the multicolour PSF engineering approaches, we have evaluated the imaging results by using the same sample found with the FRC method. We

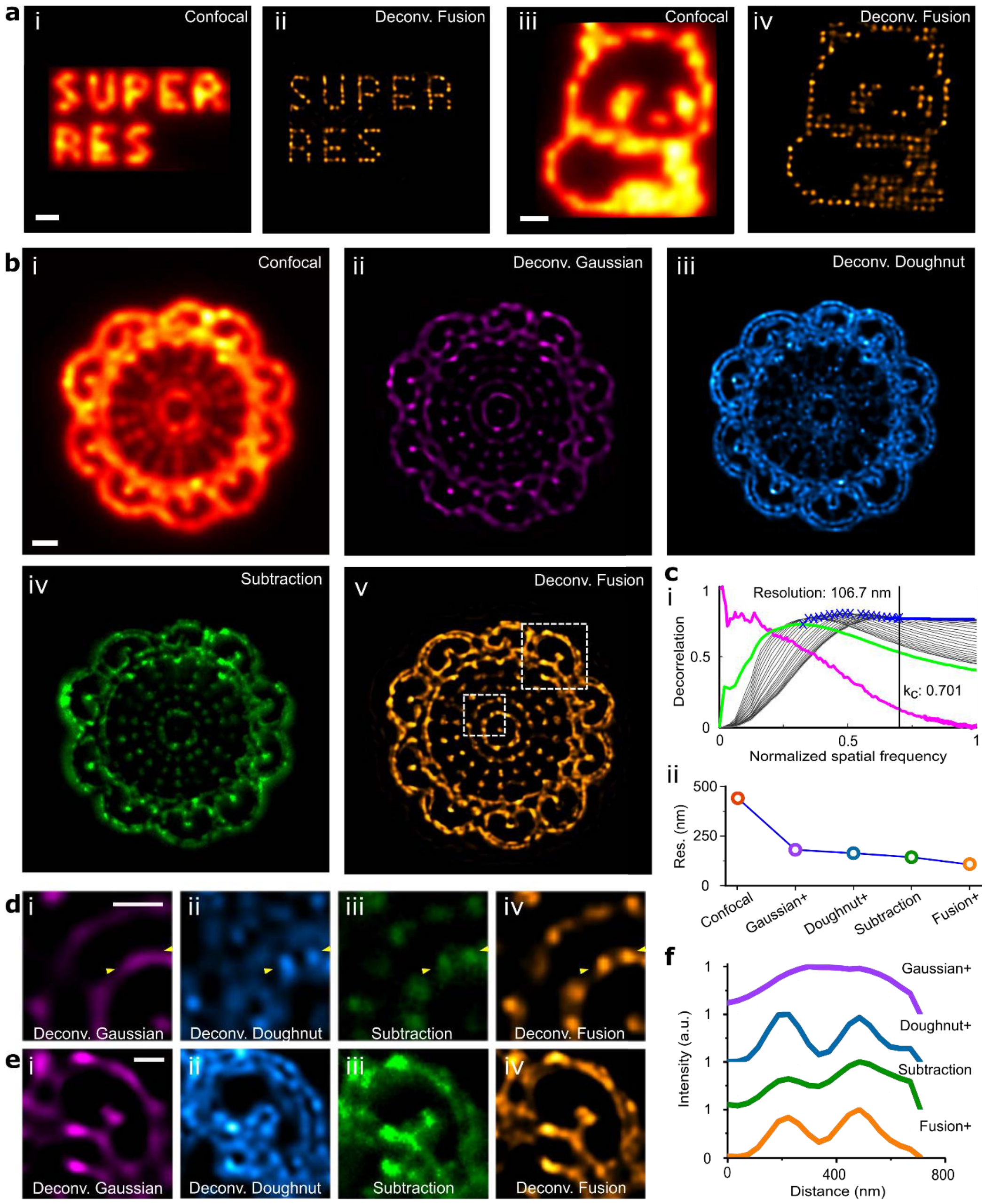

Figure 3-36 | Large-scale super resolution imaging results of the patterned structure using Fourier domain heterochromatic fusion. (**a**) (i & ii) The confocal and the Fourier domain heterochromatic fusion deconvoluted images of the 'super res' text pattern. (iii-iv) The confocal and the Fourier domain heterochromatic fusion deconvoluted images of a panda pattern. (**b**) The image results of a sunflower pattern from five processing methods. (i) Confocal imaging; (ii) Gaussian deconvolution; (iii) Doughnut deconvolution; (iv) Subtraction; (v) Fourier domain heterochromatic fusion deconvolution. (**c**) The image quality evaluation results. (i) The decorrelation analysis for the image in (b-v). The resolution is 2*(pixel size)/k_c, where k_c is expressed in normalised frequencies. (ii) The resolution comparison for the five methods in (b). (**d** & **e**) The magnified regions in (b-v). (**f**) Corresponding cross-line profiles in (d). The patterns were generated by using the electron beam lithography for etching 150 nm holes on a silicon substrate. The iteration number for all the deconvolution process is 70. The scale bars are 1 μm in (a & b), and 500 nm in (d & e).

use the 1/7 fixed threshold to obtain the effective cut-off frequencies. **Figure 3-35** shows that the multi-PSF engineering approach results have achieved a comparable resolution to our previous STED results [79].

Moreover, we apply our method of Fourier domain heterochromatic fusion to resolve UCNPs assembled into the various large-scale patterns. While confocal microscopy (**Figure 3-36a-i & iii**) cannot resolve the fine details with spacing below the diffraction limit (427 nm for 980 nm excitation), our Fourier-domain fusion method has successfully resolved the UCNPs image patterns (**Figure 3-36a-ii & iv**). We further quantify the resolving power of Fourier domain fusion by comparing the image results of a sunflower pattern from confocal imaging (**Figure 3-36b-i**), Gaussian deconvolution (**Figure 3-36b-ii**), doughnut deconvolution (**Figure 3-36b-iii**), subtraction (**Figure 3-36b-iv**) and Fourier domain fusion deconvolution methods (**Figure 3-36b-v**). The Fourier domain fusion approach clearly presents the best image quality. In our experiment, we apply a robust decorrelation analysis [27] to measure the averaged image resolution directly. **Figure 3-36c-i** shows the decorrelation analysis for the Fourier domain fusion deconvolution images (**Figure 3-36b-v**), where the original image is filtered by the high-pass Gaussian filters to emphasise the specific frequency band. These filtered images are conducted with the Pearson cross-correlation (grey curves) to find the most correlated frequencies (blue cross) between each image and its normalised low-pass image. The largest number of the most correlated frequency is the cut-off frequency (k_c), indicating the averaged resolution.

Moreover, **Figure 3-36c-ii** displays the resolutions obtained from the five methods (**Figure 3-37**), with the Fourier domain fusion achieved the best quality in resolution (106.7 nm). Notably, the resolution by decorrelation reports the image quality, and the highest resolution is around the maximum non-zero frequency value of the image in the Fourier domain (see the magenta line). **Figure 3-36d & e** present the detailed features of the two selected areas (**Figure 3-36b-v**) by the five methods. The deconvolution of confocal cannot resolve the features below the diffraction limit. The deconvoluted doughnut image shows many artifacts, due to its inherent drawback of frequency loss. Although the subtraction compensates some artifacts, it shows the missing frequency information, e.g. the middle point cannot be presented in **Figure 3-36d-iii**. According to

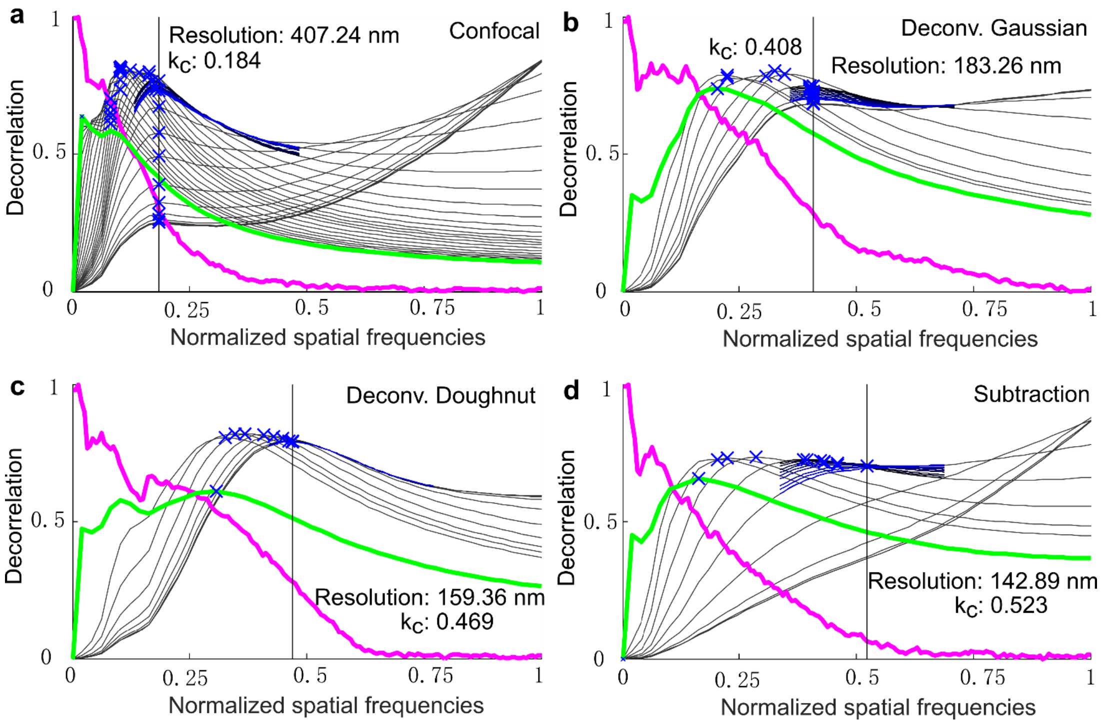

Figure 3-37 | The decorrelation analysis for the image processed by different methods. (a) The result of the confocal image. (**b**) The result of the image by Gaussian deconvolution. (**c**) The result of the image by doughnut deconvolution. (**d**) The result of the image by subtraction. The resolution is 2*(pixel size)/k_c, where k_c is expressed in normalized frequencies.

the cross-line profiles in **Figure 3-36f**, Fourier domain fusion shows the superior power in both resolving the fine features and managing the image artefacts.

3.5.6 **Discussion**

To the best of our knowledge, this is the first work exploring the multi-colour nonlinear responses and Fourier domain fusion for enhancing spatial resolution beyond the diffraction limit. It maximizes the capabilities of Fourier domain OTF fusion of multiple saturated emission PSFs in the spectral regime to improve the entire imaging quality, which can recover the otherwise hidden spatial information during the single beam scanning and confocal detection process. Compared with the temporal domain modulation of excitation modality that requires switching illumination pattern [165] or laser mode [177] with dual excitations procedure, the single scan method is simple, fast and stable. It can avoid the use of the additional optical components and procedures in correcting the sample drifts between multiple sequential recordings. The single-beam scanning mode using a simplified optics setup is compatible with the standard commercial or lab-based laser scanning microscopes; therefore, they may overcome the current

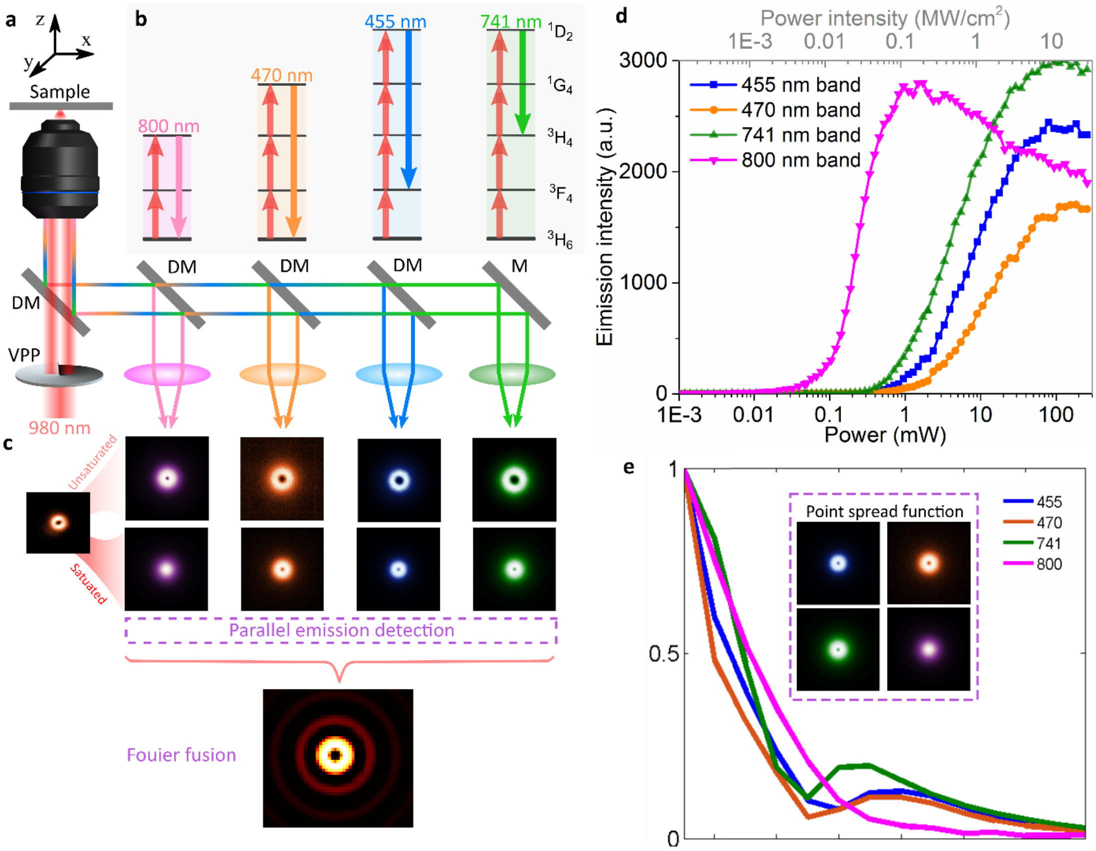

Figure 3-38 | Schematics and optical properties of upconversion nanoparticles for hyper-spectrum Fourier domain heterochromatic fusion in single beam scanning super-resolution microscopy. (**a**) Optical setup for multicolour detection under a single doughnut excitation beam. (**b**) The simplified energy level of UCNPs, 800 nm emission from two-photon level, 470 nm from three-photon level, 455 nm and 741 nm from four-photon level. (**c**) Different emission PSFs can be acquired from four distinct upconversion emission bands. The pattern can be modified by changing excitation power. The four-emission pattern can be applied to the Fourier fusion method. (**d**) The power dependence curve of the upconversion emissions from the four emission bands. (**e**) The optical transfer functions of the four emissions PSFs.

bottleneck issue associated with the system's complexity and stability. This imaging modality is compatible with point-scanning-based methods such as imaging scanning microscopy (ISM) [152] or Rescan [178], which may also help to mitigate the frequency deficiency issues. To remove the additional camera, we can further develop this technique to modulate chromatic aberrations by using multicolour phase mask [159].

Figure 3-38 shows our method can be potentially extended for simultaneous acquisition of high-quality images from hyper-spectrum bands. Judging by the emission spectrum, at least four emission bands from different energy levels can emit nonlinear power-dependent upconversion emissions (**Figure 3-38b**). In the multiple energy level system, each transition between two energy levels may result in a robust nonlinear emission and power-dependent responses (**Figure 3-38d**). By taking advantage of these nonlinear differential responses in the hyper-spectrum domain, a series of emission PSFs can be obtained through the parallel multi-colour detection channels (**Figure 3-38c**). By fusing the multi-frequency components in the Fourier domain (**Figure 3-38e**), the final image quality can be further enhanced. Similar to the algorithm we developed in the two-colour spectrum frequency fusion, the procedure is given by:

$$I_{eff} = I_{800} \times mask_{800} + I_{740} \times mask_{740} \times r_1 + I_{470} \times mask_{470} \times r_2 + I_{455} \times mask_{455} \times r_3 \qquad (3\text{-}34)$$

where I_{800}, I_{740}, I_{470}, I_{455} are the images obtained from each corresponding PSF, respectively. The $mask_{800}$, $mask_{740}$, $mask_{470}$ and $mask_{455}$ are circular/ring Fourier frequency filters, respectively. The r_1, r_2 and r_3 are the variables that modify the value ratio of the fused components towards the optimal fused system OTF.

Unfortunately, I was not able to finish the cellular immunofluorescence using UCNPs due to the outbreak of COVID-19. As a consequence, there is not enough available data for the Fourier fusion method to demonstrate its power in creating an enhanced image quality in a real biological environment.

3.6 Conclusion

In summary, this work reports a single-doughnut beam scanning microscopy for super-resolution imaging. The design principle is to encode high-frequency spatial information into the multiple colour bands and decode them by extracting the maximum coverage of Fourier components of the saturated multi-colour emission PSFs. This approach, based on Fourier domain heterochromatic fusion, opens a new perspective to perform super-resolution with minimum distortion and information loss, as it maximizes the coverage of all the spatial frequency details. This strategy has great potential in improving the resolution and artificial noise controlling for PSF engineering-based super-resolution nanoscopy, e.g. STED microscopy [179][180], GSD microscopy [123], SIM [151] and lattice light sheet (LLS) microscopy [181][182][183]. Although UCNPs meet our requirement and have been successfully used in our Fourier domain heterochromatic fusion microscopy, this work calls for new developments of other nonlinear optical responsive probes with multi-colour emitting properties. The combination of the existing fluorescent probes includes both molecular format of organic dyes [184][185] and the inorganic nanoparticles [186][187], where preferably, the emission at each band should be highly dependent on the excitation power and their nonlinear optical response to excitation saturation. I anticipate this work triggers a new conceptualization for optical or material studies to investigate methods and probes for a new generation of imaging modalities.

Chapter 4 Distinct nonlinear optical response encoded single nanoparticle for multiplexed detection

UCNPs are increasingly used as luminescent candidates in multiplexing applications due to their excellent optical properties. In the past, several encoding identities have been proposed for UCNPs, including emission colour, luminescence lifetime, intensity ratio between different emission bands, and spatial colour distribution. In this work, we develop a new optical encoding dimension for upconversion nanoparticles by exploring the nonlinear photo-response properties. A set of distinct nonlinear photo-responses in the same components with different concentrations are achieved in which tens of unique codes can potentially be generated in the same colour channel. Furthermore, we present a robust strategy to code and decode emitter properties by applying PSF engineering for imaging classification. We utilize a doughnut-shaped excitation beam to carry out the distinct nonlinear optical responses information on an emission signal detector, result in further improved the power-dependence differentiation between UCNPs, including simultaneously identifying varied species in a single colour image. Our work dramatically extends the multiplexing capacity of UCNPs and offers new opportunities for their applications in a wide range such as microarray assays, bioimaging, anti-counterfeiting, deep tissue multiplexing detection and high-density data storage.

4.1 Background

The optical multiplexing detection has attracted considerable attention, as it enables high data-storage capacity, simultaneous identification of multiple targeted chemicals and biomolecules, improved encryption, enormous amounts of the required information to be analyzed [188]. Apart from this, multiplexed detection cannot only save sample volume but also reduces assay time and cost [102]. Therefore, the development of advanced multiplexed detection has become highly prized.

In optical multiplexing techniques, the encoding dimensions play a critical role by presenting the multiplexed coding ability. Many optical encoding dimensions have been developed, including colours [189], intensities [190], polarization [191], lifetimes [192][193] and angular momentum [194]. It is worth noting that these dimensions cannot only be adopted individually for multiplexed imaging but can also be used as a combination [188]. This combination would offer a much larger encoding capacity than only using one dimension. As a consequence, it has always attracted significant interest in devising new encoding dimensions to meet the increasing requirements of various applications.

Generally, we perform optical multiplexing detection by using fluorescent dyes and luminescent nanoparticles. For the most frequently used probes, the main challenges for the organic dyes are photobleaching and emission spectral overlapping. QDots offer significant advantages over organic dyes because of their excellent photostability and excitability by a single wavelength. However, the shortcoming is their short excitation-wavelength is toxicity to the biological samples, as well as leading to relatively strong background fluorescence. UCNPs have been used as an alternative luminescent probe in multiplexing applications due to their excellent optical properties. In the past, several works have proposed new encoding methods by employing UCNPs, including emission colours, intensities, and lifetimes [188]. However, these are standard dimensions for multiplexing detection. With the superior optical properties of UCNPs, it should have large capacities in multiplexing that we have not fully explored.

In this work, we propose a new multiplexing concept for UCNPs by exploring the nonlinear optical response properties to create an optical encoding dimension. We demonstrate that the same ion-doped nanoparticles have the distinct and uniform nonlinear response curves once we normalize them. With this feature, we can generate a unique coding in the same colour channel by designing different doped concentrations. Furthermore, we develop a robust strategy to carry out the emission response properties by applying PSF engineering for imaging classification. Due to the distinct emission response curves, their emission PSFs are vastly different. For the image analyzing, there are several parameters, like the inner diameter, outer diameter, the ratio between them, as well as the centre depth. All of the parameters help to classify different particles. Our work dramatically extends the multiplexing capacity of UCNPs and offers new opportunities for their applications in a wide range such as microarray assays, bioimaging, anti-counterfeiting, deep tissue multiplexing detection and high-density data storage.

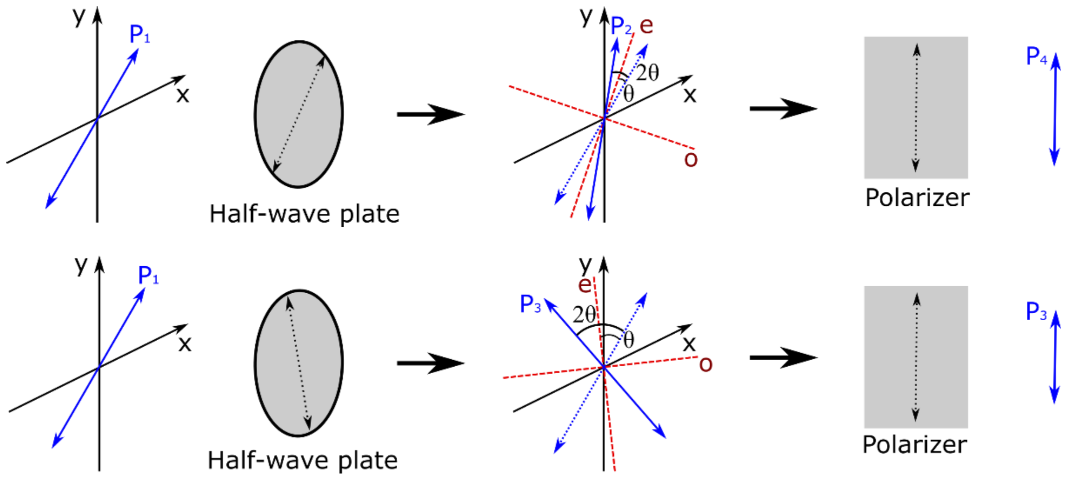

Figure 4-1 | The working principle by employing polarization to control the excitation power change. P1 is the original polarized beam. P2 and P3 are the changed polarization direction by using a half-wave plate. O axis means the original line, e axis means the extraordinary line which has a fast phase of π.

4.2 The principle of PSF engineering for imaging recognition

4.2.1 Adjusting the excitation power by polarization

For obtaining the optical emission response curve against the excitation power, we typically need to collect several emission intensities points by changing the excitation power. As introduced in the similar setup in **Figure 2-9**, we employ the polarization to electronically and precisely control the power over an extensive range.

In the case of polarized light (**Figure 4-1**), we chose the half-wave plate that has the phase difference between o-light and e-light. Although the light from the crystal plate is still plane-polarized, the vibration plane of the outgoing light rotates by 2θ angle concerning the vibration plane of the incoming light, which is the angle between the vibration plane of the incoming light and the optical axis on the crystal surface. When the polarized light passes through the half-wave plate, the outgoing light is still plane-polarized, but the vibration surface of the polarized light rotates at the certain angle 2θ, and the rotation angle only depends on the angle θ between the vibration plane of the incident light and the optical axis of the crystal. Therefore, we can adjust the output laser power by rotating the half-wave plate correspondingly. With the help of a Neutral Density (ND) filter with a suitable attenuation ratio, we can expand the power to a broad range.

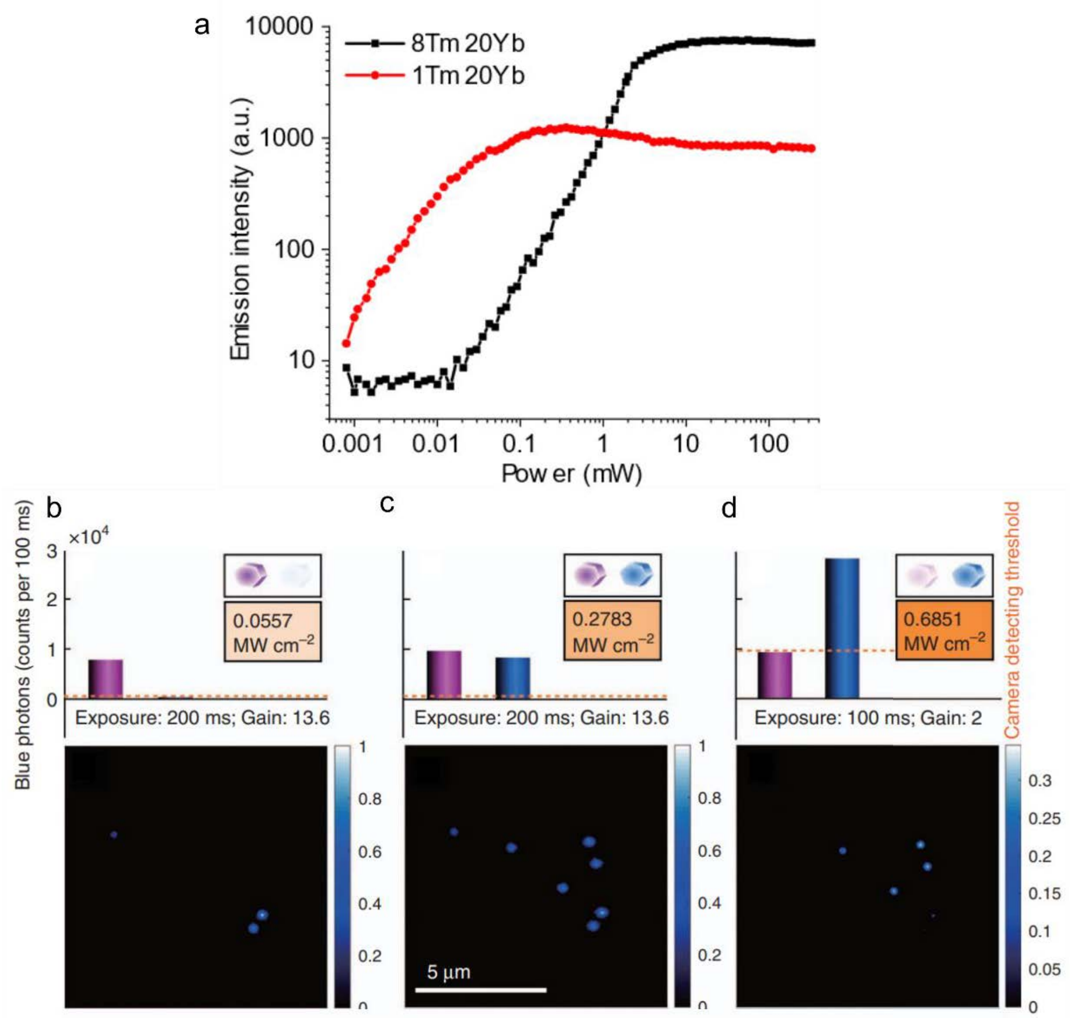

Figure 4-2 | Multiplexed detection strategy for imaging two types of UCNPs at the same emission colour band. (**a**) The optical nonlinear response curves of two different concentration doped UCNPs (1% Tm and 8% Tm). (**b**) Emission intensity and imaging under a low excitaton power. (**c**) Emission intensity and imaging under a medium excitaton power. (**d**) Emission intensity and imaging under a high excitaton power. [99]

4.2.2 Nonlinear response in UCNPs

As introduced in the previous chapters, the optical nonlinear response in UCNPs means the emission intensity is not linear to the excitation power and will be saturated when the power keeps increasing. In reality, the nonlinear response property has been applied for single nanoparticle detection [99]. As shown in **Figure 4-2a**, the two different doped particles have different response curves. The low doped UCNPs have the first take-off threshold while the high doped ones exude a stronger saturation intensity. When under a low excitation power, only the low doped particles have the emission since the high doped have not reached the threshold (**Figure 4-2b**). When applying the power to the cross-

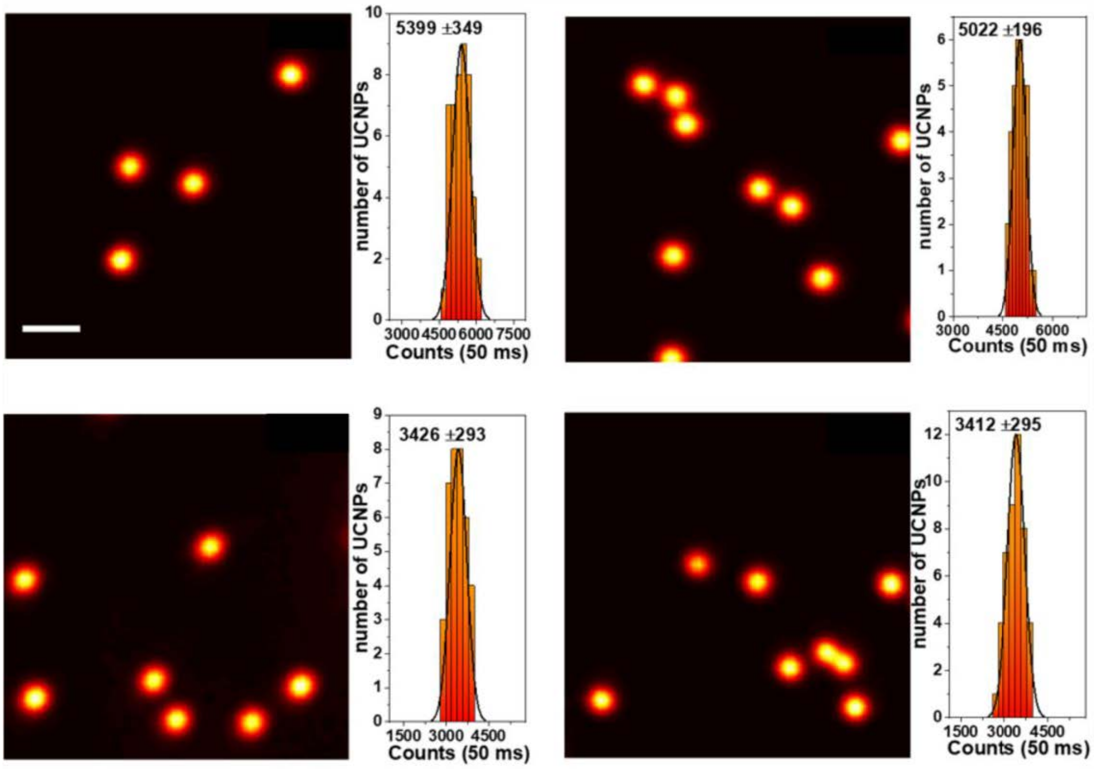

Figure 4-3 | Confocal microscopy images and statistical intensities of UCNPs. Confocal microscopy quantitative measurement of the whole spectrum luminescence emission of UCNPs under 808 nm excitation at the power density of 5.5×10^6 W/cm^2. Scale bar: 1 mm.

point, all the emissions have the same intensity (**Figure 4-2c**). By increasing the power, we can only see the high doped particles because of the intensity ratio (**Figure 4-2d**). Then we can separate the two kinds of particles from each other at the same emission colour band without any assistance of filters.

However, the emission intensity of the same doped particles exhibits a significant fluctuation, one that limits this in multiplexing applications. **Figure 4-3** demonstrates that

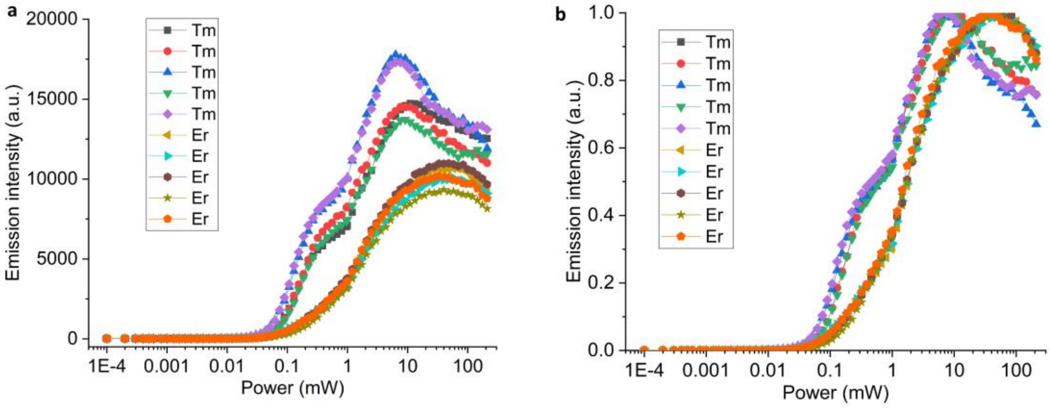

Figure 4-4 | The emission response curves of Tm and Er doped UCNPs. (**a**) The conventional response curves from Tm^{3+} and Er^{3+} doped UCNPs. (**b**) The normalized response curves.

the intensities of the single nanoparticles have an 8% error, although it seems uniform with the confocal images. The same doped UCNPs have different emission response curves (**Figure 4-4a**). However, we find the same doped particles have uniform and distinct nonlinear response curves if we normalize them (**Figure 4-4b**). Thus, we can develop a new optical encoding dimension for multiplexed imaging by exploring the whole response curves instead of the featured points.

4.2.3 **PSF engineering encoding the nonlinear response curves**

Generally, it is easy to classify two types of probes by using the standard Gaussian PSF for imaging chromatically well-separated emitters, e.g. splitting the imaging channels with filters or a dichroic mirror. However, it should encounter more challenges to simultaneously classify more types of emitters by splitting the imaging channels multiple times. With the distinct optical nonlinear response curves, our initial approach shows significantly reduced effectiveness without the requirement of the filters. We can identify

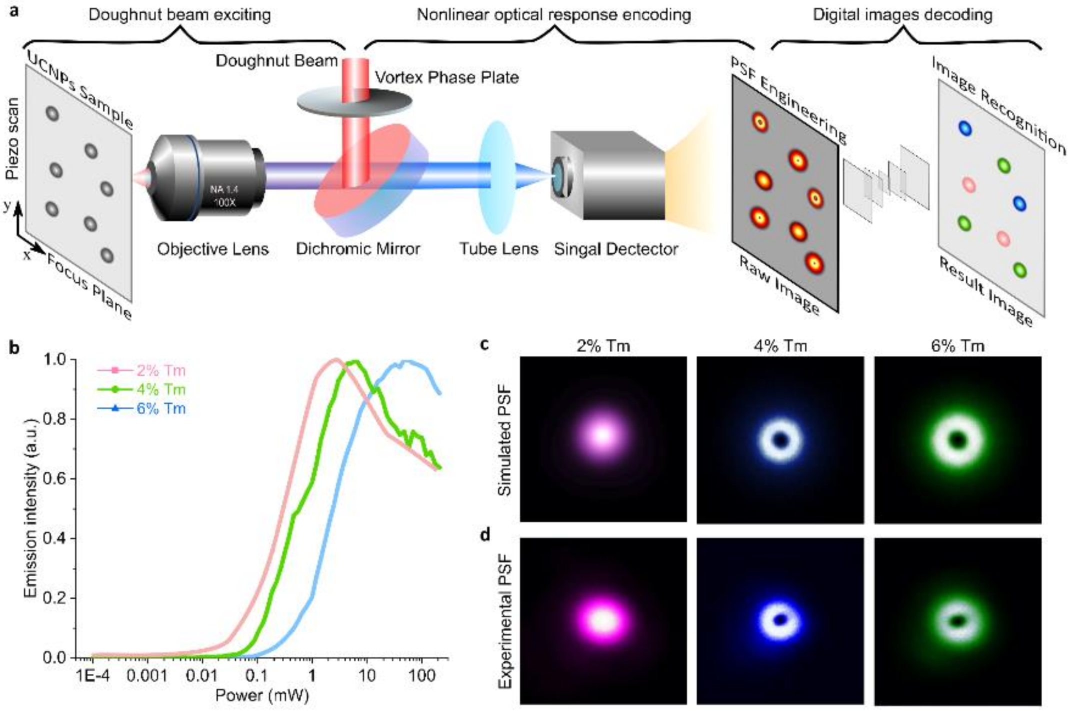

Figure 4-5 | The concept of PSF engineering encoding the nonlinear response curves for nanoparticles recognition. (**a**) The three parts for the PSF engineering recognition. We can use a doughnut beam to scan the particles, encoding the curves into the emission patterns. Finally, we can identify the nanoparticles by analyzing the emission patterns. (**b**) The normalized response curves from three different doped UCNPs: 2% Tm, 4% Tm and 6% Tm. (**c**) The simulated PSF by using a doughnut beam to carry out the response curves in (**b**). (**d**) The corresponding PSF from the experimental results.

the types of nanoparticles by recognizing the power-dependent curves instead of the conventional properties, like colour, intensity and lifetime.

However, it is time-consuming and not reliable if we measure the emission response curves one by one. From the previous chapters, we know that PSF engineering is one of the super-resolution imaging approaches to encode emitter properties in the shape of the PSF. To be specific, different response curves have different PSFs under the same excitation power (**Figure 4-5b**). So we develop a robust method by using a doughnut beam to scan the particles, encoding the curves into the emission patterns (**Figure 4-5c**).

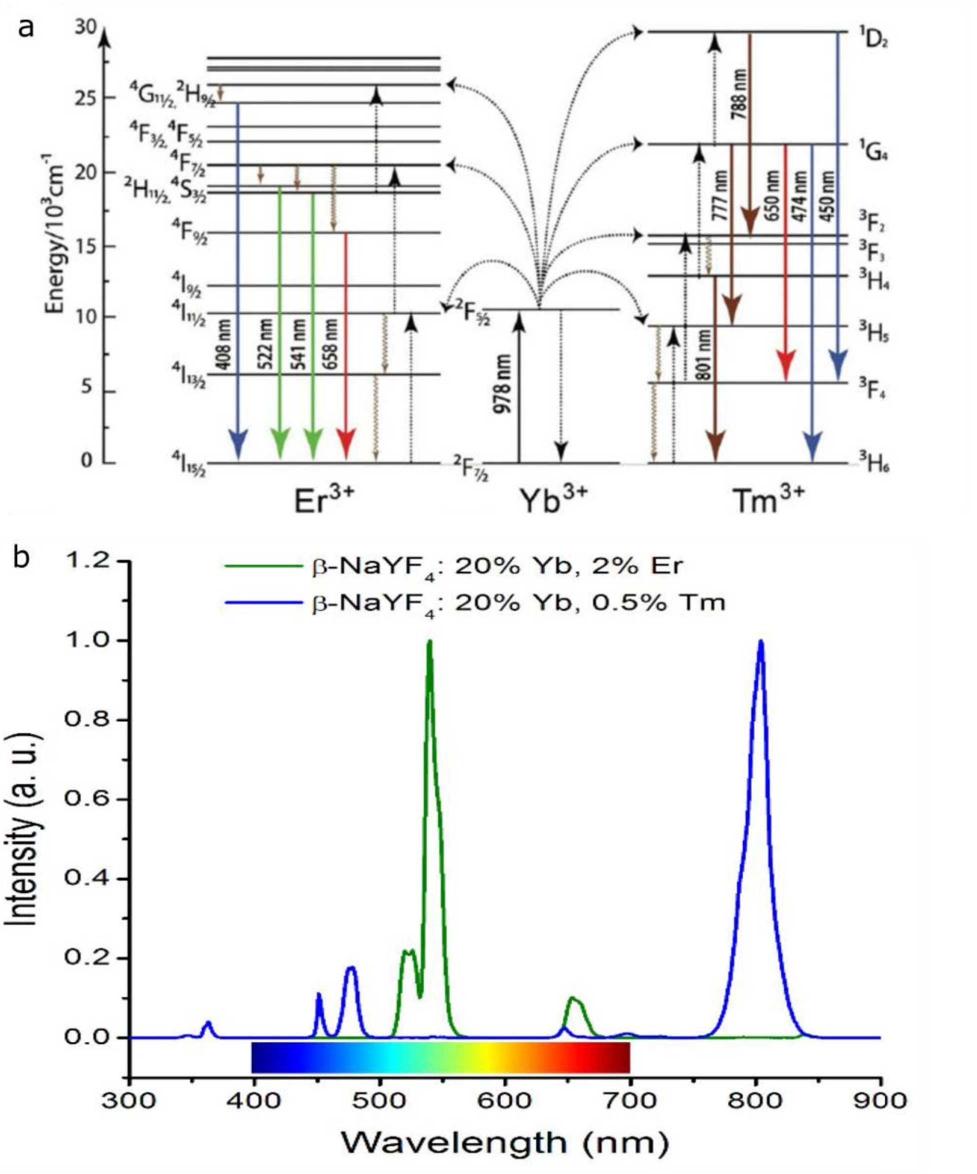

Figure 4-6 | The emission features of Tm^{3+} and Er^{3+} doped UCNPs. (**a**) The energy levels of the Tm^{3+} and Er^{3+} doped UCNPs. (**b**) The emission spectrum of the Tm^{3+} and Er^{3+} doped UCNPs, where Tm^{3+} doped UCNPs have the 800 nm and Er^{3+} doped UCNPs have the 550 nm emission. [42]

To engineer an optimized PSF for identifying the single nanoparticles by pattern recognition, we design a working flow composed of three parts (**Figure 4-5a**). The first portion is doughnut beam scanning, which generates the nonlinear response data of point sources. These signals are collected with a single-photon detector to generate the outputs as the pattern classifications for detected emitters in the image. Finally, we can identify the nanoparticles by analyzing the emission patterns.

4.3 Results and discussion

4.3.1 Verifying the PSF engineering by filters

To verify that we could discriminate between two types of UCNPs with the proposed PSF engineering method on a single photon detector, we prepare a mixed sample containing Tm^{3+} and Er^{3+} doped UCNPs. From the energy levels and emission spectrum (**Figure 4-6**), the mixed two samples featured emission peaks at 800 nm and 550 nm, respectively.

Figure 4-7a shows the confocal imaging of the two mixed UCNPs at grayscales. We can find it is hard to separate these particles if the two particles have the same emission

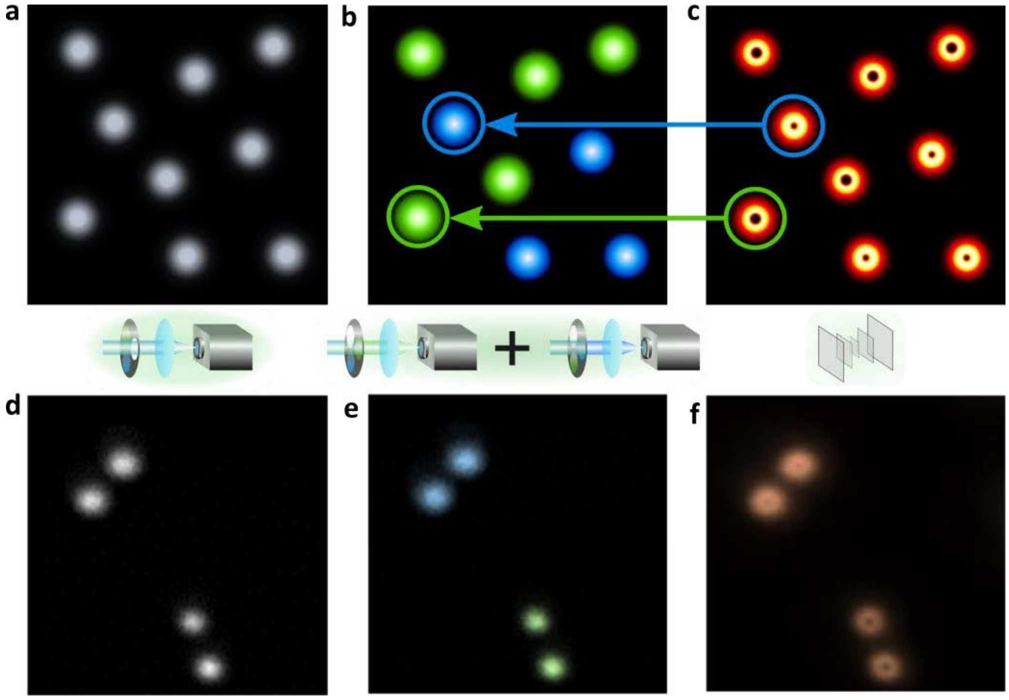

Figure 4-7 | Verifying the PSF engineering to classify the single nanoparticles by filters. (**a**) The grayscale confocal imaging of the mixed UCNPs. (**b**) Identifying the two types of UCNPs with colour filters. (**c**) PSF engineering to recognize the UCNPs. (**d**-**f**) The corresponding experimental results in (**a**-**c**).

intensity. However, it is easy to recognize them with the help of colour filters (**Figure 4-7b**). The image has a spectral 550 nm bandpass filter so that only the Er^{3+} doped UCNPs are visible (green channel); then, with another 800 nm bandpass filter so that only the Tm^{3+} doped UCNPs can be recognized (blue channel). With a doughnut-shaped beam to scan the same area, we can see the shapes of the different colours emitters are slightly different (**Figure 4-7c**). Moreover, the PSF of the Tm^{3+} doped UCNPs has a smaller hole at the central region compared to the Er^{3+} doped ones. Their optical nonlinear response curves can explain the difference in the size of the hole. The Tm^{3+} doped UCNPs have a fast take-off threshold and can research the saturation early. Thus, we can rapidly classify the different types of UCNPs by analyzing their emission patterns, which have encoded their optical response curves properties. Furthermore, **Figure 4-7d – f** demonstrates the experimental results to verify the stability of our proposed PSF engineering method for single nanoparticle identification.

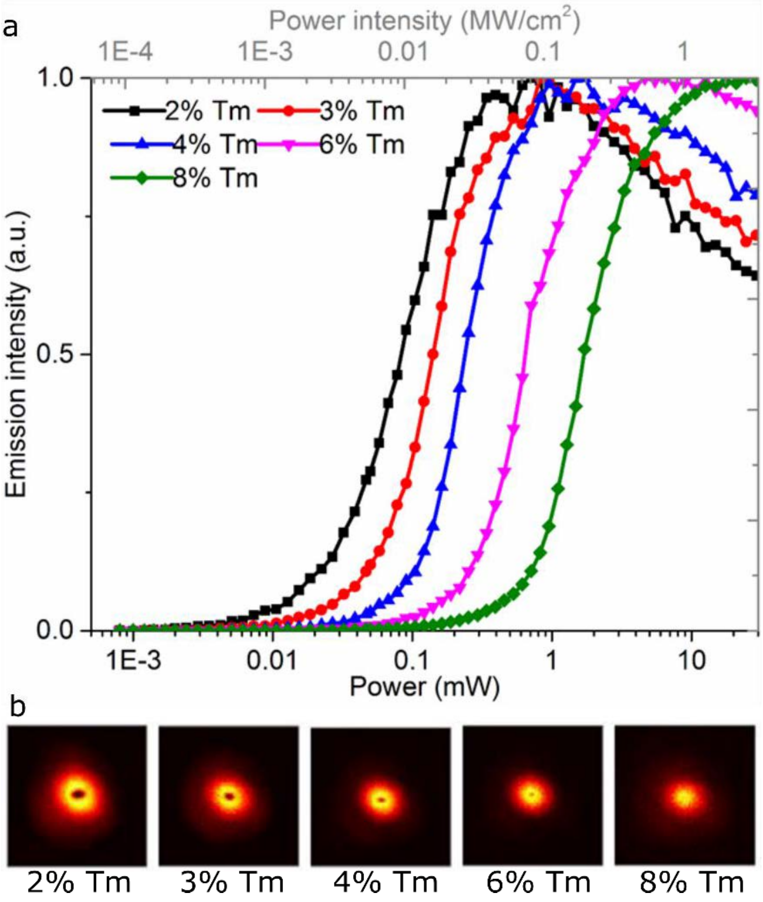

Figure 4-8 | Classifying multiple UCNPs at the same intensity with the same colour. (**a**) The optical nonlinear response curves from different concentration Tm doped UNCPs: 2% to 8%. (**b**) The corresponding PSF by using a doughnut-shaped excitation beam to carry out the response curves.

4.3.2 Classifying multiple UCNPs at the same intensity with the same colour

Then, we can extend this PSF engineering classification method for the UCNPs with the same intensity at the same colour emission. **Figure 4-8a** shows that different Tm doped UCNPs have the distinct emission response curves, even when they only have a 1% percentage difference in the Tm doping. With a doughnut-shaped excitation beam to scan though the single nanoparticles, we find that the shape and central features are slightly different in the corresponding emission PSFs. As a consequence, it is possible to robustly classify the different UCNPs at the same intensity with the same emission colour by using the PSF engineering approach.

4.3.3 Multiplexing detection of the biomarkers

We have demonstrated that we can use the nonlinear response properties of the UCNPs to be a new dimension for the multiplexing imaging. We further combine this proposed PSF engineering method with colour filters for simultaneous biomarker multiplexing detection. According to section 3.4.2.2, we can design and functionalize the several kinds of UCNPs to simultaneously detect the specific species of pathogenetic DNA sequences, which is superior to conventional suspension array assays based on microspheres (**Figure 4-9**). The sample can be divided into three schemes with colour filters and continue to be distinguished with the emission patterns.

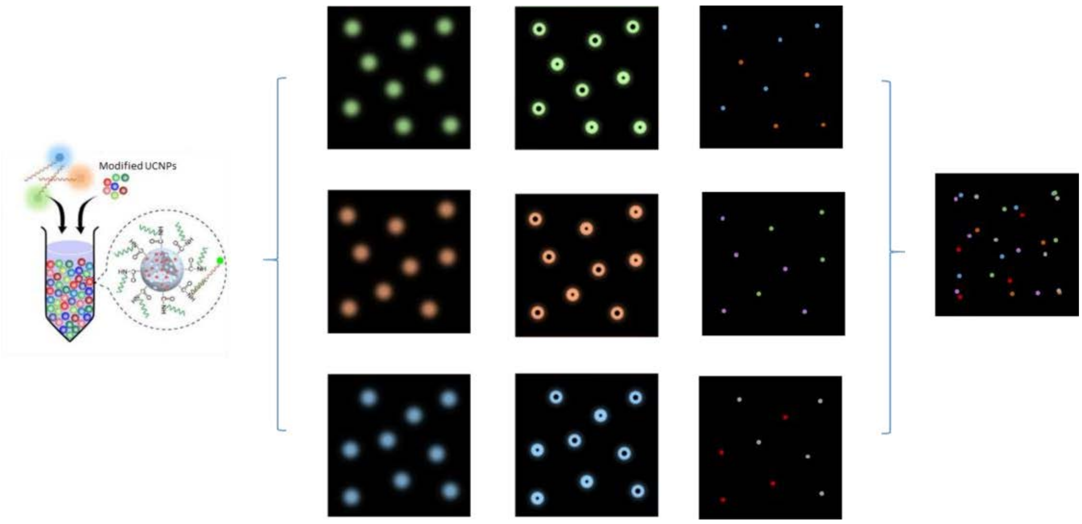

Figure 4-9 | Multiplexing detection of the biomarkers. The sample can be divided into three schemes with colour filters and continue to be recognized with the emission patterns. Finally, we are able to detect multiplexing. [192]

4.3.4 **Discussion**

For the image analyzing, there are several parameters, like the inner diameter, outer diameter, the ratio between them, as well as the centre depth (**Figure 4-10**). All of the parameters help to classify different particles. To increase the identification efficiency, we can induce machine learning for the pattern recognition. Several research works have indicated that machine learning has great potential as a powerful tool in microscopy, posited to replace existing algorithmic approaches. This approach resolves a key challenge in PSF engineering method by recognizing the slight difference among the emission patterns.

For optimizing discrimination between emitters, the PSF engineering method can be applied with net training to maximize the strengths of the reconstruction net. In current consideration, we only focus on single colour emission bands. However, one single UCNPs have multiple emission colours. The PSF engineering method can detect the emission response curves from different emission bands with an additional detector. What a pity is that we have not finished the biomarker multiplexed detection by using UCNPs due to the outbreak of COVID-19.

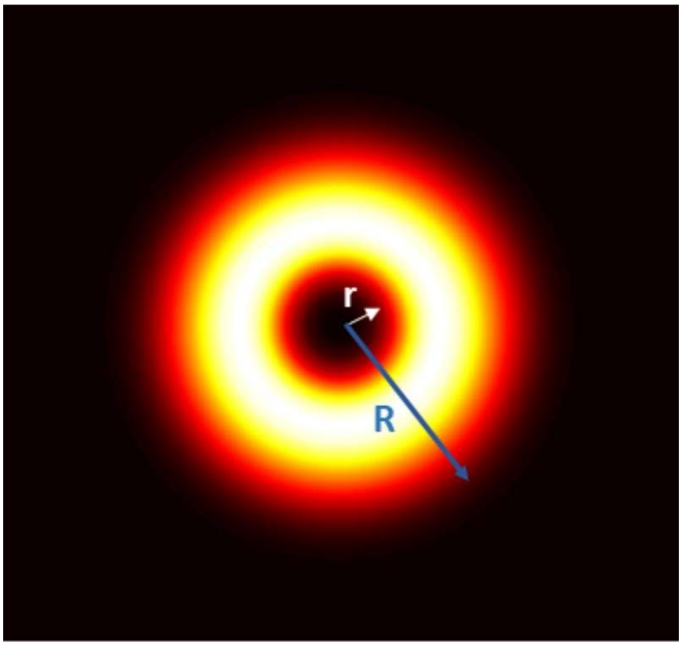

Figure 4-10 | The parameters in the emission pattern help to classify different particles accurately. R is the outer diameter of the PSF, r is the inner diameter of the centre hole. We can also use the ratio between the outer and inner diameters, as well as the centre depth (the ratio of the intensity at centre dip compared to the highest inteisty).

4.4 Conclusion

This work reports that the nonlinear photo-response curve of UCNPs is distinctive and uniform can be a new dimension for multiplexing detection. Furthermore, I present a robust strategy to code and decode emitter properties by applying PSF engineering for imaging classification. This work utilizes a doughnut-shaped excitation beam to carry out the distinct nonlinear optical response information on an emission signal detector. In turn, this results in further improving the power-dependence differentiation between UCNPs, including simultaneously identifying varied species in a single colour image. This work develops a strategy for distinguishing multiple types of UCNPs at the same emission colour band with the same intensity. This work can combine with machine learning for analysis of emission patterns. Extended here is the multiplexing capacity of UCNPs and it is one that offers new opportunities about how they can be applied.

Chapter 5 Conclusion and Future work

In this thesis, the focus has been on developing new methods to improve the performance of super-resolution microscopes. With the multiphoton nonlinear emissions of UCNPs, this thesis made several concrete advances in terms of super-resolution image depth, speed, overall quality and multiplexing. For unlocking a new mode of deep tissue super-resolution imaging, this thesis first developed the NIRES nanoscopy by taking advantage of NIR-in and NIR-out optical nonlinear response curve from the single nanoparticle. With the heterochromatic optical nonlinear response curves in a single UCNPs, this project developed a multicolour Fourier fusion algorithm to achieve the maximum spatial frequency information, yielding the overall enhanced image quality and increasing imaging speed. By realizing the uniform and distinct nonlinear emission curves from different nanoparticles, this work pointed out a new optical encoding dimension for the multiplexing imaging. This thesis had investigated and opened up some new exciting research areas. Moreover, this chapter delivers a brief discussion of the potential research topics for future works.

5.1 Conclusion

This work created the first NIR nanoscopy for deep tissue super-resolution imaging by using UCNPs. It demonstrated a multi-photon fluorescence saturation microscopy for super-resolution imaging to circumvent the specific requirement of probes in STED-like modalities. With a simple setup, this work designed NIRES microscopy to achieve the same level resolutions which were comparable to our recently reported low excitation power STED. It offered a great deal of simplicity and stability, as an advanced tool to achieve super-resolution in deep tissue, superior to the conventional MPM approaches. In contrast with conventional methods by increasing the excitation power to achieve the super-resolution, this work was the first work showing the optical resolution of UCNP nanoscopy can be modified by varying its material properties. This work emphasized the fluorescent rising slope and threshold enabled us to improve the resolution through the synthesis of probes. To achieve super-resolution imaging using low laser power and a longer wavelength, i.e. to reduce phototoxicity applied to live cells, controlled synthesis of UCNPs will further optimize the energy transfer process and resultant saturation intensity properties for bio-photonics. This makes it possible to surpass the diffraction limit.

This thesis also explored a concept that using the diverse emission responses in fluorophores will increase image resolution and imaging speed for super-resolution nanoscopy with PSF engineering. It is shown here that the different nonlinear response on different emission colour of fluorophores could simultaneously generate multiple PSFs will increase the imaging resolution through a Fourier domain heterochromatic fusion process. The work contained a theoretical simulation and a systematic experimental measurement to reveal and validate the concept, achieving sub-50 nm resolution (1/20th of the excitation wavelength). This strategy has great potential in improving the resolution, and artificial noise controlling for PSF engineering-based super-resolution nanoscopy. It marked the first time that the nonlinear process in a lanthanide-doped nanoparticle is demonstrated as able to generate multiple PSF simultaneously. It further confirmed that samples' spatial frequency information could be encoded into the PSF and decoded by using Fourier domain fusion. Moreover, this work revealed that a single beam mono scanning could achieve the FED microscopy and Fourier fusion nanoscopy with our strategy, which increases the typical imaging speed.

Furthermore, this work reported that the optical nonlinear response curve of UCNPs was uniform and this characteristic means that it can serve as a new dimension for multiplexing detection. It presented a robust strategy to code and decode emitter properties by applying PSF engineering for imaging classification. This work utilized a doughnut-shaped excitation beam to carry out the distinct nonlinear optical responses information on an emission signal detector, resulting in simultaneously identifying varied species in a single colour image. It developed a strategy for distinguishing multiple types of UCNPs at the same emission colour band with the same intensity.

5.2 Future work

The next step with the super-resolution microscopy modalities presented in this thesis would be to apply them to inspect biological samples. For future analyses, two key directions are briefly discussed here: doughnut beam with rare-earth nanocrystals and other fluorescent materials. I expect that all of the directions can further enhance the performance of the developed super-resolution imaging systems.

5.2.1 Doughnut beam with rare-earth nanocrystals

5.2.1.1 NIRES for down-shifting nanomaterials for NIR II imaging

According to the principal of NIRES, the nonlinear response curve will affect the performance of the microscopy. In Chapter 2, I employ the emission saturation curve of the two-photon state $^3H_4$ (800 nm) of the $NaYbF_4$: 4% Tm^{3+}, 20% Yb^{3+} for easily converting 980 nm photons. It shows the early onset of upconversion emissions at low excitation power density and sharp rising-up slope, reflecting its nonlinear energy transfer assisted photon upconversion process. The early take-off threshold and small saturation point can help reduce the requirement of the excitation power to achieve a high resolution in deep tissues. From the material design, one possibly future study is to continue investigating rare-earth nanocrystals with the doughnut beam, but using the like down-shifting materials for imaging with the longer emission wavelength. It has reported that cerium doping (Er/Ce co-doped $NaYbF_4$ nanoparticle core with an inert $NaYF_4$ shell) can suppress the upconversion pathway while boosting down-shifting emission intensity by ~9-fold to produce bright 1550 nm luminescence under 980 nm excitation [139]. One of the advantages of using this material is the longer wavelength allows deeper penetration. Moreover, the down-shifting emission here follows the single-photon emission process, which means the emission curve has an earlier threshold and can reach saturation easier. So, we can design several down-shifting imaging nanoparticles with emission bands located at the longer wavelength region to further enhance the NIRES microscopy.

5.2.1.2 Mirror enhanced NIRES

We also can reduce the excitation power by employing a mirror substrate [195] in NIRES microscopy. It has reported the interference of the local electromagnetic field confined the confocal PSF to a 110 nm spot axially, which enables axial super-resolution with all laser-scanning microscopes. With the assistance of the mirror, we can further optimize the nonlinear optical response curve due to self-interference. **Figure 5-1** shows that the threshold and saturation power can be left shifted when using a silver mirror surface with a 138.4 nm silica layer as a spacer. As a consequence, we can obtain a higher resolution even with the same excitation power. The inset in **Figure 5-1** indicates the resolution can

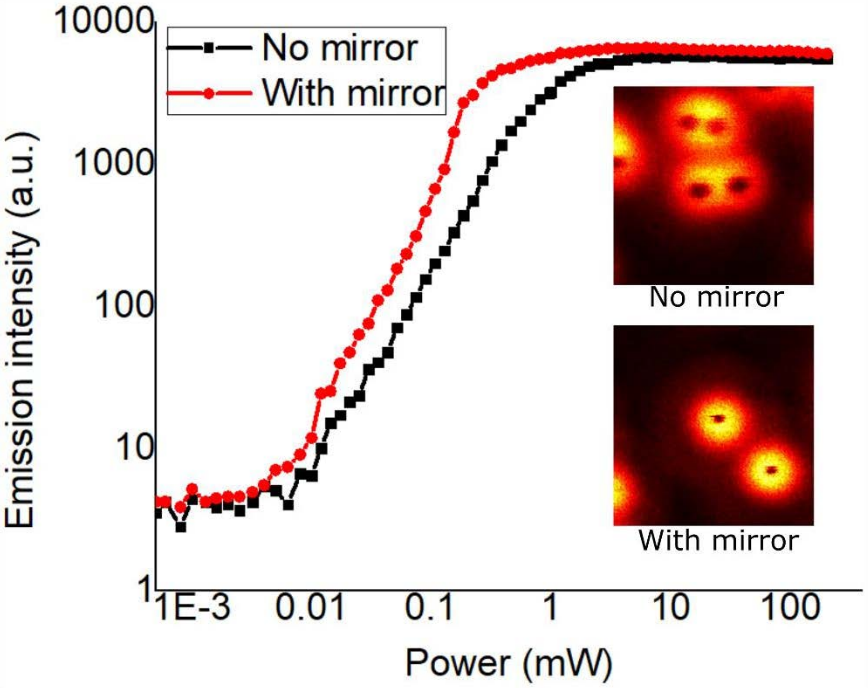

Figure 5-1 | Reducing the excitation power for NIRES microscopy using a mirror substrate. The comparison between the nonlinear optical emission response curves with and without the mirror substrate (138.4 nm silica layer as a spacer). Inset, the corresponding image with a doughnut beam at 50 mW excitation power [196].

be enhanced from 140 nm to 70 nm when using the mirror [196]. It highlights the interference effect from a mirror substrate can help obtain a high resolution under a relatively lower excitation power.

5.2.1.3 **Detecting modulation for multicolour Fourier fusion**

As introduced in Chapter 3, I develop the multicolour Fourier fusion to yield the overall enhanced imaging quality by using the heterochromatic nonlinear responses and saturated fluorescence emissions of UCNPs. In my design, I use two SPADs to detect the targeted signal with a dichroic mirror and bandpass filters. A new study can employ CCDs to replace the SPADs for fluorescence detection, like ISM [197], which may help to mitigate the frequency deficiency issues by: firstly, recording the signal that passes through the pinhole on an array detector; and secondly, capturing an image at every scan position [160].

Typically, the multicolour Fourier fusion method requires at least two cameras to collect signals simultaneously. To remove the additional camera, we can use a prism to relocalize different colour signals at the different regions on the camera, as the double viewer or quadruple viewer technologies. Furthermore, we can combine the phase mask (a single voltage pattern) [159] technique to produce the desired patterns on the CCD for the two different wavelengths. The phase mask may induce 3D information, extending the Fourier fusion approach to 3D super-resolution applications.

5.2.2 Doughnut beam with other fluorescent materials

We also can combine the doughnut beam with other materials to extend the technologies to larger communities, including both molecular format of organic dyes [184][185] and inorganic nanoparticles [186][187]. From Chapter 3, the critical points are that the emission at each band should depend highly on the excitation power and their nonlinear optical response to excitation saturation. One research work has demonstrated a new antibunching mechanism dynamic Coulomb blockade with a core-shell design [186]. When under a weak excitation, these nanoparticles emit red antibunched light (emission from quantum-confined CdSe core). At higher pump levels they exhibit an additional green band (emission from CdS shell) with bulk-like, Poissonian photon statistics. This mechanism makes it possible to generate both quantum and classical light from the same nanocrystal without any detrimental effects due to Auger decay. Thus, we can obtain two colour emissions with different response curves in one nanoparticle.

Appendix I

```
%%%%%%%%%%%%%%%%%%%%%%%%%%%%%%%%%%%%%%%%%%%%%%%%
% This code is for FED simulation      %
% Baolei Liu & Chaohao Chen 2019    %
%%%%%%%%%%%%%%%%%%%%%%%%%%%%%%%%%%%%%%%%%%%%%%%%
clear all
close all
clc
%%%%%%%%%%%%%%%%%%%%%%%%%%%%%%%%%%%%%%%%%%%%%%%%%
set(groot,'defaultFigureCreateFcn',@(fig,~)addToolbarExplorationButtons(fig))
set(groot,'defaultAxesCreateFcn',@(ax,~)set(ax.Toolbar,'Visible','off'))
%%%%%%%%%%%%%%%%%%%%%%%%%%%%%%%%%%%%%%%%%%%%%%%%%
%%%%%%%%%%%%% Generate the original pattern for simulation  %%%%%%%%%
matrix = zeros(401,401);
Io = zeros(401,401);
k=0;

for i = 16:2:28
    k = k+i;
    matrix(201,201+k) = 1;
end

for angle = 10:10:360
    matrix1 = imrotate(matrix,angle,'bicubic','crop');%nearest bilinear
    Io = Io + matrix1;
end

%%%%%%%%%%%%%%%%%%%%%%%%%%%%%%%%%%%%%%%%%%%
figure(1);imshow(Io,[]); % plot the original pattern

%%%%%%%%%%%%%%%%%%%%%%%%%%%%%%%%%%%%%%%%%%%%%%%%%
%%%%%%%%%%%%%%%%%% Generate the Gaussian PSF  %%%%%%%%%%%%%%%%
a = -100; b = 100;
x=(-100:1:100);
y=x;
[X,Y] = meshgrid(x,y);
m = (a + b)/2;
s = 35;
p1 = -.5 * ((X - m)/s) .^ 2;
p2 = (s * sqrt(2*pi));
intensity = exp(-3 * (X.^2 + Y.^2)/s^2) / p2;
intensity=intensity./max(max(intensity));

%%%%%%%%%%%%%%%%%%%%%%%%%%%%%%%%%%%%%%%%%%%%%%%%%
%%%%%%%%%%%%%%%%%% Generate the doughnut PSF  %%%%%%%%%%%%%%%%
```

```
% here we adjust the dpughnut pattern according to the experimental data %
 l =-1;        % topological charge;
 n = abs(l)+0;  % radial index; n=|l|,|l|+2,|l|+4 ...
 D = sqrt(2);   % is a constant for normalization;
Z=6; %[-] a XY-slice in the z-direction
[TH,R] = cart2pol(X,Y);
% Analytical functions
G = @(r,z) D./sqrt(1+z.^2).*exp(-r.^2./(1+z.^2)).*exp(-1i/4*(z.*r.^2)./(1+z.^2));
A = @(r,z) (sqrt(2)*r./sqrt(1+z.^2)).^abs(l).*LaguerreL((n-abs(l))/2,abs(l),2*r.^2./(1+z.^2));
PHI = @(th) exp(1i*l*th);
PSI = @(z) exp(-1i*(n+1)*atan(z));
P = @(th,r,z,t) G(r,z).*A(r,z).*PHI(th).*PSI(z).*exp(-1i*t);
p1=P(TH,R,Z,0);
p1=flipud(abs(p1).^0.06);
p1=p1./max(max(p1));

%%%%%%%%%%%%%%%%%%%%%%%%%%%%%%%%%%%%%%%%%%%%%%%%%%%%%%%%%
%%%%%%%%%%%%%%%%%%%%%%% Resize the PSF  %%%%%%%%%%%%%%%%%%
GE=intensity;
GE = imresize(GE,[105 105]);
DE=p1;
DE = imresize(DE,[105 105]);
DE(53,53)=0.5; % set the center dip has reached half maximum

%%%%%%%%%%%%%%%%%%%%%%%%%%%%%%%%%%%%%%%%%%%%%%%%%%%%%%%%%
%%%%%%%%%%%%%%%% Plot the Gaussian and doughnut PSF  %%%%%%%%%%%%
figure(2);
subplot(1,2,1); imshow(GE,[]);
subplot(1,2,2); imshow(DE,[]); colormap hot;

%%%%%%%%%%%%%%%%%%%%%%%%%%%%%%%%%%%%%%%%%%%%%%%%%%%%%%%%%
%%%%%%%%%%%%%%%% Generate the image by Gaussian PSF  %%%%%%%%%%%%
PSFsum = sum(sum(GE));
DIoT_GE = conv2(Io,GE,'same')./PSFsum;
DIoT_GE = imnoise(DIoT_GE,'poisson');
DIoT_GE = DIoT_GE./max(max(DIoT_GE));

%%%%%%%%%%%%%%%%%%%%%%%%%%%%%%%%%%%%%%%%%%%%%%%%%%%%%%%%%
%%%%%%%%%%%%%%%%% Plot the image by Gaussian PSF  %%%%%%%%%%%%%
figure(3);
imshow(DIoT_GE,[]); colormap hot; title('GE');

%%%%%%%%%%%%%%%%%%%%%%%%%%%%%%%%%%%%%%%%%%%%%%%%%%%%%%%%%
%%%%%%%%%%%%%%%% Generate the image by doughnut PSF  %%%%%%%%%%%
PSFsum = sum(sum(DE));
```

```
DIoT_DE = conv2(Io,DE,'same')./PSFsum;
DIoT_DE = imnoise(DIoT_DE,'poisson');
DIoT_DE = DIoT_DE./max(max(DIoT_DE));

%%%%%%%%%%%%%%%%%%%%%%%%%%%%%%%%%%%%%%%%%%%%%%%%%
%%%%%%%%%%%%%%%% Plot the image by doughnut PSF  %%%%%%%%%%%%%
figure(4);
imshow(DIoT_DE,[]); colormap hot; title('DE');

%%%%%%%%%%%%%%%%%%%%%%%%%%%%%%%%%%%%%%%%%%%%%%%%%
%%%%%%%%%%%%%%%%%%%% Generate FED image  %%%%%%%%%%%%%%%%
r=0.9; %  normalizing coefficient for subtraction
PSF_FED=GE-r*DE; %  Effective PSF caculation in FED
PSF_FED(PSF_FED<0)=0; % set the negative data as zero

FED=DIoT_GE-r*DIoT_DE;%  FED image caculation
FED(FED<0)=0;% set the negative data as zero
FED = FED./max(max(FED));

%%%%%%%%%%%%%%%%%%%%%%%%%%%%%%%%%%%%%%%%%%%%%%%%%
%%%%%%%%%%%%%%%%%%%%% Plot FED image  %%%%%%%%%%%%%%%%%%
figure(5);
imshow(FED,[]); colormap hot; title('FED');

%%%%%%%%%%%%%%%%%%%%%%%%%%%%%%%%%%%%%%%%%%%%%%%%%
%%%%%%%%%%%%%%%%%%%%%% Plot FED PSF  %%%%%%%%%%%%%%%%%%%
figure(6);
imshow(PSF_FED,[]); colormap hot; title('PSF_FED');

%%%%%%%%%%%%%%%%%%%%%%%%%%%%%%%%%%%%%%%%%%%%%%%%%
%%%%%%%%%%%%%%%%%% Convert PSF to OTF %%%%%%%%%%%%%%%%%%%
GE_f = fftshift(fft2(GE));
GE_f = GE_f./max(max(GE_f));
DE_f = fftshift(fft2(DE));
DE_f = DE_f./max(max(DE_f));
FED_f = fftshift(fft2(PSF_FED));
FED_f = FED_f./max(max(FED_f));

%%%%%%%%%%%%%%%%%%%%%%%%%%%%%%%%%%%%%%%%%%%%%%%%%
%%%%%%%%%%%%%%%%%%%% Plot OTF curve %%%%%%%%%%%%%%%%%%%%
figure (7);
plot(1:size(GE_f,1),abs(GE_f((size(GE_f,1)+1)/2,:).^(1/2)),'r');hold on;
plot(1:size(DE_f,1),abs(DE_f((size(DE_f,1)+1)/2,:).^(1/2)),'g');hold on;
plot(1:size(FED_f,1),abs(FED_f((size(FED_f,1)+1)/2,:).^(1/2)),'b');
title('OTF from PSF');legend('Gaussian','Donut','FED');
```

```
%%%%%%%%%%%%%%%%%%%%%%%%%%%%%%%%%%%%%%%%%%%%%%%%%%%
%%%%%%%%%%%%%%%% Plot PSF crosssection profiles %%%%%%%%%%%%%%
figure(8); fontsize=12;
Ix=GE(53,:);
Ix=Ix/max(Ix);
Iy=DE(53,:);
Iy=Iy/max(Iy);
Iz=PSF_FED(53,:);
Iz=Iz/max(Iz);
x=1:105;
plot(x,Ix,'-r','LineWidth', 2);hold on
plot(x,Iy,'-g','LineWidth', 2);hold on
plot(x,Iz,'-b','LineWidth', 2);
xlabel('x (\mum)','FontName','Times New Roman');
ylabel('Counts','FontName','Times New Roman');
title('PSF crosssection profiles');legend('Gaussian','Donut','FED');
```

```
function v = LaguerreL(varargin)
%%%%%%%%%%%%%%%%%%%%%%%%%%%%%%%%%%%%%%%%%%%%%%%%%%%
%       Plot Generalized Legendre Polynomials: LaguerreL(n,z)
%
%           Coded by Manuel Diaz, NHRI, 2018.08.28.
%               Copyright (c) 2018, Manuel Diaz.
%                       All rights reserved.
%%%%%%%%%%%%%%%%%%%%%%%%%%%%%%%%%%%%%%%%%%%%%%%%%%%
% Refs.:
% [1] Milton Abramowitz, Irene Stegun, Handbook of Mathematical Functions,
%     National Bureau of Standards, 1964, ISBN: 0-486-61272-4, LC:QA47.A34.
%%%%%%%%%%%%%%%%%%%%%%%%%%%%%%%%%%%%%%%%%%%%%%%%%%%
% Evaluates the Generalized Laguerre polynomials GL(n,k,x).
%
%  First terms:
%
%    GL(0,k,x) = 1;
%    GL(1,k,x) = 1 + k - x;
%    GL(2,k,x) = 2 + 3*k + k^2 - 4*x - 2*k*x + x^2)/2;
%    GL(3,k,x) = 6 + 11*k + 6*k^2 + k^3 - 18*x - 15*k*x - 3*k^2*x + ...
%                 9*x^2 + 3*k*x^2 - x^3)/6.
%  Recursion:
%
%    GL(0,k,X) = 1
%    GL(1,k,X) = 1 + k - x;
%
%    if 2 <= a:
```

```
%
%    GL(n,k,X) = ( (k+2*n-1-X) * GL(n-1,k,X) + (1-k-n) * GL(n-2,k,X) ) / n
%
%  Special values:
%
%    For k = 0, the associated Laguerre polynomials GL(N,K,X) are equal
%    to the Laguerre polynomials L(N,X).
%%%%%%%%%%%%%%%%%%%%%%%%%%%%%%%%%%%%%%%%%%%%%%%%%%%%
% This program and its subprograms may be freely used, modified and
% distributed under the GNU General Public License:
% http://www.gnu.org/copyleft/gpl.html
% Basic Assumptions:
% n: is a positive interger value.
% k: is a positive interger value.
% k: can be a single value or vector array.
% Function inputs:
if (nargin == 2)     % Evaluate classical Laguerre Polynomials
   n=varargin{1};
   k=0;
   x=varargin{2};
elseif (nargin == 3) % Evaluate generalized Laguerre Polynomials
   n=varargin{1};
   k=varargin{2};
   x=varargin{3};
else
   error('Usage: >> LaguerreL(n:int,k:int,x:array)');
end
% Verify inputs
if rem(n,1)~=0, error('n must be an integer.'); end
if rem(k,1)~=0, error('k must be an integer.'); end
if n < 0, error('n must be positive integer.'); end
if k < 0, error('k must be positive integer.'); end
% Initialize solution array
v = zeros(size(x));
% Compute Laguerre Polynomials
GL = zeros( numel(x), n+1 );
if n==0
   v(:) = 1.0;        % GL(0,k,x)
elseif n==1
   v(:) = 1+k-x(:);    % GL(1,k,x)
elseif n>1
   GL(:,1) = 1;        % GL(0,k,x)
   GL(:,2) = 1+k-x(:); % GL(1,k,x)
   for i = 2:n
      GL(:,i+1) = ( (k+2*i-1-x(:)).*GL(:,i) + (-k-i+1).*GL(:,i-1) )/i;
   end
```

```
   v(:) = GL(:,i+1);   % GL(n,k,x)
end
```

Appendix II

```
%%%%%%%%%%%%%%%%%%%%%%%%%%%%%%%%%%%%%%%%%%%%%%%%
% This code is for Fourier fusion simulation       %
% Baolei Liu & Chaohao Chen 2019                     %
%%%%%%%%%%%%%%%%%%%%%%%%%%%%%%%%%%%%%%%%%%%%%%%%
clear all
close all
clc
%%%%%%%%%%%%%%%%%%%%%%%%%%%%%%%%%%%%%%%%%%%%%%%%%
set(groot,'defaultFigureCreateFcn',@(fig,~)addToolbarExplorationButtons(fig))
set(groot,'defaultAxesCreateFcn',@(ax,~)set(ax.Toolbar,'Visible','off'))
%%%%%%%%%%%%%%%%%%%%%%%%%%%%%%%%%%%%%%%%%%%%%%%%%
%%%%%%%%%%%%% Generate the original pattern for simulation  %%%%%%%%%
matrix = zeros(401,401);
Io = zeros(401,401);
k=0;

for i = 16:2:28
    k = k+i;
    matrix(201,201+k) = 1;
end

for angle = 10:10:360
    matrix1 = imrotate(matrix,angle,'bicubic','crop');%nearest bilinear
    Io = Io + matrix1;
end

%%%%%%%%%%%%%%%%%%%%%%%%%%%%%%%%%%%%%%%%%
figure(1);imshow(Io,[]);% plot the original pattern

%%%%%%%%%%%%%%%%%%%%%%%%%%%%%%%%%%%%%%%%%%%%%%%%%
%%%%%%%%%%%%%%%%% Generate the Gaussian PSF  %%%%%%%%%%%%%%%
a = -100; b = 100;
x=(-100:1:100);
y=x;
[X,Y] = meshgrid(x,y);
m = (a + b)/2;
s = 35;
p1 = -.5 * ((X - m)/s) .^ 2;
p2 = (s * sqrt(2*pi));
intensity = exp(-3 * (X.^2 + Y.^2)/s^2) / p2;

%%%%%%%%%%%%%%%%%%%%%%%%%%%%%%%%%%%%%%%%%%%%%%%%%
%%%%%%%%%%%%%%%%% Generate the doughnut PSF  %%%%%%%%%%%%%%%
% here we adjust the dpughnut pattern according to the experimental data %
```

```
 l =-1;       % topological charge;
 n = abs(l)+0;  % radial index; n=|l|,|l|+2,|l|+4 ...
 D = sqrt(2);   % is a constant for normalization;
Z=6; %[-] a XY-slice in the z-direction
[TH,R] = cart2pol(X,Y);
% Analytical functions
G = @(r,z) D./sqrt(1+z.^2).*exp(-r.^2./(1+z.^2)).*exp(-1i/4*(z.*r.^2)./(1+z.^2));
A = @(r,z) (sqrt(2)*r./sqrt(1+z.^2)).^abs(l).*LaguerreL((n-
abs(l))/2,abs(l),2*r.^2./(1+z.^2));
PHI = @(th) exp(1i*l*th);
PSI = @(z) exp(-1i*(n+1)*atan(z));
P = @(th,r,z,t) G(r,z).*A(r,z).*PHI(th).*PSI(z).*exp(-1i*t);
p1=P(TH,R,Z,0);
p1=flipud(abs(p1).^0.06);
p1=p1./max(max(p1));

%%%%%%%%%%%%%%%%%%%%%%%%%%%%%%%%%%%%%%%%%%%%%%%%%%%%%%%%%%
%%%%%%%%%%%%%%%%%%%%%% Resize the PSF  %%%%%%%%%%%%%%%%%%
GE=intensity;
GE = imresize(GE,[105 105]);
DE=p1;
DE = imresize(DE,[105 105]);
DE(53,53)=0.5; % set the center dip has reached half maximum

%%%%%%%%%%%%%%%%%%%%%%%%%%%%%%%%%%%%%%%%%%%%%%%%%%%%%%%%%%
%%%%%%%%%%%%%%% Plot the Gaussian and doughnut PSF  %%%%%%%%%%%
figure(2);
subplot(1,2,1); imshow(GE,[]);
subplot(1,2,2); imshow(DE,[]); colormap hot;
xlabel('x (\mum)','FontName','Times New Roman');
ylabel('Counts','FontName','Times New Roman');

%%%%%%%%%%%%%%%%%%%%%%%%%%%%%%%%%%%%%%%%%%%%%%%%%%%%%%%%%%
%%%%%%%%%%%%%%% Generate the image by Gaussian PSF  %%%%%%%%%%%
PSFsum = sum(sum(GE));
DIoT_GE = conv2(Io,GE,'same')./PSFsum;
DIoT_GE = imnoise(DIoT_GE,'poisson');
DIoT_GE = DIoT_GE./max(max(DIoT_GE));

%%%%%%%%%%%%%%%%%%%%%%%%%%%%%%%%%%%%%%%%%%%%%%%%%%%%%%%%%%
%%%%%%%%%%%%%%%% Plot the image by Gaussian PSF  %%%%%%%%%%%%
figure(3);
imshow(DIoT_GE,[]); colormap hot; title('GE');

%%%%%%%%%%%%%%%%%%%%%%%%%%%%%%%%%%%%%%%%%%%%%%%%%%%%%%%%%%
%%%%%%%%%%%%%%% Generate the image by doughnut PSF  %%%%%%%%%%
```

```
PSFsum = sum(sum(DE));
DIoT_DE = conv2(Io,DE,'same')./PSFsum;
DIoT_DE = imnoise(DIoT_DE,'poisson');
DIoT_DE = DIoT_DE./max(max(DIoT_DE));

%%%%%%%%%%%%%%%%%%%%%%%%%%%%%%%%%%%%%%%%%%%%%%%%%
%%%%%%%%%%%%%%%% Plot the image by doughnut PSF  %%%%%%%%%%%%%
figure(4);
imshow(DIoT_DE,[]); colormap hot; title('DE');

%%%%%%%%%%%%%%%%%%%%%%%%%%%%%%%%%%%%%%%%%%%%%%%%%
%%%%%%%%%%%%%%%% Deconvolution with doughnut PSF  %%%%%%%%%%%%
iterations = 150; % internation times
lucy_dI1=deconvlucy(real(DIoT_DE),DE,iterations);
lucy_dI1 = lucy_dI1./max(max(lucy_dI1));

%%%%%%%%%%%%%%%%%%%%%%%%%%%%%%%%%%%%%%%%%%%%%%%%%
%%%%%%%%%%%%%% Polt the doughnut deconvoluted image %%%%%%%%%%%%
figure(5);
imshow([lucy_dI1],[]);colormap hot;
title('donut lucy deconv')
drawnow

%%%%%%%%%%%%%%%%%%%%%%%%%%%%%%%%%%%%%%%%%%%%%%%%%
%%%%%%%%%%%%%%%% Deconvolution with Gaussian PSF  %%%%%%%%%%%%
lucy_dI2=deconvlucy(real(DIoT_GE),GE,iterations);

%%%%%%%%%%%%%%%%%%%%%%%%%%%%%%%%%%%%%%%%%%%%%%%%%
%%%%%%%%%%%%%% Polt the Gaussian deconvoluted image %%%%%%%%%%%%
figure(6);
imshow([lucy_dI2],[]);colormap hot;
lucy_dI2 = lucy_dI2./max(max(lucy_dI2));
title('gaussian lucy deconv')
drawnow

%%%%%%%%%%%%%%%%%%%%%%%%%%%%%%%%%%%%%%%%%%%%%%%%%
%%%%%%%%%%%%%%%%%% Convert PSF to OTF %%%%%%%%%%%%%%%%%%%
I1_f = fftshift(fft2(DIoT_GE));
I1_f = I1_f./max(max(I1_f));
I2_f = fftshift(fft2(DIoT_DE));
I2_f = I2_f./max(max(I2_f));
GE_f = fftshift(fft2(GE));
GE_f = GE_f./max(max(GE_f));
DE_f = fftshift(fft2(DE));
DE_f = DE_f./max(max(DE_f));
```

```
%%%%%%%%%%%%%%%%%%%%%%%%%%%%%%%%%%%%%%%%%%%%%%%%%
%%%%%%%%%%%%%%% Design mask for Fourier fusion %%%%%%%%%%%%%%%%
factor = 0.160; % factor to set the cutoff frequency for Fourier fusion
GE_f_mask = circular_mask(GE_f,factor,false); % Low pass from Gaussian
DE_f_mask = circular_mask(DE_f,factor,true); % High pass from doughnut
I1_f_mask = circular_mask(I1_f,factor,false); % Low pass from Gaussian
I2_f_mask = circular_mask(I2_f,factor,true); % High pass from doughnut

%%%%%%%%%%%%%%%%%%%%%%%%%%%%%%%%%%%%%%%%%%%%%%%%%
%%%%%%%%%%%%%%%%%%%%% Fusion PSF %%%%%%%%%%%%%%%%%%%%%
Fusion_f = GE_f_mask+2.5.*DE_f_mask; % 2.5 is the fusion factor
Fusion_f = Fusion_f./max(max(Fusion_f));
Fusion = ifft2(Fusion_f);
Fusion = Fusion./max(max(Fusion));

%%%%%%%%%%%%%%%%%%%%%%%%%%%%%%%%%%%%%%%%%%%%%%%%%
%%%%%%%%%%%%%%%%%%%%% Fusion image %%%%%%%%%%%%%%%%%%%%%
I3_Fusion = fftshift(I1_f_mask+2.5.*I2_f_mask); % fusion factor should be same
I3_Fusion = I3_Fusion./max(max(I3_Fusion));
I3 = ifft2(I3_Fusion);
I3 = I3./max(max(I3));

%%%%%%%%%%%%%%%%%%%%%%%%%%%%%%%%%%%%%%%%%%%%%%%%%
%%%%%%%%%%%%%%%%%%%%% Plot OTF curves %%%%%%%%%%%%%%%%%%
figure (7);
plot(1:size(GE_f,1),abs(GE_f((size(GE_f,1)+1)/2,:).^(1/2)),'r');hold on;
plot(1:size(DE_f,1),abs(DE_f((size(DE_f,1)+1)/2,:).^(1/2)),'g');hold on;
plot(1:size(Fusion_f,1),abs(Fusion_f((size(Fusion_f,1)+1)/2,:).^(1/2)),'b');
title('OTF from PSF');legend('Gaussian','Donut','MISS');

%%%%%%%%%%%%%%%%%%%%%%%%%%%%%%%%%%%%%%%%%%%%%%%%%
%%%%%%%%%%%%%%%%%%%%%%% Plot OTF %%%%%%%%%%%%%%%%%%%%
figure (8);
subplot(1,3,1);
imshow(abs(GE_f).^(1/3.5),[]);title('Gaussian OTF from PSF');
subplot(1,3,2);
imshow(abs(DE_f).^(1/3.5),[]);title('Donut OTF from PSF');
subplot(1,3,3);
imshow(abs(Fusion_f.^(1/3.5)),[]);title('MISS OTF from PSF');

%%%%%%%%%%%%%%%%%%%%%%%%%%%%%%%%%%%%%%%%%%%%%%%%%
%%%%%%%%%%%%%%%%%%%%%%% Plot PSF %%%%%%%%%%%%%%%%%%%%
figure (9);
subplot(1,3,1);
imshow(GE./max(max(GE)),'InitialMagnification','fit');colormap hot;title('Gaussian PSF');
```

```
subplot(1,3,2);
imshow(DE./max(max(DE)),'InitialMagnification','fit');colormap hot;title('Donut PSF');
subplot(1,3,3);
imshow(abs(Fusion)./max(max(abs(Fusion))),'InitialMagnification','fit');colormap
hot;title('MISS PSF');

%%%%%%%%%%%%%%%%%%%%%%%%%%%%%%%%%%%%%%%%%%%%%%%%%
%%%%%%%%%%%%%%%%% Fourier fusion deconvolution %%%%%%%%%%%%%%
lucy_dI3 = deconvlucy(abs(I3),abs(Fusion),iterations);
lucy_dI3 = lucy_dI3./max(max(lucy_dI3));

%%%%%%%%%%%%%%%%%%%%%%%%%%%%%%%%%%%%%%%%%%%%%%%%%
%%%%%%%%%%%%%%%%% Plot the Fourer fusion results %%%%%%%%%%%%%%
figure (10);
subplot(2,2,1);
imshow(DIoT_GE,'InitialMagnification','fit');
colormap hot;title('Original Gaussian');
subplot(2,2,2);
imshow(DIoT_DE,'InitialMagnification','fit');
colormap hot;title('Original Donut');
subplot(2,2,3);
imshow(abs(I3),'InitialMagnification','fit');
colormap hot;title('MISS Fusion');
subplot(2,2,4);
imshow(abs(lucy_dI3),'InitialMagnification','fit');
colormap hot;title('MISS lucy deconv');

%%%%%%%%%%%%%%%%%%%%%%%%%%%%%%%%%%%%%%%%%%%%%%%%%
%%%%%%%%% Comparision of deconvoluted results with different PSFs %%%%%%
figure (11);
subplot(1,3,1);
imshow([lucy_dI2],[],'InitialMagnification','fit');
colormap hot;title('De_Gaussian');
subplot(1,3,2);
imshow([lucy_dI1],[],'InitialMagnification','fit');
colormap hot;title('De_Donut');
subplot(1,3,3);
imshow(abs(lucy_dI3),'InitialMagnification','fit');
colormap hot;title('De_Fusion');

%%%%%%%%%%%%%%%%%%%%%%%%%%%%%%%%%%%%%%%%%%%%%%%%%
%%%%%%%%%%%%%% Cross section profiles of different PSFs %%%%%%%%%%%
figure(12); fontsize=12;
Ix=GE((size(GE,1)+1)/2,:);
Ix=flipud(abs(Ix));
Ix=Ix/max(Ix);
```

```
Iy=DE((size(DE,1)+1)/2,:);
Iy=flipud(abs(Iy));
Iy=Iy/max(Iy);
If=Fusion((size(Fusion,1)+1)/2,:);
If=flipud(abs(If));
If=If/max(If);
c=(-52:1:52);
plot(c,Ix,'-.r','LineWidth', 2);hold on
plot(c,Iy,'-og','LineWidth', 2);hold on
plot(c,If,'--*b','LineWidth', 2);hold on
xlabel('x (\mum)','FontName','Times New Roman');
ylabel('Counts','FontName','Times New Roman');
legend('gaussian','doughnut','fusion');
```

```
function [ masked ] = circular_mask(data, ratio, invert)
% Name: circular_mask.m
% grating = circular_mask(grating,0.25,false);
% Description: Apply a circular mask
% Params:
%  data   - input matrix
%  ratio  - mask size
%  invert - invert mask?
dims = size(data);
width = dims(1);
height = dims(2);
[W, H] = meshgrid(1:width,1:height);

if invert
    mask = sqrt((W-width/2-1).^2 + (H-height/2-1).^2) > ratio*width/2;
else
    mask = sqrt((W-width/2-1).^2 + (H-height/2-1).^2) < ratio*width/2;
end
%%%%%%%%%%%% gaussian low pass filter %%%%%%%%%%%%%%%%%%%
w = fspecial('gaussian',[15 15],5);
mask = imfilter(mask,w);
%%%%%%%%%%%%%%%%%%%%%%%%%%%%%%%%%%%%%%%%%%%%%%
 masked = data .* mask';
end
```

References

[1] F. N. Egerton, “A History of the Ecological Sciences, Part 16: Robert Hooke and the Royal Society of London,” *Bull. Ecol. Soc. Am.*, vol. 86, no. 2, pp. 93–101, 2005.

[2] K. Uluç, G. C. Kujoth, and M. K. Başkaya, “Operating microscopes: past, present, and future,” *Neurosurg. Focus*, vol. 27, no. 3, p. E4, 2009.

[3] S. W. Hell *et al.*, “The 2015 super-resolution microscopy roadmap,” *J. Phys. D. Appl. Phys.*, vol. 48, no. 44, p. 443001, 2015.

[4] T. A. Klar, E. Engel, and S. W. Hell, “Breaking Abbe’s diffraction resolution limit in fluorescence microscopy with stimulated emission depletion beams of various shapes,” *Phys. Rev. E*, vol. 64, no. 6, p. 066613, 2001.

[5] F. Effersø, E. Auken, and K. I. Sørensen, “Inversion of band-limited TEM responses,” *Geophys. Prospect.*, vol. 47, no. 4, pp. 551–564, 1999.

[6] D. Axelrod, “Total Internal Reflection Fluorescence Microscopy in Cell Biology,” *Traffic*, vol. 2, no. 11, pp. 764–774, 2001.

[7] D. Vobornik and S. Vobornik, “Scanning Near-Field Optical Microscopy,” *Bosn. J. Basic Med. Sci.*, vol. 8, no. 1, pp. 63–71, 2008.

[8] C. Tressler, “Characterization and alignment of the STED doughnut using fluorescence correlation spectroscopy,” McMaster University, 2013.

[9] S. W. Hell and J. Wichmann, “Breaking the diffraction resolution limit by stimulated emission: stimulated-emission-depletion fluorescence microscopy,” *Opt. Lett.*, vol. 19, no. 11, p. 780, 1994.

[10] K. I. Willig, B. Harke, R. Medda, and S. W. Hell, “STED microscopy with continuous wave beams,” *Nat. Methods*, vol. 4, no. 11, pp. 915–918, 2007.

[11] M. K. S.W. Hell, “Ground-state-depletion fluorscence microscopy: a concept for breaking the diffraction resolution limit,” *Appl. Phys. B*, vol. 60, pp. 495–497, 1996.

[12] M. G. L. Gustafsson, “Nonlinear structured-illumination microscopy: Wide-field fluorescence imaging with theoretically unlimited resolution,” *Proc. Natl. Acad. Sci.*, vol. 102, no. 37, pp. 13081–13086, 2005.

[13] E. Betzig *et al.*, “Imaging Intracellular Fluorescent Proteins at Nanometer Resolution,” *Science*, vol. 313, pp. 1642–1645, 2006.

[14] M. J. Rust, M. Bates, and X. Zhuang, “Sub-diffraction-limit imaging by stochastic optical reconstruction microscopy (STORM),” *Nat. Methods*, vol. 3, no. 10, pp. 793–796, 2006.

[15] E. Cortés *et al.*, “Plasmonic Nanoprobes for Stimulated Emission Depletion Nanoscopy,” *ACS Nano*, vol. 10, no. 11, pp. 10454–10461, 2016.

[16] E. Rittweger, K. Y. Han, S. E. Irvine, C. Eggeling, and S. W. Hell, “STED microscopy reveals crystal colour centres with nanometric resolution,” *Nat. Photonics*, vol. 3, no. 3, pp. 144–147, 2009.

[17] V. Westphal, S. O. Rizzoli, M. A. Lauterbach, D. Kamin, R. Jahn, and S. W. Hell, “Video-rate far-field optical nanoscopy dissects synaptic vesicle movement,” *Science*, vol. 320, no. 5873, pp. 246–249, 2008.

[18] B. Hein, K. I. Willig, and S. W. Hell, “Stimulated emission depletion (STED) nanoscopy of a fluorescent protein-labeled organelle inside a living cell,” *Proc. Natl. Acad. Sci.*, vol. 105, no. 38, pp. 14271–14276, 2008.

[19] R. Schmidt, C. A. Wurm, S. Jakobs, J. Engelhardt, A. Egner, and S. W. Hell, “Spherical nanosized focal spot unravels the interior of cells,” *Nat. Methods*, vol. 5, no. 6, pp. 539–544, 2008.

[20] R. Schmidt, C. A. Wurm, A. Punge, A. Egner, S. Jakobs, and S. W. Hell, “Mitochondrial cristae revealed with focused light,” *Nano Lett.*, vol. 9, no. 6, pp. 2508–2510, 2009.

[21] M. Pascucci, S. Ganesan, A. Tripathi, O. Katz, V. Emiliani, and M. Guillon, “Compressive three-dimensional super-resolution microscopy with speckle-saturated fluorescence excitation,” *Nat. Commun.*, vol. 10, no. 1, p. 1327, 2019.

[22] M. G. L. Gustafsson, “Surpassing the lateral resolution limit by a factor of two using structured illumination microscopy,” *J. Microsc.*, vol. 198, no. 2, pp. 82–87, 2000.

[23] S. Quirin, S. R. P. Pavani, and R. Piestun, “Optimal 3D single-molecule localization for superresolution microscopy with aberrations and engineered point spread functions,” *Proc. Natl. Acad. Sci.*, vol. 109, no. 3, pp. 675–679, Jan. 2012.

[24] M. Yamanaka, N. I. Smith, and K. Fujita, “Introduction to super-resolution microscopy,” *Microscopy*, vol. 63, no. 3, pp. 177–192, 2014.

[25] M. J. Mlodzianoski *et al.*, “Active PSF shaping and adaptive optics enable volumetric localization microscopy through brain sections,” *Nat. Methods*, vol. 15, no. 8, pp. 583–586, 2018.

[26] R. P. J. Nieuwenhuizen *et al.*, “Measuring image resolution in optical nanoscopy,” *Nat. Methods*, vol. 10, no. 6, pp. 557–562, 2013.

[27] A. Descloux, K. S. Grußmayer, and A. Radenovic, “Parameter-free image resolution estimation based on decorrelation analysis,” *Nat. Methods*, vol. 16, no. 9, pp. 918–924, 2019.

[28] T. Dertinger, R. Colyer, G. Iyer, S. Weiss, and J. Enderlein, “Fast, background-free, 3D super-resolution optical fluctuation imaging (SOFI),” *Proc. Natl. Acad. Sci.*, vol. 106, no. 52, pp. 22287–22292, 2009.

[29] J. Schnitzbauer, M. T. Strauss, T. Schlichthaerle, F. Schueder, and R. Jungmann, “Super-resolution microscopy with DNA-PAINT,” *Nat. Protoc.*, vol. 12, no. 6, pp. 1198–1228, 2017.

[30] A. Sharonov and R. M. Hochstrasser, “Wide-field subdiffraction imaging by accumulated binding of diffusing probes,” *Proc. Natl. Acad. Sci.*, vol. 103, no. 50, pp. 18911–18916, 2006.

[31] R. Jungmann, C. Steinhauer, M. Scheible, A. Kuzyk, P. Tinnefeld, and F. C. Simmel, “Single-molecule kinetics and super-resolution microscopy by

fluorescence imaging of transient binding on DNA origami," *Nano Lett.*, vol. 10, no. 11, pp. 4756–4761, 2010.

[32] R. Jungmann, M. S. Avendaño, J. B. Woehrstein, M. Dai, W. M. Shih, and P. Yin, "Multiplexed 3D cellular super-resolution imaging with DNA-PAINT and Exchange-PAINT," *Nat. Methods*, vol. 11, no. 3, pp. 313–318, 2014.

[33] M. T. Strauss, F. Schueder, D. Haas, P. C. Nickels, and R. Jungmann, "Quantifying absolute addressability in DNA origami with molecular resolution," *Nat. Commun.*, vol. 9, no. 1, p. 1600, 2018.

[34] A. Auer, M. T. Strauss, T. Schlichthaerle, and R. Jungmann, "Fast, Background-Free DNA-PAINT Imaging Using FRET-Based Probes," *Nano Lett.*, vol. 17, no. 10, pp. 6428–6434, 2017.

[35] N. S. Deußner-Helfmann *et al.*, "Correlative Single-Molecule FRET and DNA-PAINT Imaging," *Nano Lett.*, vol. 18, no. 7, pp. 4626–4630, 2018.

[36] D. Jin, P. Xi, B. Wang, L. Zhang, and A. M. Van Oijen, "Nanoparticles for super-resolution microscopy and single-molecule tracking," *Nat. Methods*, vol. 15, pp. 415–423, 2018.

[37] C. Drees, A. N. Raj, R. Kurre, K. B. Busch, M. Haase, and J. Piehler, "Engineered Upconversion Nanoparticles for Resolving Protein Interactions inside Living Cells," *Angew. Chemie Int. Ed.*, vol. 55, no. 38, pp. 11668–11672, 2016.

[38] C. Yao *et al.*, "Near-Infrared-Triggered Azobenzene-Liposome/Upconversion Nanoparticle Hybrid Vesicles for Remotely Controlled Drug Delivery to Overcome Cancer Multidrug Resistance," *Adv. Mater.*, vol. 28, no. 42, pp. 9341–9348, 2016.

[39] G. Tian, X. Zhang, Z. Gu, and Y. Zhao, "Recent Advances in Upconversion Nanoparticles-Based Multifunctional Nanocomposites for Combined Cancer Therapy," *Adv. Mater.*, vol. 27, no. 47, pp. 7692–7712, 2015.

[40] S. H. Nam *et al.*, "Long-Term Real-Time Tracking of Lanthanide Ion Doped Upconverting Nanoparticles in Living Cells," *Angew. Chemie Int. Ed.*, vol. 50, no. 27, pp. 6093–6097, 2011.

[41] M. He *et al.*, "Monodisperse Dual-Functional Upconversion Nanoparticles Enabled Near-Infrared Organolead Halide Perovskite Solar Cells," *Angew. Chemie*, vol. 55, no. 13, pp. 4280–4284, 2016.

[42] S. Wu and H. J. Butt, "Near-Infrared-Sensitive Materials Based on Upconverting Nanoparticles," *Adv. Mater.*, vol. 28, no. 6, pp. 1208–1226, 2016.

[43] X. Gao, Y. Cui, R. M. Levenson, L. W. K. Chung, and S. Nie, "In vivo cancer targeting and imaging with semiconductor quantum dots," *Nat. Biotechnol.*, vol. 22, no. 8, pp. 969–976, 2004.

[44] O. T. Bruns *et al.*, "Next-generation in vivo optical imaging with short-wave infrared quantum dots," *Nat. Biomed. Eng.*, vol. 1, no. 4, p. 0056, 2017.

[45] F. Ren *et al.*, "Development and Investigation of Ultrastable PbS/CdS/ZnS Quantum Dots for Near-Infrared Tumor Imaging," *Part. Part. Syst. Charact.*, vol. 34, no. 2, p. 1600242, 2017.

[46] Y. Wang, G. Fruhwirth, E. Cai, T. Ng, and P. R. Selvin, "3D super-resolution imaging with blinking quantum dots," *Nano Lett.*, vol. 13, no. 11, pp. 5233–5241, 2013.

[47] Z. Zeng *et al.*, "Fast Super-Resolution Imaging with Ultra-High Labeling Density Achieved by Joint Tagging Super-Resolution Optical Fluctuation Imaging," *Sci. Rep.*, vol. 5, no. 1, p. 8359, 2015.

[48] R. Li, X. Chen, Z. Lin, Y. Wang, and Y. Sun, "Expansion enhanced nanoscopy," *Nanoscale*, vol. 10, no. 37, pp. 17552–17556, 2018.

[49] X. Yang *et al.*, "Versatile Application of Fluorescent Quantum Dot Labels in Super-resolution Fluorescence Microscopy," *ACS Photonics*, vol. 3, no. 9, pp. 1611–1618, 2016.

[50] M. Zhao, S. Ye, X. Peng, J. Song, and J. Qu, "Green emitted CdSe@ZnS quantum dots for FLIM and STED imaging applications," *J. Innov. Opt. Health Sci.*, vol. 12, no. 05, p. 1940003, 2019.

[51] J. Hanne *et al.*, "STED nanoscopy with fluorescent quantum dots," *Nat. Commun.*, vol. 6, no. 1, p. 7127, 2015.

[52] B. Zhi *et al.*, "Malic Acid Carbon Dots: From Super-resolution Live-Cell Imaging to Highly Efficient Separation," *ACS Nano*, vol. 12, no. 6, pp. 5741–5752, 2018.

[53] S. N. Baker and G. A. Baker, "Luminescent Carbon Nanodots: Emergent Nanolights," *Angew. Chemie Int. Ed.*, vol. 49, no. 38, pp. 6726–6744, 2010.

[54] A. M. Chizhik *et al.*, "Super-Resolution Optical Fluctuation Bio-Imaging with Dual-Color Carbon Nanodots," *Nano Lett.*, vol. 16, no. 1, pp. 237–242, 2016.

[55] Y. Wang, Z. Bai, Q. Wang, and G. Wang, "Experimental Investigations on Fluorescence Excitation and Depletion of Carbon Dots," *J. Fluoresc.*, vol. 27, no. 4, pp. 1435–1441, 2017.

[56] G. Leménager, E. De Luca, Y.-P. Sun, and P. P. Pompa, "Super-resolution fluorescence imaging of biocompatible carbon dots," *Nanoscale*, vol. 6, no. 15, p. 8617, 2014.

[57] L. Bu *et al.*, "One-step synthesis of N-doped carbon dots, and their applications in curcumin sensing, fluorescent inks, and super-resolution nanoscopy," *Microchim. Acta*, vol. 186, no. 10, p. 675, 2019.

[58] H. He *et al.*, "High-Density Super-Resolution Localization Imaging with Blinking Carbon Dots," *Anal. Chem.*, vol. 89, no. 21, pp. 11831–11838, 2017.

[59] G. Han *et al.*, "Membrane-Penetrating Carbon Quantum Dots for Imaging Nucleic Acid Structures in Live Organisms," *Angew. Chemie Int. Ed.*, vol. 58, no. 21, pp. 7087–7091, 2019.

[60] X. Chen *et al.*, "Small Photoblinking Semiconductor Polymer Dots for Fluorescence Nanoscopy," *Adv. Mater.*, vol. 29, no. 5, p. 1604850, 2017.

[61] X. Chen *et al.*, "Multicolor Super-resolution Fluorescence Microscopy with Blue and Carmine Small Photoblinking Polymer Dots," *ACS Nano*, vol. 11, no. 8, pp. 8084–8091, 2017.

[62] Z. Liu *et al.*, “Narrow-band polymer dots with pronounced fluorescence fluctuations for dual-color super-resolution imaging,” *Nanoscale*, vol. 12, no. 3, pp. 165–172, 2020.

[63] Z. Sun *et al.*, “Semiconducting Polymer Dots with Modulated Photoblinking for High-Order Super-Resolution Optical Fluctuation Imaging,” *Adv. Opt. Mater.*, vol. 7, no. 9, p. 1900007, 2019.

[64] S. Cox *et al.*, “Bayesian localization microscopy reveals nanoscale podosome dynamics,” *Nat. Methods*, vol. 9, no. 2, pp. 195–200, 2012.

[65] D. T. Burnette, P. Sengupta, Y. Dai, J. Lippincott-Schwartz, and B. Kachar, “Bleaching/blinking assisted localization microscopy for superresolution imaging using standard fluorescent molecules,” *Proc. Natl. Acad. Sci.*, vol. 108, no. 52, pp. 21081–21086, 2011.

[66] J. Yu *et al.*, “Low photobleaching and high emission depletion efficiency: the potential of AIE luminogen as fluorescent probe for STED microscopy,” *Opt. Lett.*, vol. 40, no. 10, p. 2313, 2015.

[67] J. Luo *et al.*, “Aggregation-induced emission of 1-methyl-1,2,3,4,5-pentaphenylsilole,” *Chem. Commun.*, vol. 18, no. 18, pp. 1740–1741, 2001.

[68] Q. Y. Zhou *et al.*, “AIE-based universal super-resolution imaging for inorganic and organic nanostructures,” *Mater. Horizons*, vol. 5, no. 3, pp. 474–479, 2018.

[69] D. Li, W. Qin, B. Xu, J. Qian, and B. Z. Tang, “AIE Nanoparticles with High Stimulated Emission Depletion Efficiency and Photobleaching Resistance for Long-Term Super-Resolution Bioimaging,” *Adv. Mater.*, vol. 29, no. 43, p. 1703643, 2017.

[70] C. Y.-W. Lo *et al.*, “Novel super-resolution capable mitochondrial probe, MitoRed AIE, enables assessment of real-time molecular mitochondrial dynamics,” *Sci. Rep.*, vol. 6, no. 1, p. 30855, 2016.

[71] D. Li *et al.*, “Aggregation-induced emission luminogen-assisted stimulated emission depletion nanoscopy for super-resolution mitochondrial visualization in live cells,” *Nano Res.*, vol. 11, no. 11, pp. 6023–6033, 2018.

[72] J. Zhou, G. Yu, and F. Huang, “AIE opens new applications in super-resolution imaging,” *J. Mater. Chem. B*, vol. 4, no. 48, pp. 7761–7765, 2016.

[73] X. Gu *et al.*, “A Mitochondrion-Specific Photoactivatable Fluorescence Turn-On AIE-Based Bioprobe for Localization Super-Resolution Microscope,” *Adv. Mater.*, vol. 28, no. 25, pp. 5064–5071, 2016.

[74] Y. L. Wang *et al.*, “AIE-based super-resolution imaging probes for β-amyloid plaques in mouse brains,” *Mater. Chem. Front.*, vol. 2, no. 8, pp. 1554–1562, 2018.

[75] X. Fang *et al.*, “Multicolor Photo-Crosslinkable AIEgens toward Compact Nanodots for Subcellular Imaging and STED Nanoscopy,” *Small*, vol. 13, no. 41, p. 1702128, 2017.

[76] G. Hong *et al.*, “Multifunctional in vivo vascular imaging using near-infrared II fluorescence,” *Nat. Med.*, vol. 18, no. 12, pp. 1841–1846, 2012.

[77] W. Zheng, P. Huang, D. Tu, E. Ma, H. Zhu, and X. Chen, “Lanthanide-doped upconversion nano-bioprobes: electronic structures, optical properties, and biodetection,” *Chem. Soc. Rev.*, vol. 44, no. 6, pp. 1379–1415, 2015.

[78] S. Han, R. Deng, X. Xie, and X. Liu, “Enhancing luminescence in lanthanide-doped upconversion nanoparticles,” *Angew. Chemie*, vol. 53, no. 44, pp. 11702–11715, 2014.

[79] Y. Liu *et al.*, “Amplified stimulated emission in upconversion nanoparticles for super-resolution nanoscopy,” *Nature*, vol. 543, no. 7644, pp. 229–233, 2017.

[80] Q. Zhan *et al.*, “Achieving high-efficiency emission depletion nanoscopy by employing cross relaxation in upconversion nanoparticles,” *Nat. Commun.*, vol. 8, no. 1, p. 1058, Dec. 2017.

[81] C. Kuang *et al.*, “Breaking the Diffraction Barrier Using Fluorescence Emission Difference Microscopy,” *Sci. Rep.*, vol. 3, no. 1, p. 1441, 2013.

[82] Q. Wu, B. Huang, X. Peng, S. He, and Q. Zhan, “Non-bleaching fluorescence emission difference microscopy using single 808-nm laser excited red upconversion emission,” *Opt. Express*, vol. 25, no. 25, p. 30885, 2017.

[83] C. Chen *et al.*, “Multi-photon near-infrared emission saturation nanoscopy using upconversion nanoparticles,” *Nat. Commun.*, vol. 9, no. 1, p. 3290, 2018.

[84] C. Chen, F. Wang, S. Wen, Y. Liu, X. Shan, and D. Jin, “Upconversion nanoparticles assisted multi-photon fluorescence saturation microscopy,” in *Nanoscale Imaging, Sensing, and Actuation for Biomedical Applications XVI*, 2019, no. 108910S, p. 25.

[85] Y. Liu *et al.*, “Super-Resolution Mapping of Single Nanoparticles inside Tumor Spheroids,” *Small*, vol. 16, no. 6, p. 1905572, 2020.

[86] Y. Liu *et al.*, “Deep tissue super-resolution microscopy mapping single nanoparticles inside multicellular spheroids,” in *Enhanced Spectroscopies and Nanoimaging 2020*, 2020, p. 51.

[87] B. Huang, Q. Wu, X. Peng, L. Yao, D. Peng, and Q. Zhan, “One-scan fluorescence emission difference nanoscopy developed with excitation orthogonalized upconversion nanoparticles,” *Nanoscale*, vol. 10, no. 45, pp. 21025–21030, 2018.

[88] A. Bednarkiewicz, E. M. Chan, A. Kotulska, L. Marciniak, and K. Prorok, “Photon avalanche in lanthanide doped nanoparticles for biomedical applications: Super-resolution imaging,” *Nanoscale Horizons*, vol. 4, no. 4, pp. 881–889, 2019.

[89] D. Denkova *et al.*, “3D sub-diffraction imaging in a conventional confocal configuration by exploiting super-linear emitters,” *Nat. Commun.*, vol. 10, no. 1, p. 3695, 2019.

[90] B. Liu *et al.*, “Upconversion Nonlinear Structured Illumination Microscopy,” *Nano Lett.*, vol. 20, no. 7, pp. 4775–4781, 2020.

[91] C. Hu *et al.*, “MUTE-SIM: multiphoton up-conversion time-encoded structured illumination microscopy,” *OSA Contin.*, vol. 3, no. 3, p. 594, 2020.

[92] B. Liu, F. Wang, C. Chen, F. Dong, and D. McGloin, "Self-evolving ghost imaging," 2020. DOI: arXiv:2008.00648 (eess).

[93] H. T. T. Duong *et al.*, "Systematic investigation of functional ligands for colloidal stable upconversion nanoparticles," *RSC Adv.*, vol. 8, no. 9, pp. 4842–4849, 2018.

[94] H. He *et al.*, "Bispecific Antibody-Functionalized Upconversion Nanoprobe," *Anal. Chem.*, vol. 90, no. 5, pp. 3024–3029, 2018.

[95] Y. Sun *et al.*, "A supramolecular self-assembly strategy for upconversion nanoparticle bioconjugation," *Chem. Commun.*, vol. 54, no. 31, pp. 3851–3854, 2018.

[96] W. Ren *et al.*, "Anisotropic functionalization of upconversion nanoparticles," *Chem. Sci.*, vol. 9, no. 18, pp. 4352–4358, 2018.

[97] S. Chen *et al.*, "Near-infrared deep brain stimulation via upconversion nanoparticle–mediated optogenetics," *Science*, vol. 359, no. 6376, pp. 679–684, 2018.

[98] K. Yadav *et al.*, "Targeted and efficient activation of channelrhodopsins expressed in living cells via specifically-bound upconversion nanoparticles," *Nanoscale*, vol. 9, no. 27, pp. 9457–9466, 2017.

[99] F. Wang *et al.*, "Microscopic inspection and tracking of single upconversion nanoparticles in living cells," *Light Sci. Appl.*, vol. 7, no. 4, p. 18007, 2018.

[100] Y. M. Bae *et al.*, "Endocytosis, intracellular transport, and exocytosis of lanthanide-doped upconverting nanoparticles in single living cells," *Biomaterials*, vol. 33, no. 35, pp. 9080–9086, 2012.

[101] G. Lin, M. A. B. Baker, M. Hong, and D. Jin, "The Quest for Optical Multiplexing in Bio-discoveries," *Chem*, vol. 4, no. 5, pp. 997–1021, 2018.

[102] Y. Zhang *et al.*, "Multicolor barcoding in a single upconversion crystal," *J. Am. Chem. Soc.*, vol. 136, no. 13, pp. 4893–4896, 2014.

[103] Y. Lu *et al.*, "Tunable lifetime multiplexing using luminescent nanocrystals," *Nat. Photonics*, vol. 8, no. 1, pp. 32–36, 2014.

[104] R. D. Frankel, "Discussion of methods for depth enhancement in single and multiphoton-stimulated emission microscopy," *J. Opt. Soc. Am. B*, vol. 33, no. 7, p. 1421, 2016.

[105] B. Yang, J. Trebbia, R. Baby, P. Tamarat, and B. Lounis, "Optical nanoscopy with excited state saturation at liquid helium temperatures," *Nat. Photonics*, vol. 9, no. 10, pp. 658–662, 2015.

[106] M. Hofmann, C. Eggeling, S. Jakobs, and S. W. Hell, "Breaking the diffraction barrier in fluorescence microscopy at low light intensities by using reversibly photoswitchable proteins," *Proc. Natl. Acad. Sci.*, vol. 102, no. 49, pp. 17565–17569, 2005.

[107] M. Ingaramo, A. G. York, E. J. Andrade, K. Rainey, and G. H. Patterson, "Two-photon-like microscopy with orders-of-magnitude lower illumination intensity via two-step fluorescence," *Nat. Commun.*, vol. 6, no. 1, p. 8184, 2015.

[108] A. G. York *et al.*, “Resolution doubling in live, multicellular organisms via multifocal structured illumination microscopy,” *Nat. Methods*, vol. 9, no. 7, pp. 749–754, 2012.

[109] P. W. Winter, P. Chandris, R. S. Fischer, Y. Wu, C. M. Waterman, and H. Shroff, “Incoherent structured illumination improves optical sectioning and contrast in multiphoton super-resolution microscopy,” *Opt. Express*, vol. 23, no. 4, p. 5327, 2015.

[110] W. Zheng *et al.*, “Adaptive optics improves multiphoton super-resolution imaging,” *Nat. Methods*, vol. 14, no. 9, pp. 869–872, 2017.

[111] K. T. Takasaki, “Development and Application of Two-Photon Excitation Stimulated Emission Depletion Microscopy for Superresolution Fluorescence Imaging in Thick Tissue,” Harvard University, 2013.

[112] K. T. Takasaki, J. B. Ding, and B. L. Sabatini, “Live-cell superresolution imaging by pulsed STED two-photon excitation microscopy,” *Biophys. J.*, vol. 104, no. 4, pp. 770–777, 2013.

[113] G. M. S. W. Hell, “Two-photon excitation STED microscopy,” *Opt. Express*, vol. 17, no. 17. pp. 14567–14573, 2009.

[114] P. Bianchini, B. Harke, S. Galiani, G. Vicidomini, and A. Diaspro, “Single-wavelength two-photon excitation-stimulated emission depletion (SW2PE-STED) superresolution imaging,” *Proc. Natl. Acad. Sci.*, vol. 109, no. 17, pp. 6390–6393, 2012.

[115] M. Zhao *et al.*, “Cellular imaging of deep organ using two-photon Bessel light-sheet nonlinear structured illumination microscopy,” *Biomed. Opt. Express*, vol. 5, no. 5, p. 1296, 2014.

[116] E. E. Hoover and J. A. Squier, “Advances in multiphoton microscopy technology,” *Nat. Photonics*, vol. 7, pp. 93–101, 2013.

[117] M. Balu, T. Baldacchini, J. Carter, T. B. Krasieva, R. Zadoyan, and B. J. Tromberg, “Effect of excitation wavelength on penetration depth in nonlinear optical microscopy of turbid media,” *J. Biomed. Opt.*, vol. 14, no. 1, p. 010508, 2009.

[118] S. W. Hell and J. Wichmann, “Breaking the diffraction resolution limit by stimulated emission: stimulated-emission-depletion fluorescence microscopy,” *Opt. Lett.*, vol. 19, no. 11, p. 780, 1994.

[119] T. A. Klar, S. Jakobs, M. Dyba, A. Egner, and S. W. Hell, “Fluorescence microscopy with diffraction resolution barrier broken by stimulated emission,” *Proc. Natl. Acad. Sci.*, vol. 97, no. 15, pp. 8206–8210, 2000.

[120] J. B. Ding, K. T. Takasaki, and B. L. Sabatini, “Supraresolution Imaging in Brain Slices using Stimulated-Emission Depletion Two-Photon Laser Scanning Microscopy,” *Neuron*, vol. 63, no. 4, pp. 429–437, 2009.

[121] Q. Li, S. S. H. Wu, and K. C. Chou, “Subdiffraction-limit two-photon fluorescence microscopy for GFP-tagged cell imaging,” *Biophys. J.*, vol. 97, no. 12, pp. 3224–3228, 2009.

[122] P. Bethge, R. Chéreau, E. Avignone, G. Marsicano, and U. V. Nägerl, “Two-photon excitation STED microscopy in two colors in acute brain slices,” *Biophys. J.*, vol. 104, no. 4, pp. 778–785, 2013.

[123] Y. Il Park, K. T. Lee, Y. D. Suh, and T. Hyeon, “Upconverting nanoparticles: a versatile platform for wide-field two-photon microscopy and multi-modal in vivo imaging,” *Chem. Soc. Rev.*, vol. 44, no. 6, pp. 1302–1317, 2015.

[124] X. Xie, N. Gao, R. Deng, Q. Sun, Q. Xu, and X. Liu, “Mechanistic Investigation of Photon Upconversion in Nd 3+ -Sensitized Core–Shell Nanoparticles,” *J. Am. Chem. Soc.*, vol. 135, no. 34, pp. 12608–12611, 2013.

[125] J. Oracz *et al.*, “Ground State Depletion Nanoscopy Resolves Semiconductor Nanowire Barcode Segments at Room Temperature,” *Nano Lett.*, vol. 17, no. 4, pp. 2652–2659, 2017.

[126] A. M. Smith, M. C. Mancini, and S. Nie, “Bioimaging: Second window for in vivo imaging,” *Nat. Nanotechnol.*, vol. 4, no. 11, pp. 710–711, 2009.

[127] G. Zhao, C. Kuang, Z. Ding, and X. Liu, “Resolution enhancement of saturated fluorescence emission difference microscopy,” *Opt. Express*, vol. 24, no. 20, pp. 23596–23609, 2016.

[128] E. Rittweger, D. Wildanger, and S. W. Hell, “Far-field fluorescence nanoscopy of diamond color centers by ground state depletion,” *EPL*, vol. 86, no. 1, p. 14001, 2009.

[129] K. Y. Han, S. K. Kim, C. Eggeling, and S. W. Hell, “Metastable dark states enable ground state depletion microscopy of nitrogen vacancy centers in diamond with diffraction-unlimited resolution,” *Nano Lett.*, vol. 10, no. 8, pp. 3199–3203, 2010.

[130] D. Liu *et al.*, “Three-dimensional controlled growth of monodisperse sub-50 nm heterogeneous nanocrystals,” *Nat. Commun.*, vol. 7, no. 1, p. 10254, 2016.

[131] G. Zhao *et al.*, “Saturated absorption competition microscopy,” *Optica*, vol. 4, no. 6, p. 633, 2017.

[132] N. T. Urban, K. I. Willig, S. W. Hell, and U. V. Nägerl, “STED nanoscopy of actin dynamics in synapses deep inside living brain slices,” *Biophys. J.*, vol. 101, no. 5, pp. 1277–1284, 2011.

[133] P. Giannios *et al.*, “Visible to near-infrared refractive properties of freshly-excised human-liver tissues: marking hepatic malignancies,” *Sci. Rep.*, vol. 6, no. 1, p. 27910, 2016.

[134] P. Giannios, S. Koutsoumpos, K. G. Toutouzas, M. Matiatou, G. C. Zografos, and K. Moutzouris, “Complex refractive index of normal and malignant human colorectal tissue in the visible and near-infrared,” *J. Biophotonics*, vol. 10, no. 2, pp. 303–310, 2017.

[135] F. Kang, J. He, T. Sun, Z. Y. Bao, F. Wang, and D. Y. Lei, “Plasmonic Dual-Enhancement and Precise Color Tuning of Gold Nanorod@SiO 2 Coupled Core–Shell–Shell Upconversion Nanocrystals,” *Adv. Funct. Mater.*, vol. 27, no. 36, p. 1701842, 2017.

[136] A. L. Feng *et al.*, “Distance-Dependent Plasmon-Enhanced Fluorescence of Upconversion Nanoparticles using Polyelectrolyte Multilayers as Tunable Spacers,” *Sci. Rep.*, vol. 5, no. 1, p. 7779, 2015.

[137] M. Sun *et al.*, “Hierarchical Plasmonic Nanorods and Upconversion Core-Satellite Nanoassemblies for Multimodal Imaging-Guided Combination Phototherapy,” *Adv. Mater.*, vol. 28, no. 5, pp. 898–904, 2016.

[138] C. Clarke *et al.*, “Large-scale dewetting assembly of gold nanoparticles for plasmonic enhanced upconversion nanoparticles,” *Nanoscale*, vol. 10, no. 14, pp. 6270–6276, 2018.

[139] Y. Zhong *et al.*, “Boosting the down-shifting luminescence of rare-earth nanocrystals for biological imaging beyond 1500 nm,” *Nat. Commun.*, vol. 8, no. 1, p. 737, 2017.

[140] T. Scheul, C. D’Amico, I. Wang, and J.-C. Vial, “Two-photon excitation and stimulated emission depletion by a single wavelength,” *Optics Express*, vol. 19, no. 19. p. 18036, 2011.

[141] I. Coto Hernández *et al.*, “Two-Photon Excitation STED Microscopy with Time-Gated Detection,” *Sci. Rep.*, vol. 6, no. 1, p. 19419, 2016.

[142] L. He *et al.*, “Near-infrared photoactivatable control of Ca2+ signaling and optogenetic immunomodulation,” *Elife*, vol. 4, no. e10024, pp. 1–25, 2015.

[143] H. L. Jo *et al.*, “Fast and background-free three-dimensional (3D) live-cell imaging with lanthanide-doped upconverting nanoparticles,” *Nanoscale*, vol. 7, no. 46, pp. 19397–19402, 2015.

[144] E. Mudry *et al.*, “Structured illumination microscopy using unknown speckle patterns,” *Nat. Photonics*, vol. 6, no. 5, pp. 312–315, 2012.

[145] H. Yilmaz, E. G. van Putten, J. Bertolotti, A. Lagendijk, W. L. Vos, and A. P. Mosk, “Speckle correlation resolution enhancement of wide-field fluorescence imaging,” *Optica*, vol. 2, no. 5, p. 424, 2015.

[146] M. J. Rust, M. Bates, and X. Zhuang, “Sub-diffraction-limit imaging by stochastic optical reconstruction microscopy (STORM),” *Nat. Methods*, vol. 3, no. 10, pp. 793–796, 2006.

[147] A. Beghin *et al.*, “Localization-based super-resolution imaging meets high-content screening,” *Nat. Methods*, vol. 14, no. 12, pp. 1184–1190, 2017.

[148] S. Chong, W. Min, and X. S. Xie, “Ground-state depletion microscopy: Detection sensitivity of single-molecule optical absorption at room temperature,” *J. Phys. Chem. Lett.*, vol. 1, no. 23, pp. 3316–3322, 2010.

[149] K. Fujita, M. Kobayashi, S. Kawano, M. Yamanaka, and S. Kawata, “High-Resolution Confocal Microscopy by Saturated Excitation of Fluorescence,” *Phys. Rev. Lett.*, vol. 99, no. 22, p. 228105, 2007.

[150] T. Grotjohann *et al.*, “Diffraction-unlimited all-optical imaging and writing with a photochromic GFP,” *Nature*, vol. 478, no. 7368, pp. 204–208, 2011.

[151] B. E. Urban *et al.*, “Super-resolution two-photon microscopy via scanning patterned illumination,” *Phys. Rev. E*, vol. 91, no. 4, p. 042703, 2015.

[152] C. B. Müller and J. Enderlein, “Image Scanning Microscopy,” *Phys. Rev. Lett.*, vol. 104, no. 19, p. 198101, 2010.

[153] G. P. J. Laporte, N. Stasio, C. J. R. Sheppard, and D. Psaltis, “Resolution enhancement in nonlinear scanning microscopy through post-detection digital computation,” *Optica*, vol. 1, no. 6, p. 455, 2014.

[154] M. Fernández-Suárez and A. Y. Ting, “Fluorescent probes for super-resolution imaging in living cells,” *Nat. Rev. Mol. Cell Biol.*, vol. 9, no. 12, pp. 929–943, 2008.

[155] Y. Shechtman, L. E. Weiss, A. S. Backer, S. J. Sahl, and W. E. Moerner, “Precise Three-Dimensional Scan-Free Multiple-Particle Tracking over Large Axial Ranges with Tetrapod Point Spread Functions,” *Nano Lett.*, vol. 15, no. 6, pp. 4194–4199, 2015.

[156] S. R. P. Pavani *et al.*, “Three-dimensional, single-molecule fluorescence imaging beyond the diffraction limit by using a double-helix point spread function,” *Proc. Natl. Acad. Sci.*, vol. 106, no. 9, pp. 2995–2999, 2009.

[157] Y. Shechtman, S. J. Sahl, A. S. Backer, and W. E. Moerner, “Optimal Point Spread Function Design for 3D Imaging,” *Phys. Rev. Lett.*, vol. 113, no. 13, p. 133902, 2014.

[158] S. Jia, J. C. Vaughan, and X. Zhuang, “Isotropic three-dimensional super-resolution imaging with a self-bending point spread function,” *Nat. Photonics*, vol. 8, no. 4, pp. 302–306, 2014.

[159] Y. Shechtman, L. E. Weiss, A. S. Backer, M. Y. Lee, and W. E. Moerner, “Multicolour localization microscopy by point-spread-function engineering,” *Nat. Photonics*, vol. 10, no. 9, pp. 590–594, 2016.

[160] E. N. Ward and R. Pal, “Image scanning microscopy: an overview,” *J. Microsc.*, vol. 266, no. 2, pp. 221–228, 2017.

[161] P. Wang *et al.*, “Far-field imaging of non-fluorescent species with subdiffraction resolution,” *Nat. Photonics*, vol. 7, no. 6, pp. 449–453, 2013.

[162] Nick Efford, *Digital Image Processing: A Practical Introduction Using Java*. Pearson Education, 2000.

[163] S. Milan, H. Vaclav, and B. Roger, *Image Processing, Analysis, and Machine Vision*. University Press, Cambridge, 2007.

[164] K. Korobchevskaya *et al.*, “Intensity Weighted Subtraction Microscopy Approach for Image Contrast and Resolution Enhancement,” *Sci. Rep.*, vol. 6, no. 1, p. 25816, 2016.

[165] G. Zhao *et al.*, “Nonlinear Focal Modulation Microscopy,” *Phys. Rev. Lett.*, vol. 120, no. 19, p. 193901, 2018.

[166] S. Wen, J. Zhou, K. Zheng, A. Bednarkiewicz, X. Liu, and D. Jin, “Advances in highly doped upconversion nanoparticles,” *Nat. Commun.*, vol. 9, no. 1, p. 2415, 2018.

[167] A. Fernandez-Bravo *et al.*, "Ultralow-threshold, continuous-wave upconverting lasing from subwavelength plasmons," *Nat. Mater.*, vol. 18, no. 11, pp. 1172–1176, 2019.

[168] E. Ortiz-Rivero *et al.*, "Single-Cell Biodetection by Upconverting Microspinners," *Small*, vol. 15, no. 46, p. 1904154, 2019.

[169] A. Lay *et al.*, "Upconverting Nanoparticles as Optical Sensors of Nano- to Micro-Newton Forces," *Nano Lett.*, vol. 17, no. 7, pp. 4172–4177, 2017.

[170] C. D. S. Brites *et al.*, "Instantaneous ballistic velocity of suspended Brownian nanocrystals measured by upconversion nanothermometry," *Nat. Nanotechnol.*, vol. 11, no. 10, pp. 851–856, 2016.

[171] F. Wang *et al.*, "Simultaneous phase and size control of upconversion nanocrystals through lanthanide doping," *Nature*, vol. 463, no. 7284, pp. 1061–1065, 2010.

[172] X. Zeng *et al.*, "Visualization of Intra-neuronal Motor Protein Transport through Upconversion Microscopy," *Angew. Chemie Int. Ed.*, vol. 58, no. 27, pp. 9262–9268, 2019.

[173] J. Liao, D. Jin, C. Chen, Y. Li, and J. Zhou, "Helix Shape Power-Dependent Properties of Single Upconversion Nanoparticles," *J. Phys. Chem. Lett.*, vol. 11, no. 8, pp. 2883–2890, 2020.

[174] Zhen Zhang, "3D Nanoscale architecture of microtubule network," 2017. [Online]. Available: https://www.nikonsmallworld.com/galleries/2017-photomicrography-competition/3d-nanoscale-architecture-of-microtubule-network.

[175] N. Banterle, K. H. Bui, E. A. Lemke, and M. Beck, "Fourier ring correlation as a resolution criterion for super-resolution microscopy," *J. Struct. Biol.*, vol. 183, no. 3, pp. 363–367, 2013.

[176] G. Tortarolo, M. Castello, A. Diaspro, S. Koho, and G. Vicidomini, "Evaluating image resolution in stimulated emission depletion microscopy," *Optica*, vol. 5, no. 1, p. 32, 2018.

[177] L. Thibon, M. Piché, and Y. De Koninck, "Resolution enhancement in laser scanning microscopy with deconvolution switching laser modes (D-SLAM)," *Opt. Express*, vol. 26, no. 19, p. 24881, 2018.

[178] I. Gregor, M. Spiecker, R. Petrovsky, J. Großhans, R. Ros, and J. Enderlein, "Rapid nonlinear image scanning microscopy," *Nat. Methods*, vol. 14, no. 11, pp. 1087–1089, 2017.

[179] L. Lanzanò, I. Coto Hernández, M. Castello, E. Gratton, A. Diaspro, and G. Vicidomini, "Encoding and decoding spatio-temporal information for super-resolution microscopy," *Nat. Commun.*, vol. 6, no. 1, p. 6701, 2015.

[180] M. J. Sarmento *et al.*, "Exploiting the tunability of stimulated emission depletion microscopy for super-resolution imaging of nuclear structures," *Nat. Commun.*, vol. 9, no. 1, p. 3415, 2018.

[181] T. Vettenburg *et al.*, "Light-sheet microscopy using an Airy beam," *Nat. Methods*, vol. 11, no. 5, pp. 541–544, 2014.

[182] T.-L. Liu *et al.*, “Observing the cell in its native state: Imaging subcellular dynamics in multicellular organisms,” *Science (80-.).*, vol. 360, no. 6386, p. eaaq1392, 2018.

[183] C. Chen, Z. Liu, and D. Jin, “Bypassing the limit in volumetric imaging of mesoscale specimens,” *Adv. Photonics*, vol. 1, no. 02, p. 1, 2019.

[184] D. Kim *et al.*, “Dual-color fluorescent nanoparticles showing perfect color-specific photoswitching for bioimaging and super-resolution microscopy,” *Nat. Commun.*, vol. 10, no. 1, p. 3089, 2019.

[185] Z. He *et al.*, “White light emission from a single organic molecule with dual phosphorescence at room temperature,” *Nat. Commun.*, vol. 8, no. 1, p. 416, 2017.

[186] C. Galland, S. Brovelli, W. K. Bae, L. A. Padilha, F. Meinardi, and V. I. Klimov, “Dynamic hole blockade yields two-color quantum and classical light from dot-in-bulk nanocrystals,” *Nano Lett.*, vol. 13, no. 1, pp. 321–328, 2013.

[187] Z. Xie *et al.*, “White-Light Emission Strategy of a Single Organic Compound with Aggregation-Induced Emission and Delayed Fluorescence Properties,” *Angew. Chemie Int. Ed.*, vol. 54, no. 24, pp. 7181–7184, 2015.

[188] Y. Fan, S. Wang, and F. Zhang, “Optical Multiplexed Bioassays for Improved Biomedical Diagnostics,” *Angew. Chemie Int. Ed.*, vol. 58, no. 38, pp. 13208–13219, 2019.

[189] L. Zhou *et al.*, “Single-band upconversion nanoprobes for multiplexed simultaneous in situ molecular mapping of cancer biomarkers,” *Nat. Commun.*, vol. 6, no. 1, p. 6938, 2015.

[190] D. J. Gargas *et al.*, “Engineering bright sub-10-nm upconverting nanocrystals for single-molecule imaging,” *Nat. Nanotechnol.*, vol. 9, no. 4, pp. 300–305, 2014.

[191] H. Zhang, J. Cadusch, C. Kinnear, T. James, A. Roberts, and P. Mulvaney, “Direct assembly of large area nanoparticle arrays,” *ACS Nano*, vol. 12, no. 8, pp. 7529–7537, 2018.

[192] L. Zhou, Y. Fan, R. Wang, X. Li, L. Fan, and F. Zhang, “High-Capacity Upconversion Wavelength and Lifetime Binary Encoding for Multiplexed Biodetection,” *Angew. Chemie Int. Ed.*, vol. 57, no. 39, pp. 12824–12829, 2018.

[193] Y. Fan *et al.*, “Lifetime-engineered NIR-II nanoparticles unlock multiplexed in vivo imaging,” *Nat. Nanotechnol.*, vol. 13, no. 10, pp. 941–946, 2018.

[194] H. Ren, X. Li, Q. Zhang, and M. Gu, “Applied physics: On-chip noninterference angular momentum multiplexing of broadband light,” *Science*, vol. 352, no. 6287, pp. 805–809, 2016.

[195] X. Yang *et al.*, “Mirror-enhanced super-resolution microscopy,” *Light Sci. Appl.*, vol. 5, no. 6, p. e16134, 2016.

[196] Zhiguang Zhou, “Single upconversion nanoparticle optical characterizations for biophotonic applications,” University of Technology Sydney, 2019.

[197] C. B. Müller and J. Enderlein, “Image Scanning Microscopy,” *Phys. Rev. Lett.*, vol. 104, no. 19, p. 198101, 2010.